Title
Polymer-Particle Composites for Additive Manufacturing

Author
Kumar, Rajan

Publication Date
2019

UNIVERSITY OF CALIFORNIA SAN DIEGO

Polymer-Particle Composites for Additive Manufacturing

A dissertation submitted in partial satisfaction of the

requirements for the degree Doctor of Philosophy

in

Nanoengineering

by

Rajan Kumar

Committee in Charge:

Professor Todd Coleman, Chair
Professor Jan Talbot, Co-Chair
Professor Patrick Mercier
Professor Tina Ng
Professor Donald Sirbuly

2019

The dissertation of Rajan Kumar is approved, and it is acceptable in quality and form for publication on microfilm and electronically:

University of California San Diego

2019

DEDICATION

To my parents and fiancée, to whom I owe an insurmountable debt of gratitude for their patience, contributions and support during times of doubt.

And to my professors, colleagues, and friends who have fostered by curiosity and ambition to solve to critical problems facing society today.

EPIGRAPH

If you can’t explain it simply, you don’t understand it well enough

Albert Einstein

Dream audaciously. Have the courage to fail forward. Act with urgency

Phil Knight

The people who are crazy enough to think they can
change the world are the ones who do

Steve Jobs

The most profound technologies are those that disappear. They weave themselves into the fabric of everyday life until they are indistinguishable from it.

Mark Weiser

TABLE OF CONTENTS

LIST OF FIGURES AND TABLES

ACKNOWLEDGEMENTS

I would like to acknowledge Professor Todd Coleman and Professor Jan Talbot for their support as my co-chair of my committee. Through multiple drafts, long nights, and frustrations with experiments, their guidance and unwavering support has proved to be invaluable.

I would also like to acknowledge the individuals and mentors in Nanobioelectronics Lab (Prof. Joseph Wang) and Laboratory for Energy Storage and Conversion (Prof. Shirely Meng). These colleagues that have become close friends and inspirational scientists, without whom my research and my ambitions would have no doubt taken longer and more difficult. It is their support and their confidence in me has given me the energy to take on great scientific challenges.

In the past five years, I have been fortunate to work with so many wonderful colleagues. Here I would like to thank Dr. Amay Bandodkar, Dr. Gabriela Valdés-Ramírez, Dr. Vinu Mohan, Dr. Jung-Min You, Dr. Jaewook Shin, Dr. Joshua Windmiller, Dr. Jayoung Kim, Rogelio Nuñez Flores, Cristian Silva López, Somayeh Imani, Rajan Kumar, Itthipon Jeerapan, Jennifer Miller, William Getz, Carlos Munoz, Karan Sheth, Xinyu Liu, Lu Yin and all the wonderful colleagues who supported me through the completion of my dissertation. I give most of the credit to my parents, my sister, and my fiancée who have encouraged and provide the resources for me to dream big. I owe my successes and growth to my family's consistent and unwavering support.

Chapter 1 is based, in part, on the material as it appears in Advanced Electronic Materials, 2017, by Dr. Jayoung Kim, Rajan Kumar, Dr. Amay Bandodkar and Joseph Wang. This review was focused on dissertation author's notion or concept of particle-polymer composites or could be commonly referred as functional inks when combined with additive manufacturing. The dissertation author was the corresponding author on this review based on doctoral research focusing on developing novel particle-polymers for many new functional devices and technologies.

Chapter 2 is based, in part, on the material as it appears in Royal Society of Chemistry, Advances, 2015, by Rajan Kumar, Melek Kristi, Fernando Soto, Jinxing Li, Virendra V. Singh, and Joseph Wang. The dissertation author was the primary investigator and author of this publication that describes the development of catalytic, printed motors through the development of catalytic composite particle.

Chapter 3 is based, in part, on the material as it appears in Scientific Reports, 2017, by Rajan Kumar, Sunmi Shin, Joog Wook Roh, Dong-Su Ko, Hyun-Sik Kim, Sang Il Kim, Lu Yin, Sarah Schlossberg, Shuang Cui, Jung-Ming You, Sooshin Kwon, Jianlin Zheng, Joseph Wang and Renkun Chen. The dissertation author was the co-investigator on key formulations of thermoelectric inks and improvements to the printing process which resulted in improved thermoelectric performance.

Chapter 4 is based, in part, on the material as it appears in Advanced Materials Technologies, 2017, by Rajan Kumar, Vinu Mohan, NamHeon Kim, Amay Bandodkar, Jung-Min You, Jonas Kurniawan, Sheng Xu, and Joseph Wang. As a corresponding author of the project, the dissertation author aided in the design and fabrication of the hybrid devices. In addition, the author was critical to analysis of their durability testing and optical characterization.

Chapter 5 is based, in part, on the materials as it appears in in Advanced Energy Materials, 2017, by Rajan Kumar, Jaewook Shin, Lu Yin, Jung-Min You, Ying Shirley

Meng, and Joseph Wang. The dissertation author is the primary author and inventor of the hyperelastic composite inks for printed, stretchable batteries. In addition, the primary author demonstrated the first analytical tool to measure strain stress analysis of composite devices, particularly for stretchable electronics.

Chapter 6, in part is currently being prepared for submission for publication of the material, by Rajan Kumar and Todd Coleman. The dissertation author is the primary investigator and author of this material.

VITA

2014	Bachelor of Nanoscale Science, College of Nanoscale Science & Engineering – SUNY Albany, NY
2016	Master of Engineering, Department of Nanoengineering University of California, San Diego
2019	Doctor of Philosophy, Department of Nanoengineering University of California, San Diego

FIELDS OF STUDY

Major Field: Nanoscale Science & Nanoengineering

Professor Todd Coleman

Professor Jan Talbot

PUBLICATIONS

1. Yin, L., Seo, J. K., Kurniawan, J., Kumar, R., Lv, J., Xie, L., Xinyu, L., Xu, S., Meng, Y. S., and Wang, J. (2018). Highly Stable Battery Pack via Insulated, Reinforced, Buckling-Enabled Interconnect Array. *Small*, *14*(43), 1800938.
2. Lu, Y., Rajan Kumar, K. Aleksandar, X. Lingye, Y. Jung-min, J. Davina, L. C. Silva, M. Jennifer and W. Joseph (2018). "From All-Printed 2D Patterns to Free-Standing 3D Structures: Controlled Buckling and Selective Bonding." Advanced Materials Technologies 3(5): 1800013.

3. Bandodkar, A. J., S. Imani, R. Nuñez-Flores, Rajan Kumar, C. Wang, A. M. V. Mohan, J. Wang and P. P. Mercier (2018). "Re-usable electrochemical glucose sensors integrated into a smartphone platform." Biosensors and Bioelectronics 101: 181-187.
4. Karshalev, E., Rajan Kumar, I. Jeerapan, R. Castillo, I. Campos and J. Wang (2018). "Multi, stimuli-Responsive Camouflage Swimmers." Chemistry of Materials 30(5): 1593- 1601.
5. Shin, Sunmi, Rajan Kumar, Jong Wook Roh, Dong-Su Ko, Hyun-Sik Kim, Sang Il Kim, Lu Yin, Sarah M. Schlossberg, Shuang Cui, Jung-Min You, Soonshin Kwon, Jianlin Zheng, Joseph Wang & Renkun Chen. "High-performance screen-printed thermoelectric films on fabrics." *Scientific reports* 7, no. 1 (2017): 7317.
6. Bandodkar, Amay, Jung-Min You, Nam-Heon Kim, Yue Gu, Rajan Kumar, Vinu Mohan AM, Jonas Felipe Kurniawan et al. "Soft, stretchable, high power density electronic skin-based biofuel cells for scavenging energy from human sweat." Energy & Environmental Science (2017).
7. Kumar, Rajan, Jaewook Shin, Lu Yin, Jung-Min You, Ying Shirley Meng, and Joseph Wang. "All-Printed, Stretchable Zn-Ag_2O Rechargeable Battery via Hyperelastic Binder for Self- Powering Wearable Electronics." Advanced Energy Materials 7, no. 8 (2017).
8. Mishra, Rupesh K., Lee J. Hubble, Aida Martín, Rajan Kumar, Abbas Barfidokht, Jayoung Kim, Mustafa M. Musameh, Ilias L. Kyratzis, and Joseph Wang. "Wearable flexible and stretchable glove biosensor for on-site detection of organophosphorus chemical threats." ACS Sensors 2, no. 4 (2017): 553-561.

9. Mohan, A. M., NamHeon Kim, Yue Gu, Amay J. Bandodkar, Jung-Min You, Rajan Kumar, Jonas F. Kurniawan, Sheng Xu, and Joseph Wang. "Merging of Thin-and Thick-Film Fabrication Technologies: Toward Soft Stretchable “Island–Bridge” Devices." Advanced Materials Technologies 2, no. 4 (2017).

10. Kim, Jayoung, Rajan Kumar, Amay J. Bandodkar, and Joseph Wang. "Advanced materials for printed wearable electrochemical devices: A review." *Advanced Electronic Materials* 3, no. 1 (2017): 1600260.

11. Bandodkar, Amay J., Cristian S. López, Allibai Mohanan Vinu Mohan, Lu Yin, Rajan Kumar, and Joseph Wang. "All-printed magnetically self-healing electrochemical devices." Science advances 2, no. 11 (2016): e1601465.

12. Imani, Somayeh, Amay J. Bandodkar, AM Vinu Mohan, Rajan Kumar, Shengfei Yu, Joseph Wang, and Patrick P. Mercier. "A wearable chemical–electrophysiological hybrid biosensing system for real-time health and fitness monitoring." Nature communications 7 (2016): ncomms11650.

13. Shin, JaeWook, Jung-Min You, Jungwoo Z. Lee, Rajan Kumar, Lu Yin, Joseph Wang, and Y. Shirley Meng. "Deposition of ZnO on bismuth species towards a rechargeable Zn-based aqueous battery." Physical Chemistry Chemical Physics 18, no. 38 (2016): 26376-26382.

14. Kassal, Petar, Jayoung Kim, Rajan Kumar, William R. de Araujo, Ivana Murković Steinberg, Matthew D. Steinberg, and Joseph Wang. "Smart bandage with wireless connectivity for uric acid biosensing as an indicator of wound status." Electrochemistry Communications 56 (2015): 6-10.

15. Kumar, Rajan, Melek Kiristi, Fernando Soto, Jinxing Li, Virendra V. Singh, and Joseph Wang. "Self-propelled screen-printable catalytic swimmers." *RSC Advances* 5, no. 96 (2015): 78986-78993.

16. Petar Kassal, Jayoung Kim, Rajan Kumar, William R. de Araujo, Ivana Murković Steinberg, Matthew D. Steinberg, Joseph Wang, Smart bandage with wireless connectivity for uric acid biosensing as an indicator of wound status, Electrochemistry Communications, Volume 56, July 2015, Pg. 6-10.

ABSTRACT OF THE DISSERTATION

Polymer-Particle Composites for Additive Manufacturing

by

Rajan Kumar

Doctor of Philosophy in Nanoengineering

University of California, San Diego, 2019

Professor Todd Coleman, Chair

Professor Jan Talbot, Co-Chair

Over the past century, society has been riding a wave of technology revolution empowered by Moore’s Law that has enabled trillion devices proliferating into every aspect of our daily lives. Only through innovation in material science of silicon-based transistors and manufacturing capability of advanced deposition and lithography process has made this possible. The next century is beginning to see a new emergence of “more than Moore” with devices attributing new properties such as conformability, transient/edible, self-healing, actuating motion and so much more. Similarly, these devices will be formed from union of new and old technologies, where they can be fabricated using high-throughput printing technologies for make them affordable and ubiquitous. This dissertation focuses on the composition of various innovations of particle-polymer composites with additive manufacturing process such as screen-printing to design and fabricate multiple technologies such as self-propelling motors, energy harvesting, energy storage, stretchable electronics, and wearable devices. The dissertation provides strategy to develop new composites for their respective technologies by sourcing the composite materials necessary to optimize the composite characteristics, which would be studied through characterization and device evaluation by varying the composite ratios. The development of new composite materials for emerging technologies is enabling a new vision of how technologies can continue to weave into every fabric of our lives.

CHAPTER 1: INTRODUCTION

1.1 Introduction and Objectives

The past decade has seen significant progress in the field of particle-polymer composites through respective innovations in particle and polymer synthesis. The particle synthesis has become its own plethora of design based on various materials, morphologies, and crystal structure. The polymers have been widely used in the plastic and coating industry for their robustness and ubiquity. These polymers have interesting functionalities that are not possible with traditional particles such as stretch ability, flexibility, electro actuating. The combination of these polymers and particles presents new opportunities for design and functionality when developed with additive manufacturing process. Yet, there are still many challenges regarding to how these materials integrated with traditional, rigid microchip that power many technologies that are accelerating change today.

Today, all of electronics are manufactured using printed circuit boards and microchips as their platform. In the future, technology will eventually become entirely flexible or even stretchable for scalable electronics, but there are still significant technological limitations in microprocessors that need to be overcome while retaining their low cost and scalability. The solution for today will be the development of hybrid electronics using rigid microprocesses with conformal circuit design and power sources. This can only be solved through innovative cross-disciplinary research and industry for innovations in materials, understanding fundamentals of manufacturing electronics, and from the humanities for user behavior.

This research attempts to overcome some of the design limitations by current state of technologies particularly for wearables and "Internet of Things" that remains bulky, rigid, limited to a selection of few compatible materials. While many approaches have been pursued to develop conformal electronics through engineering design and advanced materials, this thesis focuses on the combination of particle-polymer composites and additive manufacturing to usher in a new generation of conformal electronics. Particularly, through the development of numerous particle-polymer composites sourced from conductors, insulators, semiconductors with inorganic/organic polymers can enable complex materials with unique composite behaviors. This research has demonstrated many first examples of technologies catalytic motors, thermoelectric, biofuel cells, electrochemical sensors, and energy storage using additive manufacturing for customized design and their respective composite materials to enable new functionalities for conformal electronic applications. These devices are becoming apart of new emergence of "more than Moore" with devices with new properties such as conformability, transiency, self-healing, actuating motion, and so much more.

The following chapters focus on the development of particle-polymer composites for developing technologies that can truly become ubiquitous. These devices will assist in their use for large-area or high quantity of devices that are needed to solve many techno-economic challenges we face today. Chapter 1 reviews the materials and fabrication requirements for these composite materials and their functionalities, especially where progress has made in their composite functionality of flexibility, stretch ability, or self-healing. These composites are made through the metallic or semiconducting particles when mixed with functional polymers to formulate conductive inks. The use of conductive inks with additive manufacturing will enable these devices characterized as beyond Moore to be affordable and ubiquitous for the challenges ahead.

In Chapter 2, the development of the first catalytic, composite inks and design of screen-printed motors capable of customizable shapes and design without compromising scale. Many nanoscale, catalytic motors had been developed for nanoscale applications such as drug delivery or microscale treatment. Some work previous works were demonstrated for environmental remediation, but the economics of scale would make the application unfeasible. In Chapter 3, a similar analogy was applied to thermoelectric technologies capable of energy harvesting from the body or providing a solid-state temperature control. These devices have been widely used for space applications, but continued development in materials, especially in particle-polymer composites presents an interested opportunity to integrate these devices in wearables and smart textiles.

In Chapter 4, the first demonstration of developing stretchable electronics through multiple degrees of freedom from the deterministic design such as serpentine structures through lithographic designs incorporated with particle-polymer composites to build functional sensors and biofuel. Since many of lithographic approaches for the island-bridge have limited list of compatible materials, this process opens up new designs and materials by merging the capabilities of additive manufacturing and subtractive manufacturing, such as lithographic and chemical etching.

In Chapter 5 and Chapter 6, similar concept of advanced materials using battery materials and stretchable polymers is used to formulate a conformal, customizable energy solution for flexible electronics. Many wearables and technologies are continually getting more flexible and smaller, but current battery technologies based on their assembly and materials have limited the progress of technology. These chapters demonstrate the first, printable, stretchable battery that can be applied to any surface especially on to elastic textiles without compromising performance when deformed. Specifically, Chapter 5 describes the development of triblock, elastic polymers as a novel binder for printed, stretchable electronics without compromising energy capacity. In additional, the polymer demonstrates stable, high resolution printing on my surfaces, especially on textiles. This work also demonstrated a new method in analytical deformation analysis of stretchable composites shows the potential of testing multi-layer composites.

In Chapter 6, the research addresses the drawbacks in the printed, stretchable battery that prevent it from replacing bulky, rigid coin cells, particular for wearable devices. While the inks for the stretchable battery demonstrated very novel performance of energy capacity and durability, there were many limitations in the other components such as the electrolyte, packaging, and integration with flexible electronics. In Chapter 6 the challenges faced and potential approaches to address them. The chapter 6 includes the preliminary results for a solid-state electrolyte and non-destructive curing process to overcome them. The enablement of novel battery solutions will be the key to continue the progress in conformal electronics and have broader impact on continuous data and sensing such as healthcare where conformal electronics are capable of continuous monitoring of wearer's physiological state and health.

The Appendix includes additional work derivative or starting points for the seminal chapters described above. In Appendix A1, the core polymer-particle composite used to develop printed, stretchable batteries and epidermal electronics was utilized to develop first concept of foldable, printed electronics. This was the first demonstration of electronics printed in 2D design, but then can be released from the substrate, where the design folds and changes in 3D or even with time. This concept of foldable electronics will enable new concepts such as conductive, mechanical switches and other designs for conformal use. Appendix A2 highlights the preliminary work for the development of printed batteries, but studying the composite behavior of bismuth and zinc oxide additives to improve the rechargeability of zinc batteries. This foundational work aided improving the battery formulation when combined with the triblock, elastic polymer for the printed, stretchable battery.

The cross-disciplinary efforts of advanced composites, additive manufacturing, and device design will be essential to enable a new technological revolution that moves devices from being all consuming to become small and compact devices that will be completely wearable. This profound change in technology with the vision of becoming embedded into everything around us, until they become undistinguishable. These devices will bring about new data collections and patterns when combined with advanced algorithms to improve decision making to every industry from healthcare to machinery repair.

1.2 Polymer-Particle Composites and Additive Manufacturing

The field of printed electronics has witnessed spectacular growth due its promise to offer low-cost, high performance for a broad range of applications. These systems have opened up new avenues for body-integrated electronics that were earlier impossible to achieve. Much of the success of printed electronics systems can be attributed to innovations in materials engineering that have led to novel inks comprising of new nanomaterials, polymers and composites. New generation of printed electronics include soft, stretchable and anatomically-compliant devices that enable efficient bio-integration and withstand high tensile stress associated with on-body applications. This review provides an overview of the key material requirements for ink formulations for realizing cost-effective electronics that go beyond Moore's Law, with new form factors functionality such as stretchability, flexibility, transient, and many more that was once unimaginable.

Lithographic [1-4] and printing [5-9] methods have been the primary technologies utilized for fabricating conformal devices. Lithographic methodologies, such as photolithography, e-beam and ion-beam lithography fabricate reproducible, high performance devices. Unfortunately, the attractive attributes of these techniques come at a high financial cost. The need for clean-room facilities, expensive chemicals and labor-intensive processes make these lithographic techniques quite costly, thus increasing the cost per device. In several settings the cost of the device dictates its market penetration ability. Such cases include single-use disposable devices that are being developed for the masses (*e.g.*, RFID tags for IOT applications, blood glucose strips). In these situations, inexpensive printing techniques can significantly lower the fabrication costs while producing devices at large scale with desired precision and accuracy. Although printing technology was introduced centuries ago, it has only recently captured the imagination and attention of researchers for developing high-end devices [2]. Advances in materials science towards developing novel ink formulations, the evolution of new printing technologies coupled with this method's intrinsic cost-effective feature have been the primary driving force for the growing recent interest in this field.

Recent printing technologies that have been implemented in printed electronic devices - including electrochemical ones - can be broadly classified into template and non-template-based methodologies (Figure 1.1). Template-based printing processes can be further classified into screen printing, gravure printing, flexography, and imprinting. Screen printing involves printing inks at a low pressure using a screen mesh containing a designed pattern of uniform thickness. A metal or rubber squeegee can be used for squeezing the thixotropic fluidic ink through the patterned mesh and onto the substrate. The inks utilized in screen printing have a high viscosity but when forced through the screen mesh by the squeegee blade, they undergo sheer thinning to facilitate penetration through the screen mesh which defines the final device pattern. Upon contact with the substrate - typically a ceramic, plastic, polymeric material or paper - the ink returns to its viscous state forming the intended shape. Apart from screen printing, gravure and flexography are other genres of template-based printing technologies that are widely utilized. Gravure and flexography transfer the ink to the substrate from engraved (gravure) or raised (flexography) patterns on a roll. This process is extremely useful for high throughput production of large-area flexible devices.

On the other hand, non-template printing techniques are comprised primarily of inkjet and 3D printing. These printing methodologies rely on localized and controlled ink dispensing onto the receiving substrate in a template-free manner. Progress in the field of engineering has resulted in complex inkjet and 3D printing processes, that involve advanced dispensing technologies involving pneumatic, piezoelectric, aerosol, electrohydrodynamic and thermal processes to print intricate, high resolution architectures [10]. All of the above mentioned template and non-template based printing techniques have been extensively employed for realizing electrochemical devices, including batteries [11-14], super-capacitors[15-18], sensors [19-22] and biofuel cells.[23-25].

Although these printing technologies are well established, the field of wearable electrochemical devices mandates the development of a new class of printable inks with properties that enable the devices to perform flawlessly in conditions commonly experienced by the human body. For example, these printed devices must be small, thin, light, soft and should adhere well to the complex three-dimensional curvature of the human body without causing any irritation. Such anatomically-compliant printed devices should maintain conductive pathways under severe mechanical deformations and survive in a wide range of ambient conditions (e.g., temperature, humidity), and must be made of innocuous, biocompatible materials. Meeting these conditions is indeed challenging and requires innovations in materials science through the development of novel ink formulations. Significant progress in printing technology is thus required for realizing high-performance, conformal devices.

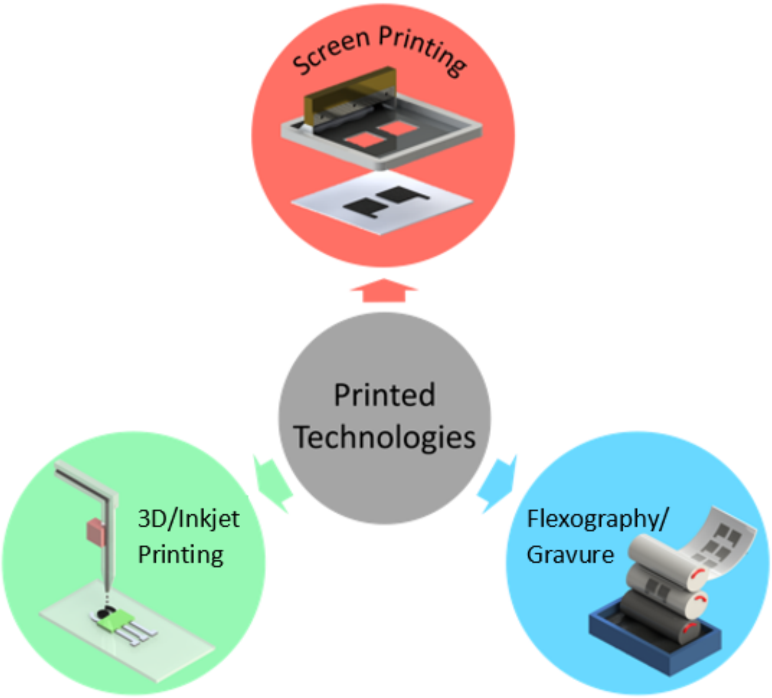

Figure 1.1: Schematic for Additive Manufacturing Method using Particle-Polymer Composites. (Reprinted with permission and Copyright 2016 Wiley). [26]

1.3 Advanced Material and Printing Requirements

A typical printing ink is comprised of fillers, binders, additives and solvents (Figure 1.2). The selection of these components ultimately depends on the type of printing methodology to be followed. The fillers are the active component of the ink that provides it with the characteristic features required for specific applications. Depending on the applications, the fillers could be metallic [27, 28], ceramic [29, 30], organic [31, 32] or a combination of thereof. With rapid advances in nanotechnology, researchers have been able to synthesize inks involving tailor-made nano-materials, such as nanosheets [33, 34], nanowires [35], nanoparticles [36, 37], or their composites.[38] Combining the attributes of nano-science with printing technology has resulted in new fields of low-cost electronics.[39] The other important component of an ink is the binder - a polymeric material that helps in homogeneous dispersion of the fillers into the ink. Upon printing, the binders play the role of holding the ink components together upon solvent evaporation and also help bind the printed trace onto the substrate. A rich variety of binders with acryclic [40], silicon [41, 42], styrene [43], fluoroelastomers [44] or urethane [45] backbones have been developed as ink binders for printing flexible, stretchable, self-healing devices. The choice of the binder ultimately depends on the properties of the fillers. By identifying the surface chemistry of the filler particles, one can select a suitable binder that allows their homogeneous dispersion within the ink. The choice of the binder also depends on the application of the printed devices. For example, water-soluble binders should be avoided for fabricating devices that will be exposed to aqueous media. Various types of UV [46, 47] and heat [48] curing binders have been developed to meet the needs of a wide range of applications. The other crucial component of the ink is the solvent, the vehicle that allows the ink to flow. The ink solvent should provide good solubility to the polymeric binder and impart favorable viscosity, surface tension, and homogeneity. The ideal solvents for a particular set binders and fillers can be selected based on Hillenbrand and Hansen solubility parameters that estimate the cohesive energy between a solvent molecule and other components of the ink. This is critical for obtaining homogeneous ink formulations and optimal printability.

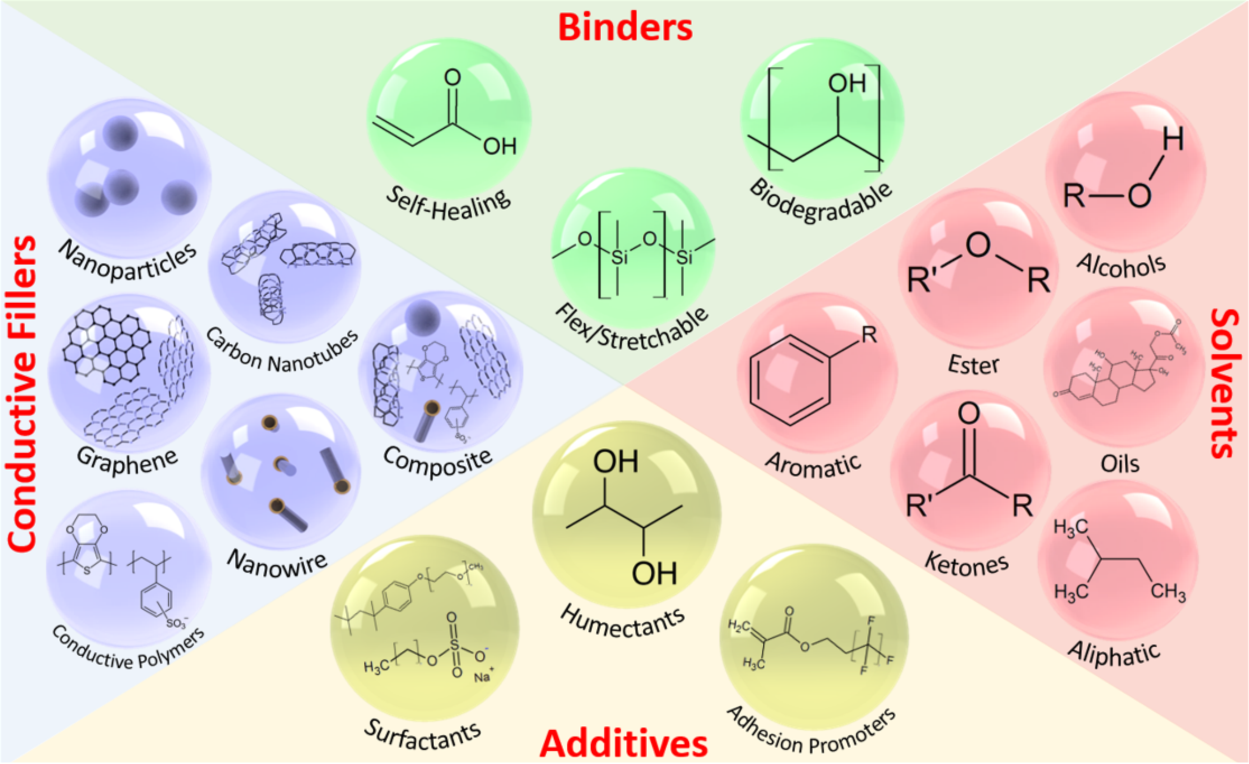

Figure 1.2: Key Components (conductive fillers, surfactants, solvents, and binders) of polymer-particle composites for printable technologies. (Reprinted with permission from Copyright 2016 Wiley). [26]

The solvent selection becomes especially challenging while printing multi-layer devices. When a fresh layer of ink is printed onto a printed film, the solvent present in the ink can potentially dissolve and damage the underlying printed film. This problem can be addressed by preparing each ink with a different set of solvent and binder so that each binder is soluble only in its corresponding solvent. However, in several cases the entire multi-layer device is printed with the same binder but using different filler components. In such cases, each ink can be carefully formulated with a mixture of solvents so that each solution has different Hillenbrand and Hansen solubility parameter for the same binder. Thus, due to the difference in the solubility parameters, the inks will have minimal effect on each other while fabricating multi-layer devices. Apart from filler, binder and solvent, additives are also included to impart desired rheological [49], wetting [50, 51], healing [52, 53] or stretching [42, 43, 54] properties to the inks. Additives in the form of surfactants [44, 55], adhesion improvers [42, 56], humectants [57], penetration promoters [58] and stabilizers [27] have thus been used to tailor the ink properties for specific applications.

The different printing methods mentioned require specific ink properties for precise resolution and performance, as compared in Table 1.1. The major advantage of screen-printing is its ability to reproducibly print high aspect ratio structures. This is achieved due to the high viscosity of the inks realized by incorporating higher binder loadings, compared to other printing techniques. The viscosity ideally reside in the range of 1000-10000 cps for thin films (25-100µm), but can go as a high as 50,000 cps for much thicker prints (>300µm).[10] Unlike screen printing, gravure or flexography are template-based printing techniques that rely on less viscous inks for fabricating thin films (<1µm). In these techniques, the design is patterned onto a roll/plate. This patterned roll/plate is connected with other rolls to draw ink from a reservoir, and applied it to the substrate at extremely high speeds of 1000 m/min while the substrate is pulled by other rollers.[10] Such high printing speeds mandate selection of suitable solvents and contact time between the substrate and roller to allow rapid solvent evaporation.[10]

Table 1.1. Feature Comparison of Different Printing Methods. (Reprinted with permission from and Copyright 2016 Wiley). [26]

Method	Screen Printing	Inkjet	Flexography/ Gravure	3D/ Dispensing
Ink Viscosity [cP]	500-5,000 (higher is possible)	10-20	50-1000	>300k
Line Width [µm]	50-100	10-50	10-100	1-100
Line Thickness [µm]	5-250	~1-10	≤1	1-100
Speed [m/min]	~70	~1	1,000	<1

In comparison, inkjet printing and 3D printing are non-template printing methods that rely on some form of dispensing technology (pneumatic, piezoelectric, aerosol, electrohydrodynamic and thermal).[10] Each type of dispensing technology relies on a specific volume displacement to drive the excess ink through a nozzle and onto the substrate. These nozzle-based systems require the inks to have low viscosities (10-20 cp) as compared to other printing mechanisms for easy, reproducible registration of ink onto the substrate.[10] The reliance on nozzles to dispense the inks restricts the range of fillers compatible with such types of printing processes. For example, low viscosity inks restrict the extent of filler loading and thus high concentration inks are not possible. Furthermore, nozzles can be easily clogged when the solid ink components are larger than the nozzle's opening. [59]

As discussed in the following sub-sections, researchers have developed highly flexible, stretchable and self-healing printed devices. Such properties are crucial for realizing "skin-like" devices that can survive mechanical stress and conformably mate with the human skin towards diverse on-body applications involving extreme tensile stress

1.2.1 Particle-Polymer Composites for Flexible Devices

A rich variety of ink formulations has been developed over the past decade for realizing printed devices that survive high flexural stress with negligible impact on their performance. [44, 60, 61] These inks are comprised of a wide range of materials, such as carbon nanotubes [62-64], graphene [33, 34, 65, 66], noble metal-based nanoparticles (Figure 1.3A) [61, 67], quantum dots [68, 69] and a combination of thereof to cater to a host of applications. Primarily, these inks have been developed for ink-jet printers [33], screen printers [70] and gravure and flexography.[70, 71] Though the exact composition of the inks depends on the choice of printing methodology utilized, all flexible printable inks must possess one key property - ability to maintain structural integrity upon multiple flexing of the printed devices. When a device is flexed, a strain is developed within the substrate and the printed components. This strain is a function of the radius of bending.[72] Therefore, it is crucial that the inks are judiciously synthesized for developing printed devices that possess the desired degree of flexibility without compromising their performance. Binders [40] and adhesion promoters/surfactants [73] are two ink components that play a vital role in dictating the flexible nature of the inks. An ideal binder must be able to uniformly disperse the strain generated during flexing with minimal effect on the filler component. The uniform dispersion of the generated strain minimizes the possibility of concentrated stress locations on the printed device that may lead to crack formations. On the other hand, suitable adhesion promoters help alleviate the shear stress experienced between the printed ink and the underlying substrate when subject to mechanical deformation. The following sub-sections will discuss important flexible ink formulations developed by various research groups.

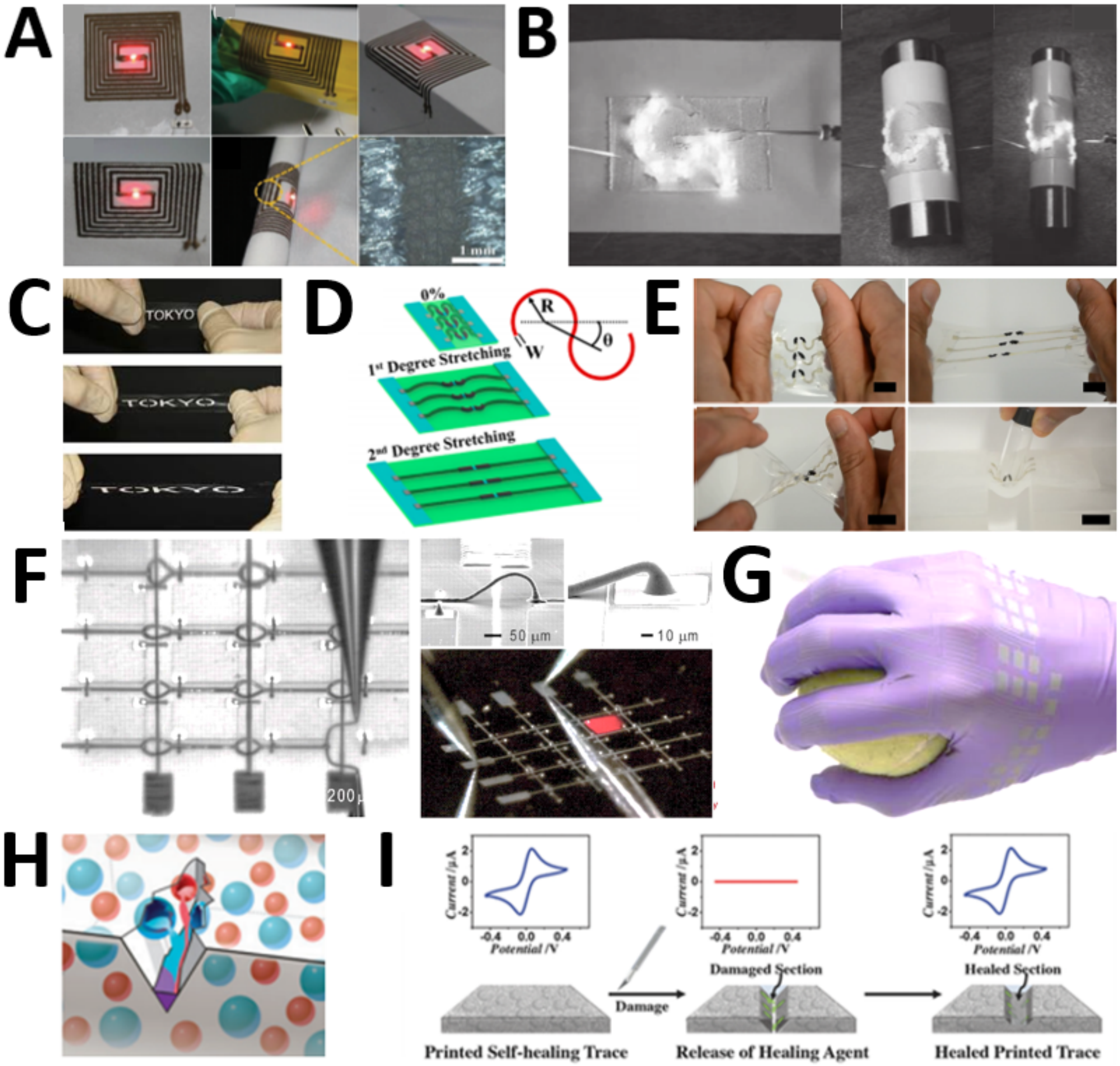

Figure 1.3: Flexible, stretchable, and self-healing printed devices. (A) PDMS/silver ink for flexible, printed coils. (B) Polyurethane/conductive adhesive for flexible interconnects with LEDs. (C) Fluoroelastomer/silver flake ink for screen-printed, stretchable electronics on elastic films or textiles. (D) Two degrees of stretchability using a serpentine design coupled with stretchable printed silver or CNTs inks for extremely, stretchable electrochemical devices demonstrated in (E). (F) Omnidirectional printing of flexible, stretchable, and spanning microelectrodes with 2 μm widths. (F) Inkjet printing of gallium-indium nanoparticles on to flexible, stretchable gloves. (J) Demonstration of self-healing capsules that heal the damaged conductive trace by releasing the solvent and dissolving the damaged area to heal the device.

Several research teams have developed carbonaceous nanomaterials-based printable inks to tap in the remarkable electronic and mechanical properties of carbon nanotubes[54, 64, 74, 75] and graphene.[76, 77] Suitable dispersion engineering can yield inks compatible with printing technologies while maintaining the attractive properties of these and other nanomaterials.[78] Over the years, flexible printable inks comprising semi-conductor [79], metallic [36, 61], carbon nanotubes [62, 71] and graphene [33, 34, 65, 66] have been formulated for a wide range of applications. These can be classified into aqueous and organic solvent-based inks. Carbon-based inks have received particular attention due to numerous attractive properties of carbonaceous nanomaterials. Preparing high quality CNT and graphene inks for printed devices involve several challenges. CNT/graphene have high surface area and thus obtaining inks with well-dispersed CNT/graphene suspension is difficult due to the strong van der Waals interactions. These interactions affect the printability, print morphology and conductive properties of the printed films.[39]

In this regard, various polymers [80-83], surfactants [84-88], and functional group generation techniques [80, 89, 90] have thus been utilized that mitigate aggregation and help realize homogeneously dispersed CNTs/graphene inks. Polymeric binders comprising of polyurethane (Figure 1.3B) [54, 91], epoxy [92, 93], acrylic [94-96], silicone [97-99], and vinyl [96,100, 101] backbones have been successfully employed to develop uniformly dispersed CNT/graphene inks. However, addition of non-conductive polymeric binders affects the conductivity of the final printed traces. Several researchers have addressed this issue by utilizing conductive polymer-based binders.[102] Apart from improving the suspension of the carbonaceous nanomaterials in the inks, these binders also impart flexibility to the inks. Incorporating polymeric binders for efficient dispersion of the CNT/graphene can increase the viscosity of the inks. This can be a major issue if low viscosity inks are required, as in the case of ink-jet printing. In this case, researchers have relied on surfactants, such as sodium dodecyl sulfate [76, 103, 104] and sodium dodecylbenzene sulfonate.[105] Another route to achieve low viscosity inks is by generating functional groups on the CNT/graphene surface via acidic treatment.[80, 89, 90] Functional polar groups augment the suspension of these carbonaceous nanomaterials in polar solvents and also help maintain a stable suspension due to electrostatic repulsion between similarly charged functional groups.

Conducting polymers represent another important class of materials that are widely used for developing flexible conductive inks. Tailored conductivity, ease of processability, low-cost, softness, and flexibility are some of the attributes of conducting polymers that have attracted the attention of researchers towards developing conductive inks for various applications where flexibility is mandated.[106-108] Printable inks based on PEDOT:PSS [32, 106], polyaniline [100, 107, 109], polypyrrole [110, 111], polyacetylene [112] and polyindole [113] have been developed over the past decade. In addition, inks comprising of conducting polymer composites with CNTs [114], graphene [115, 116], gold [117] or silver [118] have also been introduced. Such composite inks have the synergistic benefits of both the conducting polymers as well as the other incorporated nanomaterial. Representative ink compositions for flexible devices are shown in Table 1.2.

1.2.2 Particle-Polymer Composites for Stretchable Devices

In addition to being flexible, the human skin is also soft and stretchable in nature. It is therefore imperative that the printed devices developed for wearable applications possess similar characteristics. Stretchability of the device will enable the device to be seamlessly integrated with the biological tissue without causing any irritation. Acknowledging the importance of device stretchability, researchers have recently started synthesizing stretchable inks.[43, 55, 119] Unlike developing flexible inks, the synthesis of stretchable inks is a more daunting task since the device experiences significantly higher strain levels during stretching as compared to just bending. When a printed device is stretched, the mismatch between the mechanical properties of the underlying substrate and the printed film causes ruptures and delamination of the latter. Furthermore, as the device is stretched, the conductive fillers are forced apart, thus leading to increased resistance of the film.

Due to the trade-off between the mechanical and electrical properties, increasing the level of conductive filler (towards lowering the resistance) increases the material stiffness and diminishes its stretchability.[44] By carefully selecting the binder and surfactants, one can mitigate these issues. Incorporating a highly stretchable elastomeric binder is a common route to impart stretchability to the inks. Silicone [42], fluorine rubber (Figure 1.3C) [44], polyurethane (Figure 1.3D and 3E) [54, 120, 121], and isoprene block co-polymers [122, 123] are some of the most widely used binders that researchers have used to develop stretchable inks. In addition to involving a stretchable binder, in many scenarios one has to also include a suitable surfactant to circumvent the issue of delamination of the printed film upon stretching. The addition of the surfactant enhances the uniform distribution of stress throughout the printed trace and thus reduces the possibility of debonding.[124] In recent years, researchers have developed a wide range of highly stretchable inks for printed devices that include carbon nanotubes [125, 126], graphene [18], conducting polymers [42], silver nanomaterials (Figure 1.3F) [36, 119, 128, 128] or liquid metals such as gallium indium (Figure 1.3G).[129] Random composites are defined as random mix of comprising of high-aspect-ratio materials, e.g., carbon nanotubes, dispersed in a stretchable matrix, have been particularly attractive.[54, 130] Several studies on such printed stretchable devices have revealed that repeated stretching leads to alignment of the fillers along the direction of the applied strain and that such alignment helps in mitigating the deleterious effect of tensile stress on the printed trace.[131]

Specially formulated inks that allow the printed device to be linearly stretched beyond 100% have been developed recently (Figure 1.3D and 1.3E).[54] However, it must be pointed out that the term “extent of device stretchability” is quite subjective and depends on the device’s property under consideration. For example, our group demonstrated that although the resistance of our printed electrochemical device increased upon repeated linear stretching, its electrochemical characteristics remained stable until 100% strain.[42] Irrespective of which property is recorded, all stretchable printed devices ultimately fail when stretched beyond a limit. There are two obvious routes to overcome this issue: 1) increase the amount of stretchable binder to improve stretchability, and 2) tailor the device’s design so that the pattern allows the device to accommodate additional stress. The first route has obvious limits since increasing the stretchable binder content leads to increased resistivity of the final printed film. On the other hand, by carefully designing the device’s pattern one can impart additional stretchability to the device as has been demonstrated by our research.[54, 130] Representative ink compositions for stretchable devices are shown in Table 1.2.

1.2.2 Particle-Polymer Composites for Self-Healing Devices

Self-healing is a remarkable property that Nature has infused within several biotic systems. This allows the biological systems to recover when injured and thus extend their lifespan. Wearable systems regularly face mechanical deformations that can cause damage and lead to device failure. Device flexibility and stretchability protects wearable devices from such catastrophes. However, these properties can alleviate the issue of mechanical damage only up to a certain limit. For example, a device will become dysfunctional if the device is stretched or bent beyond a certain extent. One can fabricate wearable devices to survive within a predicted range of mechanical stress. However, in several scenarios, the device may experience strains well beyond the usual stress range for which the device has been designed. Such excessive stretching or bending would lead to crack formations and ultimately result in whole scale failure of the device. Such cracks are often hard to detect at an early stage. In such cases, the wearable device is bound to fail. Smart wearable devices that can self-heal and regain their performance when mechanically damaged can address this issue. Scientists have thus been developing self-healing materials that could repair internal damage all by themselves. Such bio-mimicking wearable systems thus have longer life-span as compared to their non-healing counterparts.

The remarkable self-healing of biological systems has inspired researchers to develop new repair strategies.[132-134] Man-made self-healing materials can be classified broadly into three groups: capsule based, vascular, and intrinsic (Figure 1.3H).[135] These approaches vary in the mechanism of self-healing and it is important to understand these to select the best system that can be leveraged for developing printed wearable devices. Vascular-based self-healing materials rely on incorporation of channels filled with self-healing material.[136-138] These channels usually comprise of hollow glass fibers. Developing a printable ink consisting of such fibers filled with healing agent is quite difficult and hence this approach has not been employed for developing printed self-healing systems. On the other hand, capsule-based systems involve hollow microcapsules loaded with self-healing agents.[139-144] These microcapsules can be readily included within printable inks for realizing self-healing printed electrochemical devices.[52]

White and Sottos group did pioneering work on capsule-based self-healing printed materials .[53, 139-141, 144] Both groups illustrated the first example of a printed self-healing system that relied on capsules loaded with the healing agent (organic solvent). This involved printing silver traces followed by printing an elastomeric overcoat which was comprised of microcapsules filled with the healing agent. When the printed device is mechanically damaged, the microcapsules rupture and release the encapsulated healing agent. The healing agent locally dissolves the binder and causes the rearrangement of the conductive Ag particles, which leads to recovery of the electrical contact across the damage. Unlike most of the other self-healing systems [136, 145], the capsule-based healing process is quite rapid (few seconds) and does not require an external trigger to initiate the healing process. This attribute makes this system quite attractive for applications, such as wearables, where truly autonomous healing devices are required.

One limitation of the above system is the separation of the layer containing the capsules from the underlying active printed traces. This could lead to a scenario where damages within the active trace may not initiate any damage within the overlaying elastomeric layer containing the capsules. With no rupture of the capsules, the healing process will not be initiated, thus leading to the failure of printed system to self-healing itself. Recently, we addressed this issue by formulating conductive carbon and Ag/AgCl inks loaded with the microcapsules.[52] With capsules loaded directly within the inks utilized for realizing active device components, any damage to the active components triggers the self-healing process and the device is healed within a few seconds. The fast-autonomous self-repair ability of these self-healing inks-based traces was illustrated by studying the recovery of their conductivity and cyclic voltammetric response (Figure 1.3I). Subsequently, the self-healing inks were leveraged to realize a self-healing potentiometric sodium sensor. Representative ink compositions for self-healing devices are shown in Table 1.2.

Table 1.2: List of Polymer-Particle Composites with their Composite Performance and Printing Technique (Reprinted with permission and Copyright 2016 Wiley [26]

Properties	Binder	Conductive Element	Performance	Printing Type	Ref.
Flexible	Polyurethane	PEG coated silver flakes	Flexible [1.0 x 10^{-5} Ω*cm] 2.64% flexural strain	SP	123
Flexible	Polytetra Fluoroethylene Knitted Carbon Fiber	Activated carbon	Simultaneous stretching (50%) and flexing (180°) resulted in 20% loss in capacitance	SP	34
Flexible	Sodium dodecyl sulfate	RhO_2/SWCNT	On flexible textile with capacitance of 138 F/g and energy density of 18.8 Wh/kg	DOD	50
Flexible	Ethyl cellulose	Graphene	Conductivity ~10,000 S/m,	FG	103
Flex/ Stretchable	Ecoflex	Ag/AgCl	Stretchable No change to resistance to 300%, but operable at 500%	SP	124
	Polyurethane	MWCNT			
Stretchable Elastic	Copolymer fluoroelastomer Zonyl-FS 300 Fluorosurfactant	Silver Flakes	Unstretched: 738 S/cm Stretched to 215% 182 S/cm	SP	76
Self-Healing	Hexyl acetate capsules with organic solvent	Silver particles	induced healing in 60 seconds	DOD	85

SP: Screen Printing
DOD: Drop on Demand (Inkjet/3D Printing)
FG: Flexography/Gravure

1.3 Challenges and Future Outlook

Recent advances in the development of new ink materials that meet the demands of conformal devices have been discussed. These printed devices have made a remarkable progress in the past decade due to the breakthroughs in material science, nanotechnology, and biotechnology. The examples given above illustrate the wide range of mechanically-durable materials that were introduced for printing conformal devices. These advances have led to the development of printed conformal devices that can fold, bend, stretch, and repair, and hence to the realization of on-body applications involving extreme tensile stress. Modern wearable electrochemical devices can thus accommodate severe strain while maintaining high performance. Yet, further efforts are required towards widespread commercial exploitation of printed wearable electrochemical devices. One of the major issues with printed devices is the high resistivity of the printed trace, as compared to pure filler material, due to the presence of binders. This represents a serious matter where high performance printed devices, that can rival lithographically-fabricated devices, are required. The high resistivity of printed devices is of particular concern for printed energy devices, such as batteries, supercapacitors and biofuel cells. This is also an issue for electrochemical sensors, where a large resistance can lead to higher overvoltage and larger background current, thus compromising the sensor performance. Addressing the resistivity challenge becomes even more daunting in the case of wearable printed devices, since developing inks for stretchable and self-healing devices require addition of significant proportions of non-conductive elastomeric binders and self-healing agents. In addition to the challenge of improving the conductivity of the printed systems, a whole host of deterrents exists where biological entities (e.g., enzymes) are involved. Developing printable biological inks that can maintain the activity of the biological species over long periods is indeed quite challenging. Degradation of biological entities within inks during the curing, operation and storage has hampered the development of printable biological inks. Formulating such inks will truly revolutionize the fields of printed electrochemical biosensors and biofuel cells.

While addressing these challenges, researchers working in the field of wearable printed electrochemical devices should also focus on developing devices that have self-destruction capabilities. The ability to self-destroy presents many new and exciting opportunities for wearable and implantable devices.[146] The device would perform its requisite function over a desired period of time and then disintegrate autonomously, or on-demand, into biologically benign components. The ability to self-destroy is particularly attractive for implantable devices. At present, implantable devices require a secondary surgery to remove the device after it completed its task. For espionage and wearables, these self-destroyed devices allow the user to apply them to any surface, or biological tissue, without the need to remove the device as they dissolve on demand or long after the application. These "transient" electronics that have timed degradation or triggered degradation by light or temperature stimuli, have been pioneered by Roger's group.[146] Presently, these devices are fabricated through expensive thin-film deposition and lithography. The ability to use similar biodegradable and biocompatible materials in printing technologies for developing such transient wearable/implantable devices is economically practical as long as performance is not compromised. Researchers could consider a rich variety of biodegradable conducting polymers such as polypyrrole (PPy), polyaniline (PANi), and polythiophene or inorganic materials, *e.g.,* Mg, Fe, Zn, W or Mo for realizing the active components of the self-destroying wearable electrochemical devices. Similarly, researchers can consider insulating biodegradable polymers, such as silk fibroin, poly lactic-co-glycolic acid (PGLA), polycaprolactone (PCL), poly(lactic acid) (PLA), and poly(vinyl) alcohol) as the substrates or packaging materials.[147]

Privacy has become an important consideration for society. Significant portions of customers would appreciate wearable devices that are inconspicuous to the nearby public. In addition to consumer privacy, there are several security settings that mandate invisibility of the wearable devices. In this regard, researchers must work on developing wearable devices that are completely invisible. There have been major developments in the realization of printed transparent electronic devices that include photovoltaics, solar cells, or transistors.[148-155] Indium tin oxide (ITO) is the most widely used conventional transparent electrode materials, which is not compatible with wearable applications due to its brittleness, rigidness and expensive cost. Alternative materials have been used for developing flexible and stretchable transparent devices using metal oxides, conducting polymers, carbon nanotubes, graphene, and metal-nanowire networks.[156-167] These materials can be adapted to printable inks for mass production of transparent electrodes.

A solution-processable formulation is preferred for thin and uniform printed devices, which are key factors to attain a transparent property. Printable ink for transparent electrodes can rely on carbon materials, such as CNT and graphene. Such carbon materials can be dispersed in solvent by acid treatment to form COOH groups or by adding a stabilizer (*e.g.*, PMAS, PVA, PEDOT: PSS).[74, 102] Alternately, conductive oxide inks have been developed by one-pot synthesis of diverse metal oxides using a heating process of the metal organic precursors.[168] Conductive polymers, such as PEDOT:PSS, are generally favored for printing and viscosity is tunable by side groups or solvent.[169] Printed transparent electrodes display high conductivity, excellent stability, and flexible mechanical properties. Taking inspiration from these studies should lead to wearable printed devices involving invisible sensors and optoelectronic components.

It is evident that the development of wearable printed devices will bring considerable advances to the field of wearable devices. Some of the major challenges that impede the widespread adaptation of this field for commercial applications have been addressed using the innovative approaches and advanced materials delineated above. Such new ink formulations should thus enable a variety of important new applications. Despite many advances, research and development of printed wearable electrochemical devices is still in its early stage. With continuous innovations in materials sciences and attention to existing issues, the full potential of printed wearable electrochemical devices will be realized and exploited.

Acknowledgements

Chapter 1 is based, in part, on the material as it appears in Advanced Electronic Materials, 2017, by Dr. Jayoung Kim, Rajan Kumar, Dr. Amay Bandodkar and Joseph Wang. This review was focused on dissertation author’s notion or concept of particle-polymer composites or could be commonly referred as functional inks when combined with additive manufacturing. The dissertation author was the corresponding author on this review based on doctoral research focusing on developing novel particle-polymers for many new functional devices and technologies.

1.2 References

1. Gao, W., H.Y.Y. Nyein, Z. Shahpar, H.M. Fahad, K. Chen, S. Emaminejad, Y. Gao, L.-C. Tai, H. Ota, E. Wu, J. Bullock, Y. Zeng, D.-H. Lien, and A. Javey *Wearable Microsensor Array for Multiplexed Heavy Metal Monitoring of Body Fluids*. ACS Sensors, 2016. DOI: DOI: 10.1021/acssensors.6b00287.

2. Berggren, M., D. Nilsson, and N.D. Robinson, *Organic materials for printed electronics.* Nat Mater, 2007. **6**(1): p. 3-5.

3. Gao, W., S. Emaminejad, H.Y. Nyein, S. Challa, K. Chen, A. Peck, H.M. Fahad, H. Ota, H. Shiraki, D. Kiriya, D.H. Lien, G.A. Brooks, R.W. Davis, and A. Javey, *Fully integrated wearable sensor arrays for multiplexed in situ perspiration analysis.* Nature, 2016. **529**(7587): p. 509-14.

4. Liao, Y.-T., H. Yao, A. Lingley, B. Parviz, and B.P. Otis, *A 3-CMOS glucose sensor for wireless contact-lens tear glucose monitoring.* Solid-State Circuits, IEEE Journal of, 2012. **47**(1): p. 335-344.

5. Malzahn, K., J.R. Windmiller, G. Valdes-Ramirez, M.J. Schoning, and J. Wang, *Wearable electrochemical sensors for in situ analysis in marine environments.* Analyst, 2011. **136**(14): p. 2912-2917.

6. Tamiya, E., Y. Inoue, and K. Yamanka. *Mobile/wearable electrochemical biosensors with printable electrodes*. in *CPMT Symposium Japan (ICSJ), 2015 IEEE*. 2015.

7. Jost, K., D. Stenger, C.R. Perez, J.K. McDonough, K. Lian, Y. Gogotsi, and G. Dion, *Knitted and screen-printed carbon-fiber supercapacitors for applications in wearable electronics.* Energy & Environmental Science, 2013. **6**(9): p. 2698-2705.

8. Imani, S., A.J. Bandodkar, A.M.V. Mohan, R. Kumar, S. Yu, J. Wang, and P.P. Mercier, *A wearable chemical-electrophysiological hybrid biosensing system for real-time health and fitness monitoring.* Nature communications, 2016. **7**: p. 11650-11656.

9. Windmiller, J.R. and J. Wang, *Wearable electrochemical sensors and biosensors: a review.* Electroanalysis, 2013. **25**(1): p. 29-46.

10. Suganuma, K., *Printing Technology*, in *Introduction to Printed Electronics*. 2014, Springer New York: New York, NY. p. 23-48.

11. Braam, K. and V. Subramanian, *A Stencil Printed, High Energy Density Silver Oxide Battery Using a Novel Photopolymerizable Poly(acrylic acid) Separator.* Advanced Materials, 2015. **27**(4): p. 689-694.

12. Delannoy, P.E., B. Riou, B. Lestriez, D. Guyomard, T. Brousse, and J. Le Bideau, *Toward fast and cost-effective ink-jet printing of solid electrolyte for lithium microbatteries.* Journal of Power Sources, 2015. **274**: p. 1085-1090.

13. Sousa, R.E., C.M. Costa, and S. Lanceros-Méndez, *Advances and Future Challenges in Printed Batteries.* ChemSusChem, 2015. **8**(21): p. 3539-3555.

14. Sun, K., T.-S. Wei, B.Y. Ahn, J.Y. Seo, S.J. Dillon, and J.A. Lewis, *3D Printing of Interdigitated Li-Ion Microbattery Architectures.* Advanced Materials, 2013. **25**(33): p. 4539-4543.

15. Chen, P., H. Chen, J. Qiu, and C. Zhou, *Inkjet printing of single-walled carbon nanotube/RuO2 nanowire supercapacitors on cloth fabrics and flexible substrates.* Nano Research, 2010. **3**(8): p. 594-603.

16. Choi, K.-H., J. Yoo, C.K. Lee, and S.-Y. Lee, *All-inkjet-printed, solid-state flexible supercapacitors on paper.* Energy & Environmental Science, 2016.

17. Wang, S., N. Liu, C. Yang, W. Liu, J. Su, L. Li, C. Yang, and Y. Gao, *Fully screen printed highly conductive electrodes on various flexible substrates for asymmetric supercapacitors.* RSC Advances, 2015. **5**(104): p. 85799-85805.

18. Duan, S., K. Yang, Z. Wang, M. Chen, L. Zhang, H. Zhang, and C. Li, *Fabrication of Highly Stretchable Conductors Based on 3D Printed Porous Poly (dimethylsiloxane) and Conductive Carbon Nanotubes/Graphene Network.* ACS applied materials & interfaces, 2016. **8**(3): p. 2187-2192.

19. Wang, J. and M. Musameh, *Carbon nanotube screen-printed electrochemical sensors.* Analyst, 2004. **129**(1): p. 1-2.

20. Määttänen, A., U. Vanamo, P. Ihalainen, P. Pulkkinen, H. Tenhu, J. Bobacka, and J. Peltonen, *A low-cost paper-based inkjet-printed platform for electrochemical analyses.* Sensors and Actuators B: Chemical, 2013. **177**: p. 153-162.

21. Arduini, F., L. Micheli, D. Moscone, G. Palleschi, S. Piermarini, F. Ricci, and G. Volpe, *Electrochemical biosensors based on nanomodified screen-printed electrodes: recent applications in clinical analysis.* TrAC Trends in Analytical Chemistry, 2016. **79**: p. 114-126.

22. Hayat, A. and J.L. Marty, *Disposable screen printed electrochemical sensors: Tools for environmental monitoring.* Sensors, 2014. **14**(6): p. 10432-10453.

23. Jenkins, P., S. Tuurala, A. Vaari, M. Valkiainen, M. Smolander, and D. Leech, *A comparison of glucose oxidase and aldose dehydrogenase as mediated anodes in printed glucose/oxygen enzymatic fuel cells using ABTS/laccase cathodes.* Bioelectrochemistry, 2012. **87**: p. 172-177.

24. Jia, W., X. Wang, S. Imani, A.J. Bandodkar, J. Ramírez, P.P. Mercier, and J. Wang, *Wearable textile biofuel cells for powering electronics.* J. Mater. Chem. A, 2014. **2**(43): p. 18184-18189.

25. Bandodkar, A.J. and J. Wang, *Wearable Biofuel Cells: A Review.* Electroanalysis, 2016. **28**(6): p. 1188-1200.

26. Kim, J., R. Kumar, A.J. Bandodkar, and J. Wang, *Advanced Materials for Printed Wearable Electrochemical Devices: A Review.* Advanced Electronic Materials, 2017. **3**(1): p. 1600260.

27. Kamyshny, A., J. Steinke, and S. Magdassi, *Metal-based inkjet inks for printed electronics.* The Open Applied Physics Journal, 2011. **4**(1).

28. Tay, B.Y. and M.J. Edirisinghe, *Dispersion and stability of silver inks.* Journal of Materials Science, 2002. **37**(21): p. 4653-4661.

29. Lewis, J.A., J.E. Smay, J. Stuecker, and J. Cesarano, *Direct Ink Writing of Three-Dimensional Ceramic Structures.* Journal of the American Ceramic Society, 2006. **89**(12): p. 3599-3609.

30. Pan, Z., Y. Wang, H. Huang, Z. Ling, Y. Dai, and S. Ke, *Recent development on preparation of ceramic inks in ink-jet printing.* Ceramics International, 2015. **41**(10, Part A): p. 12515-12528.

31. Hoth, C.N., S.A. Choulis, P. Schilinsky, and C.J. Brabec, *High Photovoltaic Performance of Inkjet Printed Polymer:Fullerene Blends.* Advanced Materials, 2007. **19**(22): p. 3973-3978.

32. Eom, S.H., S. Senthilarasu, P. Uthirakumar, S.C. Yoon, J. Lim, C. Lee, H.S. Lim, J. Lee, and S.-H. Lee, *Polymer solar cells based on inkjet-printed PEDOT:PSS layer.* Organic Electronics, 2009. **10**(3): p. 536-542.

33. Secor, E.B., P.L. Prabhumirashi, K. Puntambekar, M.L. Geier, and M.C. Hersam, *Inkjet Printing of High Conductivity, Flexible Graphene Patterns.* The Journal of Physical Chemistry Letters, 2013. **4**(8): p. 1347-1351.

34. Finn, D.J., M. Lotya, G. Cunningham, R.J. Smith, D. McCloskey, J.F. Donegan, and J.N. Coleman, *Inkjet deposition of liquid-exfoliated graphene and MoS2 nanosheets for printed device applications.* Journal of Materials Chemistry C, 2014. **2**(5): p. 925-932.

35. dos Reis Benatto, G.A., B. Roth, M. Corazza, R.R. Sondergaard, S.A. Gevorgyan, M. Jorgensen, and F.C. Krebs, *Roll-to-roll printed silver nanowires for increased stability of flexible ITO-free organic solar cell modules.* Nanoscale, 2016. **8**(1): p. 318-326.

36. Ahn, B.Y., E.B. Duoss, M.J. Motala, X. Guo, S.-I. Park, Y. Xiong, J. Yoon, R.G. Nuzzo, J.A. Rogers, and J.A. Lewis, *Omnidirectional Printing of Flexible, Stretchable, and Spanning Silver Microelectrodes.* Science, 2009. **323**(5921): p. 1590-1593.

37. Ahn, B.Y., D.J. Lorang, and J.A. Lewis, *Transparent conductive grids via direct writing of silver nanoparticle inks.* Nanoscale, 2011. **3**(7): p. 2700-2702.

38. Guo, S., W. Wang, C.S. Ozkan, and M. Ozkan, *Assembled graphene oxide and single-walled carbon nanotube ink for stable supercapacitors.* Journal of Materials Research, 2013. **28**(07): p. 918-926.

39. Kamyshny, A. and S. Magdassi, *Conductive Nanomaterials for Printed Electronics.* Small, 2014. **10**(17): p. 3515-3535.

40. Rohini Kumar, D.B., M. Rami Reddy, V.N. Mulay, and N. Krishnamurti, *Acrylic co-polymer emulsion binders for green machining of ceramics.* European Polymer Journal, 2000. **36**(7): p. 1503-1510.

41. Merilampi, S., T. Björninen, V. Haukka, P. Ruuskanen, L. Ukkonen, and L. Sydänheimo, *Analysis of electrically conductive silver ink on stretchable substrates under tensile load.* Microelectronics Reliability, 2010. **50**(12): p. 2001-2011.

42. Bandodkar, A.J., R. Nuñez-Flores, W. Jia, and J. Wang, *All-Printed Stretchable Electrochemical Devices.* Advanced Materials, 2015. **27**(19): p. 3060-3065.

43. Hu, M., X. Cai, Q. Guo, B. Bian, T. Zhang, and J. Yang, *Direct Pen Writing of Adhesive Particle-Free Ultrahigh Silver Salt-Loaded Composite Ink for Stretchable Circuits.* ACS Nano, 2016. **10**(1): p. 396-404.

44. Matsuhisa, N., M. Kaltenbrunner, T. Yokota, H. Jinno, K. Kuribara, T. Sekitani, and T. Someya, *Printable elastic conductors with a high conductivity for electronic textile applications.* Nature communications, 2015. **6**.

45. Ma, R., B. Kang, S. Cho, M. Choi, and S. Baik, *Extraordinarily High Conductivity of Stretchable Fibers of Polyurethane and Silver Nanoflowers.* ACS Nano, 2015. **9**(11): p. 10876-10886.

46. Kwon, G.H., J.Y. Park, J.Y. Kim, M.L. Frisk, D.J. Beebe, and S.-H. Lee, *Biomimetic Soft Multifunctional Miniature Aquabots.* Small, 2008. **4**(12): p. 2148-2153.

47. Zhu, W., J. Li, Y.J. Leong, I. Rozen, X. Qu, R. Dong, Z. Wu, W. Gao, P.H. Chung, J. Wang, and S. Chen, *3D-Printed Artificial Microfish.* Advanced Materials, 2015. **27**(30): p. 4411-4417.

48. Zuniga, C.A., J. Abdallah, W. Haske, Y. Zhang, I. Coropceanu, S. Barlow, B. Kippelen, and S.R. Marder, *Crosslinking Using Rapid Thermal Processing for the Fabrication of Efficient Solution-Processed Phosphorescent Organic Light-Emitting Diodes.* Advanced Materials, 2013. **25**(12): p. 1739-1744.

49. Mardis, W.S., *Organoclay rheological additives: Past, present and future.* Journal of the American Oil Chemists' Society, 1984. **61**(2): p. 382-387.

50. Norman, A.L., K.A. Evagelos, and J.S. Wendelin, *Graphene-stabilized copper nanoparticles as an air-stable substitute for silver and gold in low-cost ink-jet printable electronics.* Nanotechnology, 2008. **19**(44): p. 445201.

51. Suzanna, A., S. Shay, and M. Shlomo, *Flexible electroluminescent device with inkjet-printed carbon nanotube electrodes.* Nanotechnology, 2012. **23**(34): p. 344003.

52. Bandodkar, A.J., V. Mohan, C.S. López, J. Ramírez, and J. Wang, *Self-Healing Inks for Autonomous Repair of Printable Electrochemical Devices.* Advanced Electronic Materials, 2015. **1**(12): p. 150028.

53. Odom, S.A., S. Chayanupatkul, B.J. Blaiszik, O. Zhao, A.C. Jackson, P.V. Braun, N.R. Sottos, S.R. White, and J.S. Moore, *A Self-healing Conductive Ink.* Advanced Materials, 2012. **24**(19): p. 2578-2581.

54. Bandodkar, A.J., I. Jeerapan, J.-M. You, R. Nuñez-Flores, and J. Wang, *Highly Stretchable Fully-Printed CNT-Based Electrochemical Sensors and Biofuel Cells: Combining Intrinsic and Design-Induced Stretchability.* Nano Letters, 2016. **16**(1): p. 721-727.

55. Karsa, D.R., *Surfactants in polymers, coatings, inks and adhesives*. Vol. 1. 2003: Taylor & Francis US.

56. Jang, D., D. Kim, B. Lee, S. Kim, M. Kang, D. Min, and J. Moon, *Nanosized Glass Frit as an Adhesion Promoter for Ink-Jet Printed Conductive Patterns on Glass Substrates Annealed at High Temperatures.* Advanced Functional Materials, 2008. **18**(19): p. 2862-2868.

57. Walker, S.B. and J.A. Lewis, *Reactive Silver Inks for Patterning High-Conductivity Features at Mild Temperatures.* Journal of the American Chemical Society, 2012. **134**(3): p. 1419-1421.

58. Fink, J.K., *The Chemistry of Printing Inks and Their Electronics and Medical Applications*. 2014: John Wiley & Sons.

59. Lin, J. and Z. Cui, *Printing Processes and Equipments*, in *Printed Electronics*. 2016, John Wiley & Sons Singapore Pte. Ltd. p. 106-144.

60. Pagliaro, M., R. Ciriminna, and G. Palmisano, *Flexible Solar Cells.* ChemSusChem, 2008. **1**(11): p. 880-891.

61. Hu, Y., T. Zhao, P. Zhu, Y. Zhu, X. Shuai, X. Liang, R. Sun, D.D. Lu, and C.-P. Wong, *Low cost and highly conductive elastic composites for flexible and printable electronics.* Journal of Materials Chemistry C, 2016. **4**(24): p. 5839-5848.

62. Lau, P.H., K. Takei, C. Wang, Y. Ju, J. Kim, Z. Yu, T. Takahashi, G. Cho, and A. Javey, *Fully Printed, High Performance Carbon Nanotube Thin-Film Transistors on Flexible Substrates.* Nano Letters, 2013. **13**(8): p. 3864-3869.

63. Kordás, K., T. Mustonen, G. Tóth, H. Jantunen, M. Lajunen, C. Soldano, S. Talapatra, S. Kar, R. Vajtai, and P.M. Ajayan, *Inkjet Printing of Electrically Conductive Patterns of Carbon Nanotubes.* Small, 2006. **2**(8-9): p. 1021-1025.

64. Zhu, C., T. Liu, F. Qian, T.Y.-J. Han, E.B. Duoss, J.D. Kuntz, C.M. Spadaccini, M.A. Worsley, and Y. Li, *Supercapacitors Based on Three-Dimensional Hierarchical Graphene Aerogels with Periodic Macropores.* Nano Letters, 2016. **16**(6): p. 3448-3456.

65. Chen, J.H., M. Ishigami, C. Jang, D.R. Hines, M.S. Fuhrer, and E.D. Williams, *Printed Graphene Circuits.* Advanced Materials, 2007. **19**(21): p. 3623-3627.

66. Torrisi, F., T. Hasan, W. Wu, Z. Sun, A. Lombardo, T.S. Kulmala, G.-W. Hsieh, S. Jung, F. Bonaccorso, P.J. Paul, D. Chu, and A.C. Ferrari, *Inkjet-Printed Graphene Electronics.* ACS Nano, 2012. **6**(4): p. 2992-3006.

67. Skotadis, E., D. Mousadakos, K. Katsabrokou, S. Stathopoulos, and D. Tsoukalas, *Flexible polyimide chemical sensors using platinum nanoparticles.* Sensors and Actuators B: Chemical, 2013. **189**: p. 106-112.

68. Tang, A., Y. Liu, Q. Wang, R. Chen, W. Liu, Z. Fang, and L. Wang, *A new photoelectric ink based on nanocellulose/CdS quantum dots for screen-printing.* Carbohydrate Polymers, 2016. **148**: p. 29-35.

69. Wood, V., M.J. Panzer, J. Chen, M.S. Bradley, J.E. Halpert, M.G. Bawendi, and V. Bulović, *Inkjet-Printed Quantum Dot–Polymer Composites for Full-Color AC-Driven Displays.* Advanced Materials, 2009. **21**(21): p. 2151-2155.

70. Secor, E.B., S. Lim, H. Zhang, C.D. Frisbie, L.F. Francis, and M.C. Hersam, *Gravure Printing of Graphene for Large-area Flexible Electronics.* Advanced Materials, 2014. **26**(26): p. 4533-4538.

71. Cao, X., H. Chen, X. Gu, B. Liu, W. Wang, Y. Cao, F. Wu, and C. Zhou, *Screen Printing as a Scalable and Low-Cost Approach for Rigid and Flexible Thin-Film Transistors Using Separated Carbon Nanotubes.* ACS Nano, 2014. **8**(12): p. 12769-12776.

72. Lipomi, D.J., M. Vosgueritchian, B.C. Tee, S.L. Hellstrom, J.A. Lee, C.H. Fox, and Z. Bao, *Skin-like pressure and strain sensors based on transparent elastic films of carbon nanotubes.* Nature nanotechnology, 2011. **6**(12): p. 788-792.

73. Vosgueritchian, M., D.J. Lipomi, and Z. Bao, *Highly conductive and transparent PEDOT: PSS films with a fluorosurfactant for stretchable and flexible transparent electrodes.* Advanced functional materials, 2012. **22**(2): p. 421-428.

74. Small, W.R. and M. in het Panhuis, *Inkjet Printing of Transparent, Electrically Conducting Single-Walled Carbon-Nanotube Composites.* Small, 2007. **3**(9): p. 1500-1503.

75. Takei, K., Z. Yu, M. Zheng, H. Ota, T. Takahashi, and A. Javey, *Highly sensitive electronic whiskers based on patterned carbon nanotube and silver nanoparticle composite films.* Proceedings of the National Academy of Sciences of the United States of America, 2014. **111**(5): p. 1703-1707.

76. Lee, C.-L., C.-H. Chen, and C.-W. Chen, *Graphene nanosheets as ink particles for inkjet printing on flexible board.* Chemical Engineering Journal, 2013. **230**: p. 296-302.

77. Wei, D., P. Andrew, H. Yang, Y. Jiang, F. Li, C. Shan, W. Ruan, D. Han, L. Niu, C. Bower, T. Ryhanen, M. Rouvala, G.A.J. Amaratunga, and A. Ivaska, *Flexible solid state lithium batteries based on graphene inks.* Journal of Materials Chemistry, 2011. **21**(26): p. 9762-9767.

78. Secor, E.B. and M.C. Hersam, *Emerging Carbon and Post-Carbon Nanomaterial Inks for Printed Electronics.* The journal of physical chemistry letters, 2015. **6**(4): p. 620-626.

79. Pierre, A., M. Sadeghi, M.M. Payne, A. Facchetti, J.E. Anthony, and A.C. Arias, *All-Printed Flexible Organic Transistors Enabled by Surface Tension-Guided Blade Coating.* Advanced Materials, 2014. **26**(32): p. 5722-5727.

80. Ma, P.-C., N.A. Siddiqui, G. Marom, and J.-K. Kim, *Dispersion and functionalization of carbon nanotubes for polymer-based nanocomposites: A review.* Composites Part A: Applied Science and Manufacturing, 2010. **41**(10): p. 1345-1367.

81. Zu, S.-Z. and B.-H. Han, *Aqueous Dispersion of Graphene Sheets Stabilized by Pluronic Copolymers: Formation of Supramolecular Hydrogel.* The Journal of Physical Chemistry C, 2009. **113**(31): p. 13651-13657.

82. Tölle, F.J., M. Fabritius, and R. Mülhaupt, *Emulsifier-Free Graphene Dispersions with High Graphene Content for Printed Electronics and Freestanding Graphene Films.* Advanced Functional Materials, 2012. **22**(6): p. 1136-1144.

83. Liu, C.-X. and J.-W. Choi, *Improved dispersion of carbon nanotubes in polymers at high concentrations.* Nanomaterials, 2012. **2**(4): p. 329-347.

84. Lotya, M., Y. Hernandez, P.J. King, R.J. Smith, V. Nicolosi, L.S. Karlsson, F.M. Blighe, S. De, Z. Wang, I.T. McGovern, G.S. Duesberg, and J.N. Coleman, *Liquid Phase Production of Graphene by Exfoliation of Graphite in Surfactant/Water Solutions.* Journal of the American Chemical Society, 2009. **131**(10): p. 3611-3620.

85. Hasan, T., F. Torrisi, Z. Sun, D. Popa, V. Nicolosi, G. Privitera, F. Bonaccorso, and A.C. Ferrari, *Solution-phase exfoliation of graphite for ultrafast photonics.* physica status solidi (b), 2010. **247**(11-12): p. 2953-2957.

86. Vadukumpully, S., J. Paul, and S. Valiyaveettil, *Cationic surfactant mediated exfoliation of graphite into graphene flakes.* Carbon, 2009. **47**(14): p. 3288-3294.

87. McCoy, T.M., A.C.Y. Liu, and R.F. Tabor, *Light-controllable dispersion and recovery of graphenes and carbon nanotubes using a photo-switchable surfactant.* Nanoscale, 2016. **8**(13): p. 6969-6974.

88. Rastogi, R., R. Kaushal, S.K. Tripathi, A.L. Sharma, I. Kaur, and L.M. Bharadwaj, *Comparative study of carbon nanotube dispersion using surfactants.* Journal of Colloid and Interface Science, 2008. **328**(2): p. 421-428.

89. Hecht, D.S., L. Hu, and G. Irvin, *Emerging Transparent Electrodes Based on Thin Films of Carbon Nanotubes, Graphene, and Metallic Nanostructures.* Advanced Materials, 2011. **23**(13): p. 1482-1513.

90. Hu, L., D.S. Hecht, and G. Grüner, *Carbon Nanotube Thin Films: Fabrication, Properties, and Applications.* Chemical Reviews, 2010. **110**(10): p. 5790-5844.

91. Li, Z., R. Zhang, K.-S. Moon, Y. Liu, K. Hansen, T. Le, and C.P. Wong, *Highly Conductive, Flexible, Polyurethane-Based Adhesives for Flexible and Printed Electronics.* Advanced Functional Materials, 2013. **23**(11): p. 1459-1465.

92. Ma, P.-C., S.-Y. Mo, B.-Z. Tang, and J.-K. Kim, *Dispersion, interfacial interaction and re-agglomeration of functionalized carbon nanotubes in epoxy composites.* Carbon, 2010. **48**(6): p. 1824-1834.

93. Tang, L.-C., Y.-J. Wan, D. Yan, Y.-B. Pei, L. Zhao, Y.-B. Li, L.-B. Wu, J.-X. Jiang, and G.-Q. Lai, *The effect of graphene dispersion on the mechanical properties of graphene/epoxy composites.* Carbon, 2013. **60**: p. 16-27.

94. Ogihara, H., H. Kibayashi, and T. Saji, *Microcontact Printing for Patterning Carbon Nanotube/Polymer Composite Films with Electrical Conductivity.* ACS Applied Materials & Interfaces, 2012. **4**(9): p. 4891-4897.

95. Ha, H., K. Shanmuganathan, and C.J. Ellison, *Mechanically Stable Thermally Crosslinked Poly(acrylic acid)/Reduced Graphene Oxide Aerogels.* ACS Applied Materials & Interfaces, 2015. **7**(11): p. 6220-6229.

96. Sangermano, M., M. Sturari, A. Chiappone, and I. Roppolo, *Study of Ink-Jet Printable Vinyl Ether-Graphene UV-Curable Formulations.* Macromolecular Materials and Engineering, 2015. **300**(3): p. 340-345.

97. Ralphs, M.I. and N. Roberts. *Not Enough Precision to Accurately Measure the Effect of CNT Functionalization on the Thermal Conductivity of PDMS/CNT*

Composite Under Strain Using Stepped-Bar Apparatus. in *ASME 2015 International Mechanical Engineering Congress and Exposition*. 2015. American Society of Mechanical Engineers.

98. Chen, Z., C. Xu, C. Ma, W. Ren, and H.-M. Cheng, *Lightweight and Flexible Graphene Foam Composites for High-Performance Electromagnetic Interference Shielding.* Advanced Materials, 2013. **25**(9): p. 1296-1300.

99. Lee, J.-H., K.Y. Lee, M.K. Gupta, T.Y. Kim, D.-Y. Lee, J. Oh, C. Ryu, W.J. Yoo, C.-Y. Kang, S.-J. Yoon, J.-B. Yoo, and S.-W. Kim, *Nanogenerators: Highly Stretchable Piezoelectric-Pyroelectric Hybrid Nanogenerator (Adv. Mater. 5/2014).* Advanced Materials, 2014. **26**(5): p. 820-820.

100. Broza, G., K. Piszczek, K. Schulte, and T. Sterzynski, *Nanocomposites of poly(vinyl chloride) with carbon nanotubes (CNT).* Composites Science and Technology, 2007. **67**(5): p. 890-894.

101. Zhao, X., Q. Zhang, D. Chen, and P. Lu, *Enhanced Mechanical Properties of Graphene-Based Poly(vinyl alcohol) Composites.* Macromolecules, 2010. **43**(5): p. 2357-2363.

102. Mustonen, T., K. Kordás, S. Saukko, G. Tóth, J.S. Penttilä, P. Helistö, H. Seppä, and H. Jantunen, *Inkjet printing of transparent and conductive patterns of single-walled carbon nanotubes and PEDOT-PSS composites.* physica status solidi (b), 2007. **244**(11): p. 4336-4340.

103. Alshammari, A., M. Shkunov, and S.R.P. Silva, *Inkjet printed PEDOT: PSS/MWCNT nano-composites with aligned carbon nanotubes and enhanced conductivity.* physica status solidi (RRL)-Rapid Research Letters, 2014. **8**(2): p. 150-153.

104. Tortorich, R.P., E. Song, and J.-W. Choi, *Inkjet-printed carbon nanotube electrodes with low sheet resistance for electrochemical sensor applications.* Journal of The Electrochemical Society, 2014. **161**(2): p. B3044-B3048.

105. Lim, S.C., D.S. Lee, K.K. Kim, Y.C. Choi, H.S. Kim, J.H. Lee, U. Paik, and Y.H. Lee, *Fluidic Properties of Carbon Nanotube Inks and Field Emission Properties of Ink Jet-Printed Emitters.* Japanese Journal of Applied Physics, 2009. **48**(11R): p. 111601.

106. Eom, S.H., H. Park, S. Mujawar, S.C. Yoon, S.-S. Kim, S.-I. Na, S.-J. Kang, D. Khim, D.-Y. Kim, and S.-H. Lee, *High efficiency polymer solar cells via sequential inkjet-printing of PEDOT: PSS and P3HT: PCBM inks with additives.* Organic Electronics, 2010. **11**(9): p. 1516-1522.

107. Kulkarni, M.V., S.K. Apte, S.D. Naik, J.D. Ambekar, and B.B. Kale, *Ink-jet printed conducting polyaniline based flexible humidity sensor.* Sensors and Actuators B: Chemical, 2013. **178**: p. 140-143.

108. Chiolerio, A., S. Bocchini, and S. Porro, *Inkjet Printed Negative Supercapacitors: Synthesis of Polyaniline-Based Inks, Doping Agent Effect, and Advanced Electronic Devices Applications.* Advanced Functional Materials, 2014. **24**(22): p. 3375-3383.

109. Xu, Y., M.G. Schwab, A.J. Strudwick, I. Hennig, X. Feng, Z. Wu, and K. Müllen, *Screen-Printable Thin Film Supercapacitor Device Utilizing Graphene/Polyaniline Inks.* Advanced Energy Materials, 2013. **3**(8): p. 1035-1040.

110. Gangopadhyay, R. and M.R. Molla, *Polypyrrole–polyvinyl alcohol stable nanodispersion: A prospective conducting black ink.* Journal of Polymer Science Part B: Polymer Physics, 2011. **49**(11): p. 792-800.

111. Mabrook, M., C. Pearson, and M. Petty, *Inkjet-printed polypyrrole thin films for vapour sensing.* Sensors and Actuators B: Chemical, 2006. **115**(1): p. 547-551.

112. Liu, Y., T. Cui, and K. Varahramyan, *All-polymer capacitor fabricated with inkjet printing technique.* Solid-State Electronics, 2003. **47**(9): p. 1543-1548.

113. Gerard, M., A. Chaubey, and B. Malhotra, *Application of conducting polymers to biosensors.* Biosensors and Bioelectronics, 2002. **17**(5): p. 345-359.

114. Lee, H., H. Kim, M.S. Cho, J. Choi, and Y. Lee, *Fabrication of polypyrrole (PPy)/carbon nanotube (CNT) composite electrode on ceramic fabric for supercapacitor applications.* Electrochimica Acta, 2011. **56**(22): p. 7460-7466.

115. Xu, Y., I. Hennig, D. Freyberg, A.J. Strudwick, M.G. Schwab, T. Weitz, and K.C.-P. Cha, *Inkjet-printed energy storage device using graphene/polyaniline inks.* Journal of Power Sources, 2014. **248**: p. 483-488.

116. Bardpho, C., P. Rattanarat, W. Siangproh, and O. Chailapakul, *Ultra-high performance liquid chromatographic determination of antioxidants in teas using inkjet-printed graphene–polyaniline electrode.* Talanta, 2016. **148**: p. 673-679.

117. Lenhart, N., K. Crowley, A.J. Killard, M.R. Smyth, and A. Morrin, *Inkjet printable polyaniline-gold dispersions.* Thin Solid Films, 2011. **519**(13): p. 4351-4356.

118. Liu, Z., Y. Su, and K. Varahramyan, *Inkjet-printed silver conductors using silver nitrate ink and their electrical contacts with conducting polymers.* Thin Solid Films, 2005. **478**(1): p. 275-279.

119. Liang, J., K. Tong, and Q. Pei *A Water-Based Silver-Nanowire Screen-Print Ink for the Fabrication of Stretchable Conductors and Wearable Thin-Film Transistors*. Advanced Materials, 2016. DOI: DOI: 10.1002/adma.201600772.

120. Shang, S., W. Zeng, and X.-m. Tao, *High stretchable MWNTs/polyurethane conductive nanocomposites.* Journal of Materials Chemistry, 2011. **21**(20): p. 7274-7280.

121. Hansen, T.S., K. West, O. Hassager, and N.B. Larsen, *Highly Stretchable and Conductive Polymer Material Made from Poly (3, 4-ethylenedioxythiophene) and Polyurethane Elastomers.* Advanced functional materials, 2007. **17**(16): p. 3069-3073.

122. Brook, I., G. Mechrez, R.Y. Suckeveriene, R. Tchoudakov, and M. Narkis, *A novel approach for preparation of conductive hybrid elastomeric nano-composites.* Polymers for Advanced Technologies, 2013. **24**(8): p. 758-763.

123. Vural, M., A.M. Behrens, O.B. Ayyub, J.J. Ayoub, and P. Kofinas, *Sprayable elastic conductors based on block copolymer silver nanoparticle composites.* ACS nano, 2014. **9**(1): p. 336-344.

124. Lipomi, D.J., *Stretchable Figures of Merit in Deformable Electronics.* Advanced Materials, 2015. **28**: p. 4180.

125. Chun, K.-Y., Y. Oh, J. Rho, J.-H. Ahn, Y.-J. Kim, H.R. Choi, and S. Baik, *Highly conductive, printable and stretchable composite films of carbon nanotubes and silver.* Nature nanotechnology, 2010. **5**(12): p. 853-857.

126. Sekitani, T., H. Nakajima, H. Maeda, T. Fukushima, T. Aida, K. Hata, and T. Someya, *Stretchable active-matrix organic light-emitting diode display using printable elastic conductors.* Nature materials, 2009. **8**(6): p. 494-499.

127. Park, M., J. Im, M. Shin, Y. Min, J. Park, H. Cho, S. Park, M.-B. Shim, S. Jeon, D.-Y. Chung, J. Bae, J. Park, U. Jeong, and K. Kim, *Highly stretchable electric circuits from a composite material of silver nanoparticles and elastomeric fibres.* Nature nanotechnology, 2012. **7**(12): p. 803-809.

128. Yao, S. and Y. Zhu, *Wearable multifunctional sensors using printed stretchable conductors made of silver nanowires.* Nanoscale, 2014. **6**(4): p. 2345-2352.

129. Boley, J.W., E.L. White, and R.K. Kramer, *Mechanically Sintered Gallium–Indium Nanoparticles.* Advanced Materials, 2015. **27**(14): p. 2355-2360.

130. Cánovas, R., M. Parrilla, P. Mercier, F.J. Andrade, and J. Wang, *Balloon-Embedded Sensors Withstanding Extreme Multiaxial Stretching and Global Bending Mechanical Stress: Towards Environmental and Security Monitoring.* Advanced Materials Technologies, 2016.

131. Xu, F. and Y. Zhu, *Highly Conductive and Stretchable Silver Nanowire Conductors.* Advanced Materials, 2012. **24**(37): p. 5117-5122.

132. Martin, P., *Wound healing--aiming for perfect skin regeneration.* Science, 1997. **276**(5309): p. 75-81.

133. Toback, F.G., *Regeneration after acute tubular necrosis.* Kidney international, 1992. **41**(1): p. 226-246.

134. Harrington, M.J., O. Speck, T. Speck, S. Wagner, and R. Weinkamer, *Biological Archetypes for Self-Healing Materials.* 2015.

135. Blaiszik, B., S. Kramer, S. Olugebefola, J.S. Moore, N.R. Sottos, and S.R. White, *Self-healing polymers and composites.* Annual Review of Materials Research, 2010. **40**: p. 179-211.

136. Patrick, J.F., K.R. Hart, B.P. Krull, C.E. Diesendruck, J.S. Moore, S.R. White, and N.R. Sottos, *Continuous Self-Healing Life Cycle in Vascularized Structural Composites.* Advanced Materials, 2014. **26**(25): p. 4302-4308.

137. Hart, K.R., N.R. Sottos, and S.R. White, *Repeatable self-healing of an epoxy matrix using imidazole initiated polymerization.* Polymer, 2015. **67**: p. 174-184.

138. Fifo, O., K. Ryan, and B. Basu, *Glass fibre polyester composite with in vivo vascular channel for use in self-healing.* Smart Materials and Structures, 2014. **23**(9): p. 095017.

139. White, S.R., N. Sottos, P. Geubelle, J. Moore, M.R. Kessler, S. Sriram, E. Brown, and S. Viswanathan, *Autonomic healing of polymer composites.* Nature, 2001. **409**(6822): p. 794-797.

140. Caruso, M.M., D.A. Delafuente, V. Ho, N.R. Sottos, J.S. Moore, and S.R. White, *Solvent-promoted self-healing epoxy materials.* Macromolecules, 2007. **40**(25): p. 8830-8832.

141. Brown, E.N., S.R. White, and N.R. Sottos, *Microcapsule induced toughening in a self-healing polymer composite.* Journal of Materials Science, 2004. **39**(5): p. 1703-1710.

142. Samadzadeh, M., S.H. Boura, M. Peikari, S. Kasiriha, and A. Ashrafi, *A review on self-healing coatings based on micro/nanocapsules.* Progress in Organic Coatings, 2010. **68**(3): p. 159-164.

143. Yuan, Y.C., M.Z. Rong, M.Q. Zhang, J. Chen, G.C. Yang, and X.M. Li, *Self-healing polymeric materials using epoxy/mercaptan as the healant.* Macromolecules, 2008. **41**(14): p. 5197-5202.

144. Kessler, M., N. Sottos, and S. White, *Self-healing structural composite materials.* Composites Part A: applied science and manufacturing, 2003. **34**(8): p. 743-753.

145. Imato, K., M. Nishihara, T. Kanehara, Y. Amamoto, A. Takahara, and H. Otsuka, *Self‐Healing of Chemical Gels Cross‐Linked by Diarylbibenzofuranone‐Based Trigger‐Free Dynamic Covalent Bonds at Room Temperature.* Angewandte Chemie International Edition, 2012. **51**(5): p. 1138-1142.

146. Hwang, S.-W., H. Tao, D.-H. Kim, H. Cheng, J.-K. Song, E. Rill, M.A. Brenckle, B. Panilaitis, S.M. Won, Y.-S. Kim, Y.M. Song, K.J. Yu, A. Ameen, R. Li, Y. Su, M.

Yang, D.L. Kaplan, M.R. Zakin, M.J. Slepian, Y. Huang, F.G. Omenetto, and J.A. Rogers, *A physically transient form of silicon electronics.* Science, 2012. **337**(6102): p. 1640-1644.

147. Fu, K.K., Z. Wang, J. Dai, M. Carter, and L. Hu, *Transient Electronics: Materials and Devices.* Chemistry of Materials, 2016. **28**(11): p. 3527-3539.

148. Wu, J., M. Agrawal, H.A. Becerril, Z. Bao, Z. Liu, Y. Chen, and P. Peumans, *Organic light-emitting diodes on solution-processed graphene transparent electrodes.* ACS nano, 2009. **4**(1): p. 43-48.

149. Wang, X., L. Zhi, and K. Müllen, *Transparent, conductive graphene electrodes for dye-sensitized solar cells.* Nano letters, 2008. **8**(1): p. 323-327.

150. Xia, Y., K. Sun, and J. Ouyang, *Solution‐processed metallic conducting polymer films as transparent electrode of optoelectronic devices.* Advanced Materials, 2012. **24**(18): p. 2436-2440.

151. Minami, T., *Transparent conducting oxide semiconductors for transparent electrodes.* Semiconductor Science and Technology, 2005. **20**(4): p. S35.

152. Yin, Z., S. Sun, T. Salim, S. Wu, X. Huang, Q. He, Y.M. Lam, and H. Zhang, *Organic photovoltaic devices using highly flexible reduced graphene oxide films as transparent electrodes.* ACS nano, 2010. **4**(9): p. 5263-5268.

153. Park, H., P.R. Brown, V. Bulović, and J. Kong, *Graphene as transparent conducting electrodes in organic photovoltaics: studies in graphene morphology, hole transporting layers, and counter electrodes.* Nano letters, 2011. **12**(1): p. 133-140.

154. Bae, S., H. Kim, Y. Lee, X. Xu, J.-S. Park, Y. Zheng, J. Balakrishnan, T. Lei, H.R. Kim, Y.I. Song, Y.-J. Kim, K.S. Kim, B. Özyilmaz, J.-H. Ahn, B.H. Hong, and S. Iijima, *Roll-to-roll production of 30-inch graphene films for transparent electrodes.* Nature nanotechnology, 2010. **5**(8): p. 574-578.

155. Li, X., Y. Zhu, W. Cai, M. Borysiak, B. Han, D. Chen, R.D. Piner, L. Colombo, and R.S. Ruoff, *Transfer of large-area graphene films for high-performance transparent conductive electrodes.* Nano letters, 2009. **9**(12): p. 4359-4363.

156. Yoo, J.E., K.S. Lee, A. Garcia, J. Tarver, E.D. Gomez, K. Baldwin, Y. Sun, H. Meng, T.-Q. Nguyen, and Y.-L. Loo, *Directly patternable, highly conducting polymers for broad applications in organic electronics.* Proceedings of the National Academy of Sciences, 2010. **107**(13): p. 5712-5717.

157. Huang, J.-H., D. Kekuda, C.-W. Chu, and K.-C. Ho, *Electrochemical characterization of the solvent-enhanced conductivity of poly (3, 4-ethylenedioxythiophene) and its application in polymer solar cells.* Journal of Materials Chemistry, 2009. **19**(22): p. 3704-3712.

158. Argun, A.A., A. Cirpan, and J.R. Reynolds, *The First Truly All-Polymer Electrochromic Devices.* Advanced Materials, 2003. **15**(16): p. 1338-1341.

159. Zhang, F., M. Johansson, M.R. Andersson, J.C. Hummelen, and O. Inganäs, *Polymer photovoltaic cells with conducting polymer anodes.* Advanced Materials, 2002. **14**(9): p. 662-665.

160. Na, S.I., S.S. Kim, J. Jo, and D.Y. Kim, *Efficient and Flexible ITO-Free Organic Solar Cells Using Highly Conductive Polymer Anodes.* Advanced Materials, 2008. **20**(21): p. 4061-4067.

161. Zhang, M., S. Fang, A.A. Zakhidov, S.B. Lee, A.E. Aliev, C.D. Williams, K.R. Atkinson, and R.H. Baughman, *Strong, transparent, multifunctional, carbon nanotube sheets.* Science, 2005. **309**(5738): p. 1215-1219.

162. Gruner, G., *Carbon nanotube films for transparent and plastic electronics.* Journal of Materials Chemistry, 2006. **16**(35): p. 3533-3539.

163. Kim, K.S., Y. Zhao, H. Jang, S.Y. Lee, J.M. Kim, K.S. Kim, J.-H. Ahn, P. Kim, J.-Y. Choi, and B.H. Hong, *Large-scale pattern growth of graphene films for stretchable transparent electrodes.* Nature, 2009. **457**(7230): p. 706-710.

164. Becerril, H.A., J. Mao, Z. Liu, R.M. Stoltenberg, Z. Bao, and Y. Chen, *Evaluation of solution-processed reduced graphene oxide films as transparent conductors.* ACS nano, 2008. **2**(3): p. 463-470.

165. Tung, V.C., L.-M. Chen, M.J. Allen, J.K. Wassei, K. Nelson, R.B. Kaner, and Y. Yang, *Low-temperature solution processing of graphene− carbon nanotube hybrid materials for high-performance transparent conductors.* Nano letters, 2009. **9**(5): p. 1949-1955.

166. Lee, J.-Y., S.T. Connor, Y. Cui, and P. Peumans, *Solution-processed metal nanowire mesh transparent electrodes.* Nano letters, 2008. **8**(2): p. 689-692.

167. Yu, Z., Q. Zhang, L. Li, Q. Chen, X. Niu, J. Liu, and Q. Pei, *Highly Flexible Silver Nanowire Electrodes for Shape-Memory Polymer Light-Emitting Diodes.* Advanced Materials, 2011. **23**(5): p. 664-668.

168. Song, J., S.A. Kulinich, J. Li, Y. Liu, and H. Zeng, *A General One-Pot Strategy for the Synthesis of High-Performance Transparent-Conducting-Oxide Nanocrystal Inks for All-Solution-Processed Devices.* Angewandte Chemie, 2015. **127**(2): p. 472-476.

169. Sun, J., B. Zhang, and H.E. Katz, *Materials for Printable, Transparent, and Low-Voltage Transistors.* Advanced Functional Materials, 2011. **21**(1): p. 29-45.

CHAPTER 2 PRINTABLE, CATALYTIC MOTORS

2.1 Self-Propelling, Screen-Printable, Catalytic Swimmers

2.1.1 Introduction

Mimicking natural swimmer, man-made motors have received considerable recent attention [1-6] Swimming devices, whose motion can be induced by different energy sources, have thus been developed toward diverse biomedical, environmental and industrial applications. Particular attention has been given to chemically-powered micromotors, containing a catalytically active layer and capable of converting chemical energy into movement in the presence of a fuel such as hydrogen peroxide [1,3,5]. These include catalytic motors of different geometries and sizes, including bimetallic catalytic nanowires, [3] Janus microparticles, [7,8] or microtubular microengines.[5,9] Such chemically-powered motors have commonly been prepared by template electrodeposition, e-beam evaporation, sputtering, top-down photolithography, and stress-assisted rolled-up lithographic techniques.[6] Recent efforts demonstrated the ability to combine bioinspired architectures with self-propelling swimmers using 3D printing techniques [10,11] Unfortunately, current manufacturing technologies for nano/microscale machines utilize complex multi-steps, expensive instrumentation and processes, along with toxic chemicals.

The objective of this work is to demonstrate as a proof of concept that multi-functional self-propelled swimmer can be created at large scale and low cost by screen-printing of tailored-made ink materials. Screen-printing (thick-film) technology has been widely used in printed electronics as it offers large-scale, cost-effective production of a variety of electronic devices, including sensors, solar cells, transistors and touch screens.[12,13] The technology is based on depositing diverse materials (inks) onto a planar large-area substrate through a patterned stencil or mask, followed by a thermal or photo curing. The basic composition for these inks includes a conductive or insulating material, a binding agent, and a solvent. For example, carbon and silver inks have been widely used to mass produce single-use blood glucose sensor strips.[14] Technological advances in ink materials have recently led to the development of flexible, stretchable and bendable printable devices.[15] While screen-printing is widely used for fabricating diverse electronic devices, this method has not been applied for creating functional robotic structures. In particular, it would be of great interest to take advantage of existing printing technologies and modern ink materials for creating biomimetic swimmer architectures.

The present screen-printing swimmer fabrication approach offers remarkable versatility and low cost compared to traditional methods for fabricating swimmers. To illustrate the versatility of this screen-printing approach and address the challenge of mimicking the complex motion and function of natural aquatic swimmers, we designed artificial bio-inspired fish-shaped motors (3-10 mm long) capable of swimming autonomously while simultaneously performing specific applications (Figure 2.1). Sequential printing of specific layers based on different tailored-made inks has been used for incorporating various functionalities at specific areas of the fish, including its mid-body, head, tail, and entire fish, based on a predetermined AutoCAD design pattern of the corresponding stencil (Figure 2.1). A single stencil can thus be used for printing multiple (>50) high-quality fish. A variety of multifunctional swimmer architectures have been fabricated using different modified inks with pre-selected functionality. Fish with different propulsion efficiencies have been prepared by printing catalytic tail sections with inks containing different Pt loadings. Control of the fish directionality has been achieved by printing a nickel-containing carbon magnetic layer. The autonomous motion of fish with a printed activate-carbon layer has been used for adsorptive removal of chemical pollutants. Unlike micro/nanoscale motors that have gained considerable attention for biomedical or fabrication applications, scaling of printed swimmers to the millimeter size will enhance operations over large areas, e.g. environmental and security decontamination and detoxification compared to current remediation microswimmers.[16,17] The screen-printing fabrication of such large swimmers can facilitate further integration of embedded electronics and communications towards robot-like autonomous motors that are well beyond the limits of current micro/nanoscale motors. As will be illustrated in the following sections, the all-printing fish fabrication route, involving embedding different active materials at specific sections, holds considerable promise for the design of practical high-quality multi-functional self-propelled bio-inspired swimmers for a wide range of important practical applications.

2.1.2 Experimental Section

Preparation of Catalytic Chitosan-Platinum Ink.

Chitosan (85% deacetylated from crab shells, Sigma-Aldrich, USA) was used as a binder at 3.5 %wt in a 0.3 M acetic acid solution (Fluka, USA). A fixed amount of Pt-C (Sigma Aldrich, USA), corresponding to 10% wt, was mixed gradually with the selected amount of Pt-B (Pt-B; <50 nm, Sigma Aldrich, USA), ranging from 5 to 15%, and vortexed over 24 hours. Then, each of these Pt-B/Pt-C mixtures was dispersed into a previously prepared chitosan solution, followed by sonication for 10 minutes. Each composition of the catalytic ink, based on the Pt-B loading, was represented by a different color (based on the corresponding acrylic paint).

Fabrication of the Functional Fish Motor.

The fabrication process comprised of printing various functional inks using a MPM-SPM semi-automatic screen printer (Speedline Technologies, Franklin, MA). The components of the fish mid-body, head, tail, and entire fish were designed in AutoCAD (Autodesk, San Rafael, CA) and used as patterns in the 12” x 12” stainless steel stencils (Metal Etch Services, San Marcos, CA) shown in Figue 1B. A temporary tattoo paper sheet (Papilio, Rhome, TX), precoated with a water–soluble polymer, served as the substrate for the printing process. The first layer of the fabricated fish was the mid-body prepared by printing a rigid graphite ink (E3449, Ercon Inc., Wareham, MA) using the mid-body stencil pattern, and cured at 100°C for 20 minutes. The second layer of the entire fish shape, overlaid on the mid-body carbon layer, was printed with a colored acrylic paint (BASICS, Liquitex, Piscataway, NJ). Being a paint, the second layer would be cured by a simple air drying for an approximately 5-10 minutes. The final basic layer, the catalytic tail, was printed using different Pt-chitosan ink formulations, and cured for 20 minutes at a temperature of 100°C. Different colored acrylic inks were used to identity catalytic power of the as the 5% Pt-B/10% Pt-C was colored orange, 10% Pt-B/10% Pt-C (yellow), 15% Pt-B/10% Pt-C (green), and only chitosan as a control (red). Magnetically guided fish were prepared by printing a carbon ink modified with 20 wt.% Ni powder (200 mesh, ~74 microns; Sigma Aldrich, USA) and cured for 20 minutes at 100°C. For environmental application involving the dye removal, activated carbon powder was dispersed 20 wt.% into the acetic acid solution containing 2% of the chitosan binder; this ink was printed as the mid-body layer and was cured for 20 minutes at 100°C. Further details of the printing process are given in the following Results and Discussion section. Images of the stencil and printed fish, and the supplementary videos, illustrating the fabrication steps, were taken using a DLSR camera (D700, Nikon, USA) equipped with a macrolens; the 3D surface morphology was mapped using a digitial microscope (Keyence VX-1000). The speed of the fish and tracking-line images were obtained with NIS Elements AR 3.2 software.

Spectrophotometric Measurements for Environmental Application Studies.

All measurements were performed with a UV-Vis spectrophotometer (UV-2450, SHIMADZU) equipped with a constant-temperature circulating bath. The removal of the methylene blue dye was evaluated by measuring the decrease of its absorbance peak at 660 nm. The degradation efficiency was studied by quantifying the amount of *para*-nitrophenol, the hydrolysis product of methyl-paraoxon, by measuring its absorbance at 400 nm. Stock solutions (30 μM for methyl-paraoxon and 12 μM methylene blue) were prepared daily in double distilled water and subsequently diluted to the required concentration.

2.1.3 Results and Discussion

Thick-Film Fabrication of Synthetic Swimmers

Figure 2.1 depicts the screen-printing microfabrication process of the multi-functional fish-like swimmers. Such a simple strategy of designing chemically-powered swimmers involves printing various modified inks, tailored for selected functionality, onto designated locations of the fish body using a commercial screen printer. The basic all-printed fish-shaped swimmers consist of three functional layers and have different shapes and dimensions (Figure 2.1D), as determined by the predesigned patterns of the corresponding stencil designs (Figure 2.1B, C). A single stencil can thus be used for preparing a wide range of highly reproducible swimmers in connection to printing of three partially-overlaid layers (Figure 2.1A). Different functionalities can thus be localized at specific locations of the printed fish. Such screen-printing process, along with the judicious selection of the printed ink, offers fine control of the fish functionality and shape (with resolution down to 100 µm), along with remarkable versatility and low cost compared to traditional fabrication methods. Control of the ink composition and the choice of its reactive material are essential for achieving such capabilities.

Figure 2.1A illustrates a schematic of the step-by-step (layer-by-layer) printing of the fish-shaped macromotor, with individual modified inks forced through different geometric patterns (openings) in the stencil. The ability to control the shape, size and thickness of each printed layer is dependent on a custom-designed stainless-steel stencil that has the specific designs for the head, tail and mid-body section a as well as of the entire fish (Figure 2.1B, 2.1C). After the stencil is positioned on the printing board the corresponding functional ink is placed on one side of the stencil and pressed through its patterned openings with a squeege onto the substrate, thus transfering the stencil patterns to the substrate (Figures 2.1C). The substrate is a tattoo paper pre-coated with a water-soluble material that allows easy removal of the printed microfish. The printed fish can be easily released (lifted off) from the substrate by simply soaking it in water for a minute (Figure 2.1A).

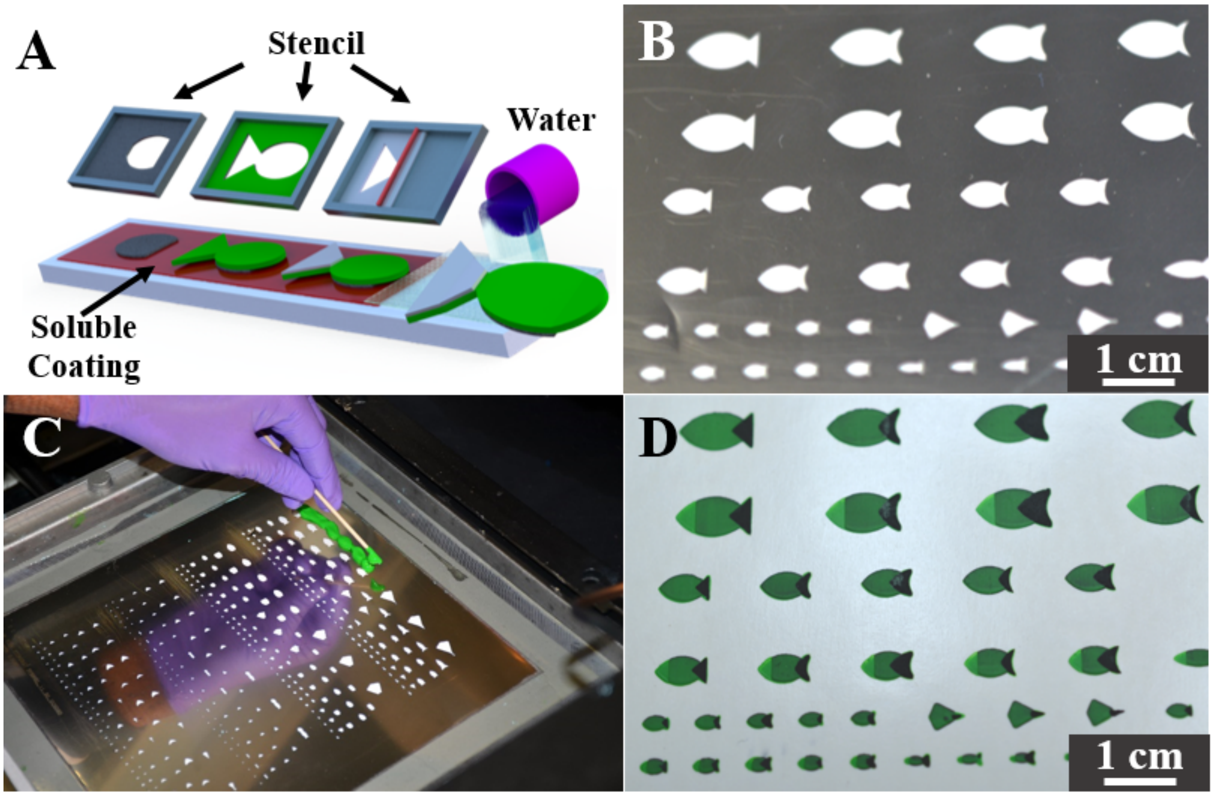

Figure 2.1: Figure of Printable Catalytic Motor Process and Final Print (A) Schematic illustration of the layer-by-layer screen-printing microfabrication of the synthetic catalytic fish: sequential printing of specific layers based on different modified inks for localizing different functionalities at specific sections of the printed fish. The first printed layer is a carbon mid-body, followed by printing of an acrylic ink (of preselected color) for the full body. Finally, a Pt-based catalytic ink is used for printing the tail section on top, with subsequent thermal curing of each layer. The complete printed fish is lifted off from the substrate using water. (B) Image of the stainless-steel stencil containing the pre-cut design of the entire fish shape using different dimensions and shapes. (C) Image of mass fabrication procedure; colored acrylic ink is physically applied onto the stencil above the pattern before a squeegee or doctor blade pushes the ink across the design. (D) Image of an array of mass-printed fish on a water-dissolvable coated substrate using the stencil shown in B. (Reprinted with permission and Copyright 2015 Royal Society of Chemistry).

The first printing step involves the fabrication of a rigid mid-body of the fish structure using a carbon ink on to a soluble substrate followed by curing. The next step involves printing of the entire fish-shape body by overlaying a colored acrylic-based ink on the initial carbon layer. Combining the carbon and acrylic layers offers the desired mechanical properties. After air drying of the acrylic ink, a Pt-containing catalytic ink is printed on top of the acrylic ink layer to define the catalytic tail section that generates the bubble thrust. Small amounts of modified ink can thus be used to mass produce a wide range of low-cost efficient catalytic swimmers. Using a single stencil leads to printing of a group of about 50 artificial well-defined fish, of diverse sizes ranging from 3 mm to 9 mm (Figure 2.1D). As illustrated in Figure 2.1D, the printed fish have distinct sections for the head and tail (green and black, respectively), with sharp edges of the individual printed layers, reflecting the high quality and resolution of the screen-printing process.

While screen-printing offers fine control of the shape and layering precision with a resolution of about 100 µm, it offers remarkable versatility and low cost compared to traditional methods for fabricating swimmers. A wide range of functional inks can be prepared for various applications and used to mass produce low-cost catalytic swimmers. Specific ink formulations can thus be prepared for imparting the selected functionality. A variety of functional inks can thus be employed for controlling the propulsion behavior and introducing specific applications. The new fabrication protocol thus offers screen-printing of artificial multifunctional swimmers that can be scaled up for variety of real-world applications. Unlike traditional methods of using templates and masks, the use of these screen-printable functional inks presents a high-throughput route of fabricating artificial swimmers by printing different architectures to impart the selected functionality (Figure 2.1A). As will be illustrated below, additional printable layers based on different functional materials can lead to new capabilities, including a nickel-based layer for magnetic guidance or an activated-carbon layer for efficient adsorption (decontamination) of environmental pollutants.

Propulsion Studies of All-Printable Swimmer

The new fabrication route of artificial fish relies on printing different sections of the body using various modified inks for imparting the selected functionality. In this particular work, these printed swimmers were designed in an arbitrary biomimetic fish shape, with a curved architecture essential for easy movement. Key for a successful printing of a chemically powered swimmer is the printing of the catalytic (Pt-based) tail section which plays a crucial role of producing the bubble thrust for autonomous motion. (Figure 2.1D). Swimmers with different propulsion efficiencies can thus be mass-produced by printing catalytic tails containing various Pt loadings. Most experiments were carried out using catalytic inks prepared by dispersing homogenously 10 mg of platinum-carbon (Pt-C) along with 15 mg platinum-black (Pt-B) in 75 mg of a chitosan solution (3.5% wt in 0.3 M acetic acid) and sonicating the mixture for 10 minutes. Chitosan served as a stable and inert binder for the Py-based catalytic ink for printing the tail section. After printing a catalytic tail, the acetic-acid solvent of the chitosan-Pt ink is completely evaporated and removed by thermal curing above the boiling point of the solvent. The catalytic Pt-B/Pt-C material thus resides on the surface of the fish tail, where it reacts with the hydrogen peroxide fuel, leading to the oxygen bubbles essential for the propulsion thrust. Higher chitosan content leads to entrapment of the catalytic Pt within the interior of the tail section and to poor propulsion behavior.

The propulsion mechanism of the synthetic fish relies on the continuous thrust of oxygen bubbles, generated by the decomposition of the hydrogen peroxide fuel at the catalytic tail of the fish. The detachment of these microbubbles from the catalytic Pt tail results in a net momentum that leads to directional propulsion thrust. A Pt-C/Pt-B mixture was used to create the catalytic tail as it resulted in a porous surface morphology and large specific surface area essential for effective catalytic decomposition of the fuel and bubble generation necessary for propulsion.[9,18] Other catalytic particles (e.g., palladium and Pt-C alone), were also tested but displayed a weak bubble generation and limited propulsion. Chitosan offers attractive properties as a binder for the catalytic ink, including chemical inertness, adhesiveness, hydrophilicity, good film formation capability and inherent biocompatibility,[19] that contribute to the minimal environmental impact of the printed fish and to its propulsion behavior. These attractive properties of chitosan material have been used in screen-printed sensor applications.[20] To further optimize the fish operation, we examined the influence of various factors, including the Pt-B loading in the catalytic tail, fish size, concentration of the peroxide fuel, and the swimming time. These effects are described in the following sections.

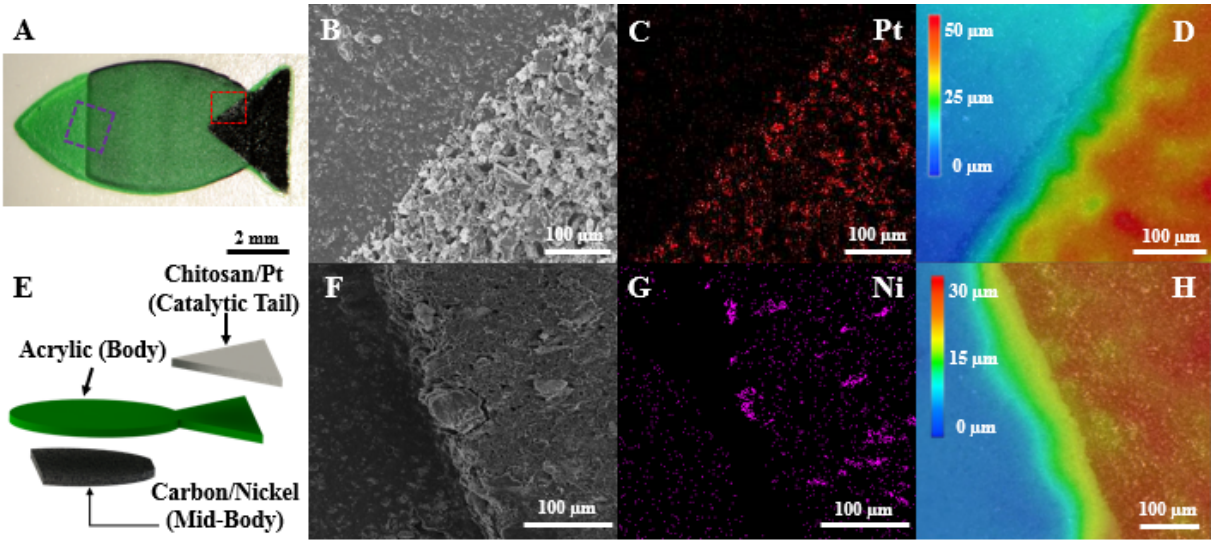

Figure 2.2: Images illustrating the different materials in particular printed regions of the fish: (A) Stereomicroscopy image of magnetically-guided catalytic fish (scale bar: 2 millimeters). (B) SEM image of the interface between the catalytic-tail and acrylic-body layers; (C) EDX spectroscopic image of the catalytic tail, which shows Pt particles in the chitosan matrix (scale bar: 100 microns). B and C were taken at the red dotted line square. (D) 3D Imaging of the interface layer between the Pt-B Tail and acrylic body. (E) Schematic of the sequentially-printed individual layers of the multifunctional fish architecture. (F) SEM image of interface of carbon/nickel and acrylic body; (G) EDX spectroscopic image of embedded Ni particles in the carbon ink (H) 3D of interface layer between the carbon/nickel ink with acrylic body. E and F were taken at the pink dotted line squares. (Reprinted with permission and Copyright 2015 Royal Society of Chemistry).

Scanning electron microscopy (SEM) imaging, shown in Figure 2.2B, indicates that the printed layers display a well-defined appearance with relatively smooth edges and no apparent defects. The energy-dispersive spectroscopic (EDX) mapping of the catalytic tail (shown in Figure 2.2C) illustrates that Pt is uniformly dispersed over the tail section, with a clear distinction from the body section. In addition, the 3D image (shown in Figure 2.2D) demonstrates the change in surface morphology between the Pt-B tail and the acrylic body, indicating similar control upon printing the catalytic ink. Figure S2 shows SEM (A) and EDX (B) images of tail-body interface areas for tails containing different catalyst loadings (5%, 10% and 15% Pt-B). The EDX data indicate a distinguishable difference between the different Pt ink compositions. As will be illustrated below, such changes in the loading of the Pt-B catalytic tail material leads to increased hydrogen peroxide decomposition efficiency and to an improved swimming behavior.

In addition to powering the printed fish, it is essential to control their directionality. The screen-printing fabrication can add such navigation capability through the printing of appropriate magnetic layers. Such incorporation of magnetic material within the inks also allows retrieval of the swimmers from the solution after specific operations, e.g., removal of remediation fish at the end of water treatment. To obtain such magnetic guidance and recovery capabilities, a magnetic ink was prepared by mixing nickel powder (~75 μm size) with a commercial carbon ink (at 20% wt. Ni). Mixing the nickel powder with the acrylic ink led to fragile fish structures. The Ni-carbon ink was printed in the mid-body to control the directionality with an applied magnetic field while keeping the architecture of the acrylic paint and the catalytic ink unchanged (Figure 2.2E). The magnetic layer does not need to be on the outer surface in order to direct the motion propulsion. Figure 2E displays the individual printed layers of the multifunctional fish architecture using different modified inks with pre-selected functionality. The SEM and EDX images of Figures 2.2F and 2.2G, respectively, indicate that the printed nickel-containing carbon layer has a well-defined appearance and a smooth edge. The smooth edge can be seen from the transition of the surface morphology between the carbon mid-body and acrylic full-body, shown in Figure 2.2H. The resulting fish can be navigated along the predetermined trajectories, under the external magnetic guidance, by simply turning a niobium-titanium (NbTi) magnet (Figure 3E). For example, Figure 2.3D displays such magnetically-guided movement following the letter “C” as the pre-selected path.

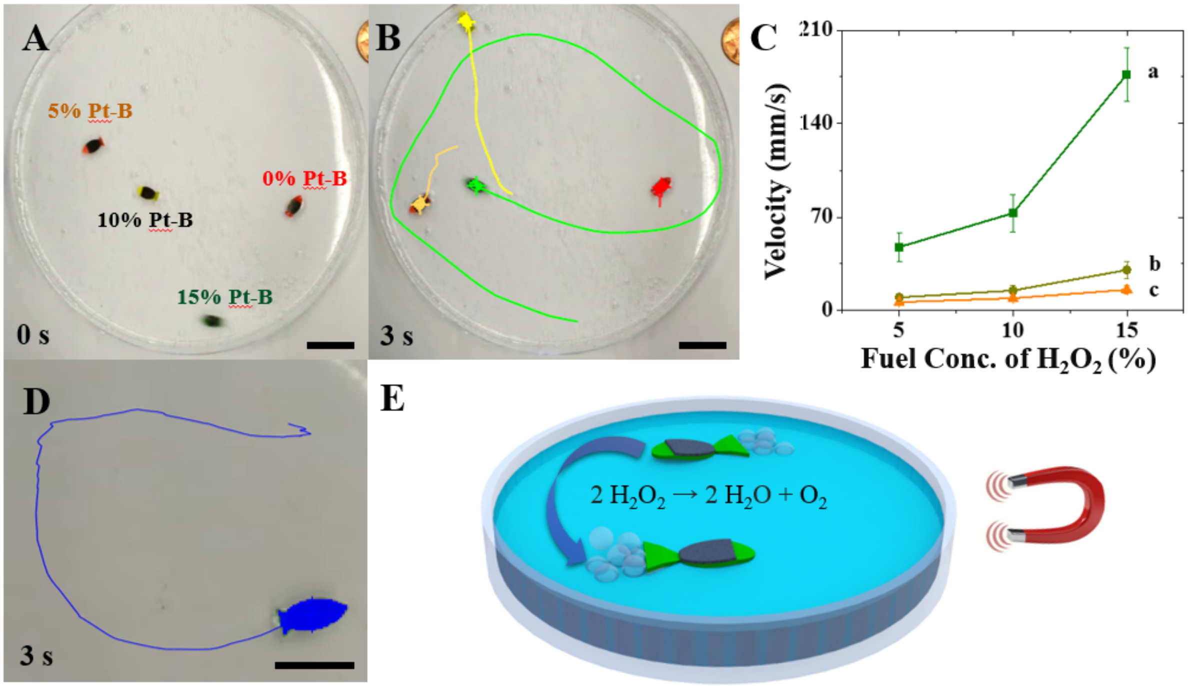

Figure 2.3: Track lines of screen-printed, catalytic fish with propulsion velocity determined by different Pt-B loadings in their tail area: 15% Pt-B/10% Pt-C (green), 10% Pt-B/10% Pt-C (yellow), 5% Pt-B/10% Pt-C (orange), and without catalytic tail as a control (red). (A) Initial location of the 4 printed fish (time 0 seconds), (B) tracking of these fish during 3 seconds (highlighted from Supplementary Video 1). (C) Dependence of the fish speed upon the peroxide fuel concentration using different Pt loadings (a, green fish; b, yellow fish; c, orange fish. (D) Tracking line (highlighted from Supplementary Video 2) of the magnetically-guided motion of the fish in a predetermined "C" shape over a 3 sec period based on the schematic illustration shown in (E) using external magnetic manipulation of the fish. Scale bar: 10 mm. (Reprinted with permission and Copyright 2015 Royal Society of Chemistry).

The rough catalytic tail surface promotes effective bubble evolution and propulsion. Printed fish with tails containing different Pt loadings were propelled first in a 15% hydrogen peroxide fuel solution (Figure 2.3A-C). The time-lapse image of Figure 2.3B, taken from supplementary video 1 (SV1), compares the swimming of these different catalytic fish in the peroxide fuel solution. These fish containing various Pt-B loadings are distinguished by their own individual colors (based the acrylic paint used: green 15%, yellow 10%, orange 5% Pt-B wt.%, and red with only chitosan). Increasing the Pt loading of the tail section results in a faster bubble generation - expected from the higher catalytic activity - and hence with higher speeds and longer swimming distances. For example, the 15 wt% Pt-B ‘green‘ fish displays a speed of 175 mm/s that corresponds to ~20 body-lengths per second, *i.e.,* covering a large distance of over 10 meters within one minute. Such swimming over large areas is essential for diverse applications, such as environmental remediation illustrated below, and represents a distinct advantage over smaller (micrometer) swimmers. Supplementary video 2 demonstrates the ultrafast speed of the 15 wt% Pt-B fish along with a rapid ejection of oxygen microbubbles from its catalytic tail section. The speed of the artificial swimmer is also strongly dependent strongly on the fuel concentration, as illustrated in Figure 2.3C for hydrogen peroxide concentrations ranging from 5% to 15%, using swimmers with different Pt loadings (a-c). For example, the speed of the 15% Pt-B loaded fish tail increases from 55 to 175 mm/s upon raising the fuel concentration between 5 and 15% hydrogen peroxide. Efficient movement was demonstrated in other media (e.g., seawater or oil-contaminated water) relevant to practical applications described later.

A lifetime study of the printed catalytic swimmer was performed using the fastest fish motor, immediately after being printed and placed in the fuel solution. Figure S3 shows the speed-time dependence profile over an 80 min period. The printed fish starts its motion with a slow speed of ~100 mm/s that increases rapidly, reaching a top speed of 170 ± 20 mm/s within 10 minutes. The initial preconditioning of the fish can be attributed to gradual penetration of the fuel into the porous catalytic tail. The speed subsequently decreases gradually due to gradual depletion of the fuel. The fish regains its top speed rapidly (~1 min) upon replenishing the peroxide solution (not shown).

Environmental Application Studies

The practical utility of the new artificial printed fish has been demonstrated by efficient cleanup (adsorption) of a model industrial pollutant and chemical decomposition of a nerve agent simulant. The continuous movement of motors containing reactive (water-purification) materials throughout contaminated samples has been shown useful for *'on-the-fly'* remediation protocols in connection to microscale motors.[16,17,21] The new 2D printing route allows convenient incorporation of such reactive remediation layers. For example, we modified our chitosan ink with activated-carbon to add an adsorbent functionality to the printed fish, as this material has been widely used for efficient removal of pollutants from aquatic media.[22-24] The autonomous motion of the printed swimmer results in high decontamination efficiency using short cleanup times. The large (mm) dimension of the screen-printed fish and corresponding motion over long (meter) distances - compared to earlier decontaminating micromotors[16,17,21,24] - holds great promise for large-scale environmental remediation.

The activated-carbon printed fish motors were evaluated first for the removal of the methylene blue (MB) model dye, commonly present in wastewater from the garment industry. Activated carbon has been widely used for the removal of dyes and pigments from industrial wastes.[25] However, conventional methods of using activated carbon commonly suffer from drawbacks of long processing times and difficulties of separation from the waste stream. In the present study, a 'remediation fish' was prepared by mixing activated carbon powder with the chitosan binder. After obtaining homogenous and viscous mixture, it was printed on the mid-body of the fish, followed by thermal curing. The activated-carbon ink was overlaid on top of the entire fish body (over the acrylic layer), except the catalytic tail.

In order to demonstrate the advantages of the dynamic movement of this remediation fish, a static activated-carbon printed fish (without catalytic tail) served as a control. The size and speed of printed micro swimmer has significant impact on the purification efficiency. For example, high speeds improve the solution mixing (and hence the adsorption rate) and offer coverage of large polluted areas. The size of the printed motor determines its adsorption capacity in view of major differences in the activated carbon surface areas of smaller and larger fishes. The removal efficiency of MB by the activated-carbon based catalytic macrofish was monitored by measuring the absorbance at 660 nm. The adsorptive removal experiments of MB were carried out by immersing four catalytic fish of the same shape and size in 20 mL of a MB-contaminated solution for 60 min. The influence of the remediation time upon the removal of MB was studied over the 5 to 60 min range in the presence of both the self-propelled and static (control) fish.

Figure 4A displays the absorbance studies of MB in the presence of the moving and static fish. This data indicates that the static fish leads to a small decrease in absorbance signal of MB observed, corresponding to a removal efficiency of 11% over the 60 min period. In contrast, moving the catalytic fish leads to a sharper decrease of the MB signal, corresponding to 57% of removal efficiency over the same period. The driving force for the enhanced adsorptive cleanup is the continuous movement of the activated carbon layer and generated microbubbles that along with the corresponding fluid dynamics and self-mixing leads to a significantly higher adsorption rate compared to its static counterparts. This adsorptive detoxification process can be extended to other target pollutants and scaled up for larger water bodies where mixing or agitation are challenging and costly.

In another experiment, the self-propelled catalytic fish (of Figure 3.2A, without activated carbon) was evaluated for the rapid peroxide-based oxidative detoxification of the nerve agent simulant methyl paraoxon (MP). The movement of the printed fish and corresponding bubble tail, provide a favorable fluid dynamic environment for such MP detoxification (without external agitation), as was previously demonstrated.[26] The efficiency of the degradation of the MP process was evaluated by measuring the absorbance of the *p*-nitrophenol (*p*-NP) hydrolysis product of MP at 400 nm. As illustrated in Figure 4B, the self-propelling fish greatly increases the rate of the peroxide-MP reaction, resulting in a 72% degradation of MP (b) compared to 17% in the case of its static counterpart (c) over the 20 min period. Such greatly enhanced degradation is achieved without mechanical stirring and peroxide activator. The extent of the fish-based accelerated MP degradation process increases upon raising the reaction time in 5-minute intervals.

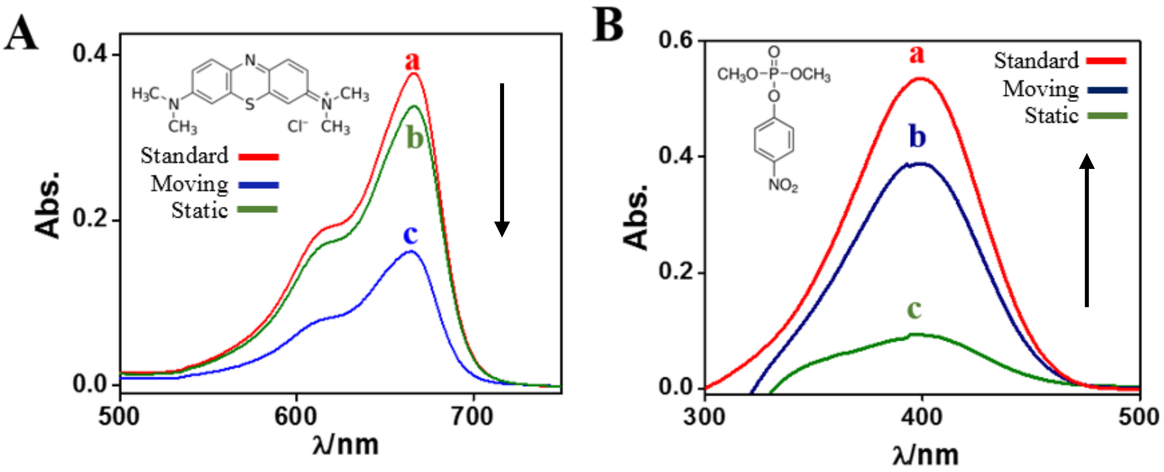

Figure 2.4. Absorbance spectra of methylene blue and p-nitrophenol, a product from the hydrolysis of the CWA simulant methyl paraoxon, showing the comparison between catalytically propelled fish and static fish: (A) "On-the-fly" adsorptive removal of methylene blue using activated carbon based moving fish: (a) absorbance spectra of methylene blue (12 µM), (b) after a 60 min treatment with static fish and (c) moving fish. (B) Fish-based degradation of CWA simulant methyl paraoxon. The efficiency of the decontamination process was estimated by measuring the absorbance of the p-nitrophenol reaction product at 400 nm. Absorbance spectra for methyl paraoxon (30 µM) after complete hydrolysis in 0.05 M NaOH with 5 min solution shaking (a), and after a 20 min treatment in H_2O_2 with moving fish (b) and using a static fish (c). Fish tail containing 15% Pt-B/10% Pt-C was used along with a fish without catalytic tail (served as a static control). Reaction conditions (b,c): 20 mL of 15% H_2O_2, and using four fish of the same shape and size (9 mm long with 15% Pt-B based tail). (Reprinted with permission and Copyright 2015 Royal Society of Chemistry).

2.1.4 Conclusions

We have demonstrated as a proof of concept that functional swimmers can be created by screen-printing of different functional materials. The new screen-printing fabrication route offers cost-effective high-throughput fabrication of self-propelled bio-inspired multi-functional catalytic swimmers capable of performing diverse tasks. Multifunctional fish architectures, consisting of several printed functional layers, have been prepared for demonstrating the versatility of the new fabrication process, including control over the fish shape, size and functionality. Preparing a wide range of ink formulations and printing them in any desired geometry thus leads to diverse swimmers, mirroring those found in nature. The practical use and versatility of the artificial fish was illustrated by using diverse functional inks that allow magnetic guidance and removal of contaminants. The screen-printing fabrication approach represents a departure from traditional approaches for preparing self-propelled swimmers involving expensive and cumbersome methods and allows functionalization of different sections with different reactive materials. Using the lessons learned from biological systems, future efforts will aim at developing biomimetic printed fish with high level of structural complexity that approach the performance of natural fish.

These future printable biomimetic fish-like swimmers will involve additional functional materials and will combine hard and soft components into a fully integrated swimmer system. Flexible joints or stretchable frameworks could thus be implemented by printing inks with elastomeric formulations[15] or stimuli-responsive soft materials. Other swimmers, based on different propulsion mechanisms, could also benefit from the versatility of the new screen-printing fabrication route. Additional tools to control the local chemical environment and catalytic activty[27,28] can be considered. The new printing fabrication route thus offers a simplified, yet highly versatile cost-effective approach for high-throughput production of wide range of multi-functional biomimetic swimmers and holds considerable promise for diverse practical applications of such swimmers.

Acknowledgements

Chapter 2 is based, in part, on the material as it appears in Royal Society of Chemistry, Advances, 2015, by Rajan Kumar, Melek Kristi, Fernando Soto, Jinxing Li, Virendra V. Singh, and Joseph Wang. The dissertation author was the primary

investigator and author of this publication that describes the development of catalytic, printed motors through the development of catalytic composite particle.

2.1.5 References

1. J. Wang, “Nanomachines: Fundamentals and Applications”, Wiley-VCH (Weinheim), 2013.

2. M. Guix, C.C. Mayorga-Martinez and A. Merkoçi, *Chem. Rev.* 2014, **114**, 6285-6322.

3. W.F. Paxton, K.C. Kistler, C.C. Olmeda, A. Sen, S.K. St. Angelo, Y. Cao, T.E. Mallouk, P.E. Lammert and V.H. Crespi, *J. Am. Chem. Soc.* 2004, **126**, 13424–13431.

4. K. Kim, J. Guo, X. Xu and D. L. Fan, *Small*, 2015, **11**, 4037-4057.

5. S. Sánchez, L. Soler and J. Katuri, *Angew. Chem. Int. Ed*. 2015, **54**, 1414-1444.

6. H. Wang and M. Pumera, *Chem. Rev.* 2015*,* **111**, 8704-8735

7. W. Gao, A. Pei, X. Feng, C. Hennessy and J. Wang, *J. Am. Chem. Soc*. 2013, **135**, 998-1001.

8. G. Zhao and M. Pumera, *Nanoscale* 2014, **6**, 11177-11180.

9. W. Gao, S. Sattayasamitsathit, J. Orozco and J. Wang, *J. Am. Chem. Soc*., 2011, **133**, 9167-9173

10. W. Zhu, J. Li, Y. J. Leong, I. Rozen, X. Qu, R. Dong, Z. Wu, W. Gao, P. H. Chung, J. Wang and S. Chen, *Adv. Mater.* 2015, **27**, 4411-4417.

11. M. M. Stanton, C. Trichet-Paredes and S. Sanchez, *Lab Chip* 2015, **15**, 1634-1637.

12. X. Cao, H. Chen, X. Gu, B. Liu, W. Wang, Y Cao, F Wu, and C. Zhou, *ACS Nano* 2014, **8**, 12769-12776.

13. M. Tudorache and C. Bala, *Anal. Bioanal. Chem*. 2007, **388**, 565-578.

14. J. Wang, *Chem. Rev.* 2008, **108**, 814-825.

15. A. J. Bandodkar, R. Nuñez-Flores, W. Jia and J. Wang, *Adv. Mater.* 2015, **27**, 3060-3065.

16. W. Gao and J. Wang, *ACS Nano* 2014, **8**, 3170-3180.

17. L. Soler and S. Sanchez, *Nanoscale* 2014, **6,** 7175-7182.

18. J. Li, Z. Liu, G. Huang, Z. An, G. Chen, J. Zhang, M. Li, R. Liu and Y. Mei, *NPG Asia Mater.* 2014, **6**, e94.

19. M.N.V.R. Kumar, *Reac. Func. Polym.* 2000, **46**, 1-27.

20. T. Tangkuaram, C. Ponchio, T. Kangkasomboon, P. Katikawong and W. Veerasai, *Biosens. Bioelectron.* 2007, **22**, 2071-2078.

21. V.V. Singh, B. Jurado-Beatriz; S. Sattayasamitsathit, J. Li, Y. Fedorak, M. J. Galarnynk, and J. Wang, *Adv. Funct. Mater.* 2015, **25**, 2147-2155.

22. S. Mattson, H. B. Mark, Jr. Activated Carbon: Surface Chemistry and Adsorption from Solution, Marcel Dekker, New York, 1971.

23. Activated Carbon Adsorption (Ed: R. C. Bansal, M. Goyal), Taylor & Francis, Boca Raton, 2005.

24. B. Jurado-Sánchez, S. Sattayasamitsathit, W. Gao, L. Santos, Y. Fedorak, V. V. Singh, J. Orozco, M. Galarnyk and J. Wang, *Small* 2015, **11**, 499–506.

25. P.K. Malik, *J. Hazard. Mater.* 2004, **113**, 81-88.

26. J. Orozco, G. Cheng, D. Vilela, S. Sattayasamitsathit, R. Vazquez-Duhalt, G. Valdés-Ramírez, O. S. Pak, A. Escarpa, C. Kan and J. Wang, *Angew. Chemie Inter. Ed*. 2013, **52**, 13276-13279.

27. P. Chen, G. Liu, Y. Zhou, K. Brown, N. Chernyak, J. Hedrick, S. He, Z. Xie, Q. Lin, V. Dravid, S.O'Neill-Slawecki and C. Mirkin, *J. Am. Chem. Soc*. 2015, **137**, 998-1001.

28. Y. Zhou, Z. Xie, K. Brown, D. Park, X. Zhou, P. Chen, M. Hirtz, Q. Lin, V. Dravid, G. Schatz, Z. Zheng and C. Mirkin, *Small* 2015, **11**, 913-918.

CHAPTER 3 PRINTABLE THERMOELECTRIC INKS

3.1 High-Performance, Screen-Printable Thermoelectric Films

3.1.1 Introduction

Thermoelectric (TE) devices have garnered tremendous interests recently due to their promise for energy harvesting and solid-state refrigeration [1-11]. Traditional approaches to fabricate TE typically involve ingot fabrication and dicing, which could be time consuming, energy intensive, and often results in rigid devices. On the other hand, there is increasing interest to fabricate TE devices on flexible substrates and using more scalable approaches, for emerging applications such as wearable TE power generation and personalized thermo-regulation [12-16]. Toward this end, high-throughput and inexpensive printing has emerged as a promising fabrication route and has been widely explored in recent years [17, 18]. Interesting applications have thus been demonstrated with printed TE devices, such as printed TE generators for harvesting human body thermal energy [19], energy harvesting for wireless sensor network applications [20, 21], integration with energy storage devices [22], as wearable TE generator on glass fabric [23].

The bottleneck of the printed TE devices still lies in the low performance of the printed TE materials. In most processes, the TE particles were often mixed with insulating polymeric binders to make the mixture suitable for printing. A high mass loading of the polymer binders would hinder the electrical conductivity. For instance, Madan and coworkers [20, 21, 24-28] developed a series of printed thermoelectric-epoxy composite films and showed TE figure of merit (ZT) up to 0.31 and 0.41 for n-type Bi_2Te_3 [20, 25-27] and p-type Sb_2Te_3 or $Bi_{0.5}Sb_{1.5}Te_3$ based materials [20, 21, 25, 28], respectively. The mass loading of the polymer binders was up to ~20%. The mixtures were typically cured at 250-350 ^{o}C to solidify the films. Lu *et al.* [29] demonstrated inkjet printing of nanoparticles to fabricate TE films which yielded maximum TE power factor of ~77 and 183 μW/m-K^2 at 75 °C for films based on $Sb_{1.5}Bi_{0.5}Te_3$ and $Sb_{1.5}Bi_{0.5}Te_3$ nanoparticles, respectively. The relatively low power factor values were attributed to the low electrical conductivity [29]. Navone *et al.* [30, 31] used screen printing and uniaxial densification at 350 ^{o}C to fabricate TE micro-modules on polyimide substrates with p- and n-type pillars with 4 and 6 μW/m-K^2 in power factor, respectively. Recently, Varghese *et al.* [32] screen printed n-type $Bi_2Te_{2.8}Se_{0.2}$ nanoplate crystals and achieved a peak ZT of 0.43. We *et al.* [33] used screen printing to fabricate n-type Bi_2Te_3 thick films. They optimized the annealing process and achieved a high ZT of 0.61 with 500 ^{o}C annealing for 15 mins. Similarly, Kim *et al.* [34] achieved a ZT of 0.41 in p-type Sb_2Te_3 thick film processed by screen-printing followed by thermal annealing.

Apart from electrically inactive binders, several teams have also attempted to add conductive polymers as binders into active TE materials to improve the electrical conductivity. For example, Kato *et al.* [35] prepared a mixture of $Bi_{0.4}Te_3Sb_{1.6}$ particles, conductive PEDOT:PSS and PAA (Poly (acrylic acid)), and other organic additives, and then spin-coated the mixture to yield thin films with a ZT of 0.2 at 300 K. Bae *et al.* [36] enhanced the TE properties of PEDOT:PSS by adding Te nanorods and using chemical treatment. However, the Seebeck coefficient (*S*) of the printed films was usually low due to the low *S* of the conductivity polymers. In addition to Bi-Te based materials, other materials have also been printed. Lee *et al.* [37, 38] screen-printed ZnSb films and yielded a power factor of 1.06 mW/m-K^2. They further fabricated a TE module using p-type ZnSb and n-type $CoSb_3$ films [38]. Hong *et al.* [39] used inkjet printing to fabricate TE ZnO and $ZnFe_2O_4$ thin films.

Despite the tremendous efforts on printed TE films, most printed devices are still limited by a relatively low ZT compared to those made from commercial bulk processes: the highest reported ZT of printed TE materials are 0.61 for n-type [33] and 0.41 for p-type [34]. As mentioned earlier, the primary reason behind the low ZT is the presence of the organic additives, such as binders, needed to make TE slurries with suitable viscosity for printing. If a large amount of these additives were used and not effectively removed, the resultant TE films would be limited by low electrical conductivity, as reported in prior work. One feasible approach to remove the organic binders is thermolysis, namely, decomposition of the organic species via burning. This process typically requires sufficient oxygen at elevated temperatures. However, exposing the TE slurries to oxygen could also oxidize the TE materials and consequently impact the TE properties. Therefore, in order to achieve a high ZT in printed TE films, it is important to: (1) use as little amount of binder as possible while maintaining the suitable viscosity for printability; (2) remove the binder as much as possible without oxidizing the TE components.

In this work, we developed a screen-printing process to fabricate high-performance TE layers. We have identified a suitable binder from a class of methyl cellulose or more known for its trade name, Methocel, to make printable TE slurries with a low concentration (0.45-0.60 wt.%), thus minimizing its detrimental effect on electrical transport. Also, it is advantageous that Methocel, which is cellulose ether, can be decomposed in an inert atmosphere, such as Ar, at a temperature that is below the typical hot pressing temperature for Bi-Te alloys (~400-450 ^{o}C)[40]. We also achieved high-quality printing of the TE layers on rough and porous fabric substrates by introducing an interface layer before printing the TE layer on the fabrics. Following printing, the binders were subsequently burnt off via sintering and hot pressing. We found reduced thermal conductivity in the n-type printed layer, which can be attributed to phonon scattering by the nanoscale defects formed after burning off the binder. With the high electrical conductivity and low thermal conductivity, the screen-printed TE layers displayed high room-temperature ZT values of 0.65 and 0.81 for p-type $Bi_{0.5}Sb_{1.5}Te_3$ and n-type $Bi_2Te_{2.7}Se_{0.3}$, respectively. These ZT values are among the highest for printed samples and indicate considerable promise for developing wearable TE devices.

3.1.2 Experimental Section

Spark Erosion

We used the spark erosion method[41] to fabricate TE particles. P-type and n-type bulk TE ingots were purchased from Thermonamic Inc. (China) with the nominal compositions of $Bi_{0.5}Sb_{1.5}Te_3$ for p-type and $Bi_2Te_{2.7}Se_{0.3}$ for n-type. The bulk ingots were shaped into two electrodes and smaller ‘charge’ pieces (~2 cm in diameter) that were immersed in a spark erosion cell filled with liquid nitrogen. The electrodes were connected to a charged capacitor that discharged high pulsed current and created sparks (micro-plasmas) between two ‘charge’ pieces with suitable distance. Large number of particles could be collected at the bottom of the spark erosion cell.

Screen Printing and Hot Pressing

The TE particles were mixed with binder solvent which consists of methyl cellulose as the binder (METHOCEL HG 90, commercially available from DOW Wolff Cellulosics), in a mixture of ethanol 60 wt.% and water 40 wt.%. The concentration of the Methocel in the solvent was varied between 1.5 and 2.0 wt.%. The mass ratio between the TE particles and the solvent was 7:3, so Methocel is 0.45-0.6 wt.% in the final TE inks. This mass loading of the Methocel was found to offer suitable viscosity for screen printing. The slurry was thoroughly mixed using gentle ball milling for a day. Once ink is prepared, the ink can be applied to stainless steel stencil with a pre-design pattern laser cut with holes to deposit ink onto any substrate.

The stainless stencil was design through computer aid design (CAD) software (AutoCad, from Autodesk). The designed pattern in AutoCAD was defined though a laser cutting service (Metal Etch Services, San Marocs, CA). The slurry was applied to the fiberglass fabric substrate (Fiberglass #00543 from Fibre Glast Development Corporation), through a stencil using an applicator. In some experiments, a Chitosan layer was printed first as the interface layer to smoothen the woven surface. The printed layer was cured at 250-300 ^{o}C for 30 mins to solidify the sample and also burn off the polymeric binders. Finally, the layer was hot pressed with a uniaxial pressure of 90 MPa at 450 ^{o}C for 5 min. The hot pressing was carried out in an Argon-filled glove box with oxygen concentration less than 80 ppm to prevent the oxidation of the TE layers.

Electrical Conductivity and Seebeck Measurements

The TE layers after screen printing and hot pressing were approximately 1 cm^2 and with thickness ranging from 10-700 μm. We used the van der Pauw method [42, 43] to measure the in-plane electrical conductivity and a custom-made setup to measure the in-plane Seebeck coefficient. For the Seebeck measurement, the sample was placed across two thermoelectric blocks maintained at two different temperatures. Two T-type thermocouples were located near the two ends of the samples to measure the temperature. The temperature difference between the thermocouples was varied from 0 to 5 K, and the resultant Seebeck voltage was recorded with the two Cu probes in the thermocouples (Fig. 3). The Seebeck coefficient of the TE layers was corrected with the *S* of Cu (1.8 µV/K) [44]. This method was calibrated with bulk BST and BTS samples (Fig. S5) as well as a Ni foil sample (Fig. S1)

Angstrom Method

The Angstrom method [45] involves the periodic heating at one end of the sample and the detection of the amplitude and phase of the resultant temperature wave at two different locations along the sample. In our setup, one end of the printed layer (approximately 1 cm long) was anchored to a Cu block, which was periodically heated using a thermoelectric module powered by a sinusoidal current. Two small thermocouples, one located near the heat source (near-side) and the other located further away (far side), were used two detect the temperature wave. The frequency range of the AC current was chosen such that the thermal penetration depth is as large as possible (to ensure a large and detectable temperature oscillation on the far end of the sample) but shorter than the distance between the two thermocouples. Under this condition, the thermal conductivity (κ) can be obtained as [45]:

$$\kappa = \frac{L^2}{2 \cdot dt \cdot \ln\left(\frac{M}{N}\right)} \rho C_P \tag{1}$$

where $L = x_2 - x_1$, *M* and *N* are the amplitudes of the temperature wave at x_1 and x_2, dt is the phase difference (in seconds) between x_1 (near-side) and x_2 (far-side). The measured thermal diffusivity was then converted to in-plane thermal conductivity ($\kappa_{\parallel} = \alpha\rho C_p$) using the bulk specific heat values ($\rho C_p = 1.26 \times 10^6 \text{ and } 1.22 \times 10^6 \text{ J/m}^3\text{.K}$ for $Bi_{0.5}Sb_{1.5}Te_3$ and $Bi_2Te_{2.7}Se_{0.3}$, respectively, based on data of Bi_2Te_3 and Sb_2Te_3 reported in Ref. [46]), where the contribution of the remained binders could be negligible owing to their little amount. Since the substrates are porous fiber glass having low thermal conductivity, we can assume that the measured sample κ is equal to that of the TE layers.

3.1.3 Results and Discussion

Screen printing

Figure 3.1 shows the schematic of the screen-printing process. We started with the fabrication of the TE particles using the spark erosion process, which can effectively break bulk TE materials into micro- and nano- particles, as reported in our prior publications [41, 47]. The starting bulk TE ingots have the compositions of $Bi_{0.5}Sb_{1.5}Te_3$ for p-type (referred to as "BST" hereafter) and $Bi_2Te_{2.7}Se_{0.3}$ for n-type (referred to as "BTS" hereafter), where ZT values at room temperature are 0.77 and 0.75, respectively (see Fig. S5). After spark erosion, the resultant particles display a bimodal size distribution consisting of large particles with > 10 μm size and smaller particles with < 1 μm size, as shown in Figure 3.2. The particles used for printing were sieved through 45-μm meshes by taking the consideration of particle production yield and the uniformity of the printed layers.

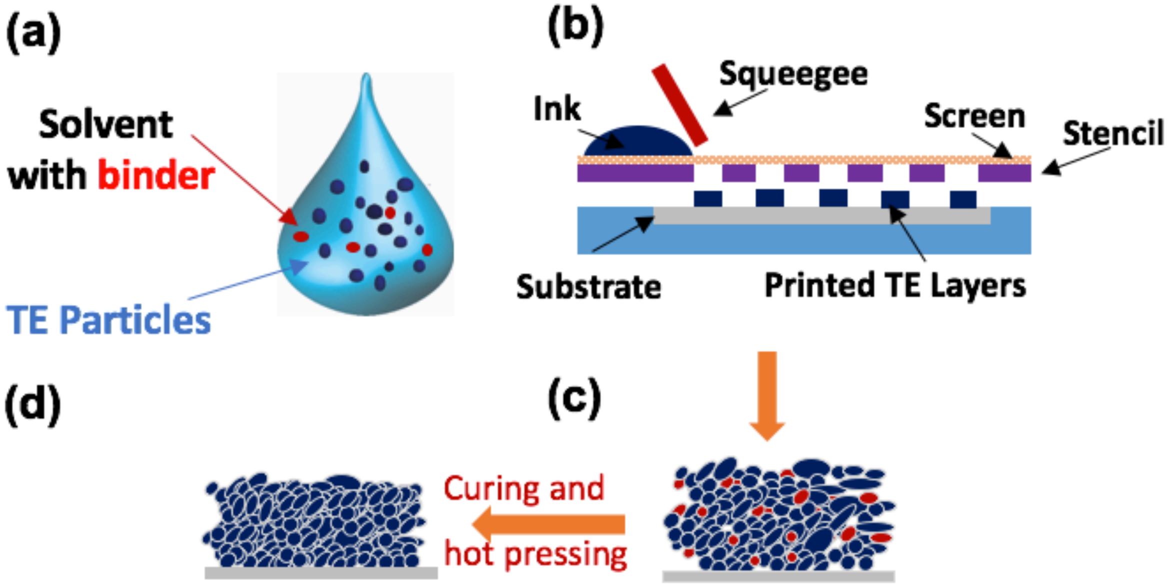

Figure 3.1: Schematic illustrations of printable thermoelectrics using (a) printable ink, (b) screen printing, (c) a screen-printed thermoelectric layer and (d) a hot-pressed layer after printing. (Reprinted under a Creative Commons Attribution 4.0 International License).

We then prepared the printing slurries by mixing the active TE particles, organic binders, and solvent, as described above. We selected Methocel as the binder because the cellulose ethers resulted in slurries with a viscosity of 3.3-3.5 Pa·s, which is within the optimal range to achieve uniform printing while minimizing the concentration of the binders.[48] Also, its low decomposition temperature makes it easier to be burnt out during sintering process. After printing and pre-heat treatment, TE powders and the binder were left on the fabric, as shown in Figure 3.2C. The as-printed TE layers had poor conductivity due to the loose contacts between the TE particles. Therefore, we used uniaxial hot pressing to densify the films, which reduced the thickness of the as-printed layers by approximately three times and greatly improved the conductivity. After hot pressing the printed layer on the fabric substrate, TE properties, including the Seebeck effect (S), electrical conductivity (σ), and thermal conductivity (κ), were evaluated at room temperature.

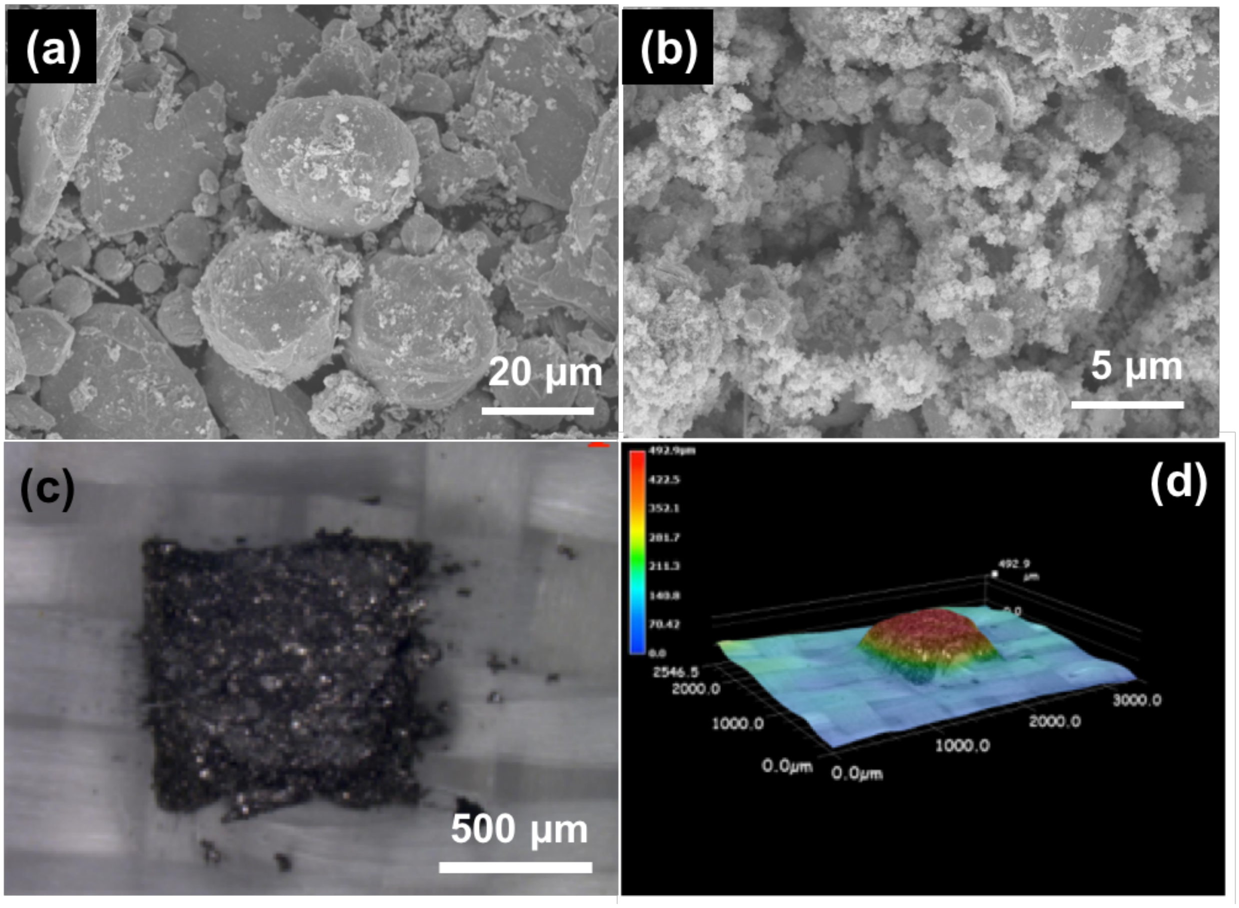

Figure 3.2: SEM images of particles with printed thermoelectric devices (a) large (> 20 µm) and (b) small diameter (≪ 1 µm). Optical images of (c) printed thick thermoelectric ink for high aspect ratio TE pillars before the hot-pressing process, with 1 mm^2 in area and 500 µm in thickness, on glass fiber fabric, and (d) Keyence 3D optical image of printed TE on the fabric. (Reprinted under a Creative Commons Attribution 4.0 International License).

Seebeck Coefficient

Figure 3.3 shows the in-plane S coefficient measurement results, where the S is determined by the linear slope in the plot of thermovoltage as a function of temperature difference (e.g., $S=-dV/dT$). Our optimized slurries showed S of 209 µV/K and -165 µV/K in p-type and n-type materials, respectively after printing and pre-heating to remove solvents. The S value for the p-type printed BST is close to that of bulk BST (220 µV/K), whereas the value for the n-type printed BTS is considerably lower than the bulk value (-208 μV/K), presumably due to the composition change during the ink formulation or hot pressing process, as evidenced from the EDS analysis. We also observed that the printed TE layers have similar *S* compared to that of TE powders, which were prepared by drop-casting the TE powders dispersed in organic solvents on a glass substrate followed by drying. This shows that the addition of the Methocel binder has minimal influence on *S*. This is because the Methocel is insulating and its amount is small (up to 0.6 wt.% of the inks), and *S* of the TE/Methocel mixture is dominantly determined by that of the TE materials.

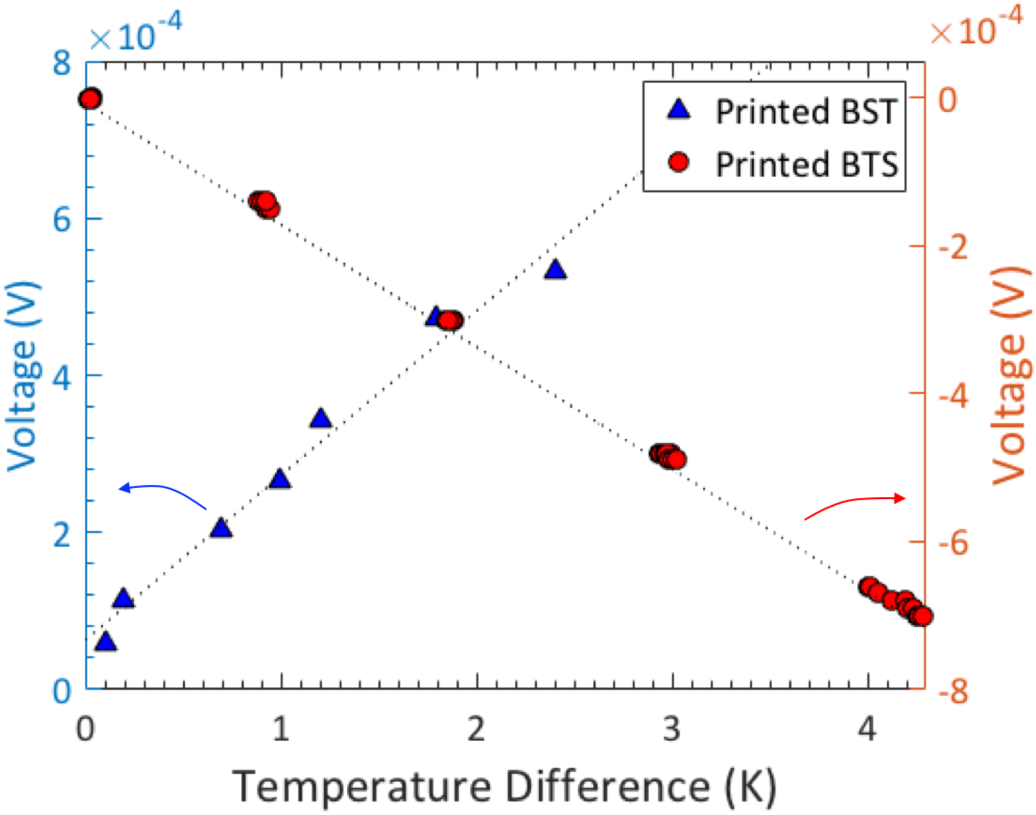

Figure 3.3. Plots of voltages as a function of temperature difference to obtain the Seebeck coefficient from the slops with p-type BST and n-type BTS. (Reprinted under a Creative Commons Attribution 4.0 International License).

Electrical Conductivity

Due to the minimal influence of the binder on S, the main hurdle to achieve a high ZT in the printed films is the electrical conductivity σ and thermal conductivity κ. One of the challenges associated with the printing on fabric is the roughness and porosity of the substrate that lead to non-uniform printed layers, which would limit the electrical conductivity. Depending on the design of the weave and the material, fabrics have a certain degree of porosity and a large roughness over 100 µm (Figure 3.4A and B), as determined using a Keyence optical surface profiler. This leads to the non-uniformity on the printed layers as some loose fibers can be embedded inside the printed layer as it cures. The infiltration of the TE material into the porous fabric also caused a large error in the determination of the layer thickness and consequently σ, especially for small layer thickness. As shown in Figure 3.4H, the σ of the printed BST layers on bare fabric was less than 200 S/cm, substantially lower than the bulk BST (σ~1000 S/cm). Also, the σ increases with the thickness of the printed and hot-pressed TE layers: σ was improved from 8.5 to 190 S/cm by increasing the thickness from 9 to 111 µm (Figure 3.4E and 3.4F), suggesting the detrimental effect of the substrate.

Our approach to mitigate the effect of the roughness and porosity of the fabric substrate is to print a non-conductive layer, referred to as the interface layer, to level the surface and block the pores in the substrate. We also increased the thickness of the TE layer to reduce the thickness ratio between the fabric and the TE layer and to minimize the adverse contribution of the fabrics. We adopted Chitosan as the interface layer, as schematically shown in Figure 3.4B. Chitosan is a well-known binder used in printing, e.g., for controlling the viscosity [49, 50] and for treatment of fabric. [51-53] The presence of the Chitosan interface layer greatly reduced the surface roughness of the fabric, to within 50 µm, as shown in Figure 3.4D. Consequently, the electrical conductivity was largely improved: at the same thickness of ~110 µm, employing the Chitosan layer increased the conductivity from 190 S/cm (Figure 3.4H) to 278 S/cm (Figure 3.4I). Thicker films printed on the Chitosan layers showed higher σ. We also carried out a similar study on n-type BTS by introducing the Chitosan layer and varying the printed TE layer thickness. As a result, the σ was improved up to 639 S/cm and 763 S/cm for p-type BST and n-type BTS on samples with Chitosan and thicker TE layers. Although the large thickness could sacrifice the flexibility of the TE layer itself, a device made of small printed TE pillars on the flexible fabric would still remain flexible.

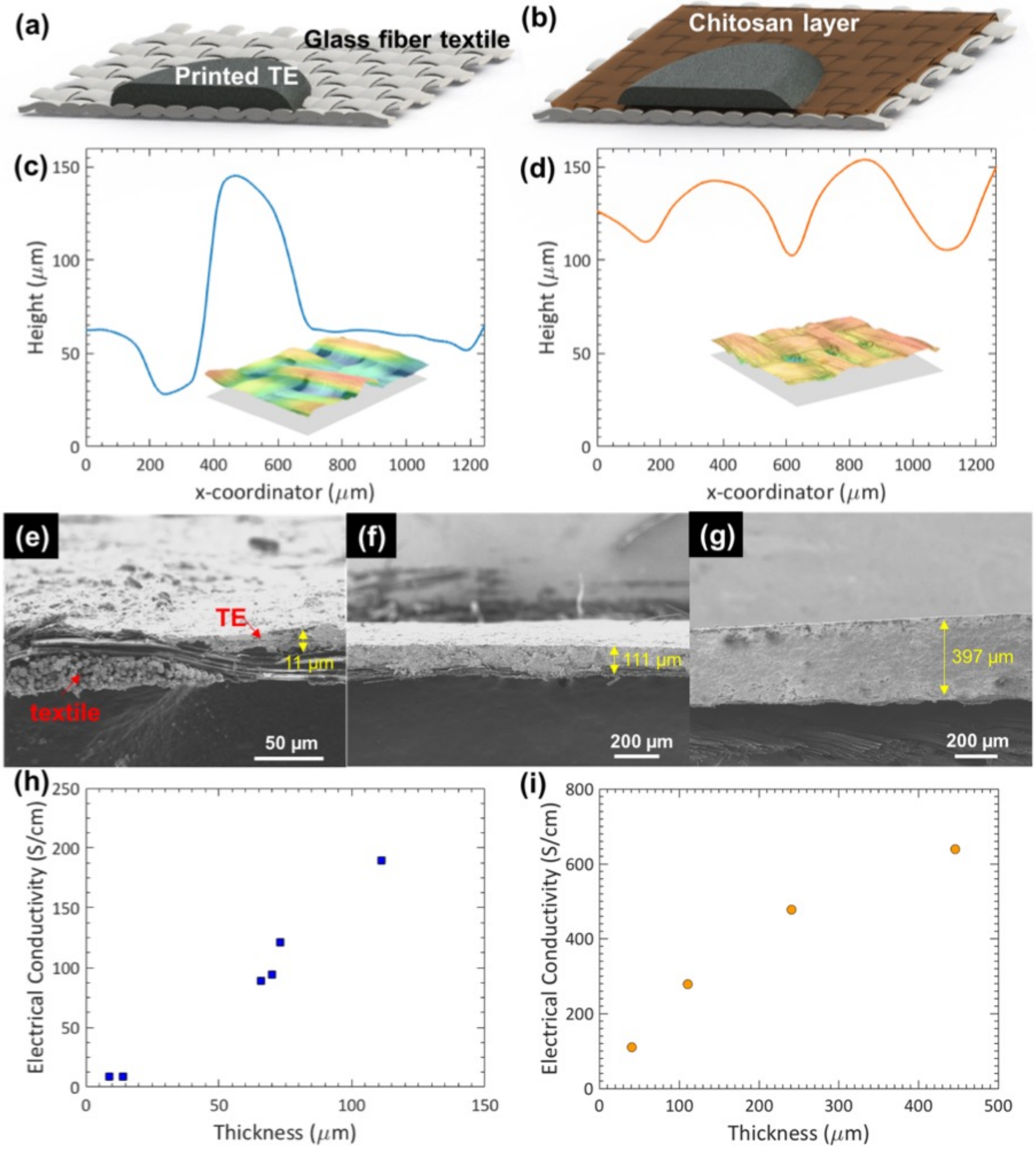

Figure 3.4: Schematics of printed thermoelectric layer on top of bare glass fiber fabric (a) and on Chitosan layer (b) used as a preliminary layer to smoothen the rough bare fabric. Optical surface profiles of bare glass fiber fabric (c) and printed Chitosan layer on top of glass fiber fabric (d) with their measured 3-dimensional surface images using a Keyence optical microscope (insets). SEM cross-sectional images of printed and hot-pressed samples on fabrics with thickness of 11 μm (e), 111 μm (f) and 395 μm (g). Plots of electrical conductivity as a function of thickness of the printed BST layers without (h) and with chitosan (i). (Reprinted under a Creative Commons Attribution 4.0 International License).

Thermal conductivity

Since S and σ were measured along the in-plane direction of the printed layers, it is imperative to also measure the thermal conductivity σ along the same orientation, which is often challenging. Here we employed the Angstrom method [45] to measure the in-plane thermal conductivity ($\kappa_{\parallel}$) of the printed TE layers. In this method, one end of the sample was heated using a sinusoidal heat source, and the temperature waves were measured at two different locations of the sample, as shown in Figure 3.5A. We calibrated our setup with measurements on borosilicate and polyethylene, which have well-known thermal conductivity values. The measured $\kappa_{\parallel}$ was found to be 1.29 and 0.77 W/m-K for the thickest (600-800 μm) p-type BST and n-type BTS layers (Table 3.1).

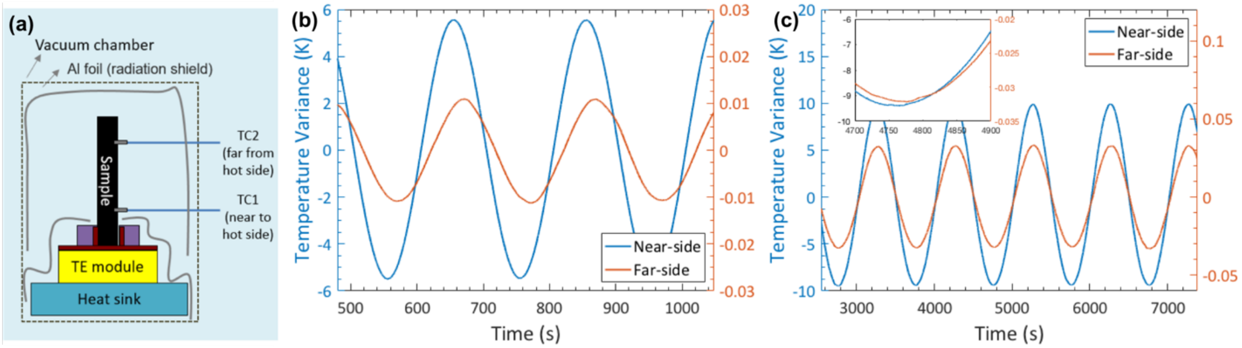

Figure 3.5. Angstrom method: (a) Schematic of the setup. Measured temperature wave of (b) p-type BST and (c) n-type BTS in the Angstrom setup. (Reprinted under a Creative Commons Attribution 4.0 International License).

To assess the anisotropy of the thermal conductivity, we also measured the cross-plane thermal conductivity ($\kappa_{\perp}$) using the 3ω technique [54, 55]. By using the slope method, we determined the $\kappa_{\perp}$ to be 1.06 and 0.83 W/m-K at 300 K, for p- and n-type TE layers, respectively. The in-plane and cross-plane thermal conductivity results suggest that the printed TE films were essentially isotropic after the uniaxial hot-pressing process.

With the measured in-plane electrical conductivity and thermal conductivity, we can estimate the lattice thermal conductivity: $\kappa_L = \kappa - L\sigma T$, where *L* is the Lorenz number, and is taken to be $1.67 \times 10^{-8}\ W\Omega K^{-2}$ and $1.74 \times 10^{-8}\ W\Omega K^{-2}$for p-type BST and n-type BTS, respectively, where the *L* was corrected with *S* [56]. The calculated κ_L is 0.97 and 0.37 W/m-K for the p-type and n-type layers, respectively. The κ_L for p-type BST is almost identical to that of the starting bulk material value (calculated to be 1.04 W/m-K by using the same *L* and the data shown in Fig. S5). However, the κ_L for n-type BST is significantly lower than the starting bulk value (1.23 W/m-K). This difference in κ_L in the p- and n-type printed layers is likely originated from the microstructures, as we shall discuss next.

Investigation of Microstructure

In order to investigate the relations between the measured thermoelectric properties and microstructures, high resolution-transmission electron microscopy (HR-TEM) was employed. The cross-sectional HR-TEM Energy-dispersive X-ray spectroscopy (EDS) element mapping images show the carbon element distributed in the p- and n-type TE layers in Fig. 6. In order to compare the amounts of carbon in the sintered samples, EDS quantifications were carried out. As shown in Table S7, the atomic percent of carbon in the samples with Methocel is similar to that in the samples without Methocel, revealing that the binders in the p-type and n-type were effectively removed without oxidizing the TE components and degrading the electrical conductivity. Therefore, the carbon elements observed with the binder in Figure 3.6 were attributed to the hydrocarbon contamination in the surface of samples.

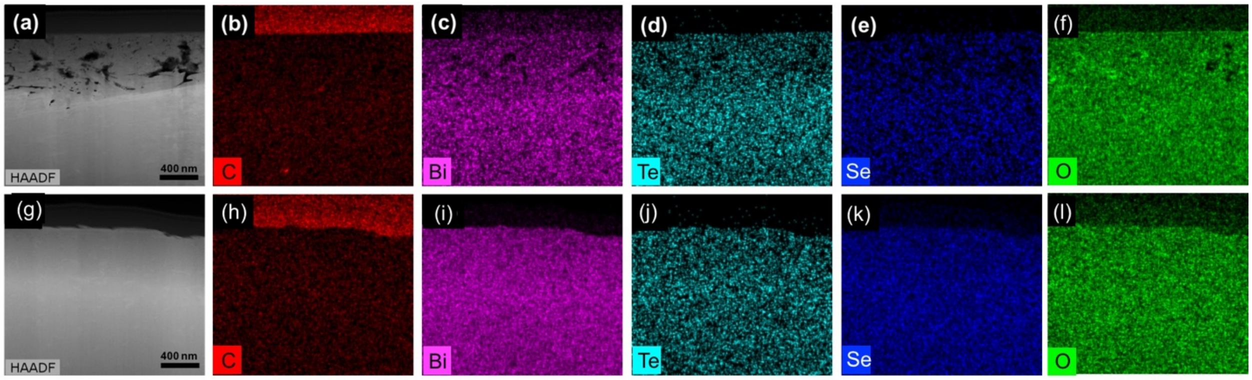

Figure 3.6. TEM EDS mapping images of hot-pressed p-type (a-f) and n-type (g-l) with Methocel. (Reprinted under a Creative Commons Attribution 4.0 International License).

For the p-type printed sample, there is no clear nanoscale feature in the high angle annular dark field (HADDF) image in Figure 3.7A, similar to the case of hot-pressed p-type BST without Methocel. This may explain the similar κ_L between the p-type printed layers and bulk samples. However, for the n-type sample, the defects with the length scale of a few hundred nanometers were clearly observed in the printed sample with Methocel after hot pressing as shown in the HADDF image in Figure 3.7B. Considering that these defects were not found in the samples without Methocel, it seems that these thin and long defects were generated by the rearrangement of n-type TE particles while the binders were burning out in the sintering process, which could have facilitated the formation of the embedded defects. The nanoscale defects can effectively scatter the phonons in addition to the boundary scattering [57, 58] due to the formation of spark-eroded particles, leading to lower lattice thermal conductivity in the printed n-type layers without significantly affecting charge transport. Thus, the thermal conductivity of the printed n-type samples is lowered compared to that of the bulk.

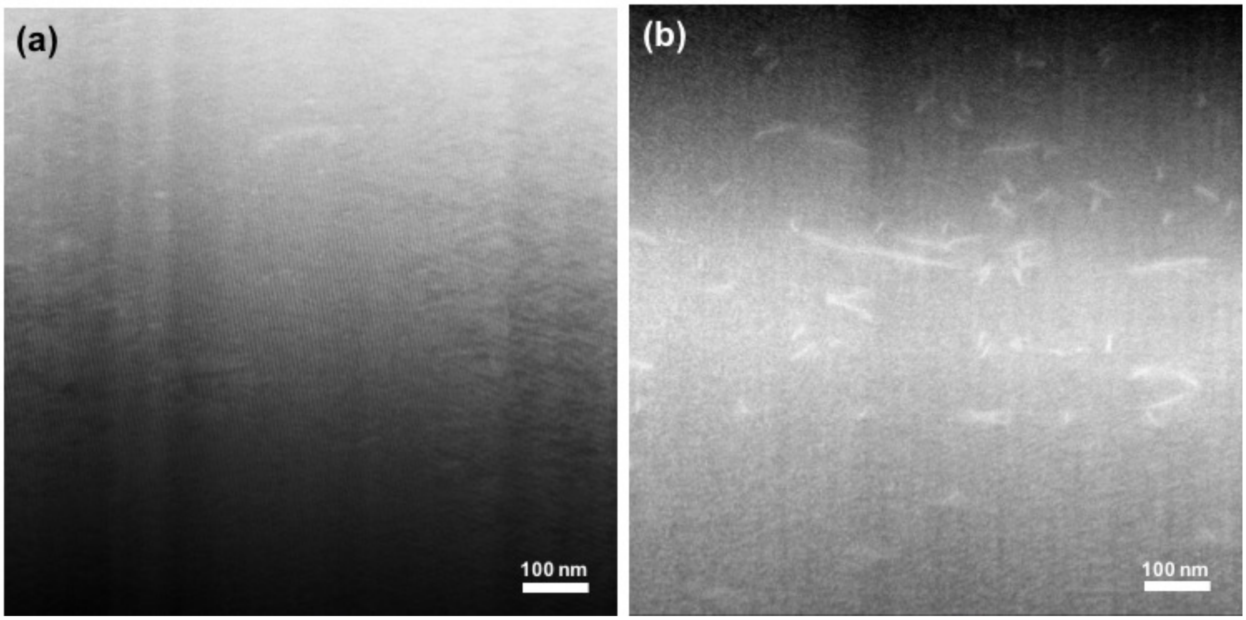

Figure 3.7. TEM HADDF images of hot-pressed p-type (a) and n-type (b) with Methocel. (Reprinted under a Creative Commons Attribution 4.0 International License).

ZT values

With the measured in-plane $S, \sigma,$ and κ, we determined the ZT values for the printed TE layers to be 0.68 and 0.81 for the p-type and n-type printed layers, respectively, as summarized in Table 3.1. These values are among the highest for the printed TE samples. The high ZT values in our samples can be attributed to the following features of our processes: (1) we minimized the amount of the organic binder present in the printing slurries by using a high viscosity binder (Methocel). (2) The binder was also effectively burnt off during the curing and hot-pressing process. (3) For the n-type printed sample, the nanoscale defects left behind after the binder burnt-off contributed to phonon scattering and thermal conductivity reduction, thereby leading to a high ZT value.

Table 3.1: Summary of thermoelectric properties of printed p-type BST and n-type BTS. (Reprinted under a Creative Commons Attribution 4.0 International License).

	P-type BiSbTe	**N-type BiTeSe**
S (μV/K)	209	-165
σ (S/cm)	639	763
κ (W/m-K)	1.29($\kappa_{\parallel}$) 1.06($\kappa_{\perp}$)	0.77($\kappa_{\parallel}$) 0.83 ($\kappa_{\perp}$)
κ_L (W/m-K)	0.97	0.37
ZT @ 300 K (using $\kappa_{\parallel}$)	0.65	0.81

3.1.4 Conclusions

We demonstrated printed TE layers with high ZTs for both p-type BST and n-type BTS (i.e., 0.65 and 0.81, respectively), which are close to the bulk values, on flexible glass fabrics. In addition to the high performance and the potential for flexible devices, introducing scale-up processes from preparing TE inks (e.g. spark erosion) to screen printing opens up the opportunities to adopt the TE generator for low-grade heat recovery in wearable devices and personalized thermo-regulation. In this study, we successfully addressed several critical issues commonly encountered in the printing of TE devices. First, we achieved high-quality printing using a small amount (0.45-0.60 wt. %) of Methocel, an insulating polymeric binder. Second, as the binder has a low decomposition temperature, we effectively burnt off the binders through sintering and hot pressing. The removal of the binders was evidenced from the microstructure analysis and the excellent electrical conductivity. Third, to ensure uniform printing, we also treated porous and rough woven fabrics by printing an interface layer using Chitosan, which enabled the printing of thick TE layers and improved the electrical conductivity. Moreover, we found additional benefit of binder decomposition: it created nanoscale defects that led to low lattice thermal conductivity for the n-type materials. The high-ZT TE layers achieved by printing on flexible fabrics reported in this work could lead to future development of low-cost flexible and wearable TE devices.

Acknowledgements

Chapter 3 is based, in part, on the material as it appears in Scientific Reports, 2017, by Rajan Kumar, Sunmi Shin, Joog Wook Roh, Dong-Su Ko, Hyun-Sik Kim, Sang Il Kim, Lu Yin, Sarah Schlossberg, Shuang Cui, Jung-Ming You, Sooshin Kwon, Jianlin Zheng, Joseph Wang and Renkun Chen. The dissertation author was the co-investigator on key formulations of thermoelectric inks and improvements to the printing process which resulted in improved thermoelectric performance.

3.2 Reference

1. Bulman, G., P. Barletta, J. Lewis, N. Baldasaro, M. Manno, A. Bar-Cohen, and B. Yang, *Superlattice-based thin-film thermoelectric modules with high cooling fluxes.* Nature Communications, 2016. **7**.

2. Majumdar, A.,*Thermoelectric devices helping chips to keep their cool.* Nature Nanotechnology, 2009. **4**(4): p. 214-215.

3. Zhao, L.D., S.H. Lo, Y.S. Zhang, H. Sun, G.J. Tan, C. Uher, C. Wolverton, V.P. Dravid, and M.G. Kanatzidis, *Ultralow thermal conductivity and high thermoelectric figure of merit in SnSe crystals.* Nature, 2014. **508**(7496): p. 373-+.

4. Rhyee, J.S., K.H. Lee, S.M. Lee, E. Cho, S. Il Kim, E. Lee, Y.S. Kwon, J.H. Shim, and G. Kotliar, *Peierls distortion as a route to high thermoelectric performance in In4Se3-delta crystals.* Nature, 2009. **459**(7249): p. 965-968.

5. Hochbaum, A.I., R.K. Chen, R.D. Delgado, W.J. Liang, E.C. Garnett, M. Najarian, A. Majumdar, and P.D. Yang, *Enhanced thermoelectric performance of rough silicon nanowires.* Nature, 2008. **451**(7175): p. 163-168.

6. Boukai, A.I., Y. Bunimovich, J. Tahir-Kheli, J.K. Yu, W.A. Goddard, and J.R. Heath, *Silicon nanowires as efficient thermoelectric materials.* Nature, 2008. **451**(7175): p. 168-171.

7. Venkatasubramanian, R., E. Siivola, T. Colpitts, and B. O'Quinn, *Thin-film thermoelectric devices with high room-temperature figures of merit.* Nature, 2001. **413**(6856): p. 597-602.

8. Snyder, G.J. and E.S. Toberer, *Complex thermoelectric materials.* Nature Materials, 2008. **7**(2): p. 105-114.

9. Zhao, L.D., G.J. Tan, S.Q. Hao, J.Q. He, Y.L. Pei, H. Chi, H. Wang, S.K. Gong, H.B. Xu, V.P. Dravid, C. Uher, G.J. Snyder, C. Wolverton, and M.G. Kanatzidis, *Ultrahigh power factor and thermoelectric performance in hole-doped single-crystal SnSe.* Science, 2016. **351**(6269): p. 141-144.

10. Bell, L.E., *Cooling, heating, generating power, and recovering waste heat with thermoelectric systems.* Science, 2008. **321**(5895): p. 1457-1461.

11. Poudel, B., Q. Hao, Y. Ma, Y.C. Lan, A. Minnich, B. Yu, X.A. Yan, D.Z. Wang, A. Muto, D. Vashaee, X.Y. Chen, J.M. Liu, M.S. Dresselhaus, G. Chen, and Z.F. Ren, *High-thermoelectric performance of nanostructured bismuth antimony telluride bulk alloys.* Science, 2008. **320**(5876): p. 634-638.

12. Du, Y., K.F. Cai, S. Chen, H.X. Wang, S.Z. Shen, R. Donelson, and T. Lin, *Thermoelectric Fabrics: Toward Power Generating Clothing.* Scientific Reports, 2015. **5**.

13. Wan, C.L., X.K. Gu, F. Dang, T. Itoh, Y.F. Wang, H. Sasaki, M. Kondo, K. Koga, K. Yabuki, G.J. Snyder, R.G. Yang, and K. Koumoto, *Flexible n-type thermoelectric materials by organic intercalation of layered transition metal dichalcogenide TiS2.* Nature Materials, 2015. **14**(6): p. 622-627.

14. Kim, G.H., L. Shao, K. Zhang, and K.P. Pipe, *Engineered doping of organic semiconductors for enhanced thermoelectric efficiency.* Nature Materials, 2013. **12**(8): p. 719-723.

15. Bubnova, O., Z.U. Khan, A. Malti, S. Braun, M. Fahlman, M. Berggren, and X. Crispin, *Optimization of the thermoelectric figure of merit in the conducting polymer poly(3,4-ethylenedioxythiophene).* Nature Materials, 2011. **10**(6): p. 429-433.

16. Bahk, J.-H., H. Fang, K. Yazawa, and A. Shakouri, *Flexible thermoelectric materials and device optimization for wearable energy harvesting.* Journal of Materials Chemistry C, 2015. **3**(40): p. 10362-10374.

17. Kim, J., R. Kumar, A.J. Bandodkar, and J. Wang, *Advanced Materials for Printed Wearable Electrochemical Devices: A Review.* Advanced Electronic Materials, 2017. **3**(1): p. 1600260-n/a.

18. See, K.C., J.P. Feser, C.E. Chen, A. Majumdar, J.J. Urban, and R.A. Segalman, *Water-Processable Polymer-Nanocrystal Hybrids for Thermoelectrics.* Nano Letters, 2010. **10**(11): p. 4664-4667.

19. Kim, M.K., M.S. Kim, S. Lee, C. Kim, and Y.J. Kim, *Wearable thermoelectric generator for harvesting human body heat energy.* Smart Materials and Structures, 2014. **23**(10).

20. Madan, D., Z.Q. Wang, P.K. Wright, and J.W. Evans, *Printed flexible thermoelectric generators for use on low levels of waste heat.* Applied Energy, 2015. **156**: p. 587-592.

21. Madan, D., Z.Q. Wang, A. Chen, P.K. Wright, and J.W. Evans, *High-Performance Dispenser Printed MA p-Type Bi0.5Sb1.5Te3 Flexible Thermoelectric Generators for Powering Wireless Sensor Networks.* Acs Applied Materials & Interfaces, 2013. **5**(22): p. 11872-11876.

22. Wang, Z., A. Chen, R. Winslow, D. Madan, R.C. Juang, M. Nill, J.W. Evans, and P.K. Wright, *Integration of dispenser-printed ultra-low-voltage thermoelectric and energy storage devices.* Journal of Micromechanics and Microengineering, 2012. **22**(9).

23. Kim, S.J., J.H. We, and B.J. Cho, *A wearable thermoelectric generator fabricated on a glass fabric.* Energy & Environmental Science, 2014. **7**(6): p. 1959-1965.

24. Chen, A., D. Madan, P.K. Wright, and J.W. Evans, *Dispenser-printed planar thick-film thermoelectric energy generators.* Journal of Micromechanics and Microengineering, 2011. **21**(10).

25. Madan, D., A. Chen, P.K. Wright, and J.W. Evans, *Dispenser printed composite thermoelectric thick films for thermoelectric generator applications.* Journal of Applied Physics, 2011. **109**(3).

26. Madan, D., A. Chen, P.K. Wright, and J.W. Evans, *Printed Se-Doped MA n-Type Bi2Te3 Thick-Film Thermoelectric Generators.* Journal of Electronic Materials, 2012. **41**(6): p. 1481-1486.

27. Madan, D., Z.Q. Wang, A. Chen, R.C. Juang, J. Keist, P.K. Wright, and J.W. Evans, *Enhanced Performance of Dispenser Printed MA n-type Bi2Te3 Composite Thermoelectric Generators.* Acs Applied Materials & Interfaces, 2012. **4**(11): p. 6117-6124.

28. Madan, D., Z.Q. Wang, A. Chen, R. Winslow, P.K. Wright, and J.W. Evans, *Dispenser printed circular thermoelectric devices using Bi and Bi0.5Sb1.5Te3.* Applied Physics Letters, 2014. **104**(1).

29. Lu, Z.Y., M. Layani, X.X. Zhao, L.P. Tan, T. Sun, S.F. Fan, Q.Y. Yan, S. Magdassi, and H.H. Hng, *Fabrication of Flexible Thermoelectric Thin Film Devices by Inkjet Printing.* Small, 2014. **10**(17): p. 3551-3554.

30. Navone, C., M. Soulier, M. Plissonnier, and A.L. Seiler, *Development of (Bi,Sb)(2)(Te,Se)(3)-Based Thermoelectric Modules by a Screen-Printing Process.* Journal of Electronic Materials, 2010. **39**(9): p. 1755-1759.

31. Navone, C., M. Soulier, J. Testard, J. Simon, and T. Caroff, *Optimization and Fabrication of a Thick Printed Thermoelectric Device.* Journal of Electronic Materials, 2011. **40**(5): p. 789-793.

32. Varghese, T., C. Hollar, J. Richardson, N. Kempf, C. Han, P. Gamarachchi, D. Estrada, R.J. Mehta, and Y.L. Zhang, *High-performance and flexible thermoelectric films by screen printing solution-processed nanoplate crystals.* Scientific Reports, 2016. **6**.

33. We, J.H., S.J. Kim, G.S. Kim, and B.J. Cho, *Improvement of thermoelectric properties of screen-printed Bi2Te3 thick film by optimization of the annealing process.* Journal of Alloys and Compounds, 2013. **552**: p. 107-110.

34. Kim, S.J., J.H. We, J.S. Kim, G.S. Kim, and B.J. Cho, *Thermoelectric properties of P-type Sb2Te3 thick film processed by a screen-printing technique and a subsequent annealing process.* Journal of Alloys and Compounds, 2014. **582**: p. 177-180.

35. Kato, K., H. Hagino, and K. Miyazaki, *Fabrication of Bismuth Telluride Thermoelectric Films Containing Conductive Polymers Using a Printing Method.* Journal of Electronic Materials, 2013. **42**(7): p. 1313-1318.

36. Bae, E.J., Y.H. Kang, K.S. Jang, and S.Y. Cho, *Enhancement of Thermoelectric Properties of PEDOT:PSS and Tellurium-PEDOT:PSS Hybrid Composites by Simple Chemical Treatment.* Scientific Reports, 2016. **6**.

37. Lee, H.B., J.H. We, H.J. Yang, K. Kim, K.C. Choi, and B.J. Cho, *Thermoelectric properties of screen-printed ZnSb film.* Thin Solid Films, 2011. **519**(16): p. 5441-5443.

38. Lee, H.B., H.J. Yang, J.H. We, K. Kim, K.C. Choi, and B.J. Cho, *Thin-Film Thermoelectric Module for Power Generator Applications Using a Screen-Printing Method.* Journal of Electronic Materials, 2011. **40**(5): p. 615-619.

39. Hoong, L.J., Y.C. Keat, A. Chik, and T.P. Leng, *Band structure and thermoelectric properties of inkjet printed ZnO and ZnFe2O4 thin films.* Ceramics International, 2016. **42**(10): p. 12064-12073.

40. Li, X.G., M.R. Huang, and H. Bai, *Thermal decomposition of cellulose ethers.* Journal of Applied Polymer Science, 1999. **73**(14): p. 2927-2936.

41. Nguyen, P.K., K.H. Lee, J. Moon, S.I. Kim, K.A. Ahn, L.H. Chen, S.M. Lee, R.K. Chen, S. Jin, and A.E. Berkowitz, *Spark erosion: a high production rate method for producing Bi0.5Sb1.5Te3 nanoparticles with enhanced thermoelectric performance.* Nanotechnology, 2012. **23**(41).

42. van der Pauw, L.J., *A method of measuring specific resistivity and Hall effect of discs of arbitrary shape.* Philips Res. Rept., 1958. **13**: p. 1.

43. van der Pauw, L.J., *A method of measuring the resistivity and Hall coefficient on Lamellae of arbitrary shape.* Philips Res. Rept., 1959. **13**: p. 220.

44. Nakama, T., A.T. Burkov, A. Heinrich, T. Oyoshi, and K. Yagasaki, *Experimental set-up for thermopower and resistivity measurements at 100-1300 K.* Xvii International Conference on Thermoelectrics, Proceedings Ict 98, 1998: p. 266-269.

45. Zhu, Y., *Heat-loss modified Angstrom method for simultaneous measurements of thermal diffusivity and conductivity of graphite sheets: The origins of heat loss in Angstrom method.* International Journal of Heat and Mass Transfer, 2016. **92**: p. 784-791.

46. Chen, X., H.D. Zhou, A. Kiswandhi, I. Miotkowski, Y.P. Chen, P.A. Sharma, A.L.L. Sharma, M.A. Hekmaty, D. Smirnov, and Z. Jiang, *Thermal expansion coefficients of Bi2Se3 and Sb2Te3 crystals from 10 K to 270 K.* Applied Physics Letters, 2011. **99**(26).

47. Moon, J., D. Lu, B. VanSaders, T.K. Kim, S.D. Kong, S.H. Jin, R.K. Chen, and Z.W. Liu, *High performance multi-scaled nanostructured spectrally selective coating for concentrating solar power.* Nano Energy, 2014. **8**: p. 238-246.

48. Cui, Z. and Z. Cui, *Introduction*, in *Printed Electronics*. 2016, John Wiley & Sons Singapore Pte. Ltd. p. 1-20.

49. Bahmani, S.A., G.C. East, and I. Holme, *The application of chitosan in pigment printing.* Journal of the Society of Dyers and Colourists, 2000. **116**(3): p. 94-99.

50. Wang, H.X., T. Guo, and H.B. Li, *Evaluation of viscosity and printing quality of chitosan-based flexographic inks: The effect of chitosan molecular weight.* Journal of Applied Polymer Science, 2016. **133**(39).

51. Choi, P.S.R., C.W.M. Yuen, S.K.A. Ku, and C.W. Kan, *Digital ink-jet printing for chitosan-treated cotton fabric.* Fibers and Polymers, 2005. **6**(3): p. 229-234.

52. Kangwansupamonkon, W., M. Suknithipol, S. Phattanarudee, and S. Kiatkamjornwong, *Inkjet printing: effects of binder particle size and chitosan pretreatment on the qualities of silk fabric.* Surface Coatings International, 2011. **94**(6): p. 216-225.

53. Noppakundilograt, S., P. Buranagul, W. Graisuwan, C. Koopipat, and S. Kiatkamjornwong, *Modified chitosan pretreatment of polyester fabric for printing by ink jet ink.* Carbohydrate Polymers, 2010. **82**(4): p. 1124-1135.

54. Dechaumphai, E., J.L. Barton, J.R. Tesmer, J. Moon, Y.Q. Wang, G.R. Tynan, R.P. Doerner, and R.K. Chen, *Near-surface thermal characterization of plasma facing components using the 3-omega method.* Journal of Nuclear Materials, 2014. **455**(1-3): p. 56-60.

55. Dechaumphai, E., D.L. Lu, J.J. Kan, J.Y. Moon, E.E. Fullerton, Z.W. Liu, and R.K. Chen, *Ultralow Thermal Conductivity of Multilayers with Highly Dissimilar Debye Temperatures.* Nano Letters, 2014. **14**(5): p. 2448-2455.

56. Kim, H.S., Z.M. Gibbs, Y.L. Tang, H. Wang, and G.J. Snyder, *Characterization of Lorenz number with Seebeck coefficient measurement.* Apl Materials, 2015. **3**(4).

57. Kim, W., J. Zide, A. Gossard, D. Klenov, S. Stemmer, A. Shakouri, and A. Majumdar, *Thermal conductivity reduction and thermoelectric figure of merit increase by embedding nanoparticles in crystalline semiconductors.* Physical Review Letters, 2006. **96**(4).

58. Yu, B., M. Zebarjadi, H. Wang, K. Lukas, H.Z. Wang, D.Z. Wang, C. Opeil, M. Dresselhaus, G. Chen, and Z.F. Ren, *Enhancement of Thermoelectric Properties by Modulation-Doping in Silicon Germanium Alloy Nanocomposites.* Nano Letters, 2012. **12**(4): p. 2077-2082.

CHAPTER 4 HYBRID, STRETCHABLE ELECTRONICS

4.1 Hybrid Fabrication Technologies for Stretchable Electronics

4.1.1 Introduction

Bio-integrated soft electronic devices are expected to play crucial roles in consumer electronics,[1] healthcare [2] and energy [3] domains to significantly transform our lifestyle. However, mating of conventional rigid electronic devices with soft biological tissues leads to significant compromise in performance.[4] The rapidly emerging field of soft, stretchable electronics has the potential to address this issue by ensuring conformal contact between wearable devices and the human body.[5] Researchers have mainly focused on using two approaches for realizing stretchable devices: deterministic[6] and random[7] composites. The deterministic composite route, also known as the “island-bridge” approach, involves fabricating the device components onto rigid islands connected by serpentine bridges and ultimately bonding the device to a soft, stretchable elastomeric substrate.[8] When subjected to external strain, the underlying elastomeric substrate and the serpentine structures accommodate most of the stress, thus leaving the crucial device components unharmed.[5,9] On the other hand, random composite-based stretchability relies on the random incorporation of functional material within or on the elastomeric matrix to develop stretchable systems.[10]

Deterministically stretchable devices have an edge over their random composite counterparts since the performance of random composite devices diminishes by incorporating the functional components within/on elastomeric substrates.[11] In contrast, deterministic systems allow fabrication of complex, stretchable devices with performance similar to conventional rigid devices.[12] However, widespread applications of such devices are hindered since these are lithographically fabricated and there are several materials that are incompatible with this fabrication route. For example, many devices rely on nanomaterials,[13] polymer composites,[14] carbonaceous,[15] biological,[16] low-temperature [17] and solvent-sensitive [18] materials. Integrating these materials in microstructured forms on elastomeric substrates, for intimate contact with biological tissues, will open up new paradigms for wearable devices. High-precision scalable fabrication of such materials onto deterministically stretchable designs thus requires reliance on other fabrication techniques.

The key focus of the present work was to develop a strategy for combining lithography (thin film) and screen-printing (thick film) techniques to realize deterministic, high-performance stretchable devices. Screen-printing has been widely used towards large-scale, cost-effective incorporation of a myriad of materials onto numerous substrates for various applications. [19,20] However, most of the printable inks form either rigid or flexible films. Developing stretch-enduring inks is challenging as only a handful of elastomeric binders and functional materials can be homogenously dispersed to achieve high performance stretchable inks. While lithographic and printing techniques have been the primary methods used for fabricating wearable devices, their distinct and complementary advantages and characteristics have not been combined.

The described new hybrid fabrication process, combining the printing of functional ink materials onto lithographically-stretchable deterministic patterns, represents an attractive route that can address the challenges of each individual technique. For example, while lithography has been exploited for realizing complex stretchable systems, they are limited to thin films (<10 μm), which are not suitable for devices requiring high loading of active materials (e.g., energy harvesting and storage devices). In addition, there are limited choices of materials that can be vacuum deposited, and solution etched. On the other hand, screen-printing enables sufficient loading of a variety of active materials into thick (20-50 µm) films, but it suffers from meeting required layout resolutions and performance. In the hybrid system, the thick-film reside over rigid isolated islands interconnected with free-standing stretchable serpentine bridges. The device can thus afford to include a wide range of rigid and lithographically incompatible materials without concern of device failure, since most of the strain is accommodated by the serpentine structures while leaving the thick-film islands unharmed. The hybrid system thus combines the best of two worlds.

4.1.2 Experimental and Results

The hybrid pattern has been realized by first lithographically fabricating the entire “island-bridge” layout of the device in gold onto an elastomeric substrate, followed by printing the ink layer on the islands (Figure 4.1A). The circular island electrodes can then be patterned with a wide range of printable inks. The soft, stretchable nature of such hybrid devices allow intimate and easy integration with the human epidermis (Figure 4.1B) while maintaining structural integrity and minimizing delamination from the skin when subject to multi-axial strains (Figure 4.1C). The versatility of such hybrid fabrication process has been demonstrated by printing various carbon, Ag/AgCl, enzyme-loaded Prussian-Blue and carbon nanotube-based inks due to their widespread use in energy, sensing and electrochromic-display applications (Figure 4.1B-F). For example, the dramatically enhanced sensing performance of the new hybrid carbon-gold thick-thin electrode system compared to its bare gold thin-film counterpart has been demonstrated for the detection of important analytes, including nitroaromatic explosives, catecholamine neurotransmitters, glucose and nucleic acids, as well as epidermal biosensing of sweat lactate.

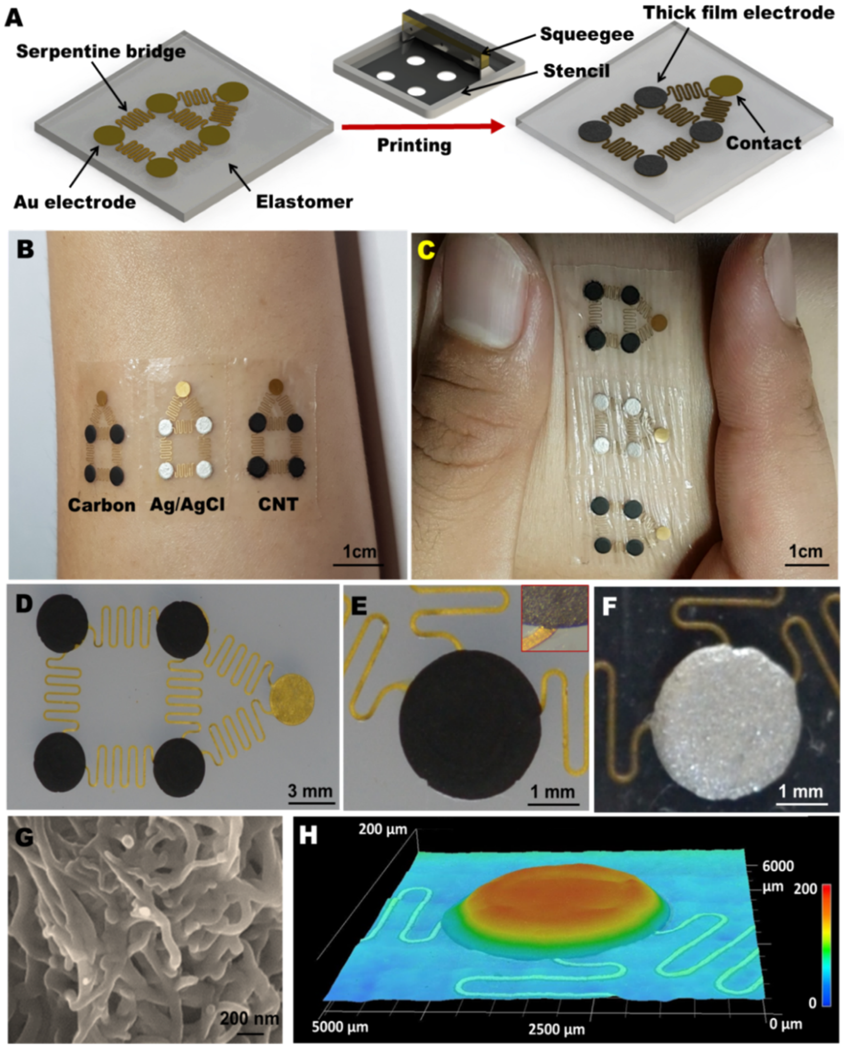

Figure 4.1: Soft stretchable devices prepared by merging thin and thick-film fabrication technologies. (A) Scheme showing fabrication of the hybrid thick-thin stretchable electrode system. (B) Image showing an array of carbon (left), Ag/AgCl (center) and CNT (right) based electrodes applied to the forearm of a human subject. (C) Image of the skin-mounted device when pinched. Optical microscopic image of the (D) entire system and close-up showing the registration of the (E) carbon (inset demonstrates close-up image of thick–thin film interface) and (F) Ag/AgCl ink onto the underlying Au electrode. (G) SEM of the CNT film printed onto the Au electrode. (H) Three-dimensional optical image clearly depicting the thick-thin feature of the hybrid electrode system. (Reprinted with permission and Copyright 2017 John Wiley and Sons).

The hybrid electrode system has been designed to endure mechanical strains caused by bodily movements. Keeping cognizance of such a requirement, it was designed in the form of a square, with the electrodes present at its corners as circular islands with free-standing serpentine interconnects, bridging the adjacent electrode islands (Figure 4.1D). While the new island-bridge hybrid concept is illustrated here using four adjacent electrodes towards wearable sensors, it could be readily scaled up to cover larger areas of the skin to meet the demands of specific applications (e.g., epidermal biofuel cells). The orthogonally located free-standing serpentine interconnects impart stretchability to the device in all directions along its plane, thus enabling it to withstand repeated uniaxial and biaxial strains common to the human epidermis.

Thin and thick-film microfabrication techniques were seamlessly combined to achieve uniform registration of printable inks onto the gold backbone, as clearly depicted in Figure 4.1E and 4.1F. These images illustrate the perfect overlap of the printed films onto the gold islands with minimal line edge roughness. Figure 4.1G showcases an SEM image focusing on the uniform printability and distribution of the CNT ink printed on top of a gold island. Apart from the homogeneous printability, the printed films must also adhere strongly to the gold surface under repeated multi-axial stretching deformations. Figure 4.1H illustrates the huge difference in thickness of Au and printed films. In general, the strain is proportional to film thickness. Hence the stretch ability of thin gold films is much larger than that of the thick printed layers. However, the mismatch between the thicknesses of the two films is not a major issue for the present system due to its island-bridge design. As illustrated in Figure 4.1C, S1 and video S1, the skin-worn hybrid system is able to defiantly withstand repeated pinching (50 times) with virtually no impact on its structural integrity. Such impressive stretchability reflects the system strategic design that leads to most of the applied strain to be accommodated by the serpentine structures while rendering the thick printed electrode unaffected.

Strain can have deleterious impact on conductivity of the system. Potential sources of such resistance variations include (1) piezoresistance of the copper and/or gold interconnects; (2) interfacial delamination between the thin metal island and the overlaid printed thick films. In the first set of experiments, a hybrid device (Figure 4.2A) was connected to a multimeter and linearly stretched in increments of ε = 25% till the strain reached ε = 75% (Figure 4.2B), followed by decreasing strain until it reached its initial state (ε = 0%, Figure 4.2C).

Figure 4.2: Endurance towards repeated stretching. Images showing the electrode system (A) before (B) during (arrow showing direction of stretching) and (C) after linear stretching (ε=75%). (D) Real-time evolution of resistance as a function of linear stretching for bare Au and C-Au electrode system (R1-R5 indicate releasing the tensile load). Images showing the electrode system (E) before, (F) during (arrow showing direction of stretching) and (G) after bi-axial stretching (ε=75%). (H) Real-time evolution of resistance as a function of biaxial stretching for bare Au and carbon on the Au electrode system. CVs recorded for C-Au electrode system after repeated uniaxial stretching (ε=75%) for (I) 10 mM ferricyanide and (J) 100 mM dopamine. CVs recorded for C-Au electrode system after repeated biaxial stretching (ε=75%) for (K) ferricyanide and (L) dopamine. (A-C; E-G) Scale bar: 5mm. Scan rate, 0.1 V/s. (Reprinted with permission and Copyright 2017 John Wiley and Sons).

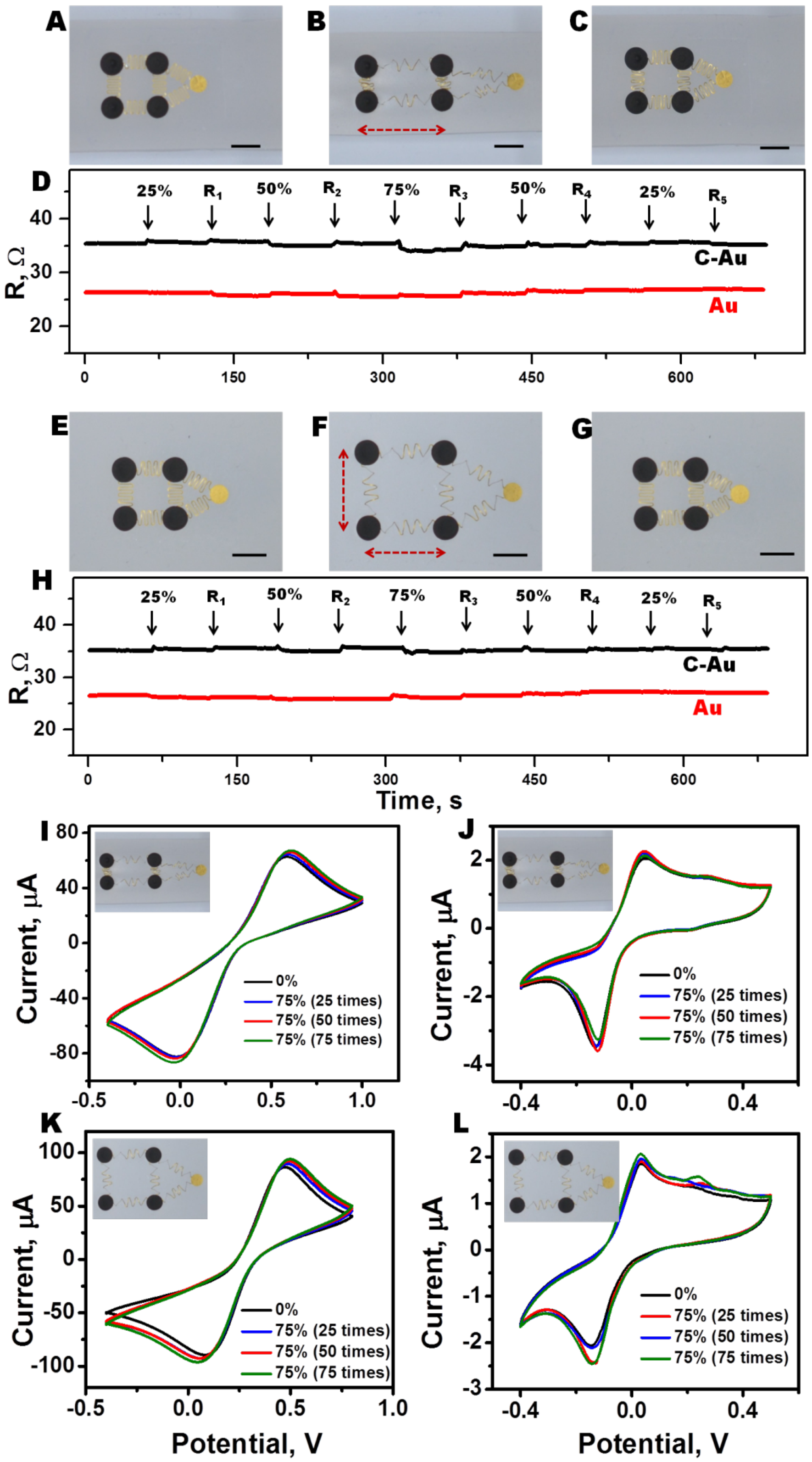
A
B
C
D
25%
R₁
50%
R₂
75%
R₃
50%
R₄
25%
R₅
C-Au
Au
R, Ω
20
30
40
0
150
300
450
600
E
F
G
H
25%
R₁
50%
R₂
75%
R₃
50%
R₄
25%
R₅
C-Au
Au
R, Ω
20
30
40
0
150
300
450
600
Time, s
I
80
40
0
-40
-80
-0.5
0.0
0.5
1.0
Current, µA
0%
75% (25 times)
75% (50 times)
75% (75 times)
J
2
0
-2
-4
-0.4
0.0
0.4
Current, µA
0%
75% (25 times)
75% (50 times)
75% (75 times)
K
100
50
0
-50
-100
-0.5
0.0
0.5
1.0
Current, µA
Potential, V
0%
75% (25 times)
75% (50 times)
75% (75 times)
L
2
1
0
-1
-2
-3
-0.4
0.0
0.4
Current, µA
Potential, V
0%
75% (25 times)
75% (50 times)
75% (75 times)

As illustrated in Figure 4.2D, the resistance of the hybrid (C-Au) electrode system varies negligibly, with Relative Standard Deviation (RSD) of 1.75%, in a manner similar to that of the thin gold electrodes (RSD = 1.26%). It is important to point out that the hybrid C-Au structure is orders of magnitude thicker than the pristine gold electrode, as clearly illustrated by the 3D optical image (Figure 4.1H); yet, its stretchability is similar to that of the thin gold electrode because of the island-bridge design. The slightly higher resistance of the C-Au hybrid system than the pristine metal structure reflects the higher resistivity of the printed carbon layer as compared to the bare gold electrode. The variation in resistance of hybrid system under bi-axial strain was also studied (Figure 4.2E-H). The strain was increased from 0% (Figure 4.2E) to 75% (Figure 4.2F) with a step of $\varepsilon = 25\%$ and finally brought back to its initial state (Figure 4.2G). Similar to the uni-axial stretching experiments, the bare thin gold electrode system and the C-Au hybrid system showed negligible variation in resistance as a function of repeated bi-axial stretching with RSD = 1.93 and 0.69%, respectively (Figure 4.2H). Close-up visual inspection of the system during these repeated physical deformations, revealed no apparent delamination of the printed layer, reflecting the strong adhesion of the printed island electrodes to the gold surface.

The elasticity of the hybrid stretchable device was analyzed by comparing its Young’s modulus (8.63 Psi) with that of a control Ecoflex substrate (7.1 Psi). As shown in Figure S2, the hybrid device leads to a very small change in elasticity versus the control substrate. Such small variation reflects that the hybrid system behaves just like an elastomeric material even when it consists of tens of micrometers thick rigid carbon film on the gold islands. Thus, rigid layers of various materials can be incorporated within the hybrid system while still maintaining its soft, stretchable nature similar to that of elastomers.

The effect of stretching on the electrochemical response of the hybrid system was analyzed by recording cyclic voltammograms (CVs) after repeated uni-axial stretching of the electrode system at ε = 75%. Ferricyanide (a common redox probe) and dopamine (an important neurotransmitter) were selected as candidates to assess potential variations in electrochemical response. The minimal impact on the voltammetric response during these tests for both ferricyanide (Figure 4.2I) and dopamine (Figure 4.2J) highlights the resilience of the system towards such strains. Moreover, the electron transfer kinetics occurring at the electrode-electrolyte interface was also studied. The gradual separation of peak and linear relation between peak current height and square root of scan rate implies that the electron transfer follows a quasi-reversible route, as reported for several printed carbon electrodes.[21] The effect of biaxial stretching on the electrochemical response of the system towards ferricyanide and dopamine was also examined. Figure 4.2K and 4.2L illustrate that repeated bi-axial stresses had a negligible impact on the voltammetric response with the recorded CVs remaining virtually identical.

The primary focus of the present work was to demonstrate the development of stretchable devices that could be realized by the synergistic effect of combining the attributes of lithography and printing. Carbonaceous materials have long been the preferred electrode material over noble metals, such as gold, due to their low background current, high over-voltage for electrolysis of water and hydrogen evolution, and hence a wide potential window, and attractive electrochemical reaction kinetics.[22] Incorporation of carbonaceous materials with the lithographically designed stretchable devices can have major implications in energy [23] and sensing [24] sectors.

The advantages of the new carbonaceous stretchable devices were demonstrated for electrochemical sensing of important analytes, including nitroaromatic explosives, catecholamine neurotransmitters and nucleic acids (Figure 4.3A-D). Figure 4.3A compares square-wave voltammograms (SWV) for the explosive DNT at the hybrid C-Au thick-thin electrode system and its bare gold counterpart. Electrochemical detection of DNT usually involves identifying the reduction peaks of its two nitro groups. [25,26] Unfortunately, the reduction occurs at quite negative potentials. Hence it is imperative to select electrode materials, such as carbon, which has high over-voltage for hydrogen evolution as compared to noble materials, like gold, wherein high background current is obtained to do electrolysis of water. Figure 4.3A illustrates that the C-Au system offers favorable well-defined and separated reduction peaks of the two nitro groups of DNT along with a low background current over the entire potential range.

In contrast, the gold system displays a single broad reduction peak and high background current starting from -0.7V (that obscures the second peak). The C-Au system was thus utilized to detect various trace concentrations of DNT in aqueous media (Figure 4.3B), offering a well-defined response, proportional to the explosive concentration, and favorable signal-to-background characteristics. The merit of printing carbon electrodes on the gold islands was further demonstrated toward the detection of single-stranded DNA using the bare gold and C-Au systems (Figure 4.3C). It is well documented that carbon electrodes offer the most favorable anodic detection of nucleic acids based on direct oxidation of guanine.[27] Figure 4.3C highlights the superior DNA detection ability of C-Au electrode as compared to Au involving sharp peak, low background current and wide anodic potential window.

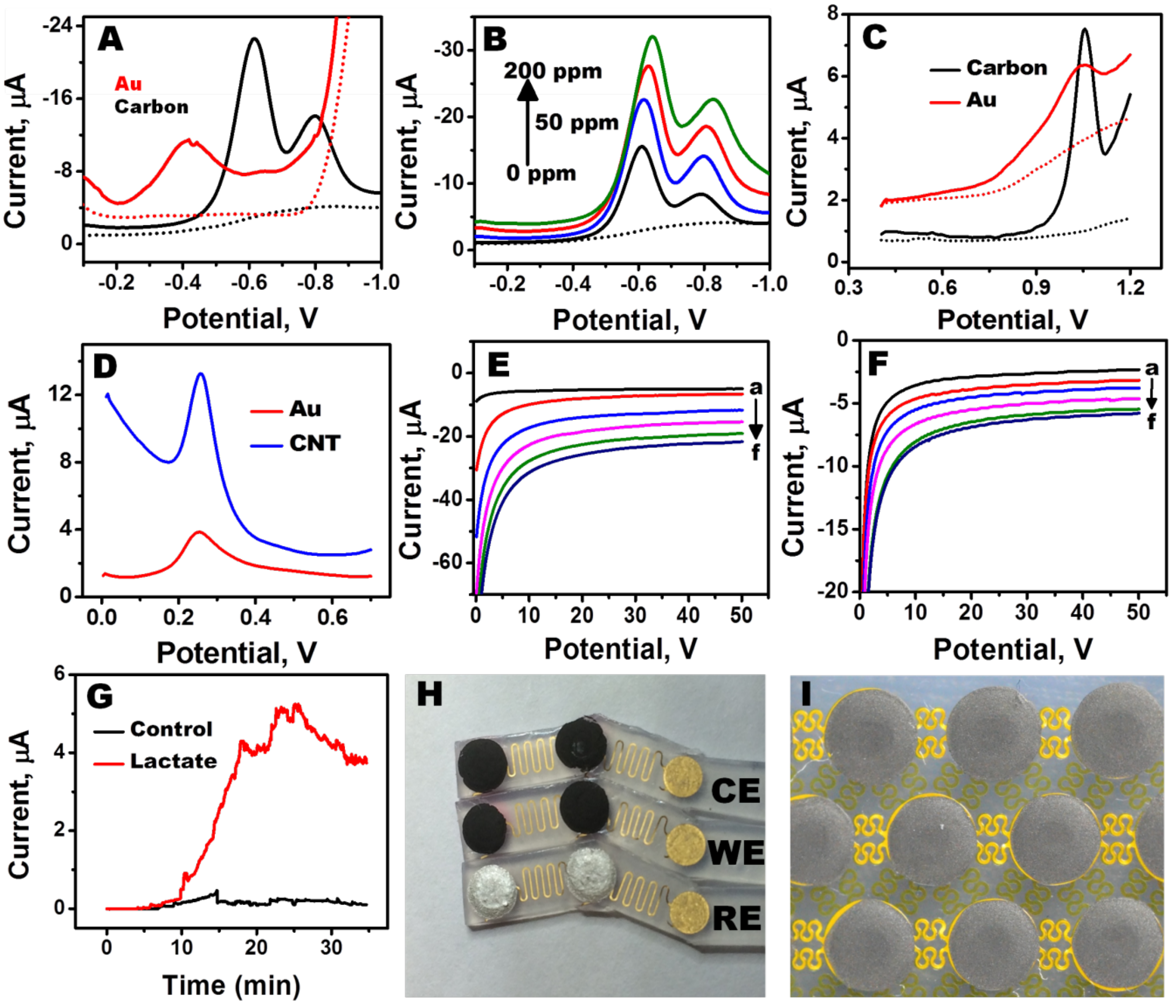

Figure 4.3: Electrochemical Testing of Hybrid Devices (A) Reductive SWVs recorded for Au (red) and carbon (black) electrode systems for 100 ppm DNT (thick lines) and 0 ppm DNT (dotted lines). (B) Reductive SWVs recorded for Au electrode system for 0-200 ppm DNT. (C) SWVs recorded for carbon (black) and Au (red) electrodes for 25 µg/mL (thick lines) and 0 µg/mL (dotted lines) ssDNA in 0.1 M acetate buffer (pH 4.65). (D) SWVs recorded for Au (red) and CNT (blue) electrode system for 100 µM dopamine. (E) Chronoamperograms recorded for Prussian Blue-carbon-GOx electrode system for 0-25 mM glucose at an applied potential of -0.2 V. (F) Chronoamperograms recorded for Prussian Blue-carbon-LOx electrode system for 0-15 mM lactate at an applied potential of -0.2 V. (G) Real-time on-body amperometric evaluation of lactate levels of a subject with (red) and without (black) enzyme modification. (H) An image showing the stretchable lactate sensor having working, reference and counter electrodes. (I) An optical image that demonstrates the feasibility of large-scale patterning of stretchable thick-thin film islands for various energy applications. (Reprinted with permission and Copyright 2017 John Wiley and Sons).

CNT-based electrode materials have several advantages in energy and sensing fields.[28] However, integration of CNTs into stretchable lithographic systems is cumbersome and expensive. Screen-printing has been used for fabricating CNT-based devices.[29] In the present work, customized CNT ink,[30] was utilized to realize CNT films onto the stretchable gold electrode system. The advantage of the CNT-Au system over its bare gold counterpart is even more pronounced toward measurements of the important neurotransmitter dopamine (Figure 4.3D). The CNT-Au electrode displays a significantly sharper and larger SWV oxidation peak compared to the bare gold electrode. The CNT-Au electrode also displayed enhanced electron-transfer characteristics toward ferrocyanide, as compared to C-Au and bare gold electrodes.

Integrating biotic and abiotic components to develop bio-integrated systems is quite essential for various healthcare applications.[31] However, most biological materials are quite labile to surrounding environment and lose their properties under harsh conditions encountered during lithographic processes. Thus, direct incorporation of biomaterials with lithography is daunting. Combining printing with lithography can provide an attractive route to functionalize lithographically patterned devices with a wide range of biotic components. Enzymatic glucose and lactate electrochemical biosensors were evaluated to demonstrate the viability of the new thick-thin hybrid fabrication process towards realizing soft bioelectronic systems. Glucose oxidase and lactate oxidase enzymes were homogeneously dispersed within Prussian Blue ink and then subsequently printed onto the gold island electrodes. Prussian Blue ink was selected due to its high selectivity towards the hydrogen peroxide product of the enzymatic reactions.[32] The data for glucose (Figure 4.3E) and lactate (Figure 4.3F) illustrate the linear response of these enzymatic electrodes towards their respective analytes. The ease with which such labile biocatalytic moieties could be successfully incorporated onto the stretchable platform emphasizes again the importance of a hybrid thick-thin fabrication process. Similar printing protocol can be employed to include other biological components for various bioelectronic applications.

The stretchable hybrid lactate biosensor was evaluated for real-time epidermal monitoring of sweat lactate.[33] The dynamic concentration changes of lactate in human perspiration were measured continuously during a 33 min intense cycling activity. The stretchable lactate sensor (Figure 4.3H) was placed on the subject’s deltoid and interfaced with a hand-held electrochemical analyzer. Figure 4.3G reveals the continuous amperometric data recorded for both lactate sensor (red) and enzyme-free control (black) stretchable electrodes during the cycling activity. In presence of enzyme, the sensor exhibits facile biocatalytic efficiency towards the oxidation of lactate in the sweat. No apparent current response is observed at the initial stages of the cycling at both the electrodes, reflecting absence of sweat. The epidermal sensor starts to measure the current response, proportional to the lactate level, as the subject begins to perspire at ~900s. The sweat lactate level increases upon increasing the cycling intensity, as indicated from the rising current signal. A decreased current signal is observed after 24 min, reflecting the decreased lactate sweat level associated with the slower exercise intensity and sweat dilution. As expected, no current response is observed using the control transducer (without the enzyme).

4.1.3 Conclusions

The hybrid “island-bridge” approach provides also the feasibility of scalable patterning of larger stretchable devices based on the requirements for diverse energy generation and storage applications. Figure 4.3l demonstrates such a hybrid array device, patterned on the stretchable substrate, that could be used as a wearable energy-harvesting device.

We reported on the amalgamation of thick and thin film fabrication techniques for preparing high-performance stretchable “island-bridge” devices with different functional materials. Screen-printing has been used to prepare the rigid printed (island) electrodes while thin-film lithography employed for fabricating the serpentine interconnects (bridges). The resulting hybrid stretchable systems display new capabilities that cannot be achieved through the individual fabrication routes. The new hybrid fabrication strategy can lead to a variety of deterministic stretchable structures with a broad range of functional materials, based on the judicious choice of the ink material and modifier. For example, the printing of various carbons or enzymes has led to a powerful platform for sensitive and selective electrochemical sensing of explosives, neurotransmitter, nucleic acids, glucose and lactate, without affecting its stretchability. While the advantages of the new thin-film/thick film deterministic approach have been demonstrated for these important sensing applications, the new hybrid fabrication route offers considerable promise for a wide range of flexible and wearable electronic applications.

Acknowledgements

Chapter 4 is based, in part, on the material as it appears in Advanced Materials Technologies, 2017, by Rajan Kumar, Vinu Mohan, NamHeon Kim, Amay Bandodkar,

Jung-Min You, Jonas Kurniawan, Sheng Xu, and Joseph Wang. As a corresponding author of the project, the dissertation author aided in the design and fabrication of the hybrid devices. In addition, the author was critical to analysis of their durability testing and optical characterization.

4.2 References

1. J. Ouyang, C. Chu, C. R. Szmanda, L. Ma, Y. Yang, *Nat. Mater.* **2004**, *3*, 918.
2. C. H. Lee, H. Kim, D. V. Harburg, G. Park, Y. Ma, T. Pan, J. S. Kim, N. Y. Lee, B. H. Kim, K. Jang, S. Kang, Y. Huang, J. Kim, K. Lee, C. Leal, J. A. Rogers. *NPG Asia Mater.* **2015**, *7*, 227.
3. M. Koo, K. Park, S. H. Lee, M. Suh, D. Y. Jeon, J. W. Choi, K. Kang, K. J. Lee, *Nano Lett.* **2012**, *12*, 4810.
4. D. Kim, R. Ghaffari, N. Lu, J. A. Rogers, *Annu. Rev. Biomed. Eng*. **2012**, *14*, 113.
5. D. H. Kim, N. Lu, R. Ma, Y. S. Kim, R. H. Kim, S. Wang, J. Wu, S. M. Won, H. Tao, A. Islam, K. J. Yu, T. Kim, R. Chowdhury, M. Ying, L. Xu, M. Li, H. J. Chung, H. Keum, M. McCormick, P. Liu, Y. W. Zhang, F. G. Omenetto, Y. Huang, T. Coleman, J. A. Rogers, *Science*, **2011**, *333*, 838.
6. D. S. Grey, J. Tien, C. S Chen, *Adv. Mater.* **2004**, *16*, 393.
7. J. A. Fan, W. Yeo, Y. Su, Y. Hattori, W. Lee, S. Jung, Y. Zhang, Z. Liu, H. Cheng, L. Falgout, M. Bajema, T. Coleman, D. Gregoire, R. J. Larsen, Y. Huang, J. A. Rogers, *Nat. Commun.* **2014**, *5*, 3266.
8. M. Melzer, G. Lin, D. Makarov, O. G. Schmidt, *Adv. Mater.* **2012**, *24*, 6468.
9. Y. Zhang, S. Xu, H. Fu, J. Lee, J. Su, K. Hwang, J. A. Rogers, Y. Huang, *Soft Matter*, **2013**, *9*, 8062.
10. M. Park, J. Im, M. Shin, Y. Min, J. Park, H. Cho, S. Park, M. Shim, S. Jeon, D. Chung, J. Bae, J. Park, U. Jeong, K. Kim, *Nat. Nanotechnol.* **2012**, *7*, 803.
11. D. J. Lipomi, *Adv. Mater.* **2016**, *28*, 4180.
12. J. A. Rogers, T. Someya, Y. Huang, *Science* **2010**, *327*, 1603.
13. P. Lee, J. Lee, H. Lee, J. Yeo, S. Hong, K. H. Nam, D. Lee, S. S. Lee, S. H. Ko, *Adv. Mater.* **2012**, *24*, 3326.
14. Z. Yu, X. Niu, Z. Liu, Q. Pei, *Adv. Mater.* **2011**, *23*, 3989.
15. Y. Zhang, Q. Chen, J. Ge, Z. Liu, *Chem. Commun.* **2013**, *49*, 9815.
16. L. Xiao, Z. Chen, C. Feng, L. Liu, Z. Bai, Y. Wang, L. Qian, Y. Zhang, Q. Li, K. Jiang, S. Fan, *Nano Lett.* **2008**, *8*, 4539.

17. S. H. Ko, H. Pan, C. P. Grigoropoulos, C. K Luscombe, J. M. J. Frechet, D. Poulikakos, *Nanotechnology* **2007**, *18*, 345202.

18. T. Sekitani, T. Someya,, *Adv. Mater*. **2010**, *22*, 2228.

19. M. Li, Y. Li, D. Li, Y. Long, *Anal. Chim. Acta* **2012**, *734*, 31.

20. A. J. Bandodkar, I. Jeerapan, J. Wang, *ACS Sens*. **2016**, *1*, 464.

21. H. Wei, J. Sun, Y. Xie, C. Lin, Y. Wang, W. Yin, G. Chen, *Anal. Chim. Acta* **2007**, *588*, 297.

22. R. L. McCreery, *Chem. Rev.* **2008**, *108,* 2646.

23. S. Xu, Y. Zhang, J. Cho, J. Lee, X. Huang, L. Jia, J. A. Fan, Y. Su, J. Su, H. Zhang, H. Cheng, B. Lu, C. Yu, C. Chuang, T. Kim, T. Song, K. Shigeta, S. Kang, C. Dagdeviren, I. Petrov, P. V. Braun, Y. Huang, U. Paik, J. A. Rogers, *Nat. Commun.* **2013**, *4*, 1543.

24. X. Wang, T. Li, J. Adams, J. Yang, *J. Mater. Chem. A*, **2013**, *1*, 3580.

25. Y. T. Yew, A. Ambrosi, M. Pumera, *Sci. Rep.*, **2016**, *6*, 33276.

26. J. Wang, *Electroanalysis* **2007**, *19*, 415.

27. J. Wang, X. Cai, J. Wang, C. Jonsson, E. Palecek, *Anal. Chem.* **1995**, *67*, 4065.
28. M. F. L. De Volder, S. H. Tawfick, R. H. Baughman, A. J. Hart, *Science* **2013**, *339*, 535.

29. J. Wang, M. Musameh, *Analyst* **2004**, *129*, 1.

30. A. J. Bandodkar, I. Jeerapan, J. You, R. Nunez-Flores, J. Wang, *Nano Lett.* **2016**, *16*, 721.

31. D. Kim, J. Viventi, J. J. Amsden, J. Xiao, L. Vigeland, Y. Kim, J. A. Blanco, B. Panilaitis, E. S. Frechette, D. Contreras, D. L. Kaplan, F.G. Omenetto, Y. Huang, K. Hwang, M. R. Zakin, B. Litt, J. A. Rogers, *Nat. Mater*. **2010**, *9*, 511.

32. A. A. Karyakin, *Electroanalysis* **2001**, *13*, 813.

33. A. J. Bandodkar, W. Jia, C. Yardımcı, X. Wang, J. Ramirez, J. Wang, *Anal. Chem*. **201**5, *87*, 394

CHAPTER 5 PRINTED BATTERY

5.1 All-Printed, Stretchable Battery

5.1.1 Introduction

The advent of flexible/stretchable electronics has cultivated the next generation of sensors,[1-5] photovoltaics,[6, 7] paper-like displays,[8, 9] wearable/implantable electronics,[10-16] e-textiles,[17, 18] optics,[19] and soft robotics.[20] Unlike their brittle and rigid predecessors, soft electronics can intimately integrate with curvilinear surfaces while withstanding the complex deformations common of human organs, textiles, or robotics.[21, 22] Unfortunately, the progress of stretchable systems, specific to their mobility and independence, is currently constrained by bulky and rigid powering sources.[23-25] Batteries hold the most promise owing to their high power and energy densities, rechargeability, and low-cost.[23] Stretchable batteries have been fabricated through many different approaches, deterministic composite [26-30] and random composite [31-34] architecture.

The deterministic approach relies on subtractive methods to render otherwise rigid materials, with bulk properties, into deterministic structures such as “island-bridge”[35, 36] or “cable-type”[29, 30] batteries[37]. By engineering elasticity with high-performance, rigid electrodes, these stretchable batteries can withstand high levels of strain without intrinsically stretching them. The random composite approach embeds percolations of highly conductive fillers ($>10^7$ S m^{-1}, silver nanowires and carbon nanomaterials) into an elastomeric matrix.[38, 39] Unlike deterministic composite, these devices are intrinsically stretchable as fillers maintain electrical contact by sliding along each other during stretching.[37] Intrinsically stretchable batteries have been reported, but none are completely elastic systems.[31-34] The cycle ability, current density, or areal capacity of these battery are compromised when a rigid component undergoes large physical strain.[32-34, 40] Unfortunately, both deterministic and random composite-designed batteries are not economical because they rely on lithographic,[11, 35, 41, 42] spray/dip coating,[31, 43] or "cut-and-paste"[2, 34, 44] fabrication routes that are extremely expensive and low-throughput.

Today, printed, non-rechargeable batteries is an emerging market supporting many wearable and disposable electronics, and expected to reach a value of $1.2 billion by 2017, CAGR 46% from 2012.[45] Individual components are fabricated using a single, inexpensive printing step through either dispensing, screen, roll-to-roll, or inkjet printing of composite inks.[40, 46] Unlike comparable coating technologies, such as spray or dip coating that may have high throughputs, screen printing can actively control the design that can potentially combine both deterministic and random composites. The higher viscosity requirements of screen printing enable high loadings of conductive fillers towards superior elastic performance and higher battery performance. The rheology of the ink is controlled by the composite formulation of electroactive fillers, a binder, and a specific solvent.[40, 46] The binder plays the role of holding the ink components together and in dictating the flexible and stretchable nature of the inks. The synthesis of stretchable inks is highly challenging since the battery experiences significantly higher strain levels during stretching as compared to just bending. The printing technologies and random composite-based inks can be used to fabricate cost-effective and intrinsically stretchable batteries.[1, 47] The fundamental challenge of using random composite is that the electrochemical properties of the fillers and elastic matrix are mutually detrimental to the other. This approach becomes overwhelmingly challenging for printed, stretchable batteries with poorly conductive, electroactive fillers (~10^5 S m^{-1}), thus the need for new innovations in highly elastic matrix is imperative.[37] Specially formulated inks must be formulated to allow the printed batteries to be stretched 100% multiple times.

Here in, we report the first all-printed stretchable Zn-Ag_2O rechargeable battery using low-cost screen printing of highly elastic, conductive inks. The novelty of this work hinges on the attractive hyperelastic properties (~1300% elongation) of polystyrene-*block*-polyisoprene-*block*-polystyrene (SIS) as a new elastic binder for stretchable batteries. Due to unique block polymeric structure of long polyisoprene chain and short polystyrene terminal ends, SIS has superior elasticity and simpler processing compared to common elastomers, e.g., exoflex®, that require an additional curing (vulcanization) step to form the 3D crosslinked network to impart truly elastic behavior.[1, 48-50] Owing to its unrivaled properties, SIS can be incorporated in higher loadings while maintaining the mechanical and electrochemical properties of the battery capable of stretching over 500%.[51, 52] The resulting rechargeable Zn-Ag_2O battery demonstrates a reversible capacity density of ~2.5 mAh cm^{-2} even after multiple iterations of 100% stretching. To our knowledge, this represents an intrinsically stretchable battery with the highest reversible capacity and discharge current density, fabricated by inexpensive printed technologies, reported to date. The new SIS-based printed battery can withstand other severe torsional strains relevant to the wearer's movement. The mechanical properties of the stretchable battery are evaluated using digital image correlation (DIC) and scanning electron microscopy (SEM) and its attractive electrochemical cycling, impedance and mechanical properties are presented.

5.1.2 Experimental Section

Chemicals and Reagents:

Super-P® Conductive Carbon Black (SP), toluene (Alfa Aesar), 200 proof Koptec (Decon Labs, King of Prussia, PA), Zn powder (Alfa Aesar), Ag_2O powder (Alfa Aesar), Bi_2O_3 (Alfa Aesar). Universal mold release (Smooth-On®). KOH, LiOH, polyacrylic acid, and SIS (14% styrene) were purchased from Sigma Aldrich.

Elastic Composite Inks Preparation:

The elastic carbon current collector ink was prepared by first dissolving 1.10 g of SIS pellets in 5 mL of toluene with analog vortex mixer (VWR) for one hour. Toluene was chosen as the SIS solvent due to their similar Hillenbrand solubility parameters. [53,54] The 0.6 g of SP is mixed into the SIS solution in a dual asymmetric centrifugal mixer (Flacktek Speedmixer^{TM}, DAC 150.1 KV-K) at 3000 rpm for 5 mins. After cooling the ink, 4 g of yttria stabilized zirconia grinding beads (3 mm diameter, Inframat® Advanced Materials) and additional 4 mL of toluene were added and underwent further mixing of 3000 rpm for 30 mins to thoroughly mix and achieve optimum viscosity.[55, 56]The elastic Zn ink was prepared by first dissolving 0.6 g of SIS pellets in 2.8 mL of 80% v/v toluene and 20% v/v ethanol with analog vortex mixer for one hour. Then, 3.4 g of composite Zn powder (30 wt% SP, 60 wt% Zn, and 10 wt% Bi_2O_3)[44] were mixed into the SIS solution in the dual asymmetric centrifugal mixer at 3000 rpm for 5 mins. After cooling the ink in air, 2 g of the yttria-stabilized zirconia grinding beads and additional 1.5 mL of the toluene/ethanol solution were added and underwent further mixing of 3000 rpm for 30 mins. The elastic Ag_2O ink was prepared by first dissolving 0.6 g of SIS pellets in 2.8 mL of 80% v/v toluene and 20% v/v ethanol with analog vortex mixer for one hour. Then, 3.0

g of composite Ag_2O powder (20 wt% SP and 80 wt% Ag_2O) [57] were mixed into the SIS solution in the dual asymmetric centrifugal mixer at 3000 rpm for 5 mins. After cooling the ink in air, 2 g of the yttria-stabilized zirconia grinding beads and additional 1.5 mL of the toluene/ethanol solution was added and underwent further mixing of 3000 rpm for 30 mins.

Stretchable Zn-Ag_2O Battery Fabrication:

The printing process employed the use of a MPM-SPM semi-automatic screen printer (Speedline Technologies, Franklin, MA). The bold “NANO” and rectangle patterns were designed in AutoCAD (Autodesk, San Rafael, CA) and patterned into a stainless steel through-hole 12 inch by 12-inch framed stencils with a thickness of 100 μm (Metal Etch Services, San Macros, CA). A thermoplastic PU sheet (ST604, Bemis Worldwide, Shirley, MA) was thermally bonded to smoothen the surface royal-blue colored high-performance spandex (Spandex World, New York, NY) using a typical drying iron (T-fal Ultraglide, Parsippany, NJ). A Keyence VHX1000 optical profiler measured the surface roughness between the ink printed directly on textile and TPU bonded textile (Figure S1A and S1B). First, carbon ink was used to print the entire “NANO” design as the current collector onto the Bemis® bonded textile and cured in an oven at 80°C for 15 mins. Subsequently, an anode electrode was printed with the Zn ink on the top half of both letter ‘N’ carbon prints and cured in an oven at 80°C for 15 mins. Lastly, a cathode electrode was printed with the Ag_2O ink on the top half of the letter’s ‘A’ and ‘O’ carbon prints and cured in an oven at 80°C for 15 mins. This design produces two batteries that are connected in series. The outline of the battery was heat-sealed with 26 μm thick PU sheet (Delstar Technologies Inc. Middletown, DE). The sealed battery was filled with the electrolyte formulated from our previous epidermal battery.[57] The "NANO" battery design was connected to a textile-embedded 3 V yellow LED (Lilypad, Sparkfun, Niwot, CO). A complete schematic of the device fabrication is demonstrated in detail in Figure S2. The DIC, SEM, and electrochemical tests were conducted using a pair of 0.9 cm by 3 cm rectangle for the current collector layer and 0.7 cm by 0.9 cm rectangle for the cathode and anode electrodes on a pre-applied PU film commercially named as 9EX-2497P Exoskin® (Dartex Coatings Inc., Slatersville, RI).

DIC Tensile Stress Analysis:

Carbon current collectors based on three different SP:SIS ratios (1:1, 1:2, and 1:3) were printed on a dog bone shaped cutout of Exoskin®. The carbon inks were using the same SIS solution as the earlier carbon ink. A while spray paint (Flat White Prime, Rust-oluem®, Vernon Hills, IL) then a random speckle black pattern (Flat Black Prime, Rust-oluem®, Vernon Hills, IL) were lightly sprayed on the printed samples. The printed samples were stretched using a motorized test stand (Mark-10, Copiague, NY) at a constant speed while a pair of high resolution, digital charge coupled device (CDD) cameras was recording a video of the sample from the relaxed to stretched state of 100%. A commercial software GOM ARAMIS (Trillion Quality Systems, Plymouth Meeting, PA) was used to convert the video into single frames for strain mapping. The black speckle on the white coating can create a grayscale matrix per pixel, which tracks the surface displacements of the deformed materials.[58] Mathematical correlation functions are applied to grayscale distribution from the speckle patterns and are analyzed among images before and after the deformation. [58, 59]

Mechanical and Conductivity Characterization of SIS Composite Inks*:*

The three current collector electrodes from the DIC experiment were used to measure the resistance during and after the stretching cycles. The sample preparation was same as the DIC experiment. The stretching tests were conducted on a custom stretching stage of a motorized linear stage and controller (A-LST0250A-E01 Stepper Motor and Controller, Zaber Technologies, Vancouver, Canada). The samples were programmed to constantly stretch at a speed of 0.1 cm second^{-1} from 0% to 100% and back to 0% as one cycle. The resistance was measured at 22 pt sec^{-1} using a digital multimeter (Agilent, Santa Clara, CA) during the ten cycles. The speed and length of the physical strain were programmed into a scripting software (Zaber console, Zaber Technologies, Vancouver, Canada). Additional mechanical characterization of the composites such as young's modulus, elongation at break, conductivity at 0% strain and conductivity prior to break were conducted. The same composite SP:SIS ratios (1:1, 1:2, and 1:3) were prepared by printing on glass slides pre-coated with universal mold release. After curing the samples, the printed samples easily release from the glass slide and mounted to the custom stretching stage. On one end of the stage, the mount was connected to a digital force gauge (Mark-10, Copiaque, NY) to measure the force applied as the sample is being strained continuously by motorized linear stage. Resistance was measured simultaneously using a digital millimeter. Further calculations based on resistance and force measurements were completed to compare the stress (kN/m^2) and conductivity (S/m) of the composite inks as they are strained.

SEM of Stretched Electrodes:

The printed carbon electrode, Zn electrode, and Ag_2O electrode were adhered onto a SEM holder. The pristine samples were adhere as printed without any stretching. The stretched samples were adhered with a 100% stretch. The relaxed samples were adhered after the electrodes were repeatedly stretched 100% for 10 cycles. The images were taken using 10 kV energy source using FEI/Philips XL30 ESEM (Philips,).

Electrochemical Properties:

All electrochemical tests were conducted at room temperature. The electrochemical cycling tests were conducting with Arbin electrochemical cycler channels. Electrochemical cycling tests were conducted with 2 mA cm^{-2} first formation cycle and 3 mA cm^{-2} discharge current and 2 mA cm^{-2} charge current for the subsequent cycles. The discharge cut-off voltage was 0.8 V and the charge cut-off voltage was 2.3 V with 20 min constant voltage step. For bending and stretching electrodes, the batteries were electrochemically cycled after being relaxed for 30 mins. The EIS was conducted using a 10^5 - 10^{-2} Hz frequency range with 10 mV amplitude using Solartron 1287 electrochemical interface. All EIS tests were conducted at the open circuit voltage upon the formation cycle.

5.1.3 Results and Discussions

The attractive mechanical properties of the SIS binder lead to intrinsically stretchable, and rechargeable printable Zn-Ag_2O battery that can withstand a variety of severe mechanical strains. Two stretchable batteries were printed in a “NANO” design directly on top of the thermoplastic PU head sealed onto the spandex (Figure 5.1A). On the “NANO” current collector, the respective electrodes were printed to form two batteries of a “NA” and “NO” designed connected in series to power a 3V wearable-based LED (Figure 5.1B). An additional seal between "A" and the second "N" was applied to avoid the short circuit. The stretchable “NANO” battery maintains a constant LED brightness regardless of severe torsional strain (Figure 5.1C), indentations (Figure 5.1D), 100% uniaxial stretching (Figure 5.1E), and biaxial stretching (Figure 5.1F). The printed battery can thus withstand high tensile stress without incurring any macrolevel cracking or debonding.

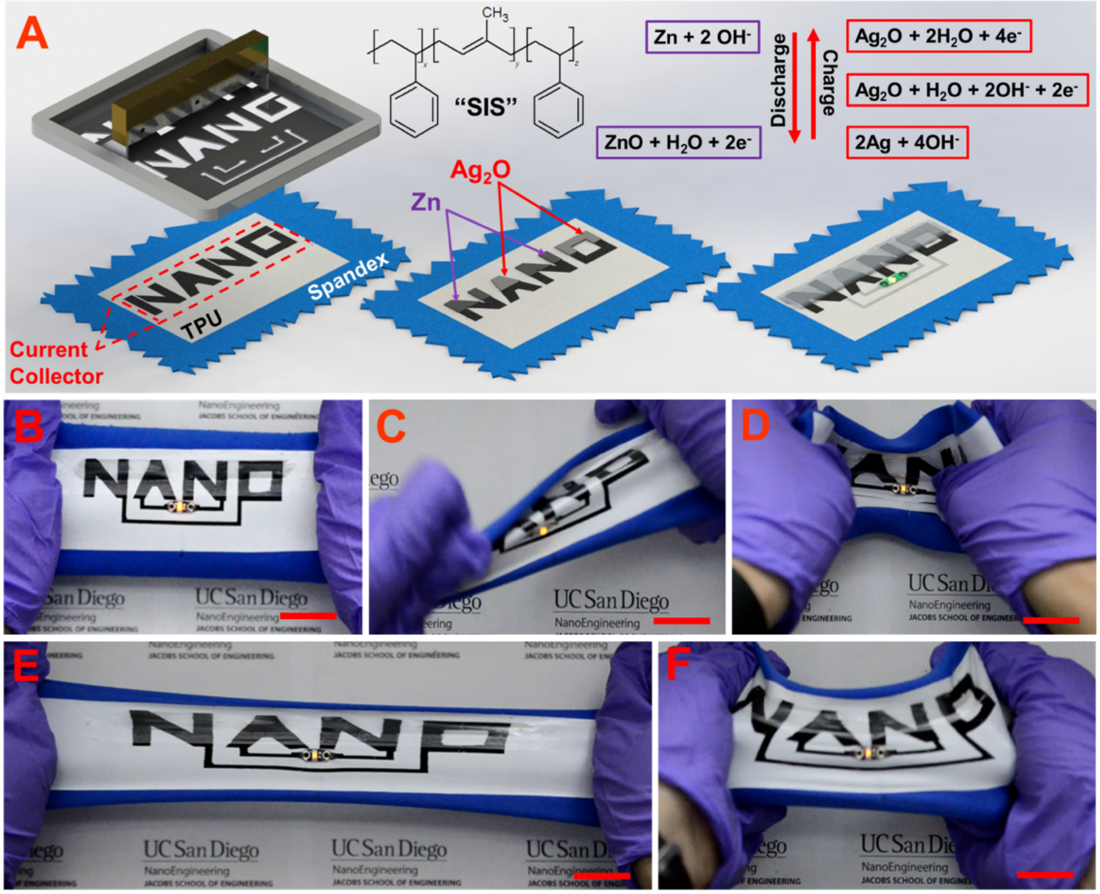

Figure 5.1: Screen-printed battery on stretchable fabric using stretchable, battery based inks: (A) Screen-printing steps of a Zn-Ag_2O battery on a stretchable textile using a SIS binder. Inset: Redox charge and discharge reaction. Photographs of sealed battery while being (B) 0% stretched, (C) twisted, (D) indentation strains, (E) 100% stretched, and (F) biaxial stretched. Scale Bar: 2.25 cm (Reprinted with permission and Copyright 2018 John Wiley and Sons).

A non-contact optical method called DIC has been utilized for strain mapping of the printed carbon electrodes of different SP:SIS ratios (1:1, 1:2, and 1:3) upon their stretching. DIC is frequently employed as a high-resolution imaging tool to analyze the deformations of macroscale objects in real-time to identify faults in materials or design [36]. In this technique, the surface is prepared with a white coat and random black speckle, a grayscale intensity pattern can be mapped for each pixel in the digital image of the sample[36]. The incremental displacements of each speckle on the surface can be tracked using this grayscale intensity between images before and after the deformation[36]. Algorithms are used to patch pixels into groups called facets, where strain on the object's surface can be correlated based on the changing dimensions of the facet [36]. The strain ($\varepsilon_{x,}$ ε_y) is calculated by the amount of change in size of the facet (traced by DIC) divided by the original size of the facet[36] Lower strain value indicates that pixel did not change much in that particular spot. If the pixel does not change much, this indicates that the facet or the location on the sample was hard to deform. Sudden increase in the strain indicates plastic deformations caused by the cracks.

A 2D strain mapping (ε_x) of the rectangular carbon electrodes (1:1 ratio, 1:2 ratio, and 1:3 ratio) is demonstrated from 0% stretching (Figure 5.2A, 5.2C, and 5.2E) to 100% stretching in the x-axis (Figure 5.2B, 5.2D, 5.2F). As the electrodes are stretched, there are significant changes in the strain mapping. For all the electrodes, the strain on the textile surface is generally higher than that of the electrode surfaces (Figure 5.2G). While a significant drop in the strain is observed at the interface between textile and the electrode, the 1:1 ratio electrode shows the larger drop. Furthermore, the strain distribution on the electrode surface is highly irregular for the 1:1 ratio electrode and is correlated to the physical cracks of the electrode. Such strain distributions are more uniform for the higher SIS-content electrodes, suggesting that electrodes with higher SIS content are not physically cracked in the optical scale.

In addition to the DIC analysis, change in resistance during the stretching cycles have been monitored (Figure 5.2H). At stretched state, the 1:1 ratio electrode has consistently high and unstable resistance due to the electrode cracking observed from the DIC (Figure 5.2J). For the other two electrodes, with higher SIS content, the resistance values are stable and similar at the stretched state at around 2.3 kΩ. However, when the electrodes are released from the stretching motion, the 1:2 ratio electrode consistently demonstrates the lowest resistance among the three electrodes with 0.65 kΩ (Figure 5.2I). In addition to DIC analysis and resistance studies, stress and conductivity of the three composite ratios were simultaneously measured as they were strained. Clearly, the 1:2 ratio electrode offers the optimum condition among the three conditions with a relatively high conductivity and low young's modulus. This ratio has thus been utilized to fabricate the carbon current collector electrode for the stretchable Zn-Ag_2O battery.

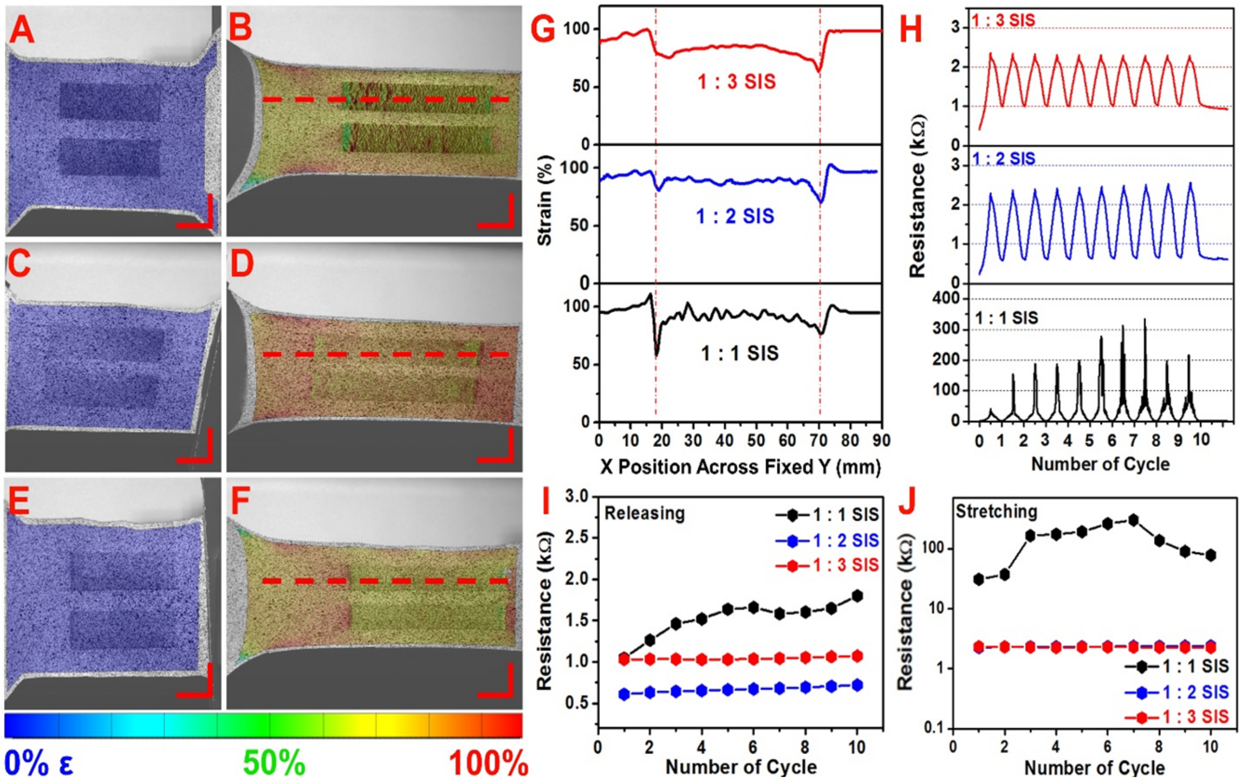

Figure 5.2: 2D strain mapping of the rectangular carbon electrodes at 0% stretching ((A) 1:1 ratio, (C) 1:2 ratio, and (E) 1:3 ratio) to 100% stretching ((B) 1:1 ratio, (D) 1:2 ratio, and (F) 1:3 ratio). (G) The strain plotted over the dotted line. (H) Respective resistance monitored during the 10 cycles of 100% stretching iterations. Respective resistances at release (I) and stretching (J). Scale Bar: 1.0 cm (Reprinted with permission and Copyright 2017 John Wiley and Sons).

Table 5.1: Mechanical Characterization of SP: SIS Composite Inks. (Reprinted with permission and Copyright 2017 John Wiley and Sons).

Composite SP:SIS Ratios	Young's Modulus (Psi)	Conductivity at 0% Strain (S/m)	Conductivity Prior to Break (S/m)	Elongation at Break (%)
1:1	-	60	7	9%
1:2	725	44	0.68	474%
1:3	145	18	0.21	598%

Although no cracks are observed in the DIC, the resistance still increases upon stretching. Since the DIC can highlight areas of cracking at the macroscale, SEM is utilized to observe physical deformations on the micron scale. Morphology of the optimized carbon electrode, Zn electrode, and Ag_2O electrode are observed before, during, and after stretching (Figure 5.3). While no cracks are observed at pristine state, upon stretching, micro cracks are observed. The cracks on these electrodes lead to increase the resistance and limit the electron conduction pathways. Per size of the cracks, carbon electrodes have the smallest cracks compared to those of the Zn and Ag_2O electrodes. For the Zn and Ag_2O electrodes, electrical contacts may be disturbed by such large cracks. Thus, it is important to keep the carbon electrode on the bottom of the Zn and Ag_2O electrodes to maintain the electrical connection. Although the carbon electrode has cracks as well, they are minute and uniformly distributed, which allow the electrical connections to be well preserved. After releasing the electrodes after 10 cycles of 100% stretching, both the carbon and Zn electrodes regained their crack-free morphology while Ag_2O displayed only a minor crack.

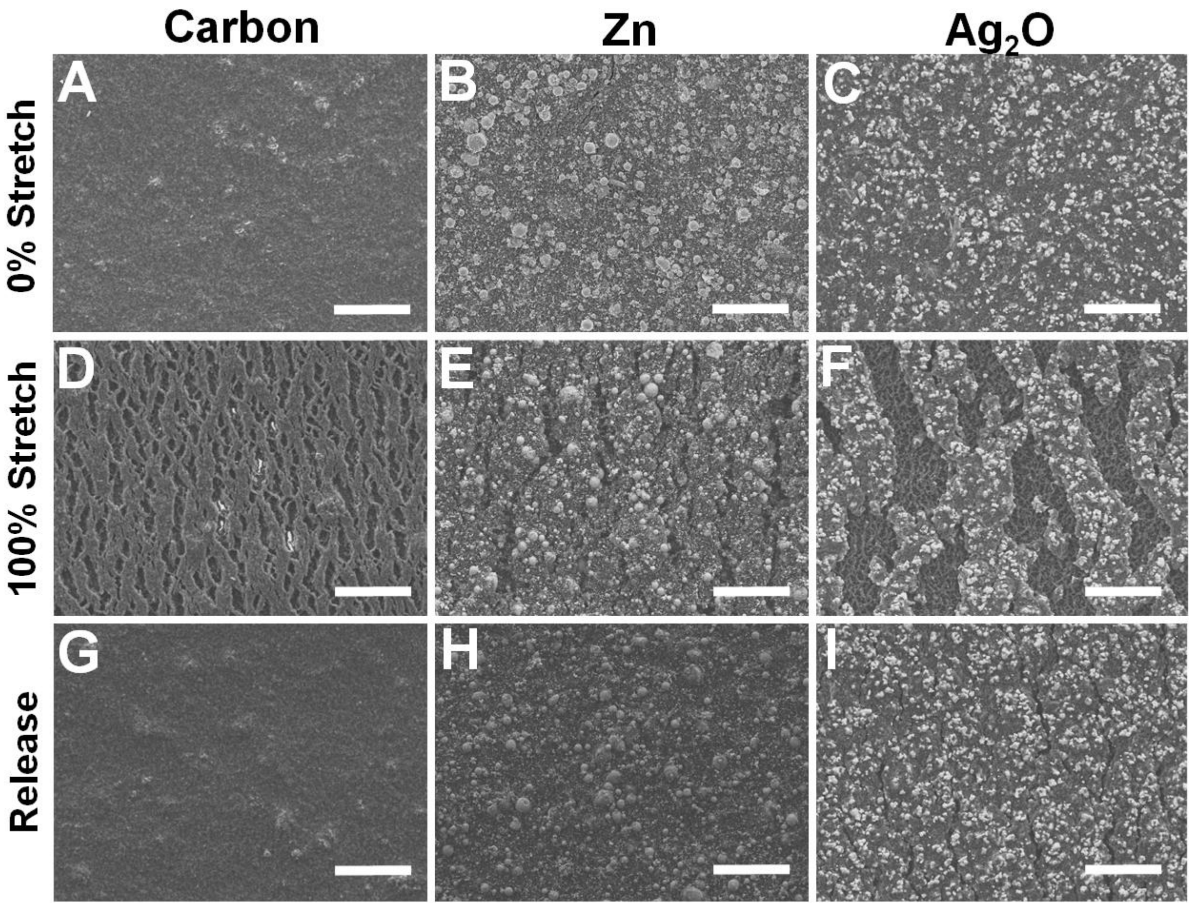

Figure 5.3: SEM images of the carbon current collector (A), Zn electrode (B), and Ag$_2$O electrode (C) as printed, carbon current collector (D), Zn electrode (E), and Ag$_2$O electrode (F) 100% stretched, and carbon current collector (G), Zn electrode (H), and Ag$_2$O electrode (I) released after ten 100% stretching iterations. Scale bar: 50 μm. (Reprinted with permission and Copyright 2017 John Wiley and Sons).

The electrochemical performance of the stretchable battery has been tested. The first cycle voltage profiles show high discharge capacity (Figure 5.4A). The pristine battery has 3.78 mAh cm^{-2} and stretching battery has 3.94 mAh cm^{-2} capacity. Upon stretching, the discharge capacity has slightly increased which is attributable to the enlarged active surface area from the cracks formed during stretching. It is notable that the average voltage decreases after stretching. This decreased voltage is due to the increased polarization and is more detrimental during the charge. The stretching battery has higher discharge capacity whereas the charge capacity is significantly lower than the pristine.

Due to the increased polarization, the second oxidation reaction, $Ag_2O + 2OH^- + 2e^- \rightarrow 2AgO + H_2O$, from the cathode has not occurred [32], resulting in lower capacity than the pristine battery during the prolonged cycle (Figure 5.4B). However, for both cases of batteries, the prolonged cycle discharge capacities are stable up to 30 cycles. The first cycle discharge capacity during the prolonged cycle, the pristine has higher capacity close to 3 mAh cm^{-2} compared to that of the stretching battery of about 2.5 mAh cm^{-2}.

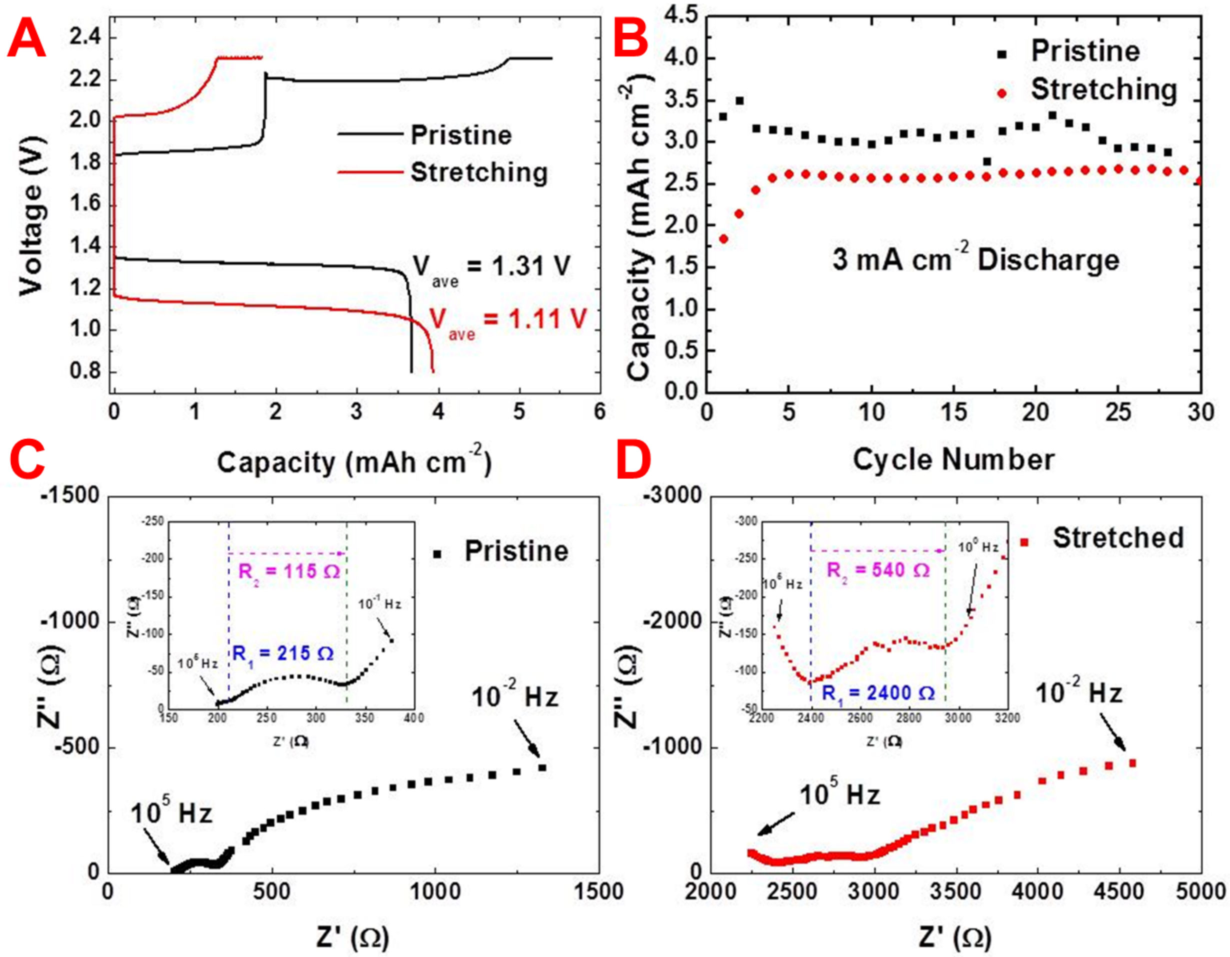

Figure 5.4: Electrochemical performance of the printed, stretchable battery (A) The first cycle voltage profile of the stretchable battery cycled with 2 mAh cm^{-2}. (B) The discharge capacity during prolonged cycle, cycled with 3 mAh cm^{-2}. Stretching battery has been 100% stretched ten times before the electrochemical cycling. (C) EIS of the pristine battery. (D) EIS of the battery stretched to 100%. (Reprinted with permission and Copyright 2017 John Wiley and Sons).

An electrochemical impedance spectroscopy (EIS) has been carried out to examine the polarization during the mechanical perturbation. The electrochemical cycling performance of the stretching battery is examined after 10 times of 100% stretching. EIS for the pristine and stretched battery are obtained at pristine state and when the battery is 100% stretched in order to understand the difference in polarization of the battery **(Figure 5.4C and 5.4D). In** the EIS, high, medium, and low frequency regions are identified with the light and dark green dotted lines. All three regions have charge transfer resistance and the constant phase elements. The depressed semicircle in the medium frequency region represents the charge transfer resistance of the ions in the electrolyte or the charge of the Zn anode and Ag_2O cathode.[60] The diameter of the depressed semicircle can be used to estimate the charge transfer resistance (R_2) on the electrodes. After being stretched, the R_2 increases from 115 Ω to 540 Ω. Before the depressed semicircle, the charge transfer resistance is representative of the uncompensated resistance or the carbon current collector electrode in the high frequency region.[60] The light green dotted line is used to estimate the charge transfer resistance (R_1) of the current collector. After being stretched, the R_1 increases from 215 Ω to 2400 Ω. After the depressed semicircle, the charge transfer resistance is related to the electrochemical reaction in the low frequency region. This highly resistive behavior is commonly observed in the EIS when the spectrum is obtained at the voltage in which electrochemical reaction can occur.[61]

The above results have illustrated the attractive properties of the SIS elastomer as the binder for highly stretchable low-cost screen-printed batteries. As a triblock copolymer (ABA), SIS forms a phase separation of soft isoprene blocks that are physically crosslinked by nanoclusters glassy styrene blocks.[52, 62, 63] This self-assembled elastic network gives SIS superior elastic properties and the lack of a vulcanization step simplifies ink synthesis.[62,63] The vulcanization is a well-known process that crosslinks the polymers where entropy drives these materials to forcibly retract to their original shape after an applied deformation is removed.[48, 62, 63] In addition, the SIS demonstrated excellent adhesion to substrate, obviating the need for adding non-conductive surfactants commonly used to prevent delamination.[1, 47, 50] The strong adhesion of the ink can be attributed to the high tack quality of polyisoprene group of the SIS binder.[34,40]. Such ability for imparting stretchability has led to printable batteries that display high performance following multiple severe mechanical strains.

DIC has been shown useful to map the tensile strain for various stretchable electronic device composed of different materials and unique compositions. In Figure 5.2A-F, the strain mapping is different between printed traces based on three SP:SIS ratios because of these printed electrodes display a different mechanical behavior that is dependent upon the ratios of inelastic or elastic during the ink synthesis. The interfaces between the materials of different elasticities such as printed electrode and the PU substrate can also be mapped. At the interface, abrupt decrease in the strain is observed for all electrodes. This is because at the interfaces, the electrode is thickest. When squeeze moves the ink across the cavities of the stencil, most amount of ink is accumulated at the edges. Upon curing, the electrode is thickest at the edges. Because the edges are thicker than the core or outside of the edges, it is harder to displace these regions. In order to compensate for the low strain on the interfaces, the textiles and thin prints exhibit the higher strains.

The stress and conductivity vs. strain measurements provided additional material characterization about the SP:SIS composites. As shown, the 1:1 ratio as an individual film and unbound had poor mechanical resilience but had the highest initial conductivity. In comparison with our resistance measurements on the 1:1 ratio printed on Exoskin® demonstrated some durability as it behaved more as a stiff-island on a soft matrix. The 1:2 ratio exhibit a trade-off of durability and conductivity between the two extreme composite ratios. This optimal composite behavior is characteristic to the engineering of rigid, conductive fillers with elastic, polymers in developing highly stretchable inks catered to the specific application.

The voltage profiles of the first cycle show that the voltage plateau decreases after stretching (Figure 5.4A). The lower voltage plateau indicates that the polarization increased. However, the SEM images reveal that the cracks formed during stretching disappears upon the release (Figure 5.3). This discrepancy is likely due to the presence of electrolyte. Although the physical cracks may disappear, the electrolyte may soak in between the cracks and hinder the electrical pathway. Furthermore, the stretched electrode shows the highest areal capacity during the first cycle (Figure 5.4A). This is because the electrolyte has soaked the cracks and has significantly increased the active surface area. When the electrode is stretched, new surface area is exposed, and the electrolyte soaks the new surface. The stretched electrodes have the wider active surface area.

In the EIS results, both R_1 and R_2 increase upon stretching (Figure 5.4C and 5.4D). The degree of rise is significantly different from each other. The R_1 escalates by a factor of 11.2 whereas the R_2 grows by a factor of 4.70. The R_1 is contributed by stretching the carbon current collector electrode and R_2 is mostly contributed by the anode and cathode. While both the resistance values increase with respect to the stretching, the R_1 increases more significantly. This suggests that the deformations derive the impedance in electric connections more so than the electrodes. If the mechanical strain on the current collector layer can be alleviated, the electrochemical performance can be greatly enhanced. One of the buckling device configurations, a serpentine configuration or cable type of configuration can be employed to alleviate the mechanical strain.[1] Since these configurations have been widely known to reduce the mechanical strain, the electrochemical performance can be largely improved with intrinsically stretchable electrodes.[1]

5.1.4 Conclusions

In summary, we have demonstrated a successful fabrication and operation of a printable, highly stretchable rechargeable Zn-Ag_2O battery based on a hyperelastic SIS as a binder. All the components of the battery are printed using high-throughput and inexpensive screen printing. In order to obtain the maximum performance of stretchable electronics, systematic and vigorous mechanical studies utilizing DIC and SEM have been conducted. The rechargeable Zn-Ag battery has reversible capacity density of ~2.5 mAh cm^{-2} at 3 mA cm^{-2} discharge current density even after the repeated cycles of 100% stretching iterations. Such performance represents an intrinsically stretchable battery with the highest reversible capacity and discharge current density. The excellent resiliency against severe battery stretching is attributed to the superior elasticity of the SIS binder associated with its long polyisoprene chains with well-spaced, physically cross-linking styrene domains.[64] We also demonstrated for the first time the utility of DIC for localized strain analysis for stretchable electronics. Further optimization of the printed deterministic structures, new materials, and expansion of DIC in the printing design (like the implementation of deterministic structures or sandwich battery designs), have the potential to enhance further the electrochemical performance and the understanding of the mechanical properties of SIS-based batteries. More importantly, SIS has the potential to outperform previous printed, stretchable electronics and is expected to pave the way to enhance other forms of energy storage technologies, including Li-ion batteries, supercapacitors, and photovoltaics towards self-power stretchable electronics. These SIS-based printed devices would allow several degrees of freedom relevant to the wearer's movement and can be conformably utilized in diverse real-life situations.

Acknowledgements

Chapter 5 is based, in part, on the materials as it appears in in Advanced Energy Materials, 2017, by Rajan Kumar, Jaewook Shin, Lu Yin, Jung-Min You, Ying Shirley Meng, and Joseph Wang. The dissertation author is the primary author and inventor of the hyperelastic composite inks for printed, stretchable batteries. In addition, the primary author demonstrated the first analytical tool to measure strain stress analysis of composite devices, particularly for stretchable electronics.

5.2 References

1. Bandodkar, A.J., I. Jeerapan, J.-M. You, R. Nuñez-Flores, and J. Wang, *Highly Stretchable Fully-Printed CNT-Based Electrochemical Sensors and Biofuel Cells: Combining Intrinsic and Design-Induced Stretchability.* Nano Letters, 2016. **16**(1): p. 721-727.

2. Lee, H., T.K. Choi, Y.B. Lee, H.R. Cho, R. Ghaffari, L. Wang, H.J. Choi, T.D. Chung, N. Lu, T. Hyeon, S.H. Choi, and D.-H. Kim, *A graphene-based electrochemical device with thermoresponsive microneedles for diabetes monitoring and therapy.* Nat Nano, 2016. **11**(6): p. 566-572.

3. Cánovas, R., M. Parrilla, P. Mercier, F.J. Andrade, and J. Wang, *Balloon-Embedded Sensors Withstanding Extreme Multiaxial Stretching and Global Bending Mechanical Stress: Towards Environmental and Security Monitoring.* Advanced Materials Technologies, 2016. **1**(5): p. n/a-n/a.

4. Amjadi, M., K.-U. Kyung, I. Park, and M. Sitti, *Stretchable, Skin-Mountable, and Wearable Strain Sensors and Their Potential Applications: A Review.* Advanced Functional Materials, 2016. **26**(11): p. 1678-1698.

5. Bandodkar, A.J., I. Jeerapan, and J. Wang, *Wearable Chemical Sensors: Present Challenges and Future Prospects.* ACS Sensors, 2016. **1**(5): p. 464-482.

6. Lee, J., J. Wu, M. Shi, J. Yoon, S.-I. Park, M. Li, Z. Liu, Y. Huang, and J.A. Rogers, *Stretchable GaAs Photovoltaics with Designs That Enable High Areal Coverage.* Advanced Materials, 2011. **23**(8): p. 986-991.

7. Lipomi, D.J., B.C.K. Tee, M. Vosgueritchian, and Z. Bao, *Stretchable Organic Solar Cells.* Advanced Materials, 2011. **23**(15): p. 1771-1775.

8. Yokota, T., P. Zalar, M. Kaltenbrunner, H. Jinno, N. Matsuhisa, H. Kitanosako, Y. Tachibana, W. Yukita, M. Koizumi, and T. Someya, *Ultraflexible organic photonic skin.* Science Advances, 2016. **2**(4).

9. Liang, J., L. Li, X. Niu, Z. Yu, and Q. Pei, *Elastomeric polymer light-emitting devices and displays.* Nat Photon, 2013. **7**(10): p. 817-824.

10. Imani, S., A.J. Bandodkar, A.M.V. Mohan, R. Kumar, S. Yu, J. Wang, and P.P. Mercier, *A wearable chemical-electrophysiological hybrid biosensing system for real-time health and fitness monitoring.* Nat Commun, 2016. **7**.

11. Xu, L., S.R. Gutbrod, Y. Ma, A. Petrossians, Y. Liu, R.C. Webb, J.A. Fan, Z. Yang, R. Xu, J.J. Whalen, J.D. Weiland, Y. Huang, I.R. Efimov, and J.A. Rogers, *Materials and Fractal Designs for 3D Multifunctional Integumentary Membranes with Capabilities in Cardiac Electrotherapy.* Advanced Materials, 2015. **27**(10): p. 1731-1737.

12. Kim, J., I. Jeerapan, S. Imani, T.N. Cho, A. Bandodkar, S. Cinti, P.P. Mercier, and J. Wang, *Noninvasive Alcohol Monitoring Using a Wearable Tattoo-Based Iontophoretic-Biosensing System.* ACS Sensors, 2016.

13. Bandodkar, A.J., W. Jia, C. Yardımcı, X. Wang, J. Ramirez, and J. Wang, *Tattoo-Based Noninvasive Glucose Monitoring: A Proof-of-Concept Study.* Analytical Chemistry, 2015. **87**(1): p. 394-398.

14. Kassal, P., J. Kim, R. Kumar, W.R. de Araujo, I.M. Steinberg, M.D. Steinberg, and J. Wang, *Smart bandage with wireless connectivity for uric acid biosensing as an indicator of wound status.* Electrochemistry Communications, 2015. **56**: p. 6-10.

15. Huang, X., Y. Liu, H. Cheng, W.-J. Shin, J.A. Fan, Z. Liu, C.-J. Lu, G.-W. Kong, K. Chen, D. Patnaik, S.-H. Lee, S. Hage-Ali, Y. Huang, and J.A. Rogers, *Materials and Designs for Wireless Epidermal Sensors of Hydration and Strain.* Advanced Functional Materials, 2014. **24**(25): p. 3846-3854.

16. Son, D., J. Lee, S. Qiao, R. Ghaffari, J. Kim, J.E. Lee, C. Song, S.J. Kim, D.J. Lee, S.W. Jun, S. Yang, M. Park, J. Shin, K. Do, M. Lee, K. Kang, C.S. Hwang, N. Lu, T. Hyeon, and D.-H. Kim, *Multifunctional wearable devices for diagnosis and therapy of movement disorders.* Nat Nano, 2014. **9**(5): p. 397-404.

17. Wu, C., T.W. Kim, F. Li, and T. Guo, *Wearable Electricity Generators Fabricated Utilizing Transparent Electronic Textiles Based on Polyester/Ag Nanowires/Graphene Core–Shell Nanocomposites.* ACS Nano, 2016. **10**(7): p. 6449-6457.

18. Meng, Y., Y. Zhao, C. Hu, H. Cheng, Y. Hu, Z. Zhang, G. Shi, and L. Qu, *All-Graphene Core-Sheath Microfibers for All-Solid-State, Stretchable Fibriform Supercapacitors and Wearable Electronic Textiles.* Advanced Materials, 2013. **25**(16): p. 2326-2331.

19. Park, S.I., D.S. Brenner, G. Shin, C.D. Morgan, B.A. Copits, H.U. Chung, M.Y. Pullen, K.N. Noh, S. Davidson, S.J. Oh, J. Yoon, K.-I. Jang, V.K. Samineni, M. Norman, J.G. Grajales-Reyes, S.K. Vogt, S.S. Sundaram, K.M. Wilson, J.S. Ha, R. Xu, T. Pan, T.-i. Kim, Y. Huang, M.C. Montana, J.P. Golden, M.R. Bruchas, R.W. Gereau Iv, and J.A. Rogers, *Soft, stretchable, fully implantable miniaturized optoelectronic systems for wireless optogenetics.* Nat Biotech, 2015. **33**(12): p. 1280-1286.

20. Lu, N. and D.-H. Kim, *Flexible and Stretchable Electronics Paving the Way for Soft Robotics.* Soft Robotics, 2013. **1**(1): p. 53-62.

21. Lipomi, D.J., *Stretchable Figures of Merit in Deformable Electronics.* Advanced Materials, 2016. **28**(22): p. 4180-4183.

22. Kim, D.-H. and J.A. Rogers, *Stretchable Electronics: Materials Strategies and Devices.* Advanced Materials, 2008. **20**(24): p. 4887-4892.

23. Berchmans, S., A.J. Bandodkar, W. Jia, J. Ramirez, Y.S. Meng, and J. Wang, *An epidermal alkaline rechargeable Ag-Zn printable tattoo battery for wearable electronics.* Journal of Materials Chemistry A, 2014. **2**(38): p. 15788-15795.

24. Sousa, R.E., C.M. Costa, and S. Lanceros-Méndez, *Advances and Future Challenges in Printed Batteries.* ChemSusChem, 2015. **8**(21): p. 3539-3555.

25. Kaltenbrunner, M. and S. Bauer, *Power Supply, Generation, and Storage in Stretchable Electronics*, in *Stretchable Electronics*. 2012, Wiley-VCH Verlag GmbH & Co. KGaA. p. 287-303.

26. Song, Z.M., X. Wang, C. Lv, Y.H. An, M.B. Liang, T. Ma, D. He, Y.J. Zheng, S.Q. Huang, H.Y. Yu, and H.Q. Jiang, *Kirigami-based stretchable lithium-ion batteries.* Scientific Reports, 2015. **5**.

27. Jung, S., S. Hong, J. Kim, S. Lee, T. Hyeon, M. Lee, and D.H. Kim, *Wearable Fall Detector using Integrated Sensors and Energy Devices.* Scientific Reports, 2015. **5**.

28. Xu, S., Y.H. Zhang, J. Cho, J. Lee, X. Huang, L. Jia, J.A. Fan, Y.W. Su, J. Su, H.G. Zhang, H.Y. Cheng, B.W. Lu, C.J. Yu, C. Chuang, T.I. Kim, T. Song, K. Shigeta, S. Kang, C. Dagdeviren, I. Petrov, P.V. Braun, Y.G. Huang, U. Paik, and J.A. Rogers, *Stretchable batteries with self-similar serpentine interconnects and integrated wireless recharging systems.* Nature Communications, 2013. **4**.

29. Kwon, Y.H., S.W. Woo, H.R. Jung, H.K. Yu, K. Kim, B.H. Oh, S. Ahn, S.Y. Lee, S.W. Song, J. Cho, H.C. Shin, and J.Y. Kim, *Cable-Type Flexible Lithium Ion Battery Based on Hollow Multi-Helix Electrodes.* Advanced Materials, 2012. **24**(38): p. 5192-5197.

30. Zamarayeva, A.M., A.M. Gaikwad, I. Deckman, M. Wang, B. Khau, D.A. Steingart, and A.C. Arias, *Fabrication of a High-Performance Flexible Silver-Zinc Wire Battery.* Advanced Electronic Materials, 2016. **2**(5).

31. Gaikwad, A.M., A.M. Zamarayeva, J. Rousseau, H.W. Chu, I. Derin, and D.A. Steingart, *Highly Stretchable Alkaline Batteries Based on an Embedded Conductive Fabric.* Advanced Materials, 2012. **24**(37): p. 5071-5076.

32. Berchmans, S., A.J. Bandodkar, W.Z. Jia, J. Ramirez, Y.S. Meng, and J. Wang, *An epidermal alkaline rechargeable Ag-Zn printable tattoo battery for wearable electronics.* Journal of Materials Chemistry A, 2014. **2**(38): p. 15788-15795.

33. Yan, C.Y., X. Wang, M.Q. Cui, J.X. Wang, W.B. Kang, C.Y. Foo, and P.S. Lee, *Stretchable Silver-Zinc Batteries Based on Embedded Nanowire Elastic Conductors.* Advanced Energy Materials, 2014. **4**(5).

34. Kettlgruber, G., M. Kaltenbrunner, C.M. Siket, R. Moser, I.M. Graz, R. Schwodiauer, and S. Bauer, *Intrinsically stretchable and rechargeable batteries for*

self-powered stretchable electronics. Journal of Materials Chemistry A, 2013. **1**(18): p. 5505-5508.

35. Xu, S., Y. Zhang, J. Cho, J. Lee, X. Huang, L. Jia, J.A. Fan, Y. Su, J. Su, H. Zhang, H. Cheng, B. Lu, C. Yu, C. Chuang, T.-i. Kim, T. Song, K. Shigeta, S. Kang, C. Dagdeviren, I. Petrov, P.V. Braun, Y. Huang, U. Paik, and J.A. Rogers, *Stretchable batteries with self-similar serpentine interconnects and integrated wireless recharging systems.* Nat Commun, 2013. **4**: p. 1543.

36. Song, Z., X. Wang, C. Lv, Y. An, M. Liang, T. Ma, D. He, Y.-J. Zheng, S.-Q. Huang, H. Yu, and H. Jiang, *Kirigami-based stretchable lithium-ion batteries.* Scientific Reports, 2015. **5**: p. 10988.

37. O'Connor, T.F., S. Savagatrup, and D.J. Lipomi, *Soft Power: Stretchable and Ultra-Flexible Energy Sources for Wearable and Implantable Devices*, in *Stretchable Bioelectronics for Medical Devices and Systems*, A.J. Rogers, R. Ghaffari, and D.-H. Kim, Editors. 2016, Springer International Publishing: Cham. p. 69-82.

38. Dickey, M.D., *Liquid Metals for Soft and Stretchable Electronics*, in *Stretchable Bioelectronics for Medical Devices and Systems*, A.J. Rogers, R. Ghaffari, and D.-H. Kim, Editors. 2016, Springer International Publishing: Cham. p. 3-30.

39. Park, M., J. Park, and U. Jeong, *Design of conductive composite elastomers for stretchable electronics.* Nano Today, 2014. **9**(2): p. 244-260.

40. Gaikwad, A.M., G.L. Whiting, D.A. Steingart, and A.C. Arias, *Highly Flexible, Printed Alkaline Batteries Based on Mesh-Embedded Electrodes.* Advanced Materials, 2011. **23**(29): p. 3251-3255.

41. Fan, J.A., W.-H. Yeo, Y. Su, Y. Hattori, W. Lee, S.-Y. Jung, Y. Zhang, Z. Liu, H. Cheng, L. Falgout, M. Bajema, T. Coleman, D. Gregoire, R.J. Larsen, Y. Huang, and J.A. Rogers, *Fractal design concepts for stretchable electronics.* Nat Commun, 2014. **5**.

42. Yan, C., X. Wang, M. Cui, J. Wang, W. Kang, C.Y. Foo, and P.S. Lee, *Stretchable Silver-Zinc Batteries Based on Embedded Nanowire Elastic Conductors.* Advanced Energy Materials, 2014. **4**(5): p. n/a-n/a.

43. Kim, H., J. Yoon, G. Lee, S.-h. Paik, G. Choi, D. Kim, B.-M. Kim, G. Zi, and J.S. Ha, *Encapsulated, High-Performance, Stretchable Array of Stacked Planar Micro-Supercapacitors as Waterproof Wearable Energy Storage Devices.* ACS Applied Materials & Interfaces, 2016. **8**(25): p. 16016-16025.

44. Yang, S., Y.-C. Chen, L. Nicolini, P. Pasupathy, J. Sacks, B. Su, R. Yang, D. Sanchez, Y.-F. Chang, P. Wang, D. Schnyer, D. Neikirk, and N. Lu, *"Cut-and-Paste" Manufacture of Multiparametric Epidermal Sensor Systems.* Advanced Materials, 2015. **27**(41): p. 6423-6430.

45. *Thin Film and Printed Battery Market, Global Forecast & Analysis (2012-2017)*. 2012, Markets and Markets.

46. Braam, K. and V. Subramanian, *A Stencil Printed, High Energy Density Silver Oxide Battery Using a Novel Photopolymerizable Poly(acrylic acid) Separator.* Advanced Materials, 2015. **27**(4): p. 689-694.

47. Jayoung Kim, R.K., Amay Bandokar, Joseph Wang, *Advanced Materials for Printed Wearable Electrochemical Devices: A Review.* Advanced Electronic Materials, 2016.

48. Coran, A.Y., *Chapter 7 - Vulcanization*, in *The Science and Technology of Rubber (Fourth Edition)*. 2013, Academic Press: Boston. p. 337-381.

49. Matsuhisa, N., M. Kaltenbrunner, T. Yokota, H. Jinno, K. Kuribara, T. Sekitani, and T. Someya, *Printable elastic conductors with a high conductivity for electronic textile applications.* Nat Commun, 2015. **6**.

50. Bandodkar, A.J., R. Nuñez-Flores, W. Jia, and J. Wang, *All-Printed Stretchable Electrochemical Devices.* Advanced Materials, 2015. **27**(19): p. 3060-3065.

51. Hu, M., X. Cai, Q. Guo, B. Bian, T. Zhang, and J. Yang, *Direct Pen Writing of Adhesive Particle-Free Ultrahigh Silver Salt-Loaded Composite Ink for Stretchable Circuits.* ACS Nano, 2016. **10**(1): p. 396-404.

52. Stoyanov, H., M. Kollosche, S. Risse, R. Waché, and G. Kofod, *Soft Conductive Elastomer Materials for Stretchable Electronics and Voltage Controlled Artificial Muscles.* Advanced Materials, 2013. **25**(4): p. 578-583.

53. Robertson, G.L., *Food packaging: principles and practice*. 2016: CRC press.

54. Olabisi, O., L.M. Robeson, and M.T. Shaw, *Chapter 4 - Methods of Enhancing Miscibility*, in *Polymer–Polymer Miscibility*. 1979, Academic Press. p. 195-214.

55. Liu, D., L.-C. Chen, T.-J. Liu, T. Fan, E.-Y. Tsou, and C. Tiu, *An Effective Mixing for Lithium Ion Battery Slurries.* Advances in Chemical Engineering and Science, 2014. **4**(4): p. 14.

56. Suganuma, K., *Printing Technology*, in *Introduction to Printed Electronics*. 2014, Springer New York: New York, NY. p. 23-48.

57. Jaewook Shin, J.-M.Y., Jungwoo Z Lee, Rajan Kumar, Lu Yin, Joseph Wang and Ying Shirley Meng *Deposition of ZnO on Bismuth Species Towards Rechargeable Zn-Based Aqueous Battery.* Physical Chemistry Chemical Physics, 2016.

58. Hong, S., D. Sycks, H.F. Chan, S. Lin, G.P. Lopez, F. Guilak, K.W. Leong, and X. Zhao, *3D Printing of Highly Stretchable and Tough Hydrogels into Complex, Cellularized Structures.* Advanced Materials, 2015. **27**(27): p. 4035-4040.

59. Bing, P., Q. Kemao, X. Huimin, and A. Anand, *Two-dimensional digital image correlation for in-plane displacement and strain measurement: a review.* Measurement Science and Technology, 2009. **20**(6): p. 062001.

60. Zhuang, Q.C., S.D. Xu, X.Y. Qiu, Y.L. Cui, L.A. Fang, and S.G. Sun, *Diagnosis of Electrochemical Impedance Spectroscopy in Lithium Ion Batteries.* Progress in Chemistry, 2010. **22**(6): p. 1044-1057.

61. Shi, Y.L., M.F. Shen, S.D. Xu, X.Y. Qiu, L. Jiang, Y.H. Qiang, Q.C. Zhuang, and S.G. Sun, *Electrochemical Impedance Spectroscopic Study of the Electronic and Ionic Transport Properties of NiF2/C Composites.* International Journal of Electrochemical Science, 2011. **6**(8): p. 3399-3415.

62. Parthiban, A., *Synthesis and Applications of Copolymers*. 2014: John Wiley & Sons.

63. Grady, B.P., S.L. Cooper, and C.G. Robertson, *Chapter 13 - Thermoplastic Elastomers*, in *The Science and Technology of Rubber (Fourth Edition)*. 2013, Academic Press: Boston. p. 591-652.

64. Morton, M., *Rubber technology*. 2013: Springer Science & Business Media.

CHAPTER 6 INTEGRATION CHALLENGES OF PRINTED BATTERIES

6.1.1 Introduction

Nearly over a decade ago, the emergence of smartphones and its widespread adoption has ushered a new generation of connectivity and data generation [1-3]. All of these devices, combined with the emerging rise of Internet of Things, are going to rely on a ubiquity of devices that, if unchecked, their contribution to the global greenhouse gas emissions by 2040 will account for more than half of the relative contribution from the whole transporting sector [4]. As the world moves to cleaner energy sources, the need for better energy storage technologies for their devices and the grid are critical to continues progression of mankind [5]. In addition, the interruption of loss of connectivity due to poor energy storage can have drastic loss life on the battlefield, loss of data from patient monitoring, or connectivity during vital financial transactions. As a result, the research efforts in advanced materials and processes for energy storage such as supercapacitors and batteries during the past decade have followed the same trend as the devices, the power them [6]. Printed or more customizable batteries are seen as a promising solution to this energy crisis as it moves away from conventional battery with rigid form factors and assembly processes that are extremely slow and difficult to integrate [7].

The battery challenge is no more important than to the emerging field of wearables, where the battery component is typically the largest component of the device in both area, thickness, and most rigid. New approaches in battery materials and process have been approached, but understanding the critical challenges associated with the power requirements for these wearables, as their design, integration, and incorporating compatible materials are critically to progressing battery technology and the devices they power them [7]. In the first challenge is rooted in the foundation of how batteries are processed and coated for mass-assembly. Today, all batteries are traditionally printed by roll to roll coating of slurries or specifically particle-polymer composites, where the particles and polymers are mixed with appropriate proportions in solvent to build a composite film after printing and drying to remove the solvent. The particles are characteristic of electroactive behavior along with conductive or electrochemical additives depending on the chemistry. The polymer needing to be electrochemically stable is typically added to help bind the particles together and retain the printed, composite structure after being printed and cured. The concept of printing batteries is unique for the aspect to provide new custom shapes using the same concept of particle-polymer composites in an additive manufacturing compared to traditionally subtractive manufacturing.

The second challenge is the power requirements that are quite unique for wearable devices, where Bluetooth communication is likely to be the most common method for wireless communication for wearable devices. Near field communication (NFC) and bluetooth are methods to wireless communicate information from the wearable device to either a smartphone or wireless network. Although NFC is attractive approach for its low-power consumption and simplicity in fabrication, but it limited to smaller communication range of 0.2 meters compared to the long-range of >100 meters for bluetooth. Although this distance seems trivial in nature, it is fundamental to the use of wearables and how their users will implement them in their lives. Many of NFC-based wearables require the user to constantly bring a reader, usually imbedded in their phone, to continuously collect and track their data. Bluetooth provides hands-free communication that does not interrupt the user's daily lives and provides uninterrupted data collection, and the key reason why bluetooth communication will the primary form of wireless communication for over 90% of smart devices, especially wearable devices in the next decade [8]. The power requirements for bluetooth communication creates challenges for the battery, where it requires high current drain of equivalent to the capacity of the battery at 200 pulses for 3-5 ms. These pulses are initiated to transfer the information between devices, and long, low-current drains for 5-10 minutes for the operation of the device for data collection. This unique power profile requires the design of the battery with key parameter of low internal resistance, which is aggregate of the components of the battery such as the electrodes, electrolytes, and sealing.

The third challenge is the packaging and integration of batteries, with their new electronic components that transitioning to substrates and materials that are typically softer and fragile. For example, many of the traditional materials used for printed circuit boards with glass fiber reinforced epoxy resin and copper foil, which are both etched based on the circuit design. As technologies advances in getting smaller, the wearable devices can be become smaller, thinner, and flexible. This is enabled by new designs and materials such as polyimide or polyethylene terephthalate (PET) and their integration of the battery using thick and rigid connectors, can compromise the devices' entire conformability. The third challenge will need to be addressed with new materials and designs with the packaging considered, so the battery cannot only perform well during storage or in use, but the battery needs to facility scalable integration for ubiquity. The key aspect is hermetically sealing of the battery without compromising the conformability of the battery. The current process of battery packaging is commonly a thick, stainless steel coin cells or aluminum coated polyimide for li-polymer batteries, where they are trying to achieve a sealed environment of a low moisture vapor transmission rate (MVTR, 0.3 g/m2/24 hours) and a low oxygen transmission rate (2.0 cc/m2/24 hours) [9]. This challenge can be addressed by replacing these materials with softer materials, but the limitation resides in the drying process of the battery, which can be destructive and time consuming [7].

The last challenge is strategy for flexible batteries through advanced materials or leveraging new structural designs that can accommodate strain [10-12]. Most common approach has been the implementation of advanced composites using materials such as elastic polymers (silicone or polyurethane) and high aspect ratio, electrochemical fillers (ex. Silver nanowires, CNTs, graphene) for better composite behavior of the conformability and energy storage [6, 12] The use of high aspect ratio fillers is extremely attractive method for new complexity in design, but the synthesis of these particles are extremely limited for scale which can become cost-prohibitive. The use of elastic polymers with traditional electrochemical fillers is a one of the more favored approaches in the industry, because they could easily replace the traditional polymers without any change of the fabrication process. These batteries did have some conformal issues for extreme applications where 100% stretching of the device was required, but they would be sufficient enough for applications today where they only needed 10-15% for wearable applications and less than 30 degree of bendability [6]. Unfortunately, the elastomer inks are only able to maintain their elastic behavior if they underwent a crosslinking or commonly known as vulcanization step. This step or additive material was a critical limitation in the scalability for storage slurries made from this approach would need to be used immediately before the slurry solidifies from the crosslinking procedure [10]. Our previous work described in chapter 5 described the advantages of thermoplastic elastomers where the crosslinking matrix needed for elastic behavior could be reformed and destroyed using solvent or heat. This work showed impressive performance with our initial work with that retained the energy capacity even after stretching 100% through multiple cycles [10]. Similarly, this work had its own commercial limitations as the emerging materials such as paper, polyurethane, or polyethylene terephthalate that are being developed and discovered for flexible electronics are very fragile to hard solvents and temperatures. The development of a particle-polymer composite for batteries will require a polymeric system with desirable features of rheology for roll-to-roll coating, binding ability at low concentrations, non-destructive curing process, and crosslinking network to retain structure after multiple deformations.

This chapter presents the approaches to implement UV-curable materials instead of thermal curing to address the challenges above to build completely flexible batteries can be easily integrated to power flexible, thin electronics. In addition, this chapter describes potential improvements to electrolyte, packaging and additive manufacturing approach to transform the materials and processes for customized battery manufacturing. The use of ultraviolet (UV) curing process instead of thermal curing could streamline battery integration and provide desired final features of the completed device, without compromising manufacturing capability. UV curing, in which a photoreactive mixture is polymerized into a solid plastic within a short timeframe of seconds or minutes, is a process used in many industries, especially in coating and ink printing, to improve reliability, eliminate VOCs, reduce costs and tremendously increase production throughput [13]. Compared to thermal curing, the UV process is smaller, simpler, and can reduce manufacturing costs by up to 80% as the speed of coating and curing can increase to greater than 150 feet/min as demonstrated by previous researchers [13]. This is in comparison to the 67 feet/min seen in to traditional curing of 67 feet/min, as demonstrated by our strategic partner [13]. Studies have shown that the removal of VOCs in the battery manufacturing process would lead to a dramatic decrease in drying costs from $54.7/kWh to $2.09/kWh and eliminate the capital investment of more than $5 million needed to store, handle, and dispose of these toxic chemicals [14]. There have been some demonstrations of UV curable batteries as simpler drying process, but many of these demonstrations have not studied the benefits of manufacturing, integration, and custom design over traditional battery manufacturing, especially application for wearable devices where their power requirements are more complex [15, 16].

In this work, we demonstrate a UV-curable, zinc-silver oxide battery that is compatible with soft packaging materials and solid-state electrolyte with high ionic conductivity for alkaline electrolytes. Our preliminary research began displacing SIS polymer with a UV-curable polymer called poly (vinyl alcohol), N-methyl-4(4'-formylstryl) pyridinium methosulfate acetal (PVA-SbQ) commonly used in UV-curable, photoemulsion for imprinting custom designs in screen-printing stencils. While typical UV-curable formulations consist of oligomers, monomers, and photo initiators, the PVA-SbQ has a unique crosslinking reaction where it can self-dimerize upon UV exposure. As this polymer contained a PVA backbone, it would present favorable conditions under alkaline conditions where PVA is known to form gel structures with aqueous solutions. The introduction of PVA-SbQ with our previous anode and cathode, electrochemical powders, we were able to develop UV-curable compositions with a low polymer concentration of less than 5%. This formulation was easily printable and capable of demonstrating a high energy density of >300 mAh/cm^3.

The UV-curable compositions are simultaneously being studied with a solid-state electrolyte using polybenzimidazole (PBI), which is common electrolyte for alkaline fuel cell membrane for its stability under alkaline electrolytes and high temperatures without compromising ionic conductivity over >10 mS/cm [17, 18]. PBI is an excellent alkaline electrolyte because of its high affinity for hydroxide absorption due to the pyridine-type nitrogen (–N=) and pyrrole-type nitrogen (–NH–) in the benzimidazole rings allow absorption and interaction with the free inorganic base (i.e., KOH), contributing to the high ionic conductivity. The individual changes in the battery components are key to building a flexible battery that can be compatible with the flexible materials and simplify the integration process.

6.1.2 Experimental Section

Chemicals and Reagents:

Super-P® Conductive Carbon Black (SP), poly(vinyl alcohol), N-methyl-4(4'-formylstryl) pyridinium methosulfate acetal (PVA-SbQ), Deionized water, Zn powder (Alfa Aesar), Ag_2O powder (Alfa Aesar), Bi_2O_3 (Alfa Aesar). Cellulose separator (FS2214 – Freudenberg), Polybenzimidazole film (PBI Products), PBI solution in dimethylacetamide (PBI Products), polyvinyl alcohol (>133K MW, Polymer Sciences), dimethyl sulfoxide (DMSO), KOH, LiOH, were purchased from Sigma Aldrich.

Solid-State, Alkaline Electrolyte:

The development of a solid-state electrolyte stable in alkaline conditions was studied by comparing the ionic conductivity of commercial cellulose separators that are commonly used in zinc batteries by soaking in alkaline electrolyte and compared with 55 micron thick PBI film from PBI products, and synthesizing a new composition of PBI/PVA composite film through solution mixing of PBI and PVA in compatible solvents. All of the electrolyte films were tested using 6M KOH electrolyte in deionized water.

The commercial cellulose films and PBI films were cut into 19 cm diameter circles and soaked in 6M KOH electrolyte for 1-3 days. The composite electrolyte of the PBI/PVA was composed by making a composite solution of 8:1 of PVA to PBI where PBI polymer is 8-10% concentration dissolved in dimethylacetamide (DMac) solvent to solubilize the polymer. The PVA is equally dissolved in DMSO solution with 5-10% concentration, where ethanol is miscible with DMac and the appropriate viscosity to make a castable film using a doctor blade with controlled thickness on glass slides. The 8:1 ratio has shown to have optimal performance and made by mixing 8 grams of 5% PVA in DMSO with 1 gram of 10% PBI in DMac at 80 degrees Celsius and mixed at 500 rpm for 80 minutes. The film was then cured at room temperature for 24 hours in vacuum to remove the excess solvent and leave a solid film. The films were difficult to remove after curing and therefore exposure to open air, which allowed the film to be cut and delaminated from the glass slides, where they were punched into 19 cm diameter circles for ionic conductivity testing, with comparison to commercial films of cellulose film.

Electrochemical Impedance Testing for Ionic Conductivity:

Through plane ionic conductivity of the membranes was measured using a cell composed of two stainless steel plates and with acrylic structures to maintain consistent pressure. The membrane was sandwiched between two stainless steel electrodes of known area (1.13 cm^2). A potentiostat with electrochemical impedance analyzer from Biologic SP200 was used to conduct the impedance measurements of KOH-soaked or doped electrolyte films. The applied direct current, voltage bias was 0 V, and 10 mV rms. Data collected were in the range from 10^6 to 1 Hz. Membrane resistance was calculated from the intercept on the real axis of the Nyquist plot [18]. The ionic conductivity (σ) was product calculation of *film* thickness, measured using a micro capiler, and the area between the electrodes and the membrane resistance measured from the EIS testing. The measurements were conducted at room temperature without any additional humidification control or temperature control.

UV-Curable Anode and Cathode

The anode and cathode were synthesized with their respective powder composites mixed with resin of 11-13% PVA-SbQ in water solution. The additional water was added to improve the viscosity for the coating procedure. The zinc anode was composed of 87% zinc powder, 5% zinc oxide to improve electrochemical stability, 3% bismuth additive to improve electrical conductivity, and 5% PVA-SbQ with additional water for viscosity and is removed after the curing process under a UV lamp (FE300, Phoseon) for 10 minutes. The zinc anode ink is then coated at 300 microns onto a 0.010 mm copper film. The silver oxide cathode is composed of 90% silver (II) oxide, 5% carbon black, and 5% PVA-SbQ with additional water for viscosity. The cathode ink was then coated at 300 microns on

0.025 mm nickel film and UV cured for the same time. The final thickness of the anode and cathode after curing was measured using a caliper, for consistency evaluations.

Battery Assembly and Testing

After curing the anode and cathode films, they were die-cut in 15 mm diameter circles where they assembled in CR2032 coin cells. The zinc anode and silver oxide cathode were separated using two 19 mm diameter cellulose separator and one cellophane film on the cathode. An additional cone spring and spacer made of stainless steel were inserted on the cathode side and sandwiched between a top and bottom gasket of the coin cells. All of the coin cells were compressed or sealed using a battery compressor at 1600 psi. The batteries were calculated to have a theoretical capacity of 7-10 mAh, and the batteries were discharged at constant current drain of 160 uA and a cut-off voltage of 1.2 V using a LANDH battery analyzer.

6.1.3 Results and Discussion

The ionic conductivity of the solid-state electrolytes was measured using electrochemical impedance. The advantages for a solid-state electrolyte are the simplification of the fabrication and sealing of flexible batteries, but it cannot compromise ionic conductivity especially for the Bluetooth pulsing requirements. In Table 6.1, the respective ionic conductivities for each film are compared under the same alkaline electrolyte, 6M KOH. The commercial PBI showed significant doping of KOH as the film's thickness expanded from 55 microns to 93 microns after soaking in KOH and dried. The film demonstrated a high ionic conductivity after soaking with KOH of 28 mS/cm. After the soaking procedure it was observed that the PBI film became significantly brittle and rigid when compared with the unsoaked PBI film. The cellulose separator, which is an extremely porous film where the KOH solution is absorbed, demonstrated the highest ionic conductivity of 55 mS/cm.

Table 6.1: Ionic Conductivity of Solid-State Electrolyte Film using Commercial Cellulose, Commercial PBI, and PVA:PBI Composite.

Description of Electrolyte Film	Initial Thickness	Final Thickness	Ionic Conductivity (mS/cm)
Commercial PBI	55 microns	93 microns	28.3
Commercial Cellulose	96 microns	96 microns	55
8:1 PBI:PVA Film	40 microns	45 microns	15

The composite film of PBI:PVA demonstrated a unique composition with a stable film with a ionic conductivity of 15 mS/cm and improved flexibility compared to the commercial PBI after KOH soaking.

The EIS testing of PBI film presented a promising solid-state electrolyte film for alkaline batteries with high ionic conductivity of over 10 mS/cm. Unfortunately, they are still many challenges for its implementation for flexible batteries over traditional liquid-based electrolytes using alkaline-soaked, cellulose separators. The commercial PBI films composed of entirely of PBI became extremely brittle or noticeable blistered after soaking in 6M KOH alkaline electrolytes. The incorporation of PVA with PBI was designed to improve ionic conductivity and durability of the electrolyte film because of PVA's hydrophilic nature and durability, which has shown to have ionic conductivity of greater 70 mS/cm and nearly 6x improved elongation compared to PBI only films [17]. Although the initial results are encouraging, the customizable design of the PVA/PBI electrolyte film in terms of the composition, thickness, additional additives that be incorporated for optimal battery performance. Incomplete sentence

The UV-curable electrodes for the anode and cathode were assembled and demonstrated specific energy density of over 300 mAh/cm^3 as shown in Figure 6.1.

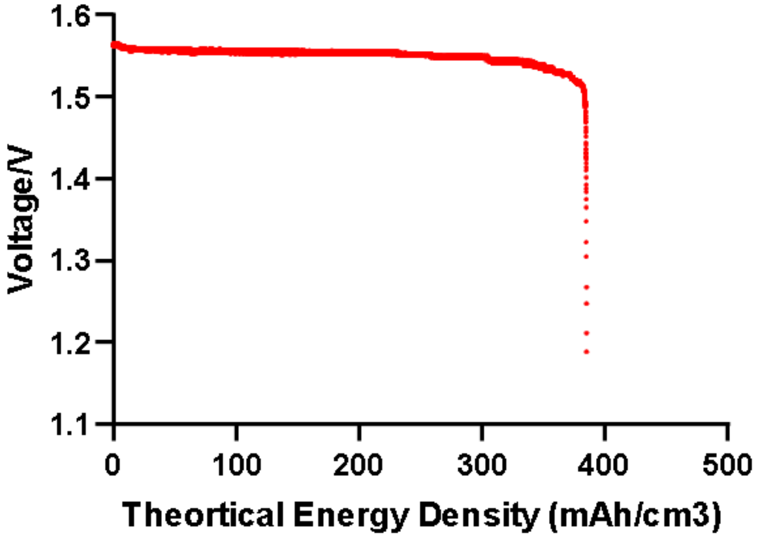

Figure 6.1: The discharge curve for UV-curable, zinc-silver oxide battery

The energy density was calculated based on the actual capacity of the battery device divided by the area and thickness of the cathode. This battery using a PVA-SbQ polymer demonstrated an open circuit voltage of 1.5V and maintains a stable voltage for the majority of the discharge curve, which is characteristic of the zinc-silver oxide chemistry. Although the performance is quite characteristic, there were considerable challenges on the consistency of the battery performance where half of the batteries synthesized in batch, immediately failed. Through further analysis of PVA-SbQ film under alkaline conditions without any electroactive powders, we noticed the film becomes extremely brittle and color changes from immediately clear to pitch black. Prior work with PVA and SbQ have hydroxide groups along its backbone, which forms a strong leaving group under strong basic conditions, which can attribute to additional crosslinking during the UV curing process. This extreme crosslinking would cause the film to become extremely brittle and opaque, which could be attributed to half of the battery failure. Additional material characterizations will need to be implemented to confirm this observation that PVA-SbQ polymer is not stable in alkaline electrolytes, and therefore not suitable for its practically application. More importantly, the formulation of UV-curable electrodes provides many packaging advantages as the curing process could be conducted at room temperature.

6.1.4 Conclusions

In summary, this chapter introduces the challenges and testing that is needed to provide a sufficient assessment of the power source for wearable devices. This chapter presents some preliminary work on high-performance, solid-state electrolyte and non-destructive curable electronics with high density, zinc-silver oxide battery with an energy density of 300 mAh/cm^3. The progression of these components is critical to combining into a high-performance, flexible battery that is easy to fabricate with softer, flexible materials and integrate them with flexible electronics. The solid-state electrolyte using PBI polymer has demonstrated high stability with alkaline electrolytes with high ionic conductivity with an excess of 10 mS/cm. Although there needs to be considerable improvement in its film synthesis and doping of KOH electrolyte, this film opens a lot of customizable and more complex, composite designs with different additives such as ZnO or Ca particles to improve battery performance [19].

In addition, preliminary work is conducted on developing a UV-curable battery to implement drying processes that are faster and non-destructive with softer packaging solutions. Both the electrolyte and the battery need to be tested with further electrochemical testing and form-factors, where they could have potential impact on each other. For example, the different shape batteries in XY-plane such as L-shape, serpentine-shape, or batteries with holes through the center can have dramatic factors on the energy and power density of the battery. This same factor can be applied to the Z-plane, where thickness of each component of the battery such as the anode, cathode, electrolyte, and current collector contribute to the internal resistance of the battery. All of these factors will need to be tested under real-time power drain for Bluetooth communication, where the high pulsing can cause significant damage to the battery's overall energy density. These parameters for the battery design will bring new understand and challenges associated with batteries specific for wearables. As the majority of battery research has been focused on innovating new materials, these additional parameters will provide new implications and directions of battery materials, assembly, and integration.

Essentially, these studies will assist in the development complex heterogeneity, multi-layer batteries of different composites, and improve energy capacity, power density, and cycle life which we only possible using expensive, slow chemical deposition technologies [20]. Semiconductor tools, such as chemical deposition and ultraviolet lithography, have been well-established for complex multilayers, allowing the microchip industry (2-10 mm^2 per computer chip processing, Intel Core i7) to double performance every year for nearly 60 years. However, these tools are not scalable for the battery industry, where the battery footprint needs to be nearly 3000% (>300 mm^2 per device) greater and capable of similar quantity for devices projected for Internet of Things [21]. The cost is prohibitive compared to traditional battery process. By utilizing particle-polymer composites that are compatible with additive manufacturing and UV curing, this level of multi-layer, heterogeneous batteries can become scalable and affordable.

The proposed combination of UV curable electrodes and additive manufacturing will present an innovative manufacturing solution of flexible batteries for flexible, wearable electronics where customization for improving form-factor and ubiquity are essential. This innovation will have great impact in the performance of the battery as new design in 2D and 3D architectures will enable in more complex battery design that can vary depending application requirements.

Acknowledgements

Chapter 6, in part is currently being prepared for submission for publication of the material, by Rajan Kumar and Todd Coleman. The dissertation author is the primary investigator and author of this material.

6.2 References

1. Kim, J., R. Kumar, A.J. Bandodkar, and J. Wang, *Advanced Materials for Printed Wearable Electrochemical Devices: A Review.* Advanced Electronic Materials, 2017. **3**(1): p. 1600260.

2. Heo, J.S., J. Eom, Y.-H. Kim, and S.K. Park, *Recent Progress of Textile-Based Wearable Electronics: A Comprehensive Review of Materials, Devices, and Applications.* Small, 2018. **14**(3): p. 1703034.

3. Chen, X., J.A. Rogers, S.P. Lacour, W. Hu, and D.-H. Kim, *Materials chemistry in flexible electronics.* Chemical Society Reviews, 2019. **48**(6): p. 1431-1433.

4. Belkhir, L. and A. Elmeligi, *Assessing ICT global emissions footprint: Trends to 2040 & recommendations.* Journal of Cleaner Production, 2018. **177**: p. 448-463.

5. Liu, W., M.S. Song, B. Kong, and Y. Cui, *Flexible and Stretchable Energy Storage: Recent Advances and Future Perspectives.* Advanced Materials, 2016. **29**(1).

6. Song, W.-J., S. Yoo, G. Song, S. Lee, M. Kong, J. Rim, U. Jeong, and S. Park, *Recent Progress in Stretchable Batteries for Wearable Electronics.* Batteries & Supercaps, 2019. **2**(3): p. 181-199.

7. Choi, K.-H., D.B. Ahn, and S.-Y. Lee, *Current Status and Challenges in Printed Batteries: Toward Form Factor-Free, Monolithic Integrated Power Sources.* ACS Energy Letters, 2018. **3**(1): p. 220-236.

8. Columbus, L., *IoT Market Predicted To Double By 2021, Reaching $520B*, Forbes, Editor. 2018.

9. Jansen, A.N., K. Amine, A.E. Newman, D.R. Vissers, and G.L. Henriksen, *Low-cost, flexible battery packaging materials.* JOM, 2002. **54**(3): p. 29-32.

10. Kumar, R., J. Shin, L. Yin, J.-M. You, Y.S. Meng, and J. Wang, *All-Printed, Stretchable Zn-Ag2O Rechargeable Battery via Hyperelastic Binder for Self-Powering Wearable Electronics.* Advanced Energy Materials, 2017. **7**(8): p. 1602096.

11. Xu, S., Y. Zhang, J. Cho, J. Lee, X. Huang, L. Jia, J.A. Fan, Y. Su, J. Su, H. Zhang, H. Cheng, B. Lu, C. Yu, C. Chuang, T.-i. Kim, T. Song, K. Shigeta, S. Kang, C. Dagdeviren, I. Petrov, P.V. Braun, Y. Huang, U. Paik, and J.A. Rogers, *Stretchable batteries with self-similar serpentine interconnects and integrated wireless recharging systems.* Nature Communications, 2013. **4**: p. 1543.

12. Yan, C., X. Wang, M. Cui, J. Wang, W. Kang, C.Y. Foo, and P.S. Lee, *Stretchable Silver-Zinc Batteries Based on Embedded Nanowire Elastic Conductors.* Advanced Energy Materials, 2014. **4**(5): p. 1301396.

13. Arnold, J.R., G. Voelker, and A. Shariaty, *UV Coating Processes to Enhance Li Ion Battery Performance and Reduce Costs.* ECS Transactions, 2017. **80**(10): p. 397-416.

14. Wood, D.L., J.D. Quass, J. Li, S. Ahmed, D. Ventola, and C. Daniel, *Technical and economic analysis of solvent-based lithium-ion electrode drying with water and NMP.* Drying Technology, 2018. **36**(2): p. 234-244.

15. Kim, S.-H., K.-H. Choi, S.-J. Cho, J. Yoo, S.-S. Lee, and S.-Y. Lee, *Flexible/shape-versatile, bipolar all-solid-state lithium-ion batteries prepared by multistage printing.* Energy & Environmental Science, 2018. **11**(2): p. 321-330.

16. Ha, H.-J., E.-H. Kil, Y.H. Kwon, J.Y. Kim, C.K. Lee, and S.-Y. Lee, *UV-curable semi-interpenetrating polymer network-integrated, highly bendable plastic crystal composite electrolytes for shape-conformable all-solid-state lithium ion batteries.* Energy & Environmental Science, 2012. **5**(4): p. 6491-6499.

17. Merle, G., M. Wessling, and K. Nijmeijer, *Anion exchange membranes for alkaline fuel cells: A review.* Journal of Membrane Science, 2011. **377**(1): p. 1-35.

18. Herranz, D., R. Escudero-Cid, M. Montiel, C. Palacio, E. Fatás, and P. Ocón, *Poly (vinyl alcohol) and poly (benzimidazole) blend membranes for high performance alkaline direct ethanol fuel cells.* Renewable Energy, 2018. **127**: p. 883-895.

19. Huang, J., G.G. Yadav, J.W. Gallaway, X. Wei, M. Nyce, and S. Banerjee, *A calcium hydroxide interlayer as a selective separator for rechargeable alkaline Zn/MnO2 batteries.* Electrochemistry Communications, 2017. **81**: p. 136-140.

20. Haro, M., V. Singh, S. Steinhauer, E. Toulkeridou, P. Grammatikopoulos, and M. Sowwan, *Nanoscale Heterogeneity of Multilayered Si Anodes with Embedded Nanoparticle Scaffolds for Li-Ion Batteries.* Advanced Science, 2017. **4**(10): p. 1700180.

21. Cortland, R. *Intel Now Packs 100 Million Transistors in Each Square Millimeter*. 2017.

CHAPTER 7 CONCLUSIONS AND FUTURE RECOMMENDATIONS

This dissertation attempts to solve both technical and feasibility challenges associated with particle-polymer composites to enable a new generation of technologies that need new form-factors and functionality. Through this research, many first demonstrations were accomplished, such as the first printable self-propelling motor to the first all-printed, stretchable battery with very high capacity and durability. Such demonstrations will highlight how the composite behavior and the judicious formulation of functional polymers and particles can yield to a vast array of devices across multiple fields of technology.

The first chapter of this dissertation describes the initial concepts for particle-polymer composites, particularly the conditions for implementing these composite formulations in additive manufacturing for building our certain devices with customization and ubiquity. There is a particular balance between the polymer and functional particles, in which the ratio is carefully designed to make sure not one element is too high in concentration that it dominates. For example, in the formulation of conductive, stretchable composites, it will typically consist of conductive fillers, such as silver flakes and elastic polymers, to impact the stretchable behavior, although not the conductivity. In many applications, especially wearables or epidermal electronics, the skin will typically stretch less than 20%. Since this application will require less stretchability, the ratio between the conductive fillers to stretchable polymer may be extremely high. These composites can be designed with the application in mind by enabling new freedoms of design in both materials and deterministic design for technological advancement. The first chapter details the foundations for the compositions and additive manufacturing that was applied to the following chapters for and their respective polymer-particle composites.

Chapter 2 presents the first demonstration of functional swimmers that could be mass produced in a variety of custom shapes and design using screen-printing. This work was possible because of the development of particle-polymer inks that had composite behavior of being catalytic and flexible. Much of the preliminary work began on designing the key architecture for enabling propulsion on the millimeter scale, which is on a greater scale length compared to their more common propulsion techniques used by nanoscale motors. This design was then modified using a chitosan polymer that was an aqueous insoluble ink but could still form a soluble gel to let the reactant-containing solution of hydrogen peroxide to react with the platinum black and platinum carbon catalytic powder mix. The resulting motor was capable of demonstrating a speed of 175 mm/s or 20 body lengths per second, which was far greater distance compared to nanomotors. In addition, this chapter describes new designs and functionality such as a magnetic head for control or a carbon black head for the removal of industrial pollutants such as methylene blue. This initial work demonstrates the potential to expand the application of self-propelling motors to new applications that demand large area coverage such as environmental remediation.

In Chapter 3, the previous foundations were applied to the emerging field of thermoelectrics. Thermoelectrics present alternative energy harvesting technology over solar, especially for wearables, where it can actively convert heat loss from the body into productive energy to power or storage energy for devices. One of challenges of these devices is that traditional fabrication approaches are often time-consuming and yield very rigid devices. The formulation of thermoelectrics was described using key polymers for the printing and sintering process to yield, printed thermoelectric devices with a high thermoelectric efficiency or ZT of 0.65 and 0.81 for p-type and n-type, respectively. This work could be a foundation for thermoelectric inks and flexible thermoelectric devices that could be combined with advanced materials, to further improve the thermoelectric efficiency and form factors for thermoelectric devices.

In Chapter 4, a hybrid of designs and materials for stretchable electronics were designed for wearables and energy harvesting concepts. In many stretchable electronics, these devices have been made stretchable through design of typically rigid materials by making them extremely thin and using serpentine configurations. Although these devises impart better reliability and performance compared to elastic composites, they have very limited material options. In this demonstration, we combine both composite, functional inks and stretchable designs with additive printing to produce the first hybrid, stretchable electronics. These devices demonstrated the same durability characteristic of serpentine devices while capable of electrochemical sensing of various analytes even during different deformations such as bending, bi-axial twisting, and torsional twisting.

As many group and companies are proceeding to develop novel, conformal electronics, there has been very few solutions for the power source. As these devices becomes flexible, stretchable, and ubiquitous they will need a portable, power source to do the same. In Chapter 5, a novel formulation for printed stretchable, electroactive inks was developed and implemented to design the first, printed, stretchable battery with a high area energy density of 2.5 mAh/cm^2 even after numerous deformations. In addition, a new optical technique, called digital image correlation, was developed to analyze and differentiate deformations in elastic-conductive composites, that was first demonstrated in this work and highlights its potential use for further studies for stretchable electronics.

In Chapter 6, the discussion continued on the challenges associated with developing printed power sources and other challenges that need to be overcome in order to enable monolithic integration of flexible batteries to develop truly flexible batteries. This chapter describes the development of a solid-state electrolyte that has improved form-factor and ionic conductivity compared to alkaline gel electrolytes used in the previous work. In addition, it describes the challenge with sealing and mounting these flexible batteries on to wearable devices.

In Appendix A1, the demonstration of foldable electronics using similar polymer-particle composites adapted from the catalytic motors to demonstrate how printed electronics design in 2D could translate from 2D and 3D with time or applied strain. These devices created interesting functionalities for structural electronics or logic-based electronics that are responsive to an external stimulus. In Appendix A2, the introduction of electrochemical additives, such as bismuth oxide and zinc oxide, were studied and used to improve the rechargeability of printed, zinc batteries from a 10 unstable charging cycles to over 50 cycles with the same area energy density of 1 mAh/cm^2. Lastly, the combination of additive manufacturing and stretchable conductive inks were used to demonstrate micrometer scale, stretchable electronics that merged both materials and design for multiple degrees in stretchable design, as shown in Appendix A3. This work demonstrated one of the unique designs of serpentine arrays using elastic, conductive inks which could have conformal design to the micron-scale morphology of skin. These devices would also be built for multiple energy harvesting and storages as a zinc-based battery or biofuel cell.

The field of polymer-particle composites for the development of the next-generation of devices using additive manufacturing is presenting new opportunities, but also challenges to address. This new science of formulating composites is extremely multi-disciplinary as it requires detail study of technologies' fundamentals, legacy fabrication systems, and implications of their use. This study is critical to understanding how to design these composite materials to improve or even replace existing technologies. As these technologies continue to progress, there are fundamental limits to which these novel composites can actually compete with traditional technologies. For example, additive manufacturing is only capable of demonstrating resolutions on the micron-scale and therefore cannot compete with the lithographic and chemical vapor deposition techniques that have <7 nm scale resolution, which has empowered Moore's law to such amazing feats. These composites are going to have their greatest impact in the next two decades in the fields of large-area electronics, especially power harvesting and energy storage, where additive manufacturing can support the ubiquity and these composites can enable new form-factors for these components of the device. All of this shows in the next twenty decades of emerging flexible or stretchable electronics will be defined by hybrid-composite electronics, where traditional microchips will be mounted onto stretchable, conductive circuits and powered by energy storage composites. This new emergence of composite electronics from the integration of multiple technologies, fabrication processes from multiple techniques for manipulating materials, and designing for the application in mind is key to the success of this next generation of electronics.

These devices will have the potential to connect and sense the world around us in so many ways beyond our imagination. It will take a team of multidisciplinary scientist, engineers, and passionate users of the devices to make the possible and open a new door of electronic design and use for today and tomorrow.

Appendix

A1: Foldable, Printed Electronics

A1.1.1 Introduction

Several generations of evolution have created three-dimensional (3D) natural structures with intermediate size and complexity (i.e. mesostructures) and wide array of functionalities. Nature has numerous examples of complex 3D mesostructures, such as macroscale honeycomb structures that maximize space utilization and stability in beehives, or microscale tree-like structures in Morpho butterflies that induce structural coloration [1-5]. Bioinspired engineered synthetic 3D structures are revolutionizing a broad spectrum of disciplines, such as electrochemistry, biomedical science, photonics, solar cells, epidermal electronics, or microactuators, that were previously limited to 2D planar designs [6-28]. Unfortunately, the practical utility of these 3D structures is currently constrained by additive manufacturing which has limited throughput, narrow choice of material, and high costs [24,28].

Digital additive manufacturing, commonly known as 3D printing, utilizes computer aided design (CAD) software to divide a 3D structure into thin cross sections and fabricate the structure layer-by-layer [29]. This 3D fabrication route relies mainly on metal powders or polymeric materials that are deposited then cooled, crosslinked, or sintered to create the desired 3D structure [24, 29]. While these approaches are very successful for expedited prototyping, the resulting printed 3D structures are typically constrained to non-functional materials and have limited functionality, based primarily on their geometrical shape.[24] Recent efforts have led to kirigami-inspired fabrication process that uses existing semiconductor fabrication to design 2D patterns of electronic materials that can morph into complex 3D structures by stress-induced buckling.[24,27,28,30] This approach uses lithography to fabricate silicon planar designs with selective sites for bonding.[24,27,28] Once this planar design is transferred onto a strained elastomer substrate, with selective bonding, the relaxation of the substrate will induce strain in unbounded locations of the design, thus converting a 2D planar design into a 3D mesostructured [24, 27, 28 31-33]. The planar device will bend from its 2D precursor into a diverse library of complex 3D constructs (*e.g.* baskets, cuboid cages, starbursts, cars, or flowers) [24]. While such photolithographic fabrication of 3D structures is scalable for microstructures and suitable for a high-performance electronic material, this approach is relatively expensive, requires rigorous operating environment and usually involves complex procedures [34]. Other methods, such as laser cutting or mechanical dicing, can be good for prototyping, but are relatively low-throughput for large scale manufacturing. Many disciplines rely on a variety of materials or composites, such as nanomaterials, smart polymers, alloys, carbonaceous, biomaterials, composites, or temperature-sensitive dyes [13, 14, 35-48].The assimilation of these diverse materials and composites is essential to the widespread use and progression of 3D mesostructures.

A1.1.2 Experimental Section

Ag-SIS Ink Formulation: A resin of 4 g/mL polystyrene-*block*-polyisoprene-*block*-polystyrene (Aldrich, styrene 14 wt%) in toluene is prepared. Stretchable, conductive ink is formulated by mixing silver flake (Aldrich~10 μm) is mixed with SIS resin in a 7:15 ratio by weight in a dual asymmetric centrifugal mixer (Flacktek Speedmixer, DAC 150.1 KV-K) at 1800 rpm for 5 minutes.

Water soluble sacrificial ink formulation: The sacrificial layer ink is based on Pullulan, a naturally occurring, fungal polysaccharide that is commonly used as food preservative. It is optimized for purpose of screen printing for the selective bonding method. The water-soluble sacrificial layer ink is composed of a 2:2:5 by weight mixture of Pullulan, Sucrose and water.

Temperature sensitive inks formulation: Inks were prepared using Fast Blue and Vermillion Red, adhesive binder, acrylic paint and water. The color before and after the temperature change can be designed using different ratios of temperature sensitive dyes with different color of acrylic paint. Dyes, acrylic paint, adhesive binder and water were mixed in a dual asymmetric centrifugal mixer for at 3000 rpm for 5 minutes.

A1.1.3 Results and Discussion

Here, we introduce a thick-film screen-printing fabrication technique that is high-throughput, low-cost, that can be used to produce diverse highly-tunable buckled 3D structures with free-standing segments composed of different materials, shapes and sizes. The novelty of the new approach hinges on the formulation and dimensions of the sacrificial layer that can be tailored to control which specific segments of the 2D precursor be bound, unbound, or free-stand (Figure A1.1).

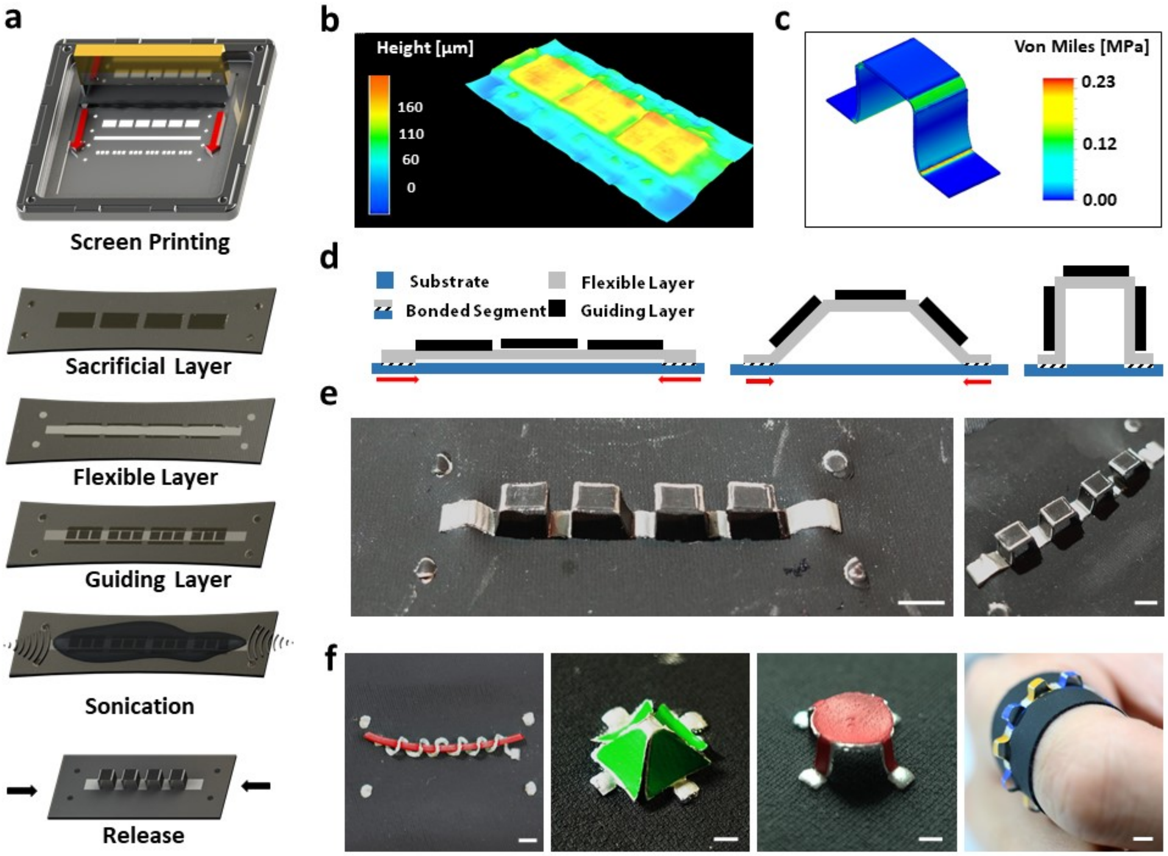

Figure A1.1: Fabrication process, analysis and demonstration of all printed 3D structures. (a) The fabrication process for the all-printed 3D structures: sacrificial layer, flexible layer and guiding layer screen printing, sacrificial layer dissolution and substrate relaxation. (b) 3D optical image profiling of a segment of the square-shape 2D precursor for thickness measurement of sacrificial layer, flexible layer and guiding layer. (c) Buckling FEA of a square-shaped segment. (d) Illustration of the buckling process. (e) Images of 3D structure from different angles. (f) Various printed 3-D structures that are coil-, pyramid-, table- and square-shaped based on different guiding layer materials. Scale bar, 2.5 mm.

The folding process towards the targeted 3D configurations can predicted by controlling the printing of the different layers. A myriad of ink compositions can thus be formulated and printed onto pre-stretched substrates in few simple and automated steps after printing the sacrificial layer. Upon removal of the sacrificial layer and release the strained substrate, a designed 2D planar structure will buckle into the desired 3D structure. An additional guiding layer, printed on top of the flexible layer, precisely controls which segments will fold reversibly to stabilize an array of complex 3D architectures - such as spirals, pyramids, or tables - upon removal of the sacrificial layer and release of the strained substrate. Fabrication of conductive 3D structures with designated free-standing segments has thus been realized by sequential screen-printing of custom-designed sacrificial, elastic-conductive composite, and guiding layers onto the surface of pre-stretched substrates. This process can be summarized in few consecutive steps illustrated in Figure A1.1a. First, the elastic textile substrate (*i.e.* Polyurethane-laminated Spandex) is pre-stretched to a certain extent of its original length. This introduces a tensile stress into the substrate, which is crucial for the directed buckling and folding into the final 3D architecture. Then, a water-soluble sacrificial layer is printed on top of the pre-stretched substrate to define the free-standing segments of the structure. Subsequently, the specially formulated elastic-conductive and guiding layers are printed. The purpose of the guiding layer is to determine the buckling points once the stress is released and the substrate is relaxed to its original length.

During this process, the tensile stress on the substrate is transformed into a compressive stress on the printed structures. These steps result in the final 3D shape where the free-standing points are printed over the sacrificial layer and the bonding segments retain their direct contact with the substrate. Under the stress, the flexible layer buckles upward, where the most stress and deformation are guided to the thinner segments between the individual guiding-layer blocks (Figure A.1d). Such use of planar screen-printed layers to create 3D shapes brings several technological advantages. Variety of complex 3D structures, based on a wide range of materials, can thus be readily mass produced at low cost.

A 3D image profile is used in Figure A1.1b to measure the difference in thickness created by adding the guiding layer. All layers have been printed using a hollowed metal 100 μm thick stencil, resulting in roughly 60, 50 and 50 μm thicknesses for the sacrificial, flexible and guiding layers, respectively. The higher thickness for the sacrificial layer reflects the higher solid loading of the printed film. A finite element analysis (FEA) is performed to study the stress distribution on the 3D structure, as shown in Figure A1.1c, where the stress localization is observed due to the addition of the sacrificial layer. Figure A.1e displays the real image of an array of square-shaped 3D structures after buckling. Distinct combination of 2D patterns of the sacrificial, flexible and guiding layers can thus lead to a wide selection of 3D structures to suit variety of applications (Figure A1.1f).

Figure A1.2 illustrates 5 initial design concepts, including their 2D sacrificial, flexible and guiding layer patterns, as well as the FEA prediction along with real images of the corresponding 3D structures. The extent of pre-stretching is calculated as the strain of substrate in both x and y directions, ε_x and ε_y, as labeled in Figure A1.2. Such extent of pre-stretch will dictate the macroscopic contact angles and the height of the 3D structure. Figure A1.2a demonstrates the design of a spiral-shaped 3D structure that is controlled only by selective bonding without a guiding layer. Figures A1.2b and A1.2c show 4 arrays of spike- and square-shaped 3D structures with varied sizes. By changing the pattern of the sacrificial layer and the guiding layer to designate the buckling points and bonding segments, square-shaped and spike-shaped 3D structures with different aspect ratios can be constructed using the same flexible layer design. Figure A1.2d and A1.2e shows two different 3D structure designs buckled using substrate pre-stretched biaxially in both x and y directions. It is worth noting that the substrate strain along the x and y directions are identical in both cases due to the symmetry of the design. In general, the substrate strain in two directions can be different for asymmetrical designs. The examples illustrated in this work only serve as a demonstration of the new concept, as the wide choice of materials, ink formulations and designs can be used to tailor for specific requirements of the desired 3D microstructures.

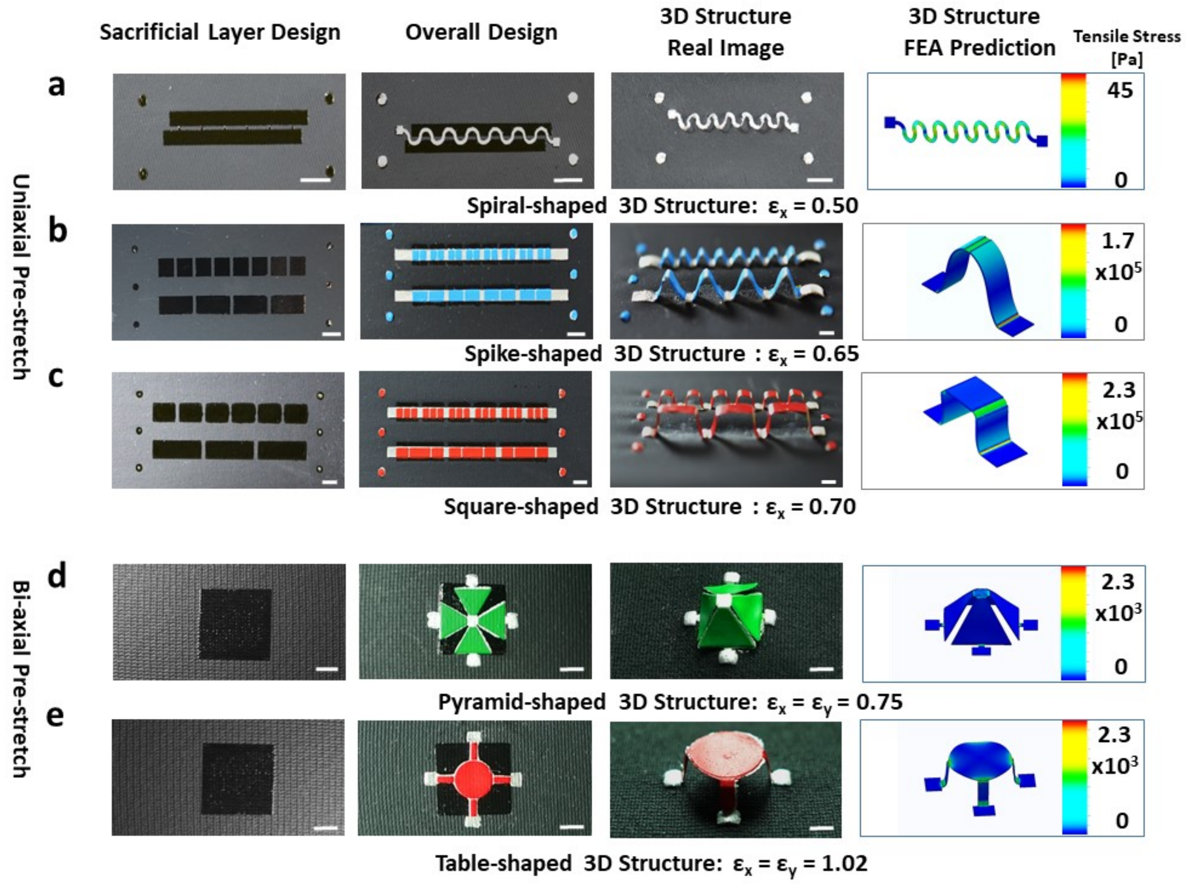

Figure A1.2: Demonstrations of sacrificial, flexible and guiding layer in the present 2D designs, FEA predictions and real images of 3D structures. Listed here are (a) spiral-shaped (b) spike-shaped (c) square-shaped (d) table-shaped (e) pyramid-shaped 3-D structures; (a)-(c) are buckled from uniaxial strain while (d)-(e) are buckled using biaxial strain. Scale bar, 5 mm.

One key element in the fabrication is to use a guiding layer to increase the thickness at different segments on the 2D patterns and hence to direct the stress to the desired buckling location. Screen-printed micrometer-thick films can play a key role in controlling the mechanical properties of different segments of the print. However, this greatly increases the tensile stress at the buckling location by multiple orders of magnitude. Controlled buckling is guided by the shearing forces at specific points of the structure, where the tensile stress is significantly higher than the rest of the structure, as shown on Figure A1.2 (Column 4). As a comparison, the coil-shaped 3D structure is buckled without any guiding layer and the tensile stress is relatively evenly distributed along the surface, with a value lower than 45 Pa. The controlled buckling, shown in the spike-shaped and square-shaped structures, displays a significantly higher tensile stress ($> 1x10^5$ Pa) at the buckling locations due to the stress concentration over a limited area. In addition, due to the high stress induced by pre-stretching in local areas, the adhesion of the bonding segments should be considerably stable. The ultimate strength of the ink composite used in this study has been measured to be $3.8x10^6$ Pa, which is sufficient for this application. Toluene was used as the solvent for the ink, ensuring good adhesion between the ink and the polyurethane lamination on the fabric substrate. Therefore, the material properties must be considered when utilizing controlled buckling in the design. Ink formulations that yield composites with good flexibility and elasticity should thus be selected to meet the maximum tensile strength required by a specific design.

With this respect, an ink composed of silver flakes and polystyrene-polyisoprene-polystyrene block copolymer (Ag-SIS) has been selected owing to its superior conductivity, stretchability and durability. Here, the reversibility and durability of the 3D structures is tested using resistance as an indicator of the structural integrity. This is of importance for soft electronics where structures may constantly undergo stretching and relaxation deformation cycles that are essential in certain applications. A single spike-shaped freestanding segment was chosen for testing the folding-unfolding deformation stress that mimics the deformation of the 3D structure printed on stretchable substrate. A commonly used conductive commercial silver ink has been used as a reference. Figure A1.3 displays comparison of a free-standing segment printed using the Ag-SIS ink (Figure A1.3a, left) and the commercial Ag ink (Figure A1.3a, right) in terms of the relative resistance change (ΔR%) during 20 deformation cycles. The Ag-SIS composite shows remarkable stability and reversibility with only ~3% resistance change, while the commercial ink exhibits a trend of increasing resistance after every cycle, indicating the formation of permanent damage on the free-standing structure. In addition, the case of over-stretching (i.e. when the substrate is stretched beyond the designed maximum strain), is also considered. The resistance plot of Figure A1.3d demonstrates the change of resistance during a 50% over-stretch deformation, in which the Ag-SIS ink shows superior recoverability due to the viscoelasticity of the SIS block copolymer. The Ag-SIS ink thus allows the structure to re-align after deformation, making the structure more adaptive to repeated buckling. Figure A1.3a also demonstrates this behavior where the over-stretched 3D structure shows a slow decrease of resistance after the cycled deformation is completed, indicating that the structure is allowed to rest, with the material allowed to relax, contract and recover. Meanwhile, the commercial Ag ink underwent irreversible damage, where the over-stretch resulted in the loss of electrical connection (to infinite resistance) due to structural failure, shown as the vertical red signal.

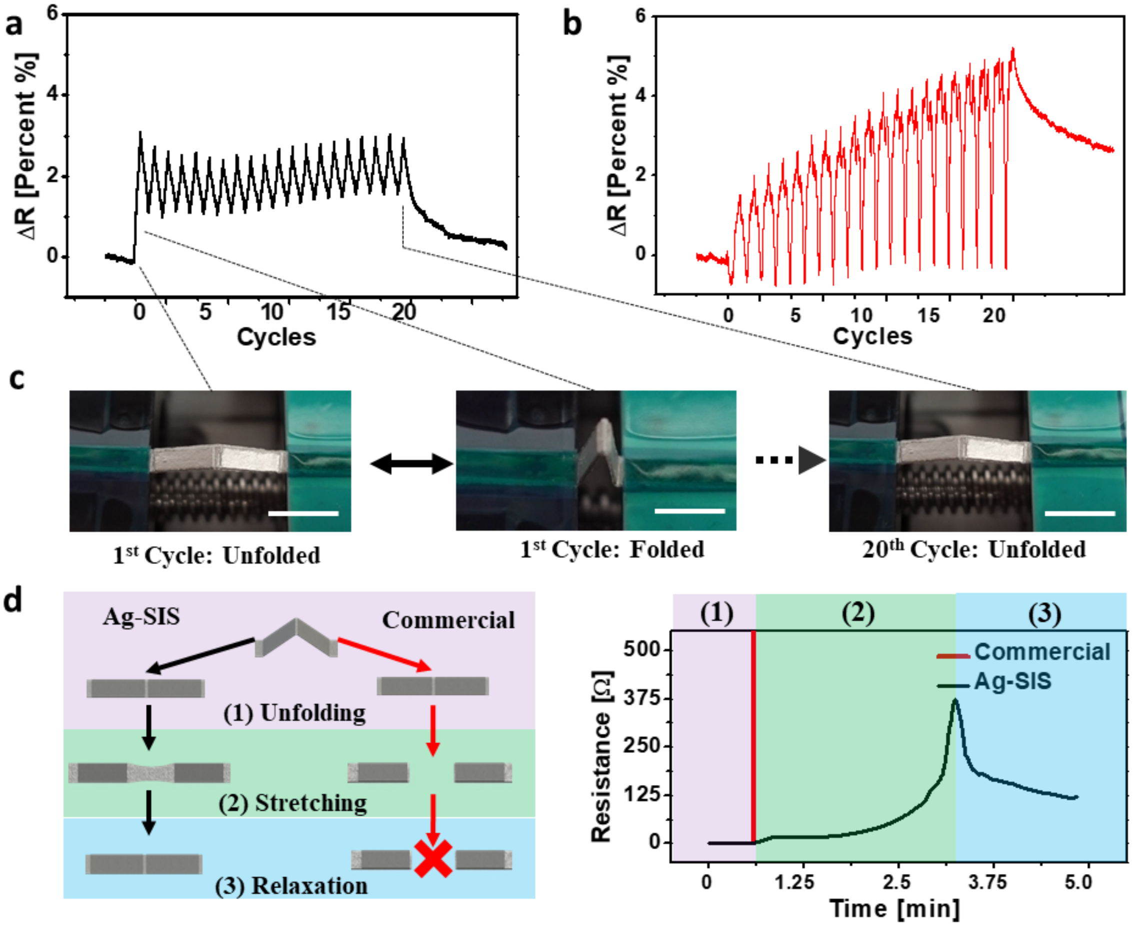

Figure A1.3: Respective resistance measurements of 3D structure under deformations for durability analysis. Resistance percentage change measurements of single spike-shaped freestanding segment of (a) SIS-Ag composite (b) commercial ink for 20 folding/unfolding deformation cycles. (c) Real image of freestanding spike-shaped ink at folded and unfolded positions for the test. (d) Schematic (left) and resistance measurement (right) of SIS-Ag composite (black) and commercial ink (red) before, during and after a 50% stretching. Scale bar, 5mm.

Selective bonding realized by applying a screen-printable water-soluble ink, can bring significant contribution to the mechanical performance of stretchable circuit interconnects.

Selective bonding can be used to create free-standing geometries printed on relaxed stretchable substrates, as shown in Figure A1.4.

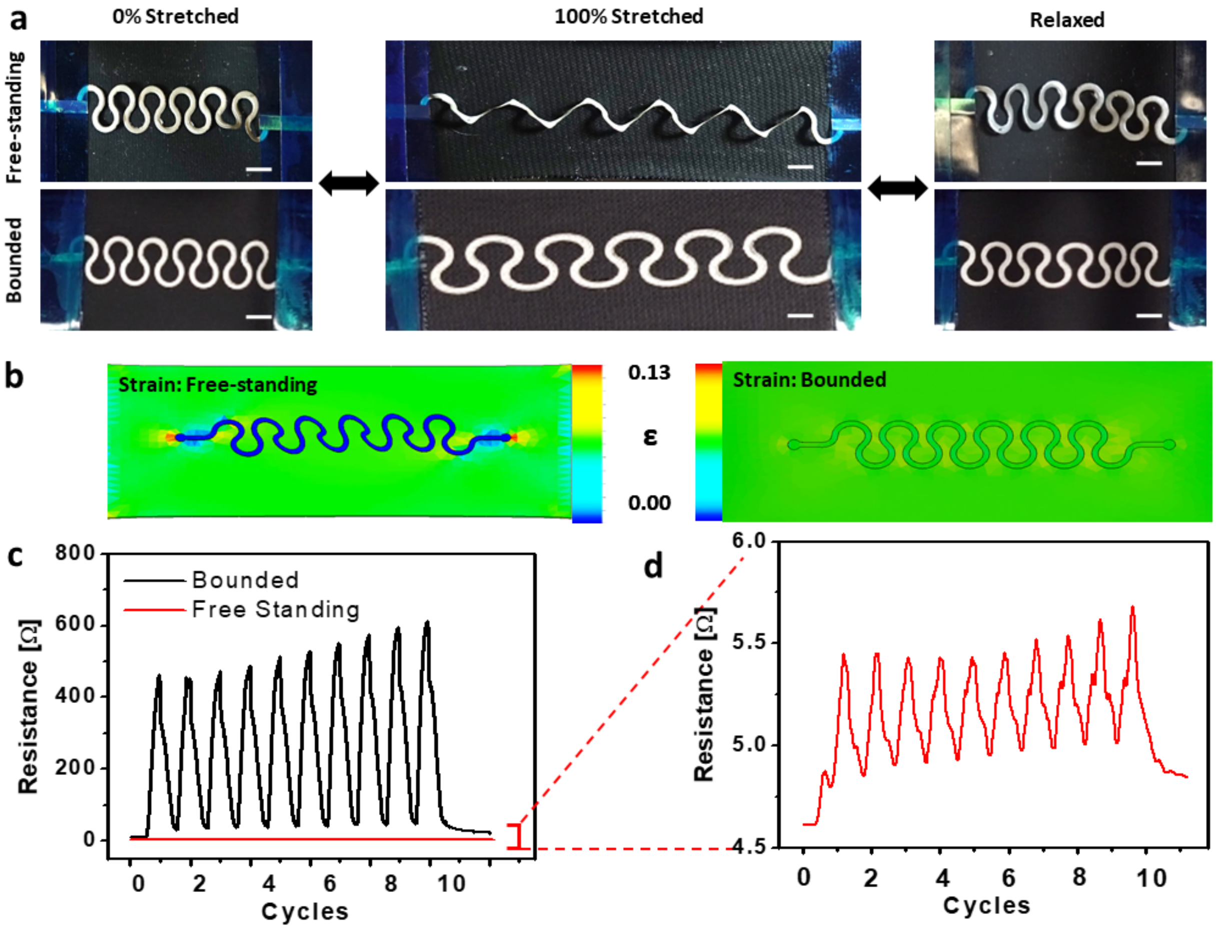

Figure A1.4: Structural durability and resistance comparison of serpentine structures. (a) Real images of bounded and free-standing serpentine before and after stretched to 100%. (b) FEA strain analysis of free-standing vs. bounded serpentine structure. (c) Resistance comparison between free-standing and bounded serpentine after 100% stretch. (d) Zoom-in view of the free-standing serpentine resistance change during the 10-cycle 100% stretch. Scale bar, 2.5mm.

Here, the effect of tensile deformation has also been examined. Compared to controlled buckling using the guiding layer, selective bonding using water-soluble sacrificial layer is of equal importance for the performance of the 3D structure. Selective bonding allows printed electronic circuit design to designate free-standing segments that can buckle without being stretched internally, resulting in minimal resistance change when the entire device undergoes large stretching deformation. Figure A1.4c and A1.4d shows comparison of the resistance change of the free-standing and bounded serpentines during a 100% stretching deformation. Due to its geometry, the free-standing serpentine buckles without any material elongations, leading to a negligible resistance change (~1 Ω) compared to the bounded serpentine (>500 Ω). FEA of the strain distribution on the serpentine structure and the substrate indicates that the free-standing serpentine experiences significantly less strain compared to the bound serpentine, which shared the same strain with the substrate upon stretching (Figure 4b). The negligible resistance change is attributed to the lack of intrinsic material elongation. Exploiting the geometrical property of serpentine shapes solely, fabrication of the freestanding architecture can be achieved by screen-printing onto the surface of the relaxed substrate. The structure obtained in that way can still display superior performance compared to all bounded 2D shapes. Previous effort has been made to implement elastic conductive ink and serpentine structures to resist the effect of deformation on the mechanical and electrical stability of screen-printed structures [34, 49]. Implementing free-standing extendable designs, such as serpentines, can further improve the stability of electrical conductivity without compromising the mechanical robustness.

Several potential applications have been considered. For example, Figure A1.5a demonstrates application of the square-shaped 3D structure where the intrinsic reversibility of the structure has been exploited. The device can be attached to a body part that performs constant repetitive motion (e.g. fingers, joints) and can be thus used to monitor and track movements by a simple on/off “switch” circuit, where the free-standing 3D structure will contact the traces printed below the free-standing segment upon applying sufficient strain on the substrate, and the entire process can be repeated for hundreds of cycles without breaking. The triggering threshold can be programmed by pre-stretching the substrate with a certain strain. There have been previous efforts on integrating pressure or strain sensors onto wearable objects, such as gloves for hand gesture tracking and sign-language interpretation.[50,51] Such mechanism relies on the constant monitoring of the resistance or capacitance change, which requires external calibration.

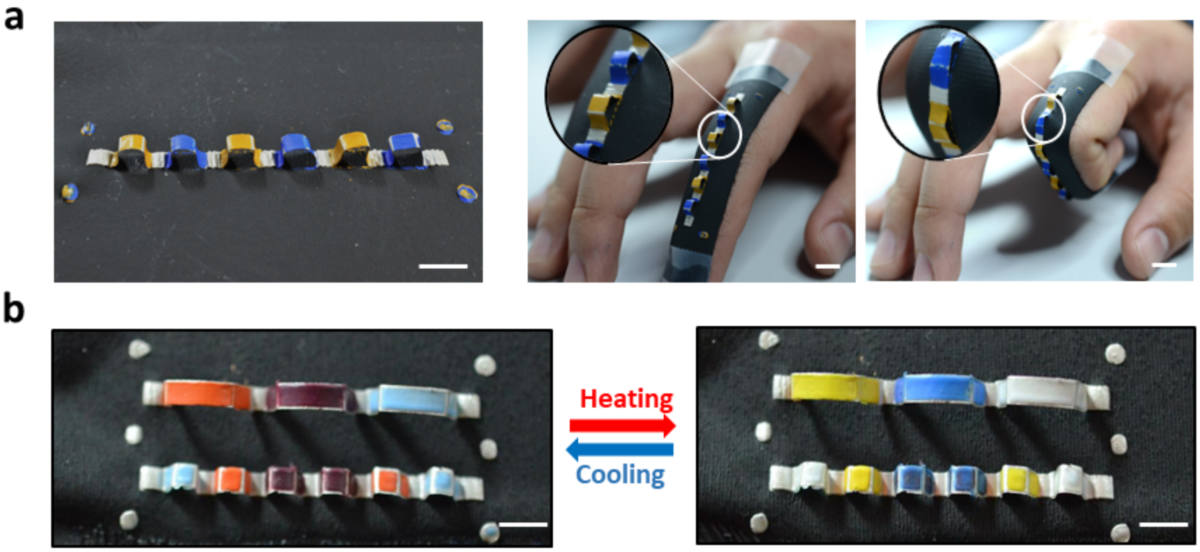

Figure A1.5: Potential applications of all-printed 3D structures. (a) Example of strain-sensitive applications. A square shaped structure array is attached to the index finger that deforms with figure. (b) Example of functionalized guiding-layer applications. The guiding layer is composed of temperature-sensitive ink and will change color when being heated.

If the “switch” mechanism using the fabrication presented here is applied, advanced logic circuits can be designed onto stretchable devices without the need of constant and parallel monitoring of the integrated sensors, hence reducing the size and weight of the device. Figure A1.5b demonstrates another direction for the potential application based on additional functionalization through modification of the guiding layer composition. As a demonstration for the diversity of the ink compatible with this mechanism, three different types of temperature-sensitive ink were printed as the modified guiding layer. After heating, the colors can undergo reversible changes from orange, dark purple and pale blue to yellow, blue and colorless (shown as white due to the color of the Ag-SIS flexible layer), respectively. Optimally exploiting the 3D geometrical space, sensing mechanism based on temperature, resistance, capacitance or electrochemistry, can be integrated onto the same location without interfering with each other. More structures inspired by kirigami and origami can be implemented using the all-printed fabrication technique for creating more complex designs that enable multi-functional 3D structure with optimized space utilization. With complex geometric shapes induced by buckling, incorporating more advanced material choices and designs, the new process could enable the fabrication of an advanced circuits using the low-cost 2D screen printing method.

A1.1.4 Conclusions

In conclusion, we have demonstrated the preparation of a wide range of tunable 3D structures through screen-printed planar designs that can transform reversibly between 2D and 3D shapes. The design and formation of 3D structures are achieved by engineered inks and stencil design patterns that determine the free-standing and bonding segments. Upon the relaxation of the substrate, the bonding segments induce stress to the free-standing counterparts, causing them to fold into their respective 3D structures. Utilizing different thicknesses of the printed layer, buckling of 3D structure can be controlled to transform into complex shapes. A commercial graphite ink, Ag-SIS ink, temperature sensitive inks as well as commercial acrylic ink have been used for the guiding layer and have found to be compatible with the new fabrication method. Other ink formulations based on different compositions and suitable mechanical properties will be investigated in the future. Although screen printing has limitations such as lower resolution of 50-100 micrometer compared to sub-micron resolution of photolithography, ink composite properties, substrate compatibility and print structural integrity, making it non-suitable for device-grade fabrication and meter-grade large scale fabrication for 3D structures, further improvement in the ink formulations, designs or use of alterative printing technologies (e.g. inkjet printing) could lead to smaller 3D structures with more advanced functionalities. The use of screen printing can enable a variety of functional materials, based on the versatility of the ink formulation to incorporate polymers, nanomaterials, particles, and solvents, and can thusly be considered as a good alternative and complement for nano/microfabrication and traditional processing techniques. Ultimately, screen printing, along with specially formulated inks, can offer many advantages to fabrication of 3D structures. These include high-throughput processing at low cost, wide selection of materials, and incorporation of numerous functional technologies. These developments and advantages are thus expected to attract a wide range of innovative explorations in different disciplines.

A1.2 Reference

1. W.-G. Bae, H. N. Kim, D. Kim, S.-H. Park, H. E. Jeong, K.-Y. Suh, *Adv. Mater.* **2014**, *26*, 675.
2. A. Quell, S. Heitkam, W. Drenckhan, C. Stubenrauch, *ChemPhysChem* **2017**, *18*, 451.
3. Q. Zhang, X. Yang, P. Li, G. Huang, S. Feng, C. Shen, B. Han, X. Zhang, F. Jin, F. Xu, T. J. Lu, *Prog. Mater. Sci.* **2015**, *74*, 332.
4. M. Gou, X. Qu, W. Zhu, M. Xiang, J. Yang, K. Zhang, Y. Wei, S. Chen, *Nat. Commun.* **2014**, *5*, 3774.
5. H. Butt, A. K. Yetisen, D. Mistry, S. A. Khan, M. U. Hassan, S. H. Yun, *Adv. Opt. Mater.* **2016**, *4*, 489.
6. N. Liu, Z. Lu, J. Zhao, M. T. McDowell, H.-W. Lee, W. Zhao, Y. Cui, *Nat. Nanotechnol.* **2014**, *9*, 187.
7. D. R. Rolison, J. W. Long, J. C. Lytle, A. E. Fischer, C. P. Rhodes, T. M. McEvoy, M. E. Bourg, A. M. Lubers, *Chem. Soc. Rev.* **2009**, *38*, 226.
8. K. P. Prasad, Y. Chen, P. Chen, *ACS Appl. Mater. Interfaces* **2014**, *6*, 3387.
9. C. Zhu, T. Liu, F. Qian, T. Y.-J. Han, E. B. Duoss, J. D. Kuntz, C. M. Spadaccini, M. A. Worsley, Y. Li, *Nano Lett.* **2016**, *16*, 3448.
10. R. K. Mishra, L. J. Hubble, A. Martín, R. Kumar, A. Barfidokht, J. Kim, M. M. Musameh, I. L. Kyratzis, J. Wang, *ACS Sensors* **2017**, *2*, 553.
11. J. Kim, R. Kumar, A. J. Bandodkar, J. Wang, *Adv. Electron. Mater.* **2017**, *3*, 1600260.
12. X. Dai, W. Zhou, T. Gao, J. Liu, C. M. Lieber, *Nat. Nanotechnol.* **2016**, *11*, 776.
13. B. Tian, J. Liu, T. Dvir, L. Jin, J. H. Tsui, Q. Qing, Z. Suo, R. Langer, D. S. Kohane, C. M. Lieber, *Nat. Mater.* **2012**, *11*, 986.
14. M. S. Mannoor, Z. Jiang, T. James, Y. L. Kong, K. A. Malatesta, W. O. Soboyejo, N. Verma, D. H. Gracias, M. C. McAlpine, *Nano Lett.* **2013**, *13*, 2634.
15. Q. Qing, Z. Jiang, L. Xu, R. Gao, L. Mai, C. M. Lieber, *Nat. Nanotechnol.* **2013**, *9*, 142.
16. T. Gissibl, S. Thiele, A. Herkommer, H. Giessen, *Nat. Photonics* **2016**, *10*, 554.
17. P. V. Braun, *Chem. Mater.* **2014**, *26*, 277.

18. A. G. Dumanli, T. Savin, *Chem. Soc. Rev.* **2016**, *45*, 6698.

19. M. Stefik, S. Guldin, S. Vignolini, U. Wiesner, U. Steiner, *Chem. Soc. Rev.* **2015**, *44*, 5076.

20. Z. Fan, H. Razavi, J. Do, A. Moriwaki, O. Ergen, Y.-L. Chueh, P. W. Leu, J. C. Ho, T. Takahashi, L. A. Reichertz, S. Neale, K. Yu, M. Wu, J. W. Ager, A. Javey, *Nat. Mater.* **2009**, *8*, 648.

21. S. Xi, T. Shi, D. Liu, L. Xu, H. Long, W. Lai, Z. Tang, *Sensors Actuators A Phys.* **2013**, *198*, 15.

22. T. Bückmann, N. Stenger, M. Kadic, J. Kaschke, A. Frölich, T. Kennerknecht, C. Eberl, M. Thiel, M. Wegener, *Adv. Mater.* **2012**, *24*, 2710.

23. J.-H. Lee, C. Y. Koh, J. P. Singer, S.-J. Jeon, M. Maldovan, O. Stein, E. L. Thomas, *Adv. Mater.* **2014**, *26*, 532.

24. S. Xu, Z. Yan, K.-I. Jang, W. Huang, H. Fu, J. Kim, Z. Wei, M. Flavin, J. McCracken, R. Wang, A. Badea, Y. Liu, D. Xiao, G. Zhou, J. Lee, H. U. Chung, H. Cheng, W. Ren, A. Banks, X. Li, U. Paik, R. G. Nuzzo, Y. Huang, Y. Zhang, J. A. Rogers, *Science* **2015**, *347*, 154.

25. S. Felton, M. Tolley, E. Demaine, D. Rus, R. Wood, *Science* **2014**, *345*, 644.

26. Z. Tang, Z. Gao, S. Jia, F. Wang, Y. Wang, *Adv. Sci.* **2017**, DOI 10.1002/advs.201600437.

27. B. Y. Ahn, E. B. Duoss, M. J. Motala, X. Guo, S.-I. Park, Y. Xiong, J. Yoon, R. G. Nuzzo, J. A. Rogers, J. A. Lewis, *Science* **2009**, *323*, 1590.

28. Y. Zhang, Z. Yan, K. Nan, D. Xiao, Y. Liu, H. Luan, H. Fu, X. Wang, Q. Yang, J. Wang, W. Ren, H. Si, F. Liu, L. Yang, H. Li, J. Wang, X. Guo, H. Luo, L. Wang, Y. Huang, J. A. Rogers, *Proc. Natl. Acad. Sci.* **2015**, DOI 10.1073/pnas.1515602112.

29. I. Gibson, D. Rosen, B. Stucker, *Additive Manufacturing Technologies: 3D Printing, Rapid Prototyping, and Direct Digital Manufacturing*, **2015**.

30. S. Sundaram, D. S. Kim, M. A. Baldo, R. C. Hayward, W. Matusik, *ACS Appl. Mater. Interfaces* **2017**, **2017**, *9*, 32290.

31. H. Fu, K. Nan, P. Froeter, W. Huang, Y. Liu, Y. Wang, J. Wang, Z. Yan, H. Luan, X. Guo, Y. Zhang, C. Jiang, L. Li, A. C. Dunn, X. Li, Y. Huang, Y. Zhang, J. A. Rogers, *Small* **2017**, DOI 10.1002/smll.201700151.

32. K. I. Jang, K. Li, H. U. Chung, S. Xu, H. N. Jung, Y. Yang, J. W. Kwak, H. H. Jung, J. Song, C. Yang, A. Wang, Z. Liu, J. Y. Lee, B. H. Kim, J. H. Kim, J. Lee, Y. Yu, B. J. Kim, H. Jang, K. J. Yu, J. Kim, J. W. Lee, J. W. Jeong, Y. M. Song, Y. Huang, Y.

Zhang, J. A. Rogers, *Nat. Commun.* **2017**, DOI 10.1038/ncomms15894.

33. Y. Zhang, F. Zhang, Z. Yan, Q. Ma, X. Li, Y. Huang, J. A. Rogers, *Nat. Rev. Mater.* **2017**, DOI 10.1038/natrevmats.2017.19.

34. A. M. V. Mohan, N. Kim, Y. Gu, A. J. Bandodkar, J.-M. You, R. Kumar, J. F. Kurniawan, S. Xu, J. Wang, *Adv. Mater. Technol.* **2017**, *2*, 1600284.

35. K. Chen, W. Gao, S. Emaminejad, D. Kiriya, H. Ota, H. Y. Y. Nyein, K. Takei, A. Javey, *Adv. Mater.* **2016**, DOI 10.1002/adma.201504958.

36. N. P. Dasgupta, J. Sun, C. Liu, S. Brittman, S. C. Andrews, J. Lim, H. Gao, R. Yan, P. Yang, *Adv. Mater.* **2014**, *26*, 2137.

37. A. Kamyshny, S. Magdassi, *Small* **2014**, 17, 3515.

38. S. Kim, B. Sanyoto, W. T. Park, S. Kim, S. Mandal, J. C. Lim, Y. Y. Noh, J. H. Kim, *Adv. Mater.* **2016**, 28, 10149.

39. J. G. Hardy, M. Palma, S. J. Wind, M. J. Biggs, *Adv. Mater.* **2016**, DOI 10.1002/adma.201505417.

40. V. K. Thakur, M. R. Kessler, *Polymer (Guildf).* **2015**, DOI 10.1016/j.polymer.2015.04.086.

41. Z. Bao, X. Chen, *Adv. Mater.* **2016**, *28*, 4177.

42. S. J. Benight, C. Wang, J. B. H. Tok, Z. Bao, *Prog. Polym. Sci.* **2013**, DOI 10.1016/j.progpolymsci.2013.08.001.

43. L. Hsu, C. Weder, S. J. Rowan, *J. Mater. Chem.* **2011**, DOI 10.1039/C0JM02383C.

44. R. Kumar, J. Shin, L. Yin, J. M. You, Y. S. Meng, J. Wang, *Adv. Energy Mater.* **2017**, DOI 10.1002/aenm.201602096.

45. A. J. Bandodkar, C. S. Lopez, A. M. V. Mohan, L. Yin, R. Kumar, J. Wang, *Sci. Adv.* **2016**, *2*, e1601465.

46. S. Srivastava, J. L. Schaefer, Z. Yang, Z. Tu, L. A. Archer, *Adv. Mater.* **2014**, DOI 10.1002/adma.201303070.

47. J. M. Ball, M. M. Lee, A. Hey, H. J. Snaith, A. V. Shah, H. Schade, M. Vanecek, J. Meier, E. Vallat-Sauvain, N. Wyrsch, U. Kroll, C. Droz, J. Bailat, X. Wu, D. A. R. Barkhouse, O. Gunawan, T. Gokmen, T. K. Todorov, D. B. Mitzi, A. Chirilă, S. Buecheler, F. Pianezzi, P. Bloesch, C. Gretener, A. R. Uhl, C. Fella, L. Kranz, J. Perrenoud, S. Seyrling, R. Verma, S. Nishiwaki, Y. E. Romanyuk, G. Bilger, A. N. Tiwari, C. J. Hibberd, E. Chassaing, W. Liu, D. B. Mitzi, D. Lincot, A. N. Tiwari, M. Graetzel, R. A. J. Janssen, D. B. Mitzi, E. H. Sargent, V. Fthenakis, E. H. Sargent,

A. Yella, H.-W. Lee, H. N. Tsao, C. Yi, A. K. Chandiran, M. K. Nazeeruddin, E. W.-G. Diau, C.-Y. Yeh, S. M. Zakeeruddin, M. Grätzel, Y. Liang, Z. Xu, J. Xia, S.-T. Tsai, Y. Wu, G. Li, C. Ray, L. Yu, R. F. Service, J.-H. Im, C.-R. Lee, J.-W. Lee, S.-W. Park, N.-G. Park, H.-S. Kim, C.-R. Lee, J.-H. Im, K.-B. Lee, T. Moehl, A. Marchioro, S.-J. Moon, R. Humphry-Baker, J.-H. Yum, J. E. Moser, M. Gratzel, N.-G. Park, A. Kojima, K. Teshima, Y. Shirai, T. Miyasaka, I. Chung, B. Lee, J. He, R. P. H. Chang, M. G. Kanatzidis, L. Etgar, P. Gao, Z. Xue, Q. Peng, A. K. Chandiran, B. Liu, M. K. Nazeeruddin, M. Grätzel, M. M. Lee, J. Teuscher, T. Miyasaka, T. N. Murakami, H. J. Snaith, Z. M. Beiley, M. D. McGehee, P. Zhang, C. Wu, Y. Han, T. Jin, B. Chi, J. Pu, L. Jian, T. Miyasaka, M. Ikegami, Y. Kijitori, C. Y. Jiang, W. L. Koh, M. Y. Leung, S. Y. Chiam, J. S. Wu, J. Zhang, E. J. W. Crossland, N. Noel, V. Sivaram, T. Leijtens, J. A. Alexander-Webber, H. J. Snaith, K. Tanaka, T. Takahashi, T. Ban, T. Kondo, K. Uchida, N. Miura, J. J. M. Halls, C. A. Walsh, N. C. Greenham, E. A. Marseglia, R. H. Friend, S. C. Moratti, A. B. Holmes, G. Yu, J. Gao, J. C. Hummelen, F. Wudl, A. J. Heeger, B. O'Regan, M. Gratzel, P. Docampo, H. J. Snaith, H. J. Snaith, N. C. Greenham, R. H. Friend, *Energy Environ. Sci.* **2013**, DOI 10.1039/c3ee40810h.

48. M. G. Kim, M. G. Kanatzidis, A. Facchetti, T. J. Marks, *Nat. Mater.* **2011**, DOI 10.1038/nmat3011.

49. A. J. Bandodkar, I. Jeerapan, J. M. You, R. Nuñez-Flores, J. Wang, *Nano Lett.* **2016**, 16. 721-727.

50. T. F. O'Connor, M. E. Fach, R. Miller, S. E. Root, P. P. Mercier, D. J. Lipomi, *PLoS One* **2017**, DOI 10.1371/journal.pone.0179766.

51. R. K. Mishra, L. J. Hubble, A. Martín, R. Kumar, A. Barfidokht, J. Kim, M. M. Musameh, I. L. Kyratzis, J. Wang, *ACS Sensors* **2017**, DOI 10.1021/acssensors.7b00051.

A2: Rechargeable Zinc Batteries with Bismuth Additives

A2.1.1 Introduction

Rechargeable or secondary batteries have become an essential part of everyday life. A battery is the most efficient way of storing energy because it does not need an external conversion mechanism [1]. While the need for a low-cost battery is rising, lithium-ion batteries (LIBs) dominate the secondary battery in the market even though the material synthesis for a LIB is energy intensive and expensive [2-5]. LIBs utilize ceramic oxides and highly ordered graphite, which require high temperature synthesis and organic electrolytes, which are flammable and require expensive casing. One attractive option to lower the cost of energy storage is to design secondary batteries with aqueous electrolyte. Zn anodes are a promising aqueous battery material because they are nontoxic, earth abundant, low-cost, and energy dense resource [6]. Utilizing Zn anode also raises the working voltage due to its low reduction voltage, thus applying a rechargeable Zn anode can dramatically drop the cost of secondary batteries [7].

Zn anodes are one of the oldest electrochemical electrodes dating back to the batteries invented by Alexssandro Volta in the 1800s, yet commercial rechargeable Zn anode implementation is scarce because the Zn anode suffers from a critical intrinsic issue. It has been long discovered that when Zn oxidizes (or discharges), zincate ions are formed and relax to ZnO.[8] The problem is that the zincate ions are soluble in aqueous alkaline electrolyte. When the zincate ions are formed, the ions detach from the Zn surface and dissolve in the electrolyte. Eventually the Zn particles lose the electrical connections rendering the anode no longer rechargeable. As Zn anode is a promising anode for both alkaline batteries [7, 9] and the metal-air batteries, [6, 10, 11] resolving the rechargeability with Zn anode is beneficial to the field of electrical energy storage.

To overcome this issue, there are numerous reports utilizing various methods including composite, electrolyte modification, and nanostructuring. [12-16] Among them, the composite addition of Bi_2O_3 is notable for its simplicity and effectiveness. Some reports show that Bi_2O_3 significantly improves the cycling performance of the Zn anode, however much of the literatures suggest that enhanced cycle performance is due to the advanced electrical conductivity [16, 17]. Moser et al. observed Bi metal formation through *in situ* powder X-ray diffraction (PXRD) and concluded that the Bi metal further increased the conductivity [17]. However, it is difficult to argue that Bi_2O_3 is the most effective additive to elevate the electrical conductivity. Bi_2O_3 exhibits p-type electronic conductivity in room temperature, but it is heavy and not easy to obtain high surface area [18]. Using Bi_2O_3 as a conductive additive makes the whole electrode too heavy without providing much electrical connection. A more optimum choice to increase the conductivity is to employ simple conductive carbon with high surface area. It is known that the benefit of Bi_2O_3 surpasses that of the carbon [19]. A more comprehensive understanding of the mechanism of a Zn and Bi_2O_3 composite electrode is needed. This paper proposes that when the zincate ions are formed, the ions are deposited onto the surface of bismuth species, which allows the Zn anode to be rechargeable. The authors prove this with various characterizations of the composite electrode at different states of electrochemical cycles.

A2.1.2 Experimental Section

Cell fabrication: All inks were prepared by first, preparing polyvinylidene fluoride (PVDF) solution. PVDF solution is made with dissolving 1 g of PVDF (MTI, EQ-Lib-PVDF) in 10 ml of n-methyl-2-pyrrolidone (NMP) (MTI EQ-Lib-NMP). The PVDF was dissolved over night after vortex mixing and sonication. Then the appropriate amount of PVDF solution was added to the composite powder. The mass ratio of the composite powder and the PVDF is illustrated in supplementary information. The active electrode area was 0.7 cm X 0.9 cm and the distance between the electrodes were kept at 2 mm. Electrode patterns were designed in AutoCAD (Autodesk, San Rafael, CA) and outsourced for fabrication on stainless steel through-hole 12 inch framed stencils (Metal Etch Services, San Marcos, CA). A conductive carbon ink (ERCON E3449) was printed as a carbon based current collector layer on a polyethylene terephthalate (PET) film. On the current collector layer, the respective electrodes were printed. The printings were performed employing an MPM-SPM semiautomatic screen printer (Speedline Technologies, Franklin, MA). For the three-electrode cell electrochemical experiments, the Zn electrode was taped to a glass slide in between two strips of Zn foils (Sigma-Aldrich 356018). The two strips of Zn foils were utilized as a counter electrode and a reference electrode. Then the gel based electrolyte was prepared with polyacrylic acid [20]. The electrolyte was extruded onto the three-electrodes *via* syringe.

Electrochemical tests: The electrochemical tests were conducted with Arbin electrochemical cycler channels. All the electrochemical cycling tests were conducted with galvanostatic discharge at 4 mA cm^{-2} current density and constant current constant voltage charge at 2 mA cm^{-2} current density and constant voltage hold for 20 mins at -0.3

V vs. Zn/Zn^{2+} for three-electrode cells and 2.05 V vs. Zn/Zn^{2+} for a full-cell. The three-electrode cells were cycled in -0.3 - 0.4 V Zn/Zn^{2+} range and the full-cell is cycled in 0.8 - 2.05 V Zn/Zn^{2+}. The three-electrode cells were cycled with a capacity limit of 1 mAh/cm^2.

PXRD: Pristine sample is the Zn + Bi_2O_3 electrode. The soaked sample is the pristine sample soaked in electrolyte for the same time as oxidized sample (45 minutes). The oxidized sample is the pristine sample after electrochemical oxidation (discharge). Both the soaked sample and the oxidized sample were washed with running D.I. water and soaked in the D.I. water overnight. Upon washing, the electrode was dried in 60 °C for 3 hours. All the PXRD data were collected at ambient temperature on a Bruker D8 Advance diffractometer at 40 kV, 40 mA for Cu K_α (λ = 1.5418 Å), with a scan speed of 1 s/step, a step size of 0.05° in 2θ, and a 2θ range of ~10-80°.

A2.1.3 Results and Discussion

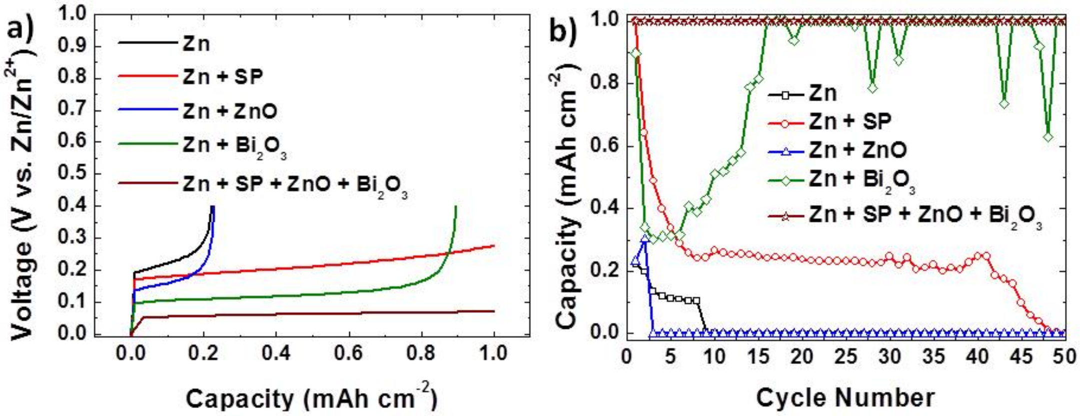

Figure A2.1. Electrochemical testing of zinc battery with various additive combinations. a) First discharge voltage profile and b) discharge cycle retention of various Zn electrode electrochemically cycled in a three-electrode cell. All electrodes contain PVDF as the polymer binder but PVDF is omitted for clarity. All electrodes are cycled at current density of 4 mA cm^{-2} and a capacity limit of 1 mAh cm^{-2}.

The three-electrode system of various Zn cells is electrochemically cycled (Figure A2.1). When the electrode only contains Zn, the cell cycles for only 8 times with a small capacity, followed by a rapid capacity failure. With the addition of Super-P (SP), a conductive carbon additive, the capacity retention exponentially decays in the first ten cycles, gradually decreases until 40 cycles, and finally has no capacity after 50 cycles. By inserting ZnO, the electrode cycles for only two times and outputs no capacity. When added with Bi_2O_3, the capacity exponentially decays for the first three cycles but increases back to 1 mAh cm^{-2} over the next 12 cycles. This Zn electrode with Bi_2O_3 additive is referred to as the Bi_2O_3 electrode. With the addition of all three additives, the capacity remains at 1 mAh cm^{-2} for at least 50 cycles. Bi_2O_3 compared to SP, increases in capacity after the exponential decay and after 15 cycles, the capacity retention stays mostly at 1 mAh cm^{-2}. Although adding all three additives improves the capacity retention, it is worthwhile to understand the role of Bi_2O_3 to form strategies to further enhance the rechargeability.

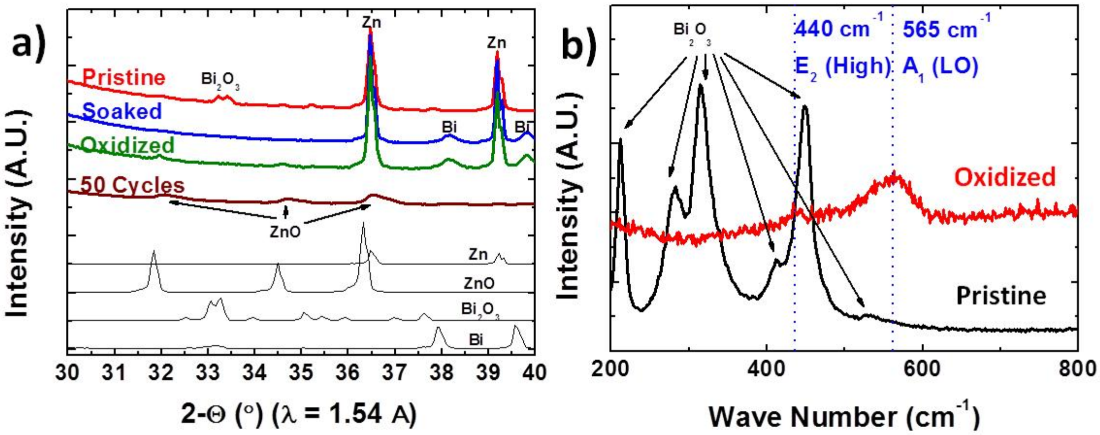

Figure A2.2. PXRD characterization of Bismuth additive in electrode. a) PXRD of the Bi_2O_3 electrode at various states in color and raw materials in black. b) Raman spectra of the Bi_2O_3 electrode at pristine and oxidized (first discharged). The pristine sample is the Bi_2O_3 electrode after curing. The soaked sample is the Bi_2O_3 electrode after soaking in the electrolyte. The oxidized sample is the Bi_2O_3 electrode after first electrochemical oxidation or discharge.

Since the Zn oxidizes to form ZnO crystals, PXRD of the Bi_2O_3 electrode is obtained at various states (Figure A2.2a). In the pristine electrode, there are clear reflections from both Zn metal and Bi_2O_3. After being soaked in the electrolyte, the Bi_2O_3 reflections disappear, but reflections corresponding to Bi metal appear. To confirm the absence of Bi_2O_3 reflections, same mass amount of Zn and Bi_2O_3 is mixed and soaked in the electrolyte. It shows the absence of Bi_2O_3 and Bi metal-like reflections. The Bi_2O_3 is reduced without electrochemical bias. The Zn and Bi_2O_3 particles in the electrolyte do not form a new crystal phase separately. A new phase is only formed when Zn is present with the Bi_2O_3 in the electrolyte.

After 50 cycles, the ZnO reflections become obvious but the Zn and Bi metal-like reflections vanish. This suggests that the Bi metal-like species is actively involved during the electrochemical cycling, however, the ZnO growth is not very clear upon first oxidation. To elucidate the electrochemical reaction that occurs in the Bi_2O_3 electrode, Raman spectra are obtained before and after the electrochemical oxidation reaction (Figure A2.2b). Before the electrochemical reaction, the pristine electrode only shows the typical Bi_2O_3 vibration modes. Upon oxidation reaction, the Bi_2O_3 vibration modes disappear, similar to the Bi_2O_3 reflections in PXRD, and only two broad peaks appear near 440 cm^{-1} (E_2 (High) mode) and 565 cm^{-1} (A_1 (longitudinal optical or LO) mode). These two peaks indicate ZnO formation. The E_2 (High) mode is typically an intense and sharp signal originated from the vibrational motion of oxygen atoms in the ZnO [21]. The low intensity and the broadening imply a disorder in the crystal structure [21,22]. The disorder can be a result of lattice mismatching from relaxation, reconstruction, structural imperfection, and adsorbed impurities [23]. A_1 (LO) mode is typically a low intensity signal from c-face ZnO. The enhancement of this signal is due to the Raman resonance effect.[24] The observed resonance effect is most likely due to ZnO that is not nucleated as an isolated compound but rather deposited on a conductive substrate/surface. The Raman signal may be contributed by the passivation ZnO layer on the Zn metal or on the Bi metal-like species. Further experiments are conducted to identify the exact location of the ZnO.

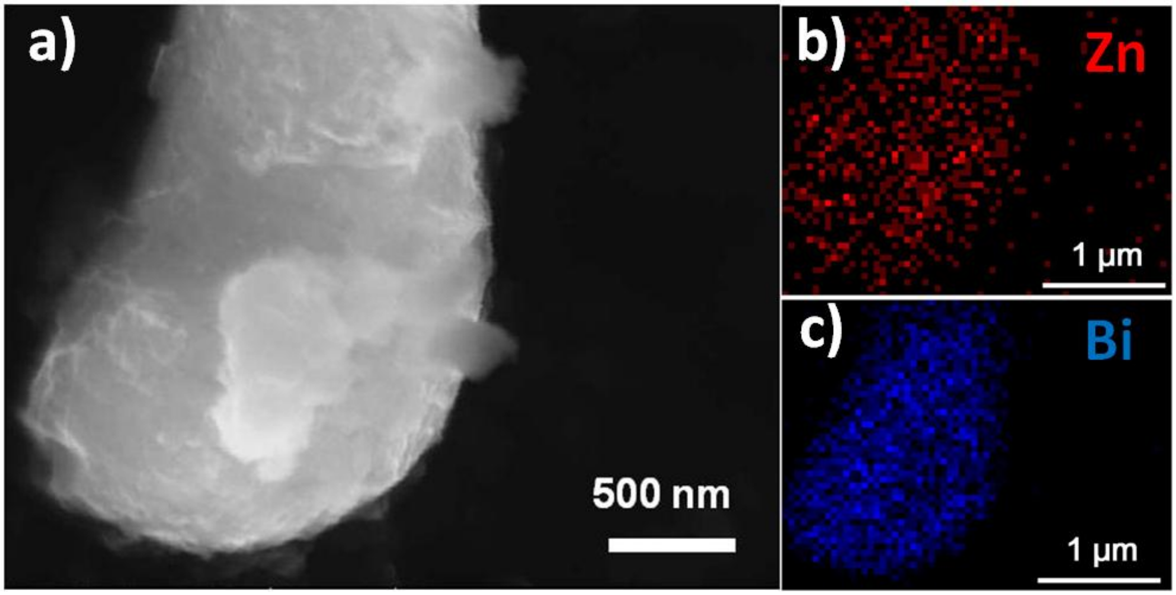

Figure A2.3. SEM/EDS mapping of the bismuth species. a) SEM image of the bismuth species after oxidation. b) EDS mapping of Zn Kα_1 and c) Bi Mα_1. The EDS mapping is performed on the same particle as the SEM image (a).

The Raman spectra suggests that the ZnO is formed on a conductive surface, yet it is not clear whether the ZnO observed in Raman is a passivation layer on the Zn metal or on the surface of the bismuth species. SEM images along with the EDS mapping are collected after oxidation. Pristine Bi_2O_3 particles are about 2 μm in size. EDS mapping of a 2 μm particle shows that this particle is composed of both zinc atoms and bismuth atoms (Figure A2.3). This mapping suggests that the ZnO is deposited on the surface of the bismuth species. Furthermore, EDS mapping of a particle after 50 cycles also exhibit both Zn and Bi. Unlike after the first oxidation, this particle is about 8 μm and the concentration of the Zn is much higher than that of Bi. The growth of the particle size and the change in atomic concentration clearly indicate that the ZnO continues to grow on the surface of the bismuth species over prolonged cycles. Without the electrochemical bias, both Bi_2O_3 and Bi metal are soaked in a 6 M $Zn(NO_3)_2$ solution. A clear change in surface morphology is found, which supports that the Zn^{2+} deposits onto the surface of bismuth species due to thermodynamic reasons rather than electrochemical side reaction.

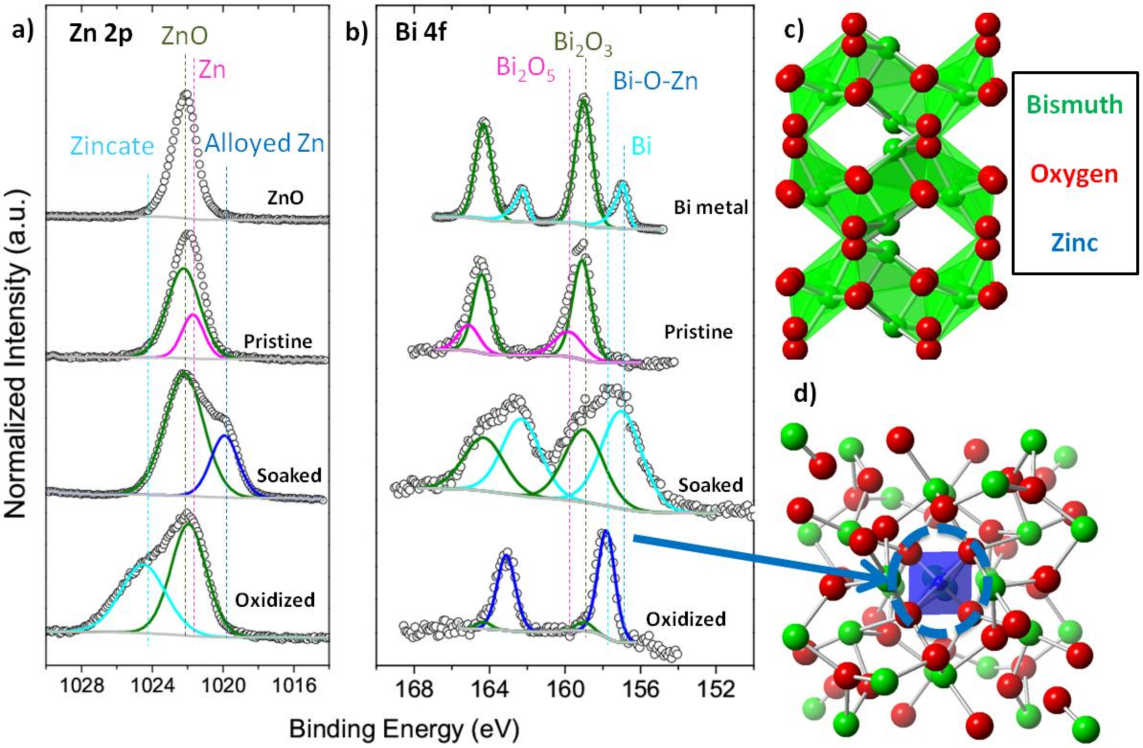

Figure A2.4. Crystal structure of Zn and Bismuth oxide a) Zn 2p and b) Bi 4f XPS of the Bi_2O_3 electrode at various states along with ZnO and Bi metal as baseline materials. Crystal structure of c) α-Bi_2O_3 and d) $Bi_{38}ZnO_{58}$. Green: Bismuth, Red: Oxygen, and Blue: Zinc. In d) $Bi_{38}ZnO_{58}$, the Zn site is partially occupied by Zn and Bi.

To confirm the ZnO deposition on the bismuth species, XPS is collected for the pristine, electrolyte soaked, and oxidized electrode. The survey scans are provided to ensure the absence of electrolyte salt or other impurities. The pristine electrode contains

Zn metal and Bi_2O_3 with respective surface passivation layers (**Figure A2.4**) [25-27]. After being soaked in electrolyte, the Zn metal peak shifts to lower binding energy indicative of the Zn alloying [28]. In the Bi 4f spectra, the Bi_2O_5 passivation layer disappear and a Bi metal peak appear. The absence of Bi_2O_5 and the presence of Bi metal support the hypothesis that the Zn reduces the bismuth species. Furthermore, compared to the Bi metal baseline spectrum, the spectrum of the soaked sample is much broader. This is likely due to the Bi-Zn alloying.

Upon oxidation, the Zn alloy peak disappears, and zincate peak appears. This suggests that the alloyed Zn is electrochemically active to form zincate ion. As mentioned earlier, the zincate ion is soluble in aqueous electrolyte. Thus, the formation of zincate ion leads the active material loss because the ZnO is developed in the electrolyte disconnected from the electrode. However, the presence of zincate peak implies that the zincate ion is well bound to the electrode even after the rigorous washing. In the Bi 4f spectra, upon oxidation, the Bi metal peak disappears, and a new peak appears in between Bi_2O_3 and Bi metal peaks. Since the Bi^{2+} is unstable and undergoes disproportionation reaction, this new peak most likely originates from some Bi^{3+}/Zn^{2+} compound [29].

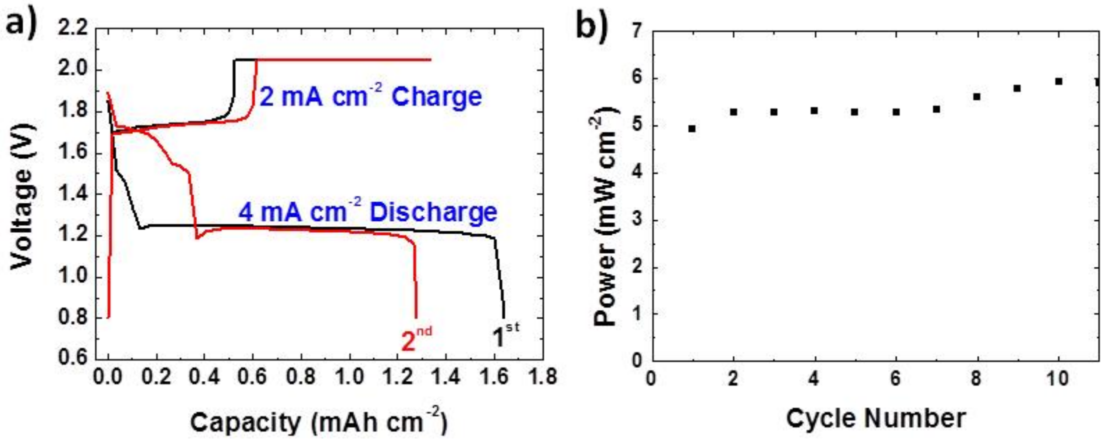

Figure A2.5. Electrochemical Performance of Rechargeable Battery. a) Voltage profile and b) power density of Zn-Ag full-cell battery performance with all the additives added in the Zn anode. The full-cell is cycled with current density at 4 mA cm^{-2} without a capacity limit.

It is clear that Bi_2O_3 provides the vital assistance in prolonging the cyclability of the Zn anode. However, the Bi_2O_3 added electrode suffers from a rapid decay in the retention during the first few cycles. By adding the three additives (Bi_2O_3, SP and ZnO), the cycling performance of the three-electrode cell noticeably improves (Figure 1.b). ZnO is required to match the extra charging capacity of the Ag_2O cathode [20]. With this anode, a Zn-Ag full-cell is constructed (Figure A2.5). The full-cell is fully functional even with the high discharging current of 4 mA cm^{-2}. To the best of our knowledge, among Zn-based printable batteries, 4 mA cm^{-2} of discharge current density in this work is among the highest and for printable batteries, the highest current density to date is 1.4 mA cm^{-2} [20, 30-35]. During discharge, a consistent high-power output of about 5 mW cm^{-2} is achieved. The capacity of the full-cell is above 1.2 mAh cm^{-2} (Figure A2.5a). Gaikwad et al. achieved about 3.5 mAh cm^{-2}, their battery is not rechargeable [30]. Among the rechargeable printable batteries, the highest capacity is 1.2 mAh cm^{-2} [20]. Although the cycling retention degrades only after 6 cycles, this is attributed to the decay in the cathode side.

The bare Zn anode's poor cycling performance originates from the large crystal transformation during the electrochemical reaction and the Ag cathode also undergoes a significant crystal transformation [20].

The Zn particles are conductive itself, yet when Zn starts to oxidize, the Zn surface gets etched away, losing the electrical connections and eventually no capacity is given off, as shown in figure A2.1. Conductive additive is needed even though the Zn particles are conductive. Utilizing Zn plates bypasses such issue; however, Zn plates suffer from dendritic deposition of ZnO [36]. Both SP and the Bi_2O_3 are conductive additives and they provide electrical connection. Compared to that of the Bi_2O_3, the SP electrode decays in capacity slowly. This is attributable to the fact that SP has much wider surface area than Bi_2O_3, making it be capable of maintaining better network of electrical connection. However, the SP electrode eventually uses up the electrical network and does not give off capacity. The Bi_2O_3 electrode has low retention between first and 15th cycle. Given the high rate cycling, the low retention of the Bi_2O_3 electrode is most likely due to the delay in the relaxation of zincate ions into ZnO. Lastly, ZnO additive is insulating. Although it helps giving extra capacity at the second cycle by reducing to Zn metal during the first reduction/charge, it does not allow a stable electrical conductivity.

The PXRD and XPS results suggest the reduction of Bi_2O_3 into Zn-Bi alloy. Although Zn is kinetically stable in aqueous electrolyte, it is not thermodynamically stable because Zn has lower reduction potential compared to hydrogen. Zn anode in aqueous electrolyte oxidizes, which is called self-discharge [37,38]. Self-discharging can be suppressed by the presence of bismuth species [37,38]. Besides the hydrogen, Bi^{3+} also has higher reduction potential than Zn. The Bi^{3+} reduces to form Bi^{2+} or Bi metal to oxidize the Zn and after reducing to Bi^{2+}, the Bi^{2+} undergoes disproportionation reaction to develop Bi metal [29]. Bi metal-like reflections have been formed and reported in the literature [17].

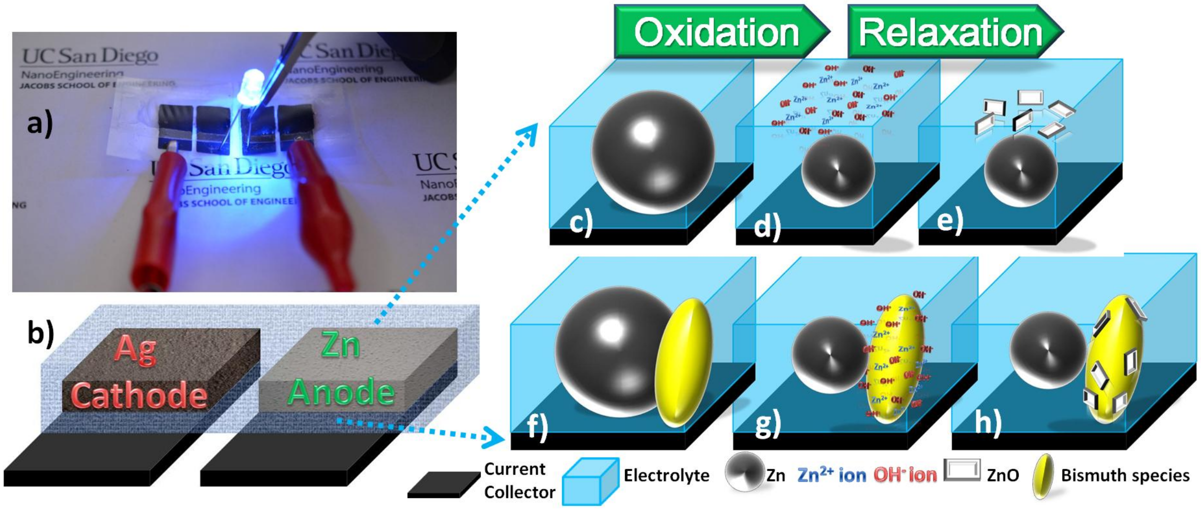

Figure A2.6. Design of Lateral, Printed Battery and Schematic of Possible Reactions between Charge and Discharge. a) Two Zn-Ag full-cells lighting up an LED. b) A conceptual image illustrating the full-cell configuration. Schematics illustrating possible reaction mechanisms for the Zn electrode (c-e) and the Zn with Bi_2O_3 additive electrode (f-h). In the scheme, the phase transformation of bismuth species, PVDF polymer binder, and polyurethane sealing are omitted for clarity.

In the XPS result, a Bi^{3+}/Zn^{2+} mixed phase is found. At the room temperature, monoclinic α-Bi_2O_3 phase is stable and all the Bi^{3+} coordination environments are distorted half-octahedron: [BiO_5E] (E denotes an unshared electron pair). At higher temperature, a body-centered cubic (BCC) γ-Bi_2O_3 is the stable phase and some Bi^{3+} coordination environments are tetrahedron: [BiO_4] [39]. Furthermore, in the presence of Zn^{2+}, the BCC phase is stable at the room temperature [39-41]. $Bi_{38}ZnO_{58}$, part of the sillenite family, is a BCC phase with the tetrahedron coordination environment. Although it is hard to conclude that $Bi_{38}ZnO_{58}$ is formed, but we can be certain that a new phase with [BiO_4] local bonding has formed.

The improvement on the rechargeability of the Bi_2O_3 electrode over time is related to the deposition of ZnO rather than conductivity. While this work describes various bismuth-based species involved during the cycling process, the zincate ions deposit on the surface of the bismuth species regardless of the bismuth species. Based on the findings of this study, a possible reaction mechanism is proposed in figure A2.6. Without the Bi_2O_3 additive, the Zn particles in the electrode upon oxidation, form zincate ions. The zincate ions are dissolved into the electrolyte and into ZnO. Since ZnO is not on the electrode where electron pathways are, this electrode is not rechargeable. By adding Bi_2O_3, the zincate ions deposit on the surface of the bismuth species and relax into ZnO on the bismuth species, making this electrode rechargeable.

A2.1.4 Conclusions

Various additives are mixed into the Zn electrodes and their electrochemical performances are presented. Among the additives, Bi_2O_3 is the critical additive in improving the cycle life of the Zn electrode. Through carefully characterizing the Bi_2O_3 containing Zn electrode, we gained the comprehensive mechanistic role of Bi_2O_3. Firstly, upon oxidation, the zincate ions are formed and deposited on the surface of the bismuth species. Secondly, the zincate ions relax into ZnO on the bismuth species. The electrode is fully rechargeable because the electrical connection is retained for the ZnO. Notable additional phenomena were discovered in this work. The Zn-Bi alloy and the new Bi^{3+}/Zn^{2+} mixed oxide phases were found. Although the exact crystal structure of these phases is unknown, the identification of the phases can be achieved through series of computational modeling and experimental investigation. Nevertheless, the benefit of adding Bi_2O_3 is previously assumed to be in conductivity, however this work confirms that the vital role of Bi_2O_3 is providing surfaces for the ZnO to deposit. This work clearly defines the mechanistic role of Bi_2O_3 in the Zn electrode. The findings in this work can potentially help gaining a better understanding on the large crystal transformation systems such as conversion systems in LIBs.

A2.2 References

1. Deane, J.P., B.P.O. Gallachoir, and E.J. McKeogh, *Techno-economic review of existing and new pumped hydro energy storage plant.* Renewable & Sustainable Energy Reviews, 2010. **14**(4): p. 1293-1302.

2. Pearce, J.M., *Thermodynamic Limitations to Nuclear Energy Deployment as a Greenhouse Gas Mitigation Technology.* International Journal of Nuclear Governance, Economy and Ecology, 2008. **2**(1): p. 17.

3. Walker, W., S. Grugeon, O. Mentre, S. Laruelle, J.M. Tarascon, and F. Wudl, *Ethoxycarbonyl-Based Organic Electrode for Li-Batteries.* Journal of the American Chemical Society, 2010. **132**(18): p. 6517-6523.

4. Walker, W., S. Grugeon, H. Vezin, S. Laruelle, M. Armand, J.M. Tarascon, and F. Wudl, *The effect of length and cis/trans relationship of conjugated pathway on secondary battery performance in organolithium electrodes.* Electrochemistry Communications, 2010. **12**(10): p. 1348-1351.

5. Nakahara, K., S. Iwasa, M. Satoh, Y. Morioka, J. Iriyama, M. Suguro, and E. Hasegawa, *Rechargeable batteries with organic radical cathodes.* Chemical Physics Letters, 2002. **359**(5-6): p. 351-354.

6. Toussaint, G., P. Stevens, L. Akrour, R. Rouget, and F. Fourgeot, *Development of a rechargeable zinc-air battery.* Metal/Air and Metal/Water Batteries, 2010. **28**(32): p. 25-34.

7. Chen, H., T.N. Cong, W. Yang, C. Tan, Y. Li, and Y. Ding, *Progress in electrical energy storage system: A critical review.* Progress in Natural Science, 2009. **19**(3): p. 291-312.

8. Kim, H.I., E.J. Kim, S.J. Kim, and H.C. Shin, *Influence of ZnO precipitation on the cycling stability of rechargeable Zn-air batteries.* Journal of Applied Electrochemistry, 2015. **45**(4): p. 335-342.

9. Minakshi, M., *Alkaline-Earth Oxide Modified MnO2 Cathode: Enhanced Performance in an Aqueous Rechargeable Battery.* Industrial & Engineering Chemistry Research, 2011. **50**(14): p. 8792-8795.

10. Ma, H., C.S. Li, Y. Su, and J. Chen, *Studies on the vapour-transport synthesis and electrochemical properties of zinc micro-, meso- and nanoscale structures.* Journal of Materials Chemistry, 2007. **17**(7): p. 684-691.

11. Li, Q., P. Xu, B. Zhang, H.H. Tsai, J. Wang, H.L. Wang, and G. Wu, *One-step synthesis of Mn3O4/reduced graphene oxide nanocomposites for oxygen reduction in nonaqueous Li-O-2 batteries.* Chemical Communications, 2013. **49**(92): p. 10838-10840.

12. Liu, Z., T. Cui, G. Pulletikurthi, A. Lahiri, T. Carstens, M. Olschewski, and F. Endres, *Dendrite-Free Nanocrystalline Zinc Electrodeposition from an Ionic Liquid Containing Nickel Triflate for Rechargeable Zn-Based Batteries.* Angewandte Chemie-International Edition, 2016. **55**(8): p. 2889-2893.

13. Mcbreen, J. and E. Gannon, *Bismuth Oxide as an Additive in Pasted Zinc Electrodes.* Journal of Power Sources, 1985. **15**(2-3): p. 169-177.

14. Mcbreen, J. and E. Gannon, *The Electrochemistry of Metal-Oxide Additives in Pasted Zinc Electrodes.* Electrochimica Acta, 1981. **26**(10): p. 1439-1446.

15. Simons, T.J., M. Salsamendi, P.C. Howlett, M. Forsyth, D.R. MacFarlane, and C. Pozo-Gonzalo, *Rechargeable Zn/PEDOT Battery with an Imidazolium-Based Ionic Liquid as the Electrolyte.* Chemelectrochem, 2015. **2**(12): p. 2071-2078.

16. Huang, H., S.J. Gu, Y.P. Gan, X.Y. Tao, and W.K. Zhang, *ZnO/ZnO-Bi2O3 nanocomposite as an anode material for Ni-Zn rechargeable battery.* Advances in Chemical Engineering, Pts 1-3, 2012. **396-398**: p. 1725-1729.

17. Moser, F., F. Fourgeot, R. Rouget, O. Crosnier, and T. Brousse, *In situ X-ray diffraction investigation of zinc based electrode in Ni-Zn secondary batteries.* Electrochimica Acta, 2013. **109**: p. 110-116.

18. Harwig, H.A. and A.G. Gerards, *Electrical-Properties of Alpha, Beta, Gamma and Delta Phases of Bismuth Sesquioxide.* Journal of Solid State Chemistry, 1978. **26**(3): p. 265-274.

19. Tao, H.S., X. Tong, L. Gan, S.Q. Zhang, X.M. Zhang, and X. Liu, *Effect of adding various carbon additives to porous zinc anode in rechargeable hybrid aqueous battery.* Journal of Alloys and Compounds, 2016. **658**: p. 119-124.

20. Berchmans, S., A.J. Bandodkar, W.Z. Jia, J. Ramirez, Y.S. Meng, and J. Wang, *An epidermal alkaline rechargeable Ag-Zn printable tattoo battery for wearable electronics.* Journal of Materials Chemistry A, 2014. **2**(38): p. 15788-15795.

21. Peles, A., V.P. Pavlovic, S. Filipovic, N. Obradovic, L. Mancic, J. Krstic, M. Mitric, B. Vlahovic, G. Rasic, D. Kosanovic, and V.B. Pavlovic, *Structural investigation of mechanically activated ZnO powder.* Journal of Alloys and Compounds, 2015. **648**: p. 971-979.

22. Liu, H.F., S. Tripathy, G.X. Hu, and H. Gong, *Surface optical phonon and A(1)(LO) in ZnO submicron crystals probed by Raman scattering: Effects of morphology and dielectric coating.* Journal of Applied Physics, 2009. **105**(5).

23. Prutton, M., ed. *Surface Physics*. 2 ed. 1983, Thetford, Oxford University Press.

24. Tringe, J.W., H.W. Levie, S.K. McCall, N.E. Teslich, M.A. Wall, C.A. Orme, and M.J. Matthews, *Enhanced Raman scattering and nonlinear conductivity in Ag-doped hollow ZnO microspheres.* Applied Physics a-Materials Science & Processing, 2012. **109**(1): p. 15-23.

25. Nakata, A., H. Arai, T. Yamane, T. Hirai, and Z. Ogumi, *Preserving Zinc Electrode Morphology in Aqueous Alkaline Electrolytes Mixed with Highly Concentrated Organic Solvent.* Journal of the Electrochemical Society, 2016. **163**(2): p. A50-A56.

26. Fan, H.Y., G.N. Wang, and L.L. Hu, *Infrared, Raman and XPS spectroscopic studies of Bi2O3-B2O3-Ga2O3 glasses.* Solid State Sciences, 2009. **11**(12): p. 2065-2070.

27. Tahar, N.B. and A. Savall, *Electrochemical degradation of phenol in aqueous solution on bismuth doped lead dioxide: a comparison of the activities of various electrode formulations.* Journal of Applied Electrochemistry, 1999. **29**(3): p. 277-283.

28. Wang, X.J., N. Liu, S. Shi, and Y.X. Chen, *XPS Depth Study on the Liquid Oxidation of Sn-Bi-Zn-X(Al/P) Alloy and the Effect of Al/P on the Film.* Advances in Materials Science and Engineering, 2015.

29. Hanna, T.A., A.L. Rieger, P.H. Rieger, and X.Y. Wang, *Evidence for an unstable Bi(II) radical from Bi-O bond homolysis. Implications in the rate-determining step of the SOHIO process.* Inorganic Chemistry, 2002. **41**(14): p. 3590-3592.

30. Gaikwad, A.M., A.M. Zamarayeva, J. Rousseau, H.W. Chu, I. Derin, and D.A. Steingart, *Highly Stretchable Alkaline Batteries Based on an Embedded Conductive Fabric.* Advanced Materials, 2012. **24**(37): p. 5071-5076.

31. Kettlgruber, G., M. Kaltenbrunner, C.M. Siket, R. Moser, I.M. Graz, R. Schwodiauer, and S. Bauer, *Intrinsically stretchable and rechargeable batteries for self-powered stretchable electronics.* Journal of Materials Chemistry A, 2013. **1**(18): p. 5505-5508.

32. Yan, C.Y., X. Wang, M.Q. Cui, J.X. Wang, W.B. Kang, C.Y. Foo, and P.S. Lee, *Stretchable Silver-Zinc Batteries Based on Embedded Nanowire Elastic Conductors.* Advanced Energy Materials, 2014. **4**(5).

33. Winslow, R., C.H. Wu, Z. Wang, B. Kim, M. Keif, J. Evans, and P. Wright, *Development and manufacture of printable next-generation gel polymer ionic liquid*

electrolyte for Zn/MnO2 batteries. 13th International Conference on Micro and Nanotechnology for Power Generation and Energy Conversion Applications (Powermems 2013), 2013. **476**.

34. Tsukamoto, T. and S. Tanaka, *Printable on-chip micro battery for disposal bio-sensing device.* 15th International Conference on Micro and Nanotechnology for Power Generation and Energy Conversion Applications (Powermems 2015), 2015. **660**.

35. Braam, K.T., S.K. Volkman, and V. Subramanian, *Characterization and optimization of a printed, primary silver-zinc battery.* Journal of Power Sources, 2012. **199**: p. 367-372.

36. Gupta, T., A. Kim, S. Phadke, S. Biswas, T. Luong, B.J. Hertzberg, M. Chamoun, K. Evans-Lutterodt, and D.A. Steingart, *Improving the cycle life of a high-rate, high-potential aqueous dual ion battery using hyper-dendritic zinc and copper hexacyanoferrate.* Journal of Power Sources, 2016. **305**: p. 22-29.

37. Lee, S.M., Y.J. Kim, S.W. Eom, N.S. Choi, K.W. Kim, and S.B. Cho, *Improvement in self-discharge of Zn anode by applying surface modification for Zn-air batteries with high energy density.* Journal of Power Sources, 2013. **227**: p. 177-184.

38. Yano, M., S. Fujitani, K. Nishio, Y. Akai, and M. Kurimura, *Effect of additives in zinc alloy powder on suppressing hydrogen evolution.* Journal of Power Sources, 1998. **74**(1): p. 129-134.

39. Guha, J.P., S. Kune, and D. Suvorov, *Phase equilibrium relations in the binary system Bi2O3-ZnO.* Journal of Materials Science, 2004. **39**(3): p. 911-918.

40. Radaev, S.F. and V.I. Simonov, *Structure of Sillenites and Atomic Mechanisms of Isomorphous Substitutions in Them.* Kristallografiya, 1992. **37**(4): p. 914-941.

41. Mel'nikova, T.I., G.M. Kuz'micheva, N.B. Bolotina, V.B. Rybakov, Y.V. Zubavichus, N.V. Sadovskaya, and E.A. Mar'ina, *Structural features of compounds of the sillenite family.* Crystallography Reports, 2014. **59**(3): p. 353-361.

A.3 All-Printed, Island-Bridge, Stretchable Electronics

A3.1.1 Introduction

After a decade of smartphones and wearable products proliferating into every aspect of our daily lives, the drive for smaller, thinner, and more conformal electronics has invoked a shift in the electronics industry. A new generation of electronics, such as sensors,[1-5] e-textiles,[6-8] soft robotics, [9, 10] wearables electronics,[11] energy storage device,[12-16] and hemispherical eye cameras,[17] have been engineered to have great flexibility and stretchability to the point that they become indistinguishable from the our own skin or clothing we come in contact every day. The re-engineering of once traditionally, rigid, bulky electronics to conform and deform with its attached structure, hence the division of “stretchable electronics” was conceptualized. This new class of electronics relies on its ability to seamlessly mate with curvilinear surfaces while maintaining a stable performance, even under extreme strain is applied. Stretchable electronics enables novel form factors and applications that were not possible with conventional electronics.

The fabrication of stretchable electronics relies on modifying composites via three approaches: deterministic design,[18, 19] intrinsic material properties,[20, 21] and random composite [6, 22]. The deterministic composite approach turns geometrically patterned, traditionally rigid materials into a stretchable device. In this fabrication method, extremely thin, serpentine-/coil-shaped interconnections (“bridges”) are integrated to accommodate strain between non-deformable functional components (“islands”) and binds them onto a soft, stretchable substrate [23] to form the complete device. The island-bridge approach thus represents an attractive route for realizing stretchable electronics.

The deterministic approach offers a distinct advantage since the functional components maintain consistent performance when being stretched due to their intrinsic rigidity [23]. Stretching can be achieved through in and out of plane buckling using selective bonding of islands to the substrate [24, 25]. However, the fabrication of devices that rely on a deterministic design that is often composed of complicated processing steps by either cleanroom lithographic or “cut-and-paste” [24-26]. The use of such subtractive fabrication methods has limited choice of compatible materials, in addition to being, expensive, difficult, time-consuming and overall low-throughput [19, 21]. A Recent study demonstrated a hybrid approach for creating a high-performance device leveraging IB structure, where the backbone IB structure is fabricated using a typical lithographic deposition, followed by the thick-film screen-printing deposition of carbon and polymer-based functional material composite [19]. The current progress of stretchable electronics is being bottlenecked by the complexity of the lithographic fabrication, which prevents such versatile and conformal devices to be commercially adaptable.

Alternatively, the intrinsically stretchable approach utilizes conducting polymers where their molecular structures can be fine-tuned to enable stretchability [20, 21]. The simplicity of conductive polymers through solution processing presents a more cost-effective, scalable fabrication and a new approaches for transferring stretchable electronics from 2D substrate to 3D surfaces [27].Unfortunately, the use of conductive polymers still has inferior electric conductivity compared to bulk counterparts that have been actively developed and widely studied [28]. The random composite approach, a hybrid of both the intrinsic and deterministic, stretchable designs, randomly mixes conductive fillers and elastic polymers that support the robust mechanical stability of the device [21]. The conductive fillers are typical powder or nanomaterials that maintain electrical conductivity where at the optimal percolation threshold, they can maintain electrical characteristic as they slide along each other during strain [21].

Here in, we describe the first example of using all-printing techniques to create an ‘island-bridge” (IB) deterministic structures for epidermal or textile applications. As illustrated in Figure A4.1, such all-printed IB architectures relies on the judicious combination of random composite inks and deterministic patterning for printing variety of active components reside at the islands and the electrical bridge interconnects. This method of depositing inks on to surfaces is already a commercial standard in printing colorful, artistic designs for temporary tattoos, textiles, and electrochemical devices for glucose monitoring because of its affordability, high-throughput, and simplicity [29-31]. The design of the conductive ink formulation included a block-polystyrene-block-polyisoprene-block-polystyrene copolymer, which acts as the binder that gave the ink superior mechanical performance. In the composite, due to the affinity of styrene to each other, the block-polystyrene part of polymer chains formed a physical crosslinking, while all the block-polystyrene crosslinking center were interconnected by long chains from the block-polyisoprene. Hence, a self-assembled hyperelastic nanostructure of hard connected by “soft domains were formed in the elastic composite ink. Unlike previous works using lithographic or cut-and-paste fabrication, the method presented in this work relies solely on the thick-film printing of both the island and bridge structures. Attention in printing the stretchable serpentine silver interconnects is the influence of the sinuous geometry (line width or angle) upon the observed performance and the interface of these serpentine bridges with the printed functional composite islands. A macro level of structural stretchability leveraging IB designs is thus merged with a micro level inherent stretchability of the composite ink.

In previous studies, we have demonstrated a hybrid design combining random composite and deterministic structures using entanglement based binder, such as polyurethane and carbon-based nanomaterials [5]. The simple processing of these thermoplastic elastomers can incorporate virtually unlimited choices and combinations of conductive, functional fillers. In the case of the serpentine bridges, where the high conductivity and stretchability are required simultaneously, the random composite ink, consisting of a hyperelastic binder and highly conductive silver flakes, displayed high-performance in both conductivity and durability. The functional islands are manufactured with conductive inks with any filler (micron powder, nanomaterials, composite) for a wide range of printed electronics, stretchable electronics, robotics, sensing, or display applications. These functional islands can also undergo an interesting stretching profile compared to traditional lithographically-fabricated rigid islands.

The inclusion of random composite approach with deterministic approach enables this hybrid approach to be extremely versatile by embedding any combination of conductive fillers into an elastic matrix to form an elastic, conductive composite[28]. A random composite is an attractive approach for its versatility, as the electrical and mechanical performance can be tailored based on the ratio of composite materials[12]. Also, the unlimited range of material choices, such as nanomaterials or carbon composites with various morphological shapes, already seeing implementation in multiple technologies and disciplines and can be easily incorporated in this process [32, 33]. The scope and limitations of the new printing strategy with an example of its practical use: a skin-worn, printed zinc battery with an area density capacity of 1.5 mAh/cm^{-2}, is demonstrated and discussed in detail in this work.

A3.1.2 Results & Discussion

As stretchable electronics continues to evolve from rigid technologies listed previously, it is imperative for the polymer-particle composites to be compatible with any substrates. The primary challenge for epidermal and textile-based electronics is that with a fabrication that is inexpensive and scalable as well. The versatility of composite ink formulations and simple processing of thick-film screen-printing, the complexity and unique characteristics offered by nanomaterials is applicable for inexpensive, high-performance, stretchable electronics. With the rise of complexity and geometries presented by nanomaterials, the versatility of composite ink formulations and simple processing of thick-film screen-printing, here are now unlimited possibilities for inexpensive, high-performance and stretchable electronics.

In the present study, the IB stretchable electronics structure have been fabricated by screen-printing of stress-enduring silver and carbon-composite inks, respectively. Figure A3.1 demonstrates the step-by-step printing of the IB structure and its integration with textile and epidermal (E-skin) applications. A thre**e** by 3 array of functional “islands," connected with serpentine “bridges," was fabricated in two simple steps illustrated in Figure A3,1A. Utilizing a simple computer-aid design (CAD) software, any desired design patterns into a custom designed stainless-steel stencil to control where the ink deposits onto the substrate. In step 1 of Figure A3,1A, any ink composite of any desired conductive filler and polymers, in this case, a commercial graphitic or elastic/graphitic ink, can be printed as functional islands onto any substrate to printing technologies. In Figure A3,1B, a segment of a water-soluble tape was used to aid the final transfer of device onto the epidermis or textile. After curing the first printed layer, a highly conductive Ag-flake mixing in a resin of elastic polymer in organic solvents. The composite ink then printed directly on top in a specific serpentine, therefore acting as an elastic interconnect between the functional islands (Figure A3, 1C). Having a thorough understanding of each ink component is key to the optimization of the composite's elastic and conductive properties, discussed in detail. After curing the printed inks on to a water-soluble tape, the tape can be peeled from the carrier paper, flipped and attached to skin that is pre-sprayed with medical adhesives, (Figure A3,1D). After applying considerable pressure to ensure adhesion, the water-soluble tape dissolves by rinsing gently with cold water for 30 seconds or less. The printed device remains on the skin with a high resolution without any residue of substrate, and is capable of undergo multiple forms of deformation, such as compression, pinching, indentations. (Figure A3,1E, A3,1F, A3,1G). By reversing the order of printing, the device can be printed directly on to the surface of a textiles, where both island and bridges can undergo the same deformations (Figure A3,1H-J). Interactive curvilinear surfaces will such as textiles, epidermis, robotic skins will completely cover with stretchable electronics (Figure A3,1K).

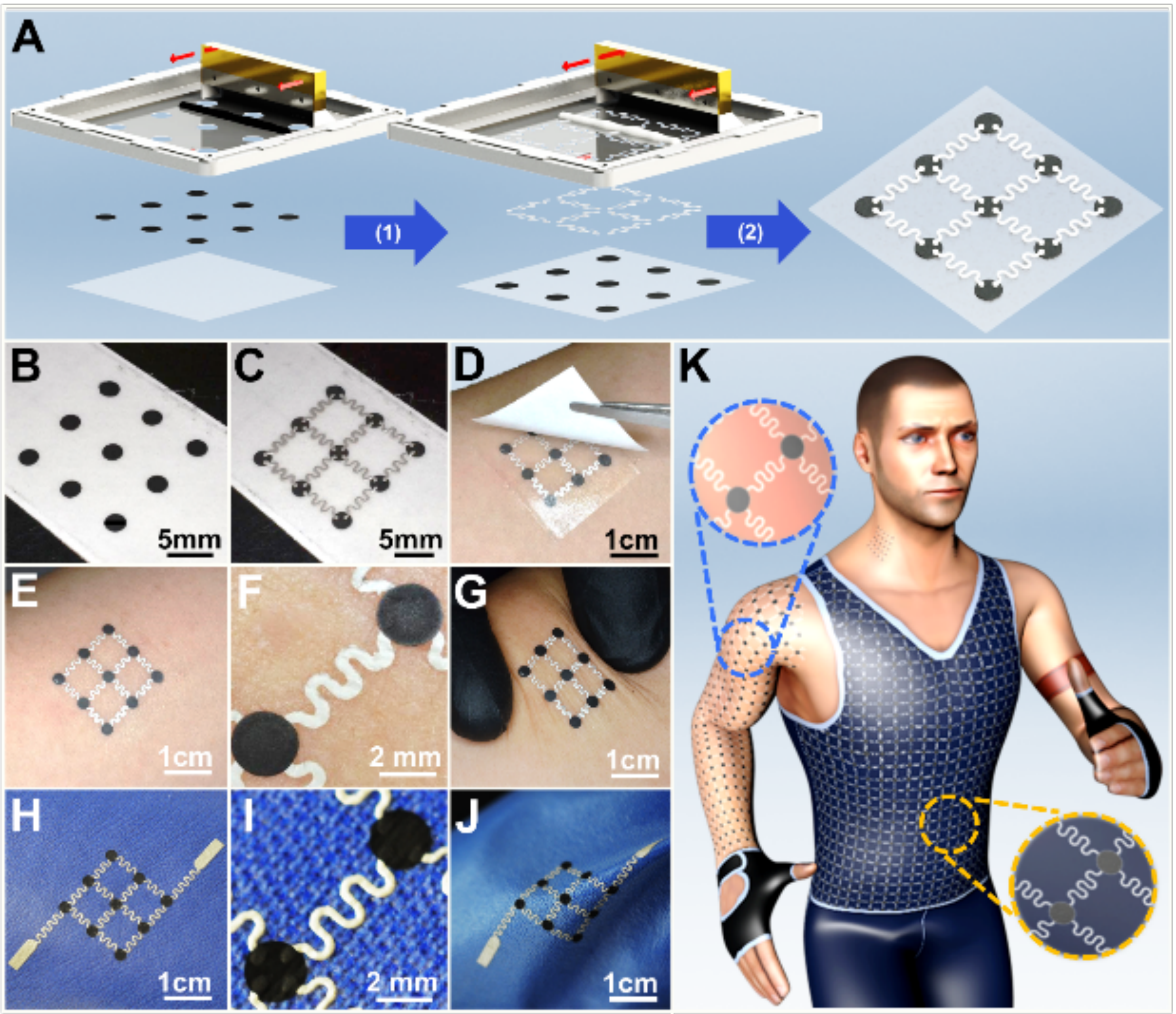

Figure A3.1: All-Printed, Stretchable “Island-Bridge” Electronics. (A) Screen-printing, fabrication steps of elastic carbon ink as functional islands and followed by elastic, silver bridges in serpentine configuration (line width >150 microns). (B) Printed elastic carbon ink on water-soluble tape and (C) elastic, serpentine bridge printed on top of carbon. (D) After curing, the sample is transferred to the skin and water-soluble tape is removed with a simple washing step. (E) Printed sample transferred on to skin, (F) zoomed in, and (G) compressed device/skin. (H) Printed island-bridge directly onto textile, (I) zoom in, (J) folding device/textile. (K) Concept of these devices that can be expanded for large-area electronics on skin and textiles.

Having a thorough understanding of each ink component is key to the optimization of the composite’s elastic and conductive properties. The formulation of the elastic inks is tailored based on the ratio of conductive fillers and elastomer- binder to achieve great contact with the rough skin surface. Polystyrene-block-polyisoprene-block-polystyrene

(SIS) is chosen as the binder for its ability to remain highly elasticity (elongation >1500% for pristine sample) while binding a significant amount of conductive fillers such as silver flakes or carbon micron powder, in the ink formulation[23]. The unique structure of SIS consists of both polyisoprene elastic blocks and polystyrene plastic blocks that physically self-crosslinks into a network with high elasticity.

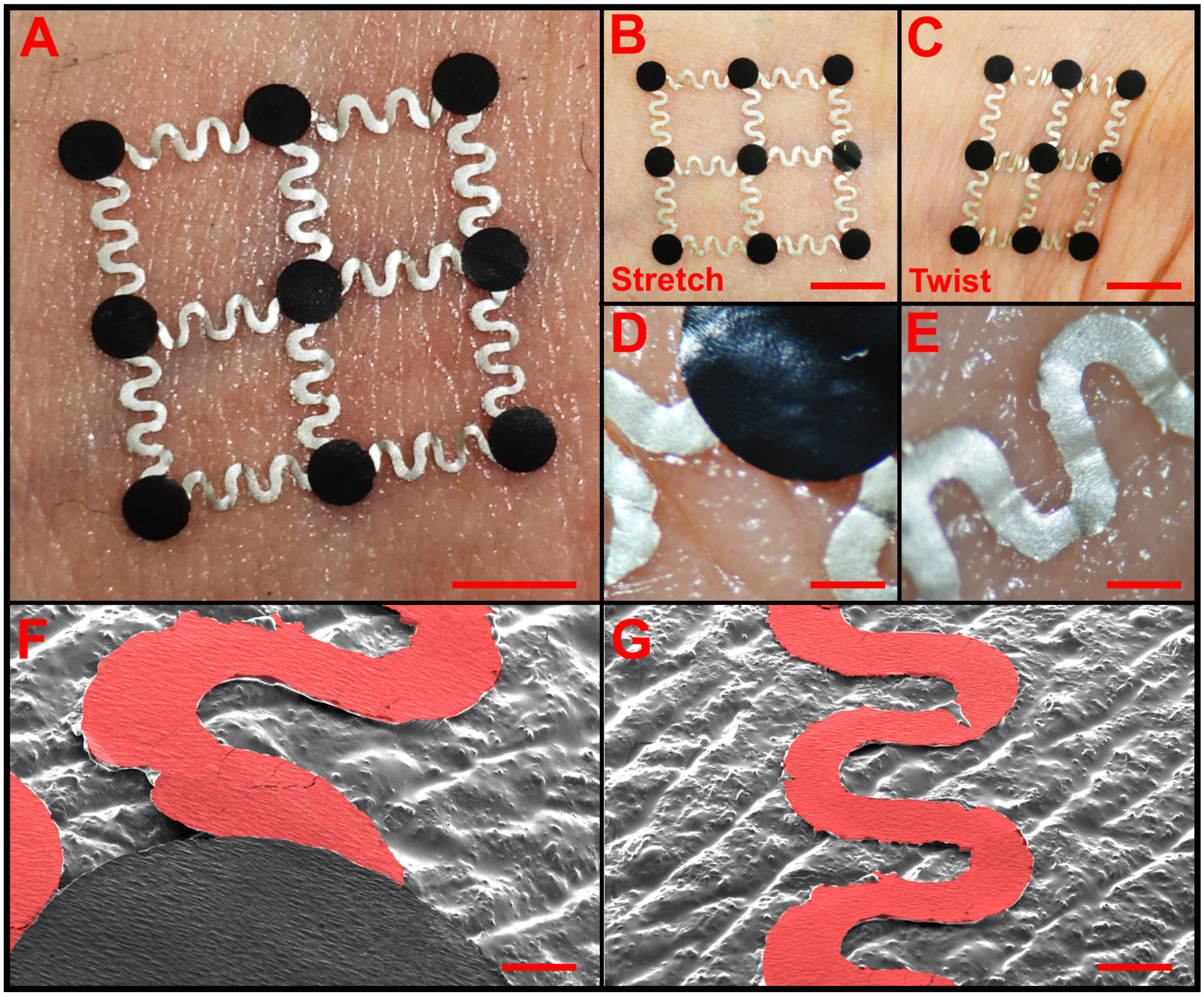

Figure 3.2: Imaging of Stretchable, Composite Inks Transferred to Skin. Optimal image of printed IB device transfer from PVA tape to skin with spray-on-adhesive, under no deformation (A), stretch (B), and twist (C), scale bar 5 mm. The microscopic morphology of the connection with functional island (D) and conductive, serpentine bridge (E) of the device on skin, scale bar 500 microns (F, G) Colorized SEM image of printed IB of serpentine bridge (red) and functional island (black) on a skin replica, silicon mold, scale bar 250 microns.

Due to the thin structure and innate elasticity of the composite ink, the printed IB structure can conform to the uneven surface of the skin even when the skin is stretched or twisted, are shown in Figure A3.2A-C. A micrograph of the interface between the IB structure and the skin is demonstrated in Figure A3.2D, where the serpentine interconnects are capable of embedding itself into the large crevices of the skin and the more rigid carbon islands that lay across. SEM images of the printed IB structure applied to a silicone mold of synthetic skin are used to investigate the interfacial contact with the finer features of the skin surface. Figure A3.2F and A3.2G demonstrates the level of conformality of the printed IB structure to the surface of the synthetic skin. The serpentine bridges here conform less to the fine features of the skin compared to figure A3.2E, where the crevices are shallower. The thickness and modulus of the printed directly correlates to the conformality of the structure to skin's surface. Due to the thick-film fabrication technique used for the IB structures which deposits material in ~10^{-4} m thicknesses, the performance of the serpentines, which were studied comprehensively for those fabricated photolithographically (thickness of 10^{-6} m), can have large discrepancies with their photolithographic counterparts. Therefore, the study of the printed island-bridge structure is of great importance.

Serpentine Bridge Printing and Conductivity-Strain Measurements

Metal-based serpentines fabricated photolithographically or laser-cut, due to their drastically different mechanical properties compared to soft composites, shows little expansion when stretched, and the serpentine structure may buckle out of the plane when the adhesion with the substrate is low [24]. The overall stretchability of the structure heavily depends on the design of the serpentine, where the structures undergo elastic then inelastic buckling to compensate for the deformation. When the designed maximal allowed strain is exceeded, such structures will quickly rip, break and disconnect, due to the lack of elasticity of metals. The printed serpentine, on the other hand, has drastically lower Youngs modulus of roughly 3.8 MPa, which bond tightly to the substrate, and can withstand much higher strain before irreversible damage is done to the structure form [25]. Hence, the effect of varying designs on the performance of serpentines will differ from ones that are metal-based and should be carefully studied.

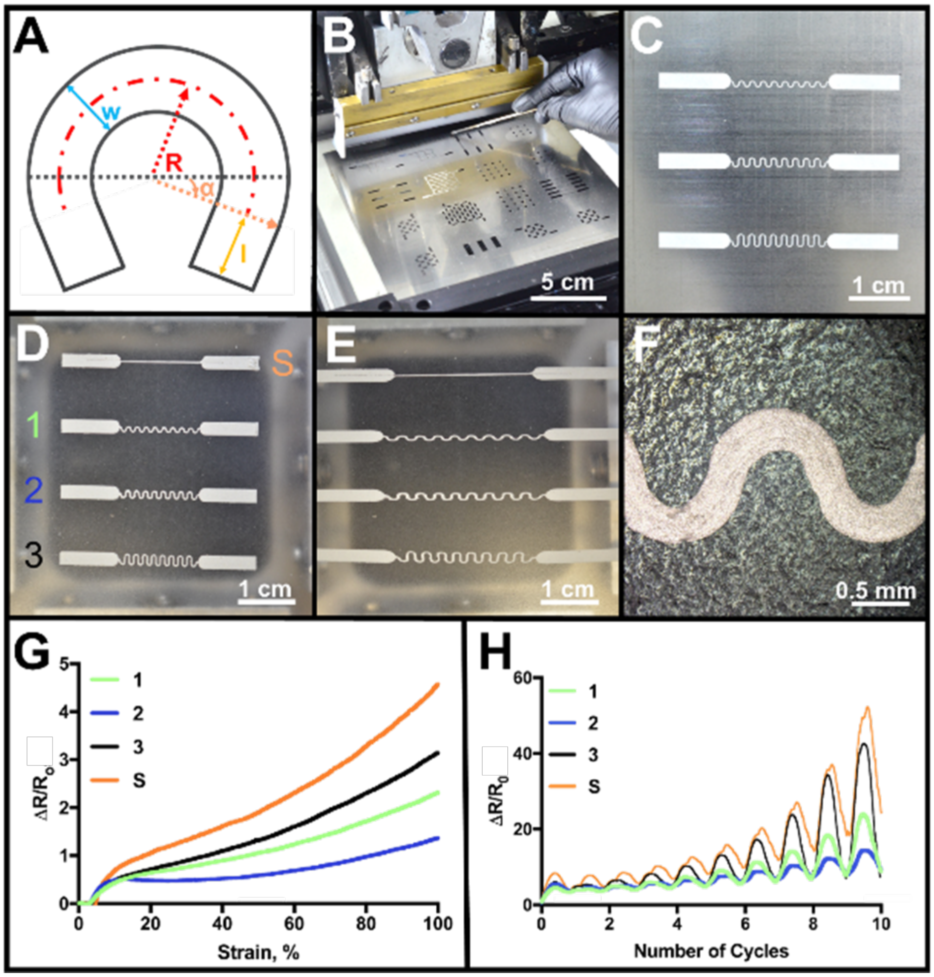

Figure A3.3: Uniaxial Stretching of Serpentine Bridges. (A) Geometric parameters for width, length, and angle of serpentine bridges. (B) Image of stencil employed for printing electronics of pre-cut design. (C) Image of stencil design for serpentine bridge with varied line width (w = 150, 250, 500 micron/um). Optical images of printed, stretchable inks using varied serpentine design at (D) 0%,(E) 100% stretch, and (F) detailed image of the serpentine design. (G) Change of resistance as each printed design is stretched 100% and (H) tested for 10 cycles of repetitive stretching.

The serpentine bridges are composed of single “horseshoe” units depicted in Figure A3.3A where its parameters of arc width (w), arc radius (R), arc angle (α), and linear arm length (l) can be modified along with its mechanical behavior. These features can be specially designed using a computer-aided design (CAD) software to be cut into a stainless stencil (Figure A.3B) for screen-printing. For initial tests, designs with line width (w = 250 μm), radius (R = 425 μm), arc angle (α = 0º), and only linear arm length was varied (l = 0, 500, and 1000 μm), as shown in the section of the stencil (Figure 3.3C). A straight line with the same line width is also added as the baseline of to the serpentine designs. An elastic polyurethane (PU) sheet is chosen for its superior stretchability, and the aforementioned straight line (denoted “S”) and three serpentines with increasing arm length (denoted “1”, “2” and “3”) are printed using the formulated silver ink. (Figure 3.3D) The prints were stretched from 0% to 100% (Figure 3.3E) over multiple iterations. It is worth noting that even after several 100% stretching iterations, the print, depicted in Figure 3F, can reset to its original shape with no noticeable damage. The adhesion of the composite to the PU substrate is evident as well, showing no signs of delamination.

The measurement of the resistance of each device is conducted while being strained at a constant speed. Compared to the printed straight line, all three printed serpentine structures demonstrated less change in resistance throughout the 100% stretch. However, irregular trend is observed in Figure 3G, as the serpentine structure #2 with 500 μm arm length demonstrated the best stability, followed by the serpentine structure #1 with 0 μm arm length, with the 1000 μm arm length serpentine structure (#3) least stable. Evident from the cycling test, shown in Figure 3H, serpentine #2 also continues to display superior stability compared to the straight line and other serpentine designs. As opposed to metal-based serpentine designs whose stretchability increases with the arm length, the stability of printed serpentines does not increase with the armlength. Such irregularity is suspected to be caused by the good adhesion between the print and the substrate, where the printed composites will experience similar strain as the substrate and hence have decreases in conductivity due to the lateral expansion of the prints. As the linear arm length increase, after a certain point, the expansion of linear arm segments becomes the dominant factor of resistance change. This can be attributed to how serpentine #3 demonstrated poor durability compared to serpentine #2. The tight binding is inhered from the use of toluene as a solvent, which can cause temporary swelling of PU-based substrates. Thus, encouraging bonding between the composite polymer and the substrate after curing. As a tradeoff, when the IB structure is being stretched, the serpentine is unable to unbuckle from the substrate, hence being internally expanded along with the substrate, leading to the increase in resistance. However, this tight bonding eliminates the serpentine structures from experiencing detrimental deformation and loss in connection, even when the serpentine design is being stretched over its metal-based counterparts' maximum strains? Another explanation, considering from the fabrication point of view, is due to the increase in overall structural length, the possibility of defects forming also increases. For thick-film fabrication techniques such as screen-printing that have limited resolutions compared to photolithography/laser-cutting, the complexity and finesse of the designs are tightly correlated to the formation of defects.

Printed “Island-Bridge” Architectures and Conductivity-Strain Measurements

The remarkable stretchability of the fine screen-printed serpentine designs needs to be studied in conjunction with functional islands. Unlike deterministic approaches that rely on serpentine bridges to accommodate all the strain, these printed “island-bridges” will see both the serpentine and functional islands stretch when strain is applied.

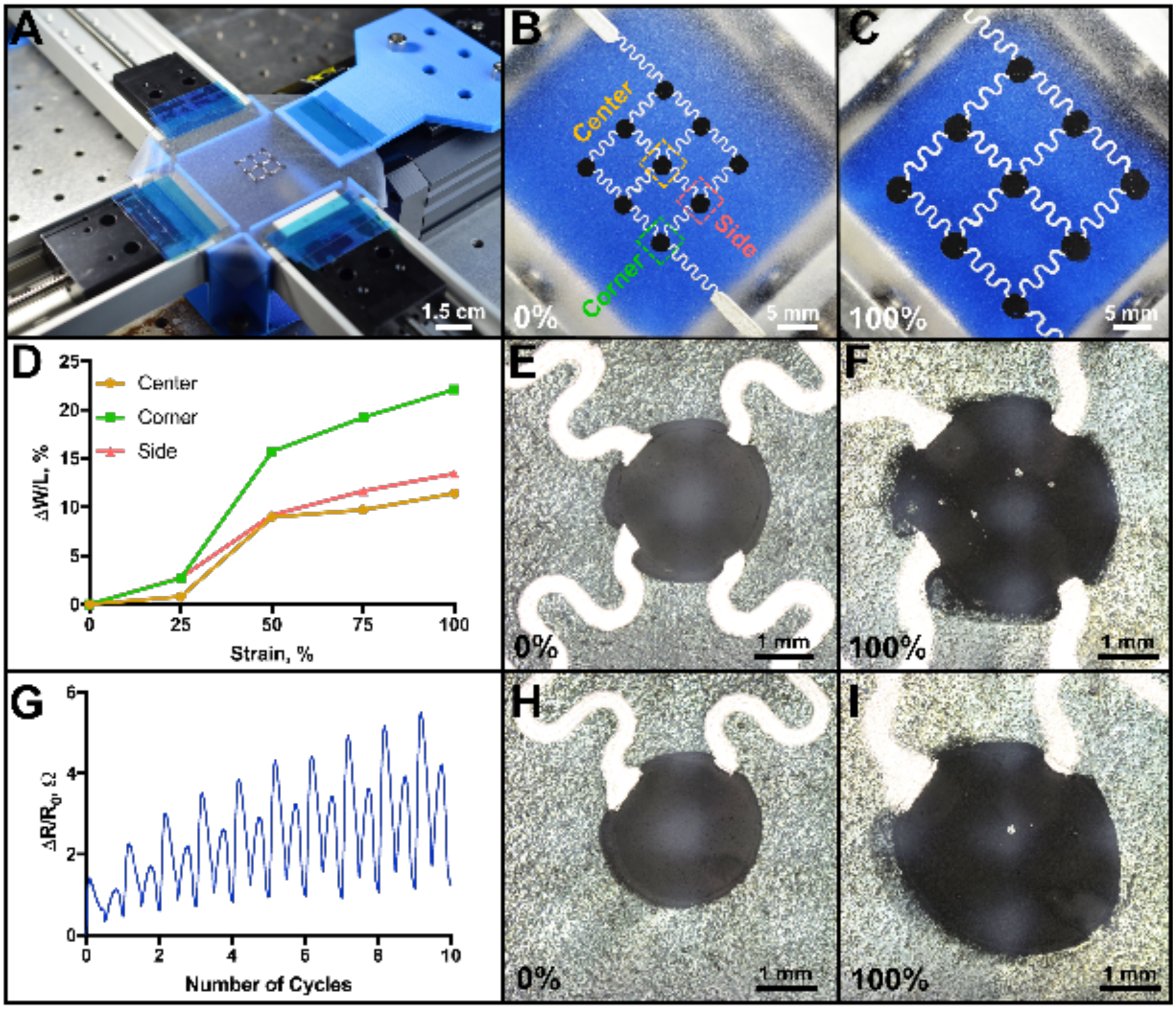

Figure A3.4: Uniaxial Stretching of Serpentine Bridges. (A) Printed sample on PU mounted onto a custom-made, motorized stage. (B) Un-stretched and (C) stretched image of 3 by 3 island-bridge array with designed imaging of island deformation. (D) Deformation of islands at different island-serpentine pairs from 0% to 100%. Microscopic image of center island at (E) 0% and (F) 100% stretch. (G) Conductivity measurements of biaxial stretching to 50% over 10 cycles. Microscopic image of corner island at (H) 0% and (I) 100% stretch.

In the costumed mechanical stretching stage (see supporting information), the formulated silver ink is printed as serpentine bridges onto PU substrate, followed by the printing of a formulated elastic carbon ink (Figure A3.4a). In the design, there are different numbers of serpentine bridges, connected to a specific bridge, such as the "side," “center," and "corner", designated in Figure A3.4B. From the naked eye, the complete device stretches uniformly, despite the different numbers of serpentine connections that could add further strain or the risk of delamination, as illustrated in Figure A3.4C.

When the functional islands are evaluated at under a microscope, the lack of uniform expansion is noticeable with the asymmetric connections of the “side” and “corner” when compared to the “center” island. In Figure A3.4D, the ratio of cross-sectional diameters should have a consistent ratio of 1 to maintain the circular shape, but that is only demonstrated with the "center" island. This is demonstrated by the center island from 0% stretch (Figure A3.4E) and at 100% stretch (Figure A3.4F). The other “corner” and “side” islands exhibit higher strain along the lengths of the serpentine connections, reflecting the formation of an elliptical shape when strained from 0% (Figure A3.4H) to 100% (Figure A3.4I). Also, pinholes are visible in the carbon ink at the interfaces between the PU substrate, carbon island, and silver serpentine bridge when the ink is stretched. The pinholes can be attributed to the different composite ratios between the “island” and “bridge” components, which has been common to stretchable composite inks [26]. Since the “island” components require higher loadings of conductive carbon fillers to compensate for their low conductivity, compared to the stretchable silver serpentine, the carbon “island” is shifted more in proportion of the silver ink. When the printed devices stretch, pinholes appear in the center of the carbon island, delamination occurs around the connection site, and disproportional deformation at different sites of the array. This presents an interesting aspect compared to lithographic IB where each printed island and its respective connections provides a new dimension and challenge to designing printed, stretchable IB-based electronics. New intricate designs can be arranged in diverse arrangements such as a triangular, hexagon, and many other array connections between the stretchable island/bridge configuration, that will lead to a different behavior, especially evaluating the depth of the connection. Also, these assorted designs will dramatically change the amount of surface area available for the functional islands, as the IB array sacrifices active area to provide more durability.

Printed “Island-Bridge” Zinc-Silver Oxide Battery

The design of the island-bridge structure is quite adaptable to various technologies, especially for electrochemical devices such as batteries, biofuel cells, supercapacitors, and chemical sensors that require two opposing electronics. To demonstrate the applicability of the printed "island-bridge," a printed battery was shown demonstrated using inks modified from our previous printed, stretchable zinc battery. The individual inks are synthesized for zinc and silver-oxide electrodes are powder composites of active material, conductive additives, and other metals to improve the rechargeability. The zinc chemistry was selected for its safety and ability to print in the air, but essentially any battery chemistry can be applied to this format.

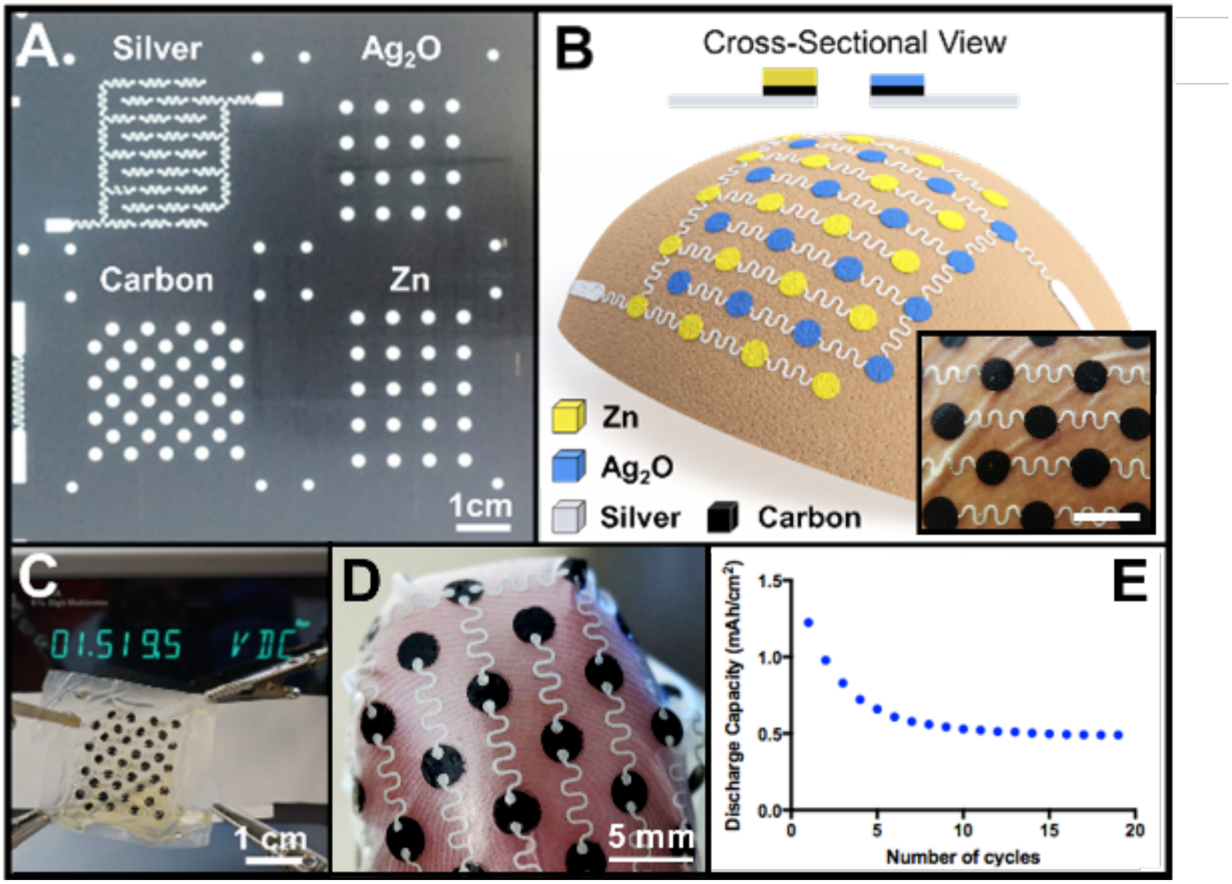

Figure A3.5: Printed Battery in Island-Bridge Configuration (A) Stencil design for serpentine bridge. (B) Epidermal energy storage in an interdigitated design of island-bridge all printed steps completed with inset image of the device on skin, 0.5 mm scale bar (C) Final print of stretchable and its voltage output and (D) surrounded around a thumb finger. (E) Discharge capacity (mAh/cm^2) curves for the rechargeable epidermal battery.

The island-bridge array is modified into an interdigitated design of zinc anode and silver (II) oxide cathode shown in Figure A3.5A and final printed device demonstrated in shown Figure A3.5B. The silver serpentine connections are printed first onto a polyurethane substrate, where they are all connected by carbon islands. The zinc and cathode islands are then printed, followed by a polyurethane pack filled with a gel electrolyte and finally sealed.

The printed battery demonstrates good electrical (Figure A3.5C) and mechanical durability as the device can be easily wrapped around an index finger (Figure A3.5D). The charge and discharge curves of the first cycle at 2 mA/cm are displayed in Figure 5E and followed by its cycling study (shown in Figure A3.5F). The complete battery design covering an area of ~8 cm^2 demonstrated an average discharge capacity of 0.48 mAh, with an effective areal capacity of 0.6 mAh/cm^2 for the 4.91 mm^2 area for 16 pairs of functional islands. The capacity decreased rapidly after several cycles and stabilized at 0.5 mAh. The poor cycling could be attributed to the poor electrical insulation of the serpentine interconnect and the dissolution of the anode into the electrolyte. Further optimization of the stretchable inks as well as the printed electrolyte could enable thin-film electrochemical devices for epidermal electronics.

A3.1.4 Conclusions

We have demonstrated the first “island-bridge” design for stretchable electronics that combines both deterministic and intrinsic composite architectures through an inexpensive, high-throughput screen-printing process. The stretchable deterministic devices are developed using novel elastic composite inks that can be tailored with any conductive fillers and polymers specific to the application. Mechanical deformation studies evaluating the serpentine designs and radial deformation of islands show the complexity of the island-bridge. The effect of the printed serpentine pattern upon the mechanical and electrical properties have been investigated along with the interface of the printed bridges with the printed islands. Composite inks of varied compositions and materials exhibit unique strain-stress profiles. These results highlight the complexity of the collective conformability of the printed "island-bridge." Further improvements to the conductive inks include high-aspect-ratio fillers, such as silver nanowires and carbon nanotubes that can be formulated. Other combinations of elastic polymer and conductive fillers can provide more durable and high-performance epidermal electronics. The challenge will be that ability to formulate the appropriate viscosity to print these fine features, a design of the stencils, a balance of rigid fillers with elastic polymers, and serpentine design.

Expensive and complex processing steps of lithographic, subtractive techniques have been the widely used to developed stretchable electronics. The low-cost and scalability of screen-printing introduces a cost-effective alternative to custom-design conformal electronics in a single, additive printing step. More importantly, the materials applicable to the semiconductor process are very limited; typically to one metal. The use of tailored ink formulations allows any combination of types, morphologies, or nanostructures of conductive fillers and composite materials that vary in complexity across any technology. The development of a printed IB can lead to a wide range of inexpensive stretchable electronics for a variety of applications. The serpentine designs are bound to the substrate, but mechanical durability can be improved by freeing the design from the substrate. The method of synthesizing and tailoring inks for large-scale printing of stretchable devices holds great promise for a new class of conformal electronics using printed “island-bridge” structures.

A3.2 References

1. Bandodkar, A.J., R. Nuñez-Flores, W. Jia, and J. Wang, *All-Printed Stretchable Electrochemical Devices.* Advanced Materials, 2015. **27**(19): p. 3060-3065.

2. Park, S.I., D.S. Brenner, G. Shin, C.D. Morgan, B.A. Copits, H.U. Chung, M.Y. Pullen, K.N. Noh, S. Davidson, S.J. Oh, J. Yoon, K.-I. Jang, V.K. Samineni, M. Norman, J.G. Grajales-Reyes, S.K. Vogt, S.S. Sundaram, K.M. Wilson, J.S. Ha, R. Xu, T. Pan, T.-i. Kim, Y. Huang, M.C. Montana, J.P. Golden, M.R. Bruchas,

R.W. Gereau Iv, and J.A. Rogers, *Soft, stretchable, fully implantable miniaturized optoelectronic systems for wireless optogenetics.* Nat Biotech, 2015. **33**(12): p. 1280-1286.

3. Gong, S., W. Schwalb, Y. Wang, Y. Chen, Y. Tang, J. Si, B. Shirinzadeh, and W. Cheng, *A wearable and highly sensitive pressure sensor with ultrathin gold nanowires.* Nature Communications, 2014. **5**: p. 3132.

4. Kim, J., R. Kumar, A.J. Bandodkar, and J. Wang, *Advanced Materials for Printed Wearable Electrochemical Devices: A Review.* Advanced Electronic Materials, 2017. **3**(1): p. 1600260-n/a.

5. Bandodkar, A.J., I. Jeerapan, J.-M. You, R. Nuñez-Flores, and J. Wang, *Highly Stretchable Fully-Printed CNT-Based Electrochemical Sensors and Biofuel Cells: Combining Intrinsic and Design-Induced Stretchability.* Nano Letters, 2016. **16**(1): p. 721-727.

6. Matsuhisa, N., M. Kaltenbrunner, T. Yokota, H. Jinno, K. Kuribara, T. Sekitani, and T. Someya, *Printable elastic conductors with a high conductivity for electronic textile applications.* Nature Communications, 2015. **6**: p. 7461.

7. Weng, W., P. Chen, S. He, X. Sun, and H. Peng, *Smart Electronic Textiles.* Angewandte Chemie International Edition, 2016. **55**(21): p. 6140-6169.

8. Jin, H., N. Matsuhisa, S. Lee, M. Abbas, T. Yokota, and T. Someya, *Enhancing the Performance of Stretchable Conductors for E-Textiles by Controlled Ink Permeation.* Advanced Materials, 2017: p. 1605848-n/a.

9. Lu, N. and D.-H. Kim, *Flexible and stretchable electronics paving the way for soft robotics.* Soft Robotics, 2014. **1**(1): p. 53-62.

10. Larson, C., B. Peele, S. Li, S. Robinson, M. Totaro, L. Beccai, B. Mazzolai, and R. Shepherd, *Highly stretchable electroluminescent skin for optical signaling and tactile sensing.* Science, 2016. **351**(6277): p. 1071-1074.

11. Wang, X., L. Dong, H. Zhang, R. Yu, C. Pan, and Z.L. Wang, *Recent Progress in Electronic Skin.* Advanced Science, 2015. **2**(10): p. 1500169-n/a.

12. Kumar, R., J. Shin, L. Yin, J.-M. You, Y.S. Meng, and J. Wang, *All-Printed, Stretchable Zn-Ag2O Rechargeable Battery via, Hyperelastic Binder for Self-Powering Wearable Electronics.* Advanced Energy Materials, 2016: p. 1602096-n/a.

13. Song, Z., X. Wang, C. Lv, Y. An, M. Liang, T. Ma, D. He, Y.-J. Zheng, S.-Q. Huang, H. Yu, and H. Jiang, *Kirigami-based stretchable lithium-ion batteries.* Scientific Reports, 2015. **5**: p. 10988.

14. Xu, S., Y. Zhang, J. Cho, J. Lee, X. Huang, L. Jia, J.A. Fan, Y. Su, J. Su, H. Zhang, H. Cheng, B. Lu, C. Yu, C. Chuang, T.-i. Kim, T. Song, K. Shigeta, S. Kang, C. Dagdeviren, I. Petrov, P.V. Braun, Y. Huang, U. Paik, and J.A. Rogers, *Stretchable batteries with self-similar serpentine interconnects and integrated wireless recharging systems.* Nature Communications, 2013. **4**: p. 1543.

15. Xie, K. and B. Wei, *Materials and Structures for Stretchable Energy Storage and Conversion Devices.* Advanced Materials, 2014. **26**(22): p. 3592-3617.

16. Ko, H.C., M.P. Stoykovich, J. Song, V. Malyarchuk, W.M. Choi, C.-J. Yu, J.B. Geddes Iii, J. Xiao, S. Wang, Y. Huang, and J.A. Rogers, *A hemispherical electronic eye camera based on compressible silicon optoelectronics.* Nature, 2008. **454**(7205): p. 748-753.

17. Fan, J.A., W.-H. Yeo, Y. Su, Y. Hattori, W. Lee, S.-Y. Jung, Y. Zhang, Z. Liu, H. Cheng, L. Falgout, M. Bajema, T. Coleman, D. Gregoire, R.J. Larsen, Y. Huang, and J.A. Rogers, *Fractal design concepts for stretchable electronics.* Nature Communications, 2014. **5**: p. 3266.

18. Mohan, A.M.V., N. Kim, Y. Gu, A.J. Bandodkar, J.-M. You, R. Kumar, J.F. Kurniawan, S. Xu, and J. Wang, *Merging of Thin- and Thick-Film Fabrication Technologies: Toward Soft Stretchable "Island–Bridge" Devices.* Advanced Materials Technologies, 2017: p. 1600284-n/a.

19. Trung, T.Q. and N.-E. Lee, *Recent Progress on Stretchable Electronic Devices with Intrinsically Stretchable Components.* Advanced Materials, 2017. **29**(3): p. 1603167-n/a.

20. Wang, Y., C. Zhu, R. Pfattner, H. Yan, L. Jin, S. Chen, F. Molina-Lopez, F. Lissel, J. Liu, N.I. Rabiah, Z. Chen, J.W. Chung, C. Linder, M.F. Toney, B. Murmann, and Z. Bao, *A highly stretchable, transparent, and conductive polymer.* Science Advances, 2017. **3**(3).

21. Park, M., J. Im, M. Shin, Y. Min, J. Park, H. Cho, S. Park, M.-B. Shim, S. Jeon, D.-Y. Chung, J. Bae, J. Park, U. Jeong, and K. Kim, *Highly stretchable electric circuits from a composite material of silver nanoparticles and elastomeric fibres.* Nat Nano, 2012. **7**(12): p. 803-809.

22. Li, R., M. Li, Y. Su, J. Song, and X. Ni, *An analytical mechanics model for the island-bridge structure of stretchable electronics.* Soft Matter, 2013. **9**(35): p. 8476-8482.

23. Su, Y., X. Ping, K.J. Yu, J.W. Lee, J.A. Fan, B. Wang, M. Li, R. Li, D.V. Harburg, Y. Huang, C. Yu, S. Mao, J. Shim, Q. Yang, P.-Y. Lee, A. Armonas, K.-J. Choi, Y. Yang, U. Paik, T. Chang, T.J. Dawidczyk, Y. Huang, S. Wang, and J.A. Rogers, *Stretchable Electronics: In-Plane Deformation Mechanics for Highly Stretchable Electronics (Adv. Mater. 8/2017).* Advanced Materials, 2017. **29**(8): p. n/a-n/a.

24. Fan, J.A., W.-H. Yeo, Y. Su, Y. Hattori, W. Lee, S.-Y. Jung, Y. Zhang, Z. Liu, H. Cheng, L. Falgout, M. Bajema, T. Coleman, D. Gregoire, R.J. Larsen, Y. Huang, and J.A. Rogers, *Fractal design concepts for stretchable electronics.* 2014. **5**: p. 3266.

25. Yang, S., Y.-C. Chen, L. Nicolini, P. Pasupathy, J. Sacks, B. Su, R. Yang, D. Sanchez, Y.-F. Chang, P. Wang, D. Schnyer, D. Neikirk, and N. Lu, *“Cut-and-Paste” Manufacture of Multiparametric Epidermal Sensor Systems.* Advanced Materials, 2015. **27**(41): p. 6423-6430.

26. Lipomi, D.J., *Stretchable Figures of Merit in Deformable Electronics.* Advanced Materials, 2016. **28**(22): p. 4180-4183.